



Universiteit
Leiden
The Netherlands

Towards artificial photosynthesis on the lipid bilayer of liposomes

Klein, D.M.

Citation

Klein, D. M. (2022, September 15). *Towards artificial photosynthesis on the lipid bilayer of liposomes*. Retrieved from <https://hdl.handle.net/1887/3458516>

Version: Publisher's Version

License: [Licence agreement concerning inclusion of doctoral thesis in the Institutional Repository of the University of Leiden](#)

Downloaded from: <https://hdl.handle.net/1887/3458516>

Note: To cite this publication please use the final published version (if applicable).

Towards artificial photosynthesis on the lipid bilayer of liposomes

Proefschrift

ter verkrijging van
de graad van doctor aan de Universiteit Leiden,
op gezag van rector magnificus prof.dr.ir. H. Bijl,
volgens besluit van het college voor promoties
te verdedigen op donderdag 15 september 2022
klokke 10.00 uur

door

David Maarten Klein
geboren te Haarlem
in 1993

Promotores:

Prof. dr. S. A. Bonnet

Prof. dr. A. M. Brouwer (Universiteit van Amsterdam)

Promotiecommissie:

Prof. dr. H. S. Overkleeft

Prof. dr. E. Bouwman

Prof. dr. L. J. C. Jeuken

Prof. dr. J. N. H. Reek (Universiteit van Amsterdam)

Prof. dr. J. A. Killian (Universiteit Utrecht)

This work has been financially supported by the Netherlands Organization of Scientific Research via a Holland Research School of Molecular Chemistry PhD scholarship

Printed by Gildeprint

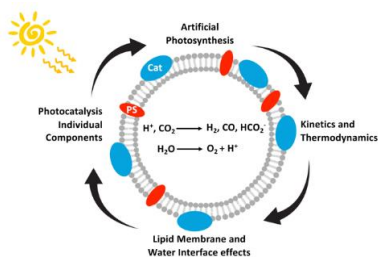
Table of contents

CHAPTER 1	7
Roadmap towards solar fuel synthesis at the water interface of liposome membranes	
CHAPTER 2	59
Unidirectional transmembrane photoinduced electron transfer with membrane-embedded metalloptides	
CHAPTER 3	75
Influence of the alkyl chain length of liposome-supported photosensitisers and catalysts for photocatalytic CO ₂ reduction	
CHAPTER 4	97
A stable alkylated cobalt catalyst for photocatalytic H ₂ generation in liposomes	
CHAPTER 5	117
Degradation of lipid-based drug delivery formulations during nebulisation	
CHAPTER 6	127
Summary, conclusions and outlook	
Appendix A	137
Supporting information for Chapter 1	
Appendix B	143
Supporting information for Chapter 2	
Appendix C	177
Supporting information for Chapter 3	
Appendix D	215

Supporting information for Chapter 4	
Samenvatting in het Nederlands	223
List of publications	228
Curriculum Vitae	230
Acknowledgements	232

Roadmap towards solar fuel synthesis at the water interface of liposome membranes

Artificial photosynthesis has experienced rapid developments aimed at producing photocatalytic systems for the synthesis of chemical energy carriers. Conceptual advances of solar fuel systems have been inspired by improved understanding of natural photosynthesis and its key operational principles: (a) light harvesting, (b) charge separation, (c) directional proton and electron transport between reaction centres and across membranes, (d) water oxidation and (e) proton or CO₂ reduction catalysis. Recently, there has been a surge of bio-inspired photosynthetic assemblies that use liposomes as nanocompartments to confine reaction spaces and enable vectorial charge transport across membranes. This approach, already investigated in the 1980's, offers in principle a promising platform for solar fuel synthesis. However, the fundamental principles governing the supramolecular assemblies of lipids and photoactive surfactant-like molecules in membranes, are intricate, and mastering membrane-supported photochemistry requires thorough understanding of the science behind liposomes. In this chapter, we provide an overview of approaches and considerations to construct a (semi)artificial liposome for solar fuel production. Key features to consider for the use of liposomes in solar fuel synthesis are highlighted, including the understanding of the orientation and binding of different components along the membrane, the controlled electron transport between the reaction centres, and the generation of proton gradients as driving force. Together with a list of experimental techniques for the characterisation of photoactive liposomes, this chapter provides the reader with a roadmap towards photocatalytic fuel production at the interface of lipid membranes and aqueous media.



This chapter has been published as a tutorial review: Andrea Pannwitz*, David M. Klein*, Santiago Rodríguez-Jiménez, Carla Casadevall, Hongwei Song, Erwin Reisner, Leif Hammarström, and Sylvestre Bonnet, *Chemical Society Reviews* **2021**, *50*, 4833-4855. * These authors contributed equally to this work.

1.1 Introduction to photocatalysis on lipid bilayers

1.1.1 Motivation

Natural photosynthesis provides a biological blueprint for a scalable process to store solar energy in the chemical bonds of complex organic molecules. In the light-dependent reactions of oxygenic photosynthesis, photon absorption in the thylakoid membrane drives water oxidation (Equation 1.1), which provides electrons and protons for the generation of the biological reductant dihydronicotinamide adenine dinucleotide phosphate (NADPH) together with energy carrier molecules of adenosine triphosphate (ATP). The latter are subsequently used in the dark reaction of the Calvin cycle to fix CO₂ as carbohydrates (Equation 1.2), or to reduce protons (Equation 1.3) in photobiological H₂ production by redirecting reduced nicotinamide-adenine-dinucleotide (phosphate) (NAD(P)H) towards hydrogenases in some unicellular algae and cyanobacteria under special conditions.^{1,2}

Water oxidation half reaction		E° (V) vs SHE at pH 7	
2 H ₂ O	→ O ₂ + 4 H ⁺ + 4 e ⁻	0.81	Equation 1.1
Proton and selected CO ₂ reduction half reactions		E° (V) vs SHE at pH 7	
6 CO ₂ + 24 H ⁺ + 24 e ⁻	→ C ₆ H ₁₂ O ₆ + 6 H ₂ O	-0.43	Equation 1.2
2 H ⁺ + 2 e ⁻	→ H ₂	-0.41	Equation 1.3
CO ₂ + 2 H ⁺ + 2 e ⁻	→ CO + H ₂ O	-0.53	Equation 1.4
CO ₂ + H ⁺ + 2 e ⁻	→ HCO ₂ ⁻	-0.39	Equation 1.5
CO ₂ + 6 H ⁺ + 6 e ⁻	→ CH ₃ OH + H ₂ O	-0.38	Equation 1.6

The thylakoid membrane consists of the supramolecular assembly of lipids and additives into a flexible, fluid two-dimensional membrane that hosts an array of protein units that organise the light reactions and separate them from the dark reactions. The absorption of solar energy occurs mainly via chlorophylls and accessory pigments in the light harvesting complexes (LHCs), which act as antenna for light collection (Figure 1.1, left). The chlorophylls pass energy through a series of chromophores on to the reaction centres of Photosystems II (PSII) and I (PSI), where the central chlorophyll pigments P680 and P700, respectively, induce charge separation and subsequent unidirectional electron transfer. Such electron transfer occurs over a long distance, and follows an electron transport chain of small-

distance electron transfer steps within the protein scaffold and redox mediators of the thylakoid membrane.³ Overall, long-lived charge separation across the thylakoid membrane is achieved with high quantum efficiency via a Z-scheme energy-storage architecture. Electrons are first transferred from the photoexcited P680 in PSII to the plastoquinones (PQs) embedded in the thylakoid membrane, then to the Cytochrome b_6f complex (Cyt_{b_6f}), where plastocyanin collects the electrons to reduce $P700^+$ in PSI.³ The latter is an oxidised species generated from photoexcitation of PSI and electron transfer to ferredoxin (Fd, an iron-sulfur protein) and ferredoxin NAD(P)⁺ reductase (FNR) in the stroma of the chloroplasts. Ultimately, P680 is regenerated in PSII by electrons liberated from water oxidation in the lumen. The unidirectional flow of electrons and protons across the membrane generates a proton gradient that powers the conversion of ADP to ATP by ATP synthase (ATP_{ase} , Figure 1.1, left).

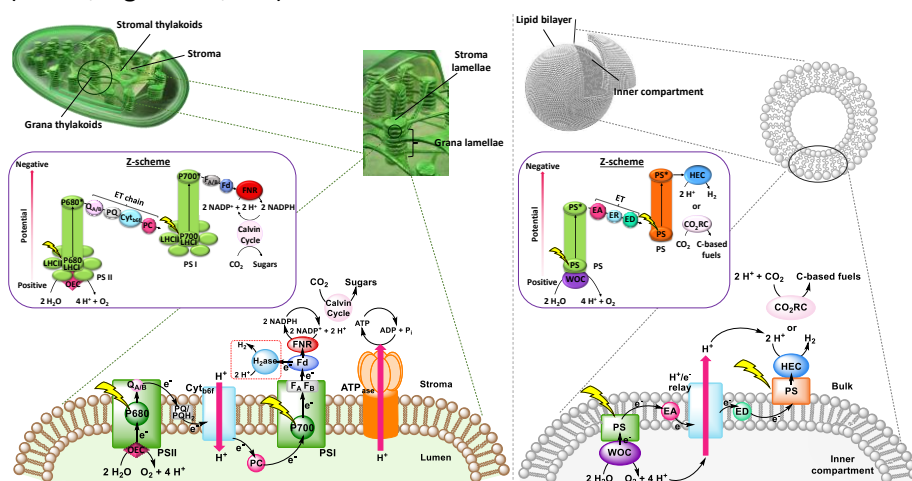


Figure 1.1. Left: Scheme of a natural chloroplast showing light-induced charge transfer across the thylakoid membrane, connecting PSII, PSI and the reaction centres for CO_2 reduction and ATP generation. The left inset shows the respective energy-storing Z-scheme pathway. Right: Scheme of a synthetic vesicle as a platform for an artificial photosynthetic assembly. The right inset shows the respective Z-scheme. PC = photoredox catalyst, PSI = photosystem I, PSII = photosystem II, Ph = pheophytin, PQ = plastoquinone, PC = plastocyanin, b_6f = cytochrome b_6f , Fd = ferredoxin, FNR = ferredoxin-NADP⁺ reductase, LHCI = light-harvesting complex I, LHCI = light-harvesting complexes II, OEC = oxygen evolving complex, P680 and P700 = reaction centres in PSII and PSI respectively, WOC = water oxidation catalyst, PS = photosensitiser, EA = electron acceptor, ED = electron donor, HEC = hydrogen evolution catalyst, CRC = CO_2 reduction catalyst, and ER = electron relay.

A crucial feature of the thylakoid membrane is that it separates the oxidative from the reductive catalytic centres by compartmentalisation of the different redox half-reactions within the chloroplast lumen and stroma (Figure 1.1, left). Such organisation minimises charge recombination reactions, which by recombining holes and electrons, or oxidised and reduced molecular species, are detrimental for the reaction. PSI and ATP_{ase} do not fit into the space between the stacked membranes and are therefore mainly located in the stromal lamellae. PSII is located in the grana lamellae and thereby spatially separated from PSI and ATP_{ase}, preventing the uncontrolled spill-over of excitons from PSII to PSI.⁴ This heterogeneity of the thylakoid membrane maximises the packing density of photosynthetic complexes and plays an important role in optimising light harvesting and energy transfer under changing light conditions. In contrast, established approaches in artificial photosynthesis rarely take compartmentalisation into account.⁵⁻⁷

Mimicry of natural photosynthesis by synthetic design is an appealing strategy for the development of sustainable methodologies to produce solar fuels. Apart from the electrocatalytic oxidation of water into oxygen with the concomitant release of protons, and the reduction of CO₂ and water into carbon-based fuels and H₂, respectively, light harvesting with various photosensitisers and charge separation have been investigated. The concept of using self-assemblies in biomimetic lipid bilayer membranes for artificial photosynthesis was already approached in the 70's and 80's,⁷ but is receiving increased attention today due to the dramatically improved choice of catalysts and photosensitisers that can be spatially arranged to generate transmembrane potentials and compartmentalised artificial photosynthetic systems (Figure 1.1, right).^{7,8} The use of the spherical membranes of liposomes as biologic mimics of the thylakoid membrane is a promising approach to confine redox half reactions, facilitate charge separation, and avoid cross-reactivity. While synthetic catalysts are continuously improving in terms of stability and activity in solar-to-chemical conversion, nature also provides evolutionarily optimised biological catalysts (enzymes) that are also appealing for building semiartificial photosynthetic systems due to their excellent catalytic activity.⁹ Amphiphilic polymers have also been proposed as alternative for lipids, as they can be tuned to self-assemble into thicker

and often more solid membranes, though sometimes at the cost of biocompatibility (e.g., to accommodate transmembrane proteins). Photocatalytic polymersomes are also part of a larger effort to develop compartmentalised vesicle-based catalytic systems^{10–13} for tandem catalysis, which has been reviewed elsewhere and remains out of the scope of this chapter. This roadmap focuses on lipid-based photocatalytic vesicles for biomimetic solar fuel production, provides guidelines on how to construct such liposomes, and helps understanding the basic physical-chemical concepts, opportunities, and challenges, of using self-assembled lipid bilayer membranes as a supramolecular platform for (semi)artificial photosynthesis.

1.1.2 Lipid bilayers

Lipid bilayers are supramolecular self-assemblies formed from amphipathic lipids in an aqueous solution. Generally speaking, amphipathic (or amphipolar) molecules consist of a polar moiety (*i.e.*, a hydrophilic head group), covalently connected to a non-polar hydrophobic part (*e.g.*, an alkyl chain). Usually, lipids are also amphiphilic in the sense that they possess affinity for both aqueous and oil-like phases, with their preference expressed by their log P value (see below). Most amphipathic molecules are also amphiphilic, and consequently both terms “amphiphilic” and “amphipathic” are usually used as synonyms, although they are conceptually different. One should also note that some lipids can be plain hydrophobic, such as cholesterol or fat (triglycerides), in which case they are not amphipathic enough to generate bilayers in water. In all cases, for amphiphilic lipid molecules the polar head groups interact with water *via* ion-dipole or dipole-dipole interactions when exposed to an aqueous environment, whereas the interaction of the hydrophobic alkyl chain is unfavourable with water, leading to the hydrophobic effect that causes the hydrophobic groups to interact. In the case of lipids, the resulting self-assembled structure is a bilayer membrane, which generates an interface between the water phase and the more hydrophobic environments of the interior of the membrane. This hydrophobic environment can also be observed in oil-water emulsions, in foams, or in micelles-containing aqueous solutions.

Due to their amphiphilicity, lipids are also surface-active and hence surfactants. Surface activity and interfacial behaviour can be measured via tensiometry (surface pressure measurements). At a low concentration in water, surfactant amphiphiles concentrate at the interface to air, and with increasing surfactant bulk concentration, the surface tension is increasingly lowered with no aggregation being observed in the bulk solution. Increasing the surfactant concentration further will reach a point known as the critical micelle concentration (CMC), where aggregates start forming in the bulk aqueous phase. At concentrations above the CMC, only a very small fraction of the surfactant is dissolved as monomers in water ($c_{\text{max}} = \text{CMC}$), while all other molecules are dynamically forming self-assembled aggregates. Depending on the surfactant's molecular geometry, different self-assemblies may form, such as micelles, reverse micelles, bilayers, and vesicles. Lipids typically form bilayer membranes and vesicles. Depending on the lipids, addition of salts and differences in temperature may induce changes in aggregation dynamics and hence in the CMC.

Lipids can generally be classified according to their head groups: zwitterionic, anionic, cationic, and non-ionic.¹⁴ Examples for each class of bilayer-forming lipids are depicted in Figure 1.2: the zwitterionic 1,2-dipalmitoyl-sn-glycero-3-phosphocholine (DPPC), the anionic 1,2-dimyristoyl-sn-glycero-3-phosphonate(1'-rac-glycerol) (sodium salt) (DMPG), the cationic 1,2-dioleoyl-sn-glycero-3-[phospho-rac-(3-lysyl(1-glycerol))] (chloride salt) (O-Lysyl PG), and the non-ionic 1-palmitoyl-2-oleoyl-3-bis(β -D-glucosyl)-sn-glycerol (16:0-18:1 GlcGlcDAG). Further distinction can be made according to the counterion (Cl^- , Br^- , I^- , Na^+ , K^+ etc.) or the chemical character of the alkyl chain (e.g., hydrocarbon or fluorocarbon, saturated or unsaturated).

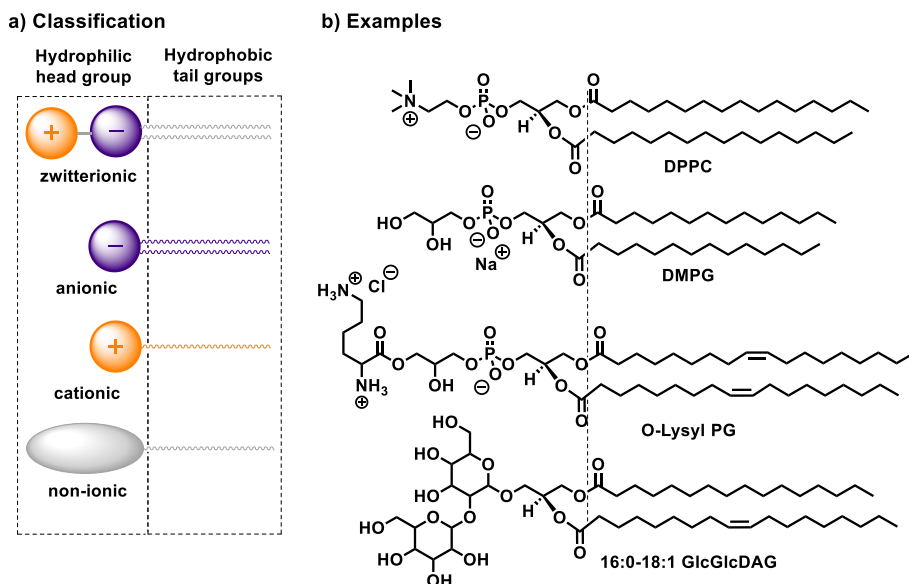


Figure 1.2. a) Classification^{14,15} and b) practical examples of bilayer-forming amphiphiles: DPPC, DMPG, O-Lysyl PG, and 16:0-18:1 GlcGlcDAG.

A common way to characterise the hydrophilicity and hydrophobicity of a molecule is to determine its water-octanol partition coefficient ($\log P$). This dimensionless number is obtained by measuring experimentally the concentrations c_{oct} and c_{water} of the molecule in each phase of a biphasic n-octanol/water mixture at the thermodynamic equilibrium. Then, the decadic logarithm, $\log P$, is calculated as follows (Equation 1.7):

$$\log P = \log (c_{\text{oct}}/c_{\text{water}}) \quad \text{Equation 1.7}$$

Typically, hydrophilic compounds like tetraethylammonium iodide ($\text{Et}_4\text{N}^+\text{I}^-$) have a low negative $\log P$ value (-2.82)¹⁶ and more hydrophobic compounds like triethylamine (Et_3N) have a high, positive $\log P$ value ($+1.44$)¹⁶. Amphiphilic molecules have a $\log P$ value close to zero, *i.e.* at the equilibrium, they distribute in similar quantities in the octanol and aqueous phases. For example, nitromethane has a $\log P = 0.08$,¹⁶ even if this molecule is not expected to have surface-active properties. On the other hand, decyltrimethylammonium iodide (C13, $\log P = -0.16$)¹⁶ has one carbon less than the water-soluble tributylethylammonium iodide (C14, $\log P = -1.30$)¹⁶,

but due to its single long alkyl tail it is more hydrophobic, also reaching a zone of less negative log P values typical for amphiphilic molecules. In addition, due to its dissymmetric “head-tail” geometry it has surface-active properties, which is also typical for lipids. One should note that other concepts to characterise surfactant-like molecules have been proposed, such as the “hydrophilic lipophilic balance” (HLB). This numerical approximation characterises the interfacial behaviour of an amphiphile in the presence of a mixture of an organic solvent and water, as described in details elsewhere.¹⁴

In absence of organic co-solvents, amphiphiles dissolved in water usually form either membrane bilayers or micelles, depending on their geometry and steric properties.¹⁷ For bilayer formation the most suitable geometry of an amphiphile is close to a cylindrical shape (Figure 1.3a). On the other hand, to obtain spherical and rod-shaped micelles a conical shape of the amphiphile is required (Figure 1.3b). To assess a priori if an amphiphile forms bilayers or micelles, the packing parameter x can be used (Equation 1.8).

$$x = v / (a_0 \cdot l_c) \quad \text{Equation 1.8}$$

In Equation 1.8, v is the volume of the hydrophobic part, a_0 is the area of the headgroup at the surface, and l_c is the length of the hydrophobic tail.¹⁷ The values for v , a_0 , and l_c can be obtained from crystallographic data of the amphiphile or molecular modelling. Spherical micelles are the preferred structure when $x \leq 1/3$, non-spherical micelles when $1/3 < x < 1/2$, cylindrical or rod-like micelles when $x \approx 1/2$, above $x = 1/2$ various interconnected structures, and finally curved to planar bilayers when x approaches or equals 1.¹⁷ For example, phospholipids such as DPPC have commonly $x > 0.67$ and self-assemble into curved bilayers, i.e., vesicles.¹⁷ The size of these self-assembled micelles or lipid bilayer vesicles can be measured via dynamic light scattering (DLS). As discussed before, these aggregates only form at bulk lipid concentrations higher than the critical micelle concentration (CMC). Bilayer-forming lipids usually have a very low CMC compared to micelle-forming amphiphiles. For instance, the zwitterionic phospholipid DPPC has a CMC of 4.6×10^{-10} M,¹⁵ while the micelle-forming hexaethylene glycol monododecyl ether has a CMC of 8.7×10^{-5} M.¹⁴ Overall, the self-assembly of lipids depends

on many intrinsic molecular properties of a lipid such as its charge, rigidity, size, and the hydrophilicity/hydrophobicity of its polar and apolar parts; but it also largely depends on the experimental conditions, including (and not limited to) the lipid bulk concentration, the temperature, the presence of salts or additives in the aqueous solution, and the composition of a lipid mixture, for example.

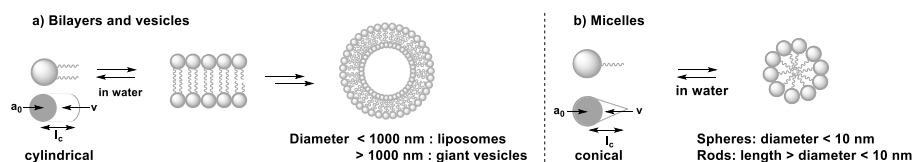


Figure 1.3. a) Self-assembly of cylindrical amphiphiles in water into bilayers and vesicles. b) Self-assembly of conical amphiphiles in water into spherical and rod-shaped micelles.

1.1.3 Individual components for artificial photosynthesis at lipid bilayers

Several synthetic or biological functional components are necessary to build a compartmentalised system for artificial photosynthesis.⁶ Basically, these functional molecules can be divided into four main categories: photosensitisers, catalysts, sacrificial reagents, and charge carriers. Important considerations have been established over the years to target these components towards different regions of the lipid bilayer and construct photocatalytic membranes. These considerations can be sorted into the four following general strategies (Figure 1.4): a) covalent attachment of the functional group to a lipid that inserts in the membrane, b) electrostatic attraction of charged functional molecules to the charged head groups of the lipids, c) integration of the functional group into an amphiphilic molecule, which targets the interface between the bulk water phase and the hydrophobic core of the lipid membrane, and d) building enough hydrophobicity in the functional molecule to embed it within the hydrophobic core of the membrane.

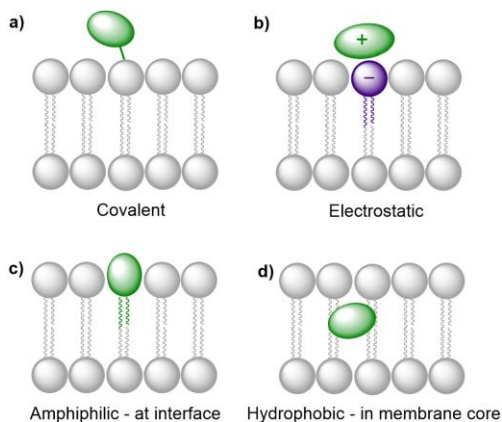


Figure 1.4. Strategies to integrate functional molecules in lipid bilayer membranes.

Photosensitisers. A photocatalytic cycle starts with irradiation of a photosensitiser (PS), yielding an electronically excited species, PS^* , which can act as a strong oxidant or reductant (Figure 1.5).¹⁸ Quenching of the excited state via electron transfer with an electron donor (ED, reductive quenching), or electron acceptor (EA, oxidative quenching) generates the respective reduced (PS^-) or oxidised (PS^+) species. These reactive species may transfer their charge to the catalyst which undergoes further substrate reduction or oxidation, respectively. However, at each step of this charge transfer chain charge recombination may occur between an oxidised donor and a reduced acceptor. Achieving efficient artificial photosynthesis requires productive charge transfer towards the photoproduct to be faster than charge recombination. Furthermore, there are three additional obstacles when PSs are incorporated into lipid bilayer membranes, and all of them are related to their high local concentration. Firstly, excited states PS^* may quench each other by mechanisms such as triplet-triplet annihilation between two molecules. Secondly, self-quenching (concentration quenching) may occur by other PS molecules in their ground state. Thirdly, liposome dimensions are similar to the wavelength of visible light, and at a high local concentration of PS the light available to each PS is reduced. While this does not decrease harvesting efficiency of the incoming light, it means that each PS is running less efficiently, and that one maybe uses an unnecessary high amount of PS. Similarly, a high bulk concentration of PS may reduce light penetration into the solution, and make a large part of the solution rather inactive. These

effects could be countered by using a low PS loading to maximise the photon energy available to the system (*i.e.*, increase quantum yield and efficiency);¹⁹ although this strategy may also lead to a decreased solar energy conversion yield. The same considerations are important in the design of photobioreactors with photosynthetic microorganisms, and genetic reduction of the photosynthetic antenna is a strategy to find an optimum between a high cell concentration and good light penetration. The use of compartmentalisation in liposomes should be an appropriate strategy to improve the PS efficiency and performance. For instance, natural light-harvesting antennas employ close proximity of many pigment molecules and self-quenching via energy transfer is avoided by careful control of intermolecular distances and electronic coupling.²⁰

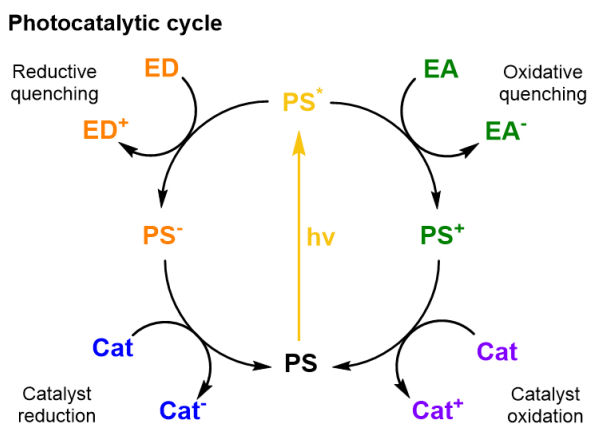


Figure 1.5. Schematic photocatalytic cycles of a PS including quenching reactions with an ED or EA and the reductive and oxidative reactions with a catalyst.

Thermodynamics (*i.e.*, redox potentials in ground and excited states), and kinetics (*i.e.*, excited state lifetime and charge transfer dynamics) must be well orchestrated in different PSs to couple efficient light collection with electron transfer and catalysis within the assembled components.⁶ Furthermore, the spectral properties of the PS influence its ability to absorb photons. The most relevant properties here are how the absorption spectrum (extinction coefficient) of the PS overlaps with the irradiance spectrum of the light source (e.g., the sun); what are the relative quantum yields for non-radiative deactivation, electron transfer, and photon emission;

and last but not least, what is the photostability of the PS under photocatalytic conditions. Ideally, the other components of the system should show little absorption where the PS absorbs most, to avoid competition for light (filter effect) and photon loss.

One of the most widely used type of PS molecules are polypyridine ruthenium(II) complexes such as $[\text{Ru}(\text{bpy})_3]\text{Cl}_2$ (**PS1**, bpy = 2,2'-bipyridine, Figure 1.6a).^{6,18} The positive charge of this complex and the limited hydrophobicity of the bipyridine ligands makes it quite hydrophilic ($\log P = -2.50$),²¹ which prevents it from interacting strongly with positively charged or neutral lipid bilayers. A negatively charged membrane is therefore required to attract **PS1** electrostatically (Figure 1.4b). An alternative strategy consists in functionalising the bpy ligand in **PS1** with hydrophobic groups such as alkyl chains, to yield the amphiphilic analogues **PS2** and **PS3** (Figure 1.6a). These molecules can be readily immobilised within lipid bilayers (Figure 1.4c). For instance, **PS2** was employed in lipid vesicles for photocatalytic hydrogen evolution¹⁹ and water oxidation reactions,^{22,23} whereas **PS3** was used in unilamellar vesicles for photocatalytic carbon dioxide reduction.²⁴ In the presence of a lipid bilayer these amphiphilic molecules may either assemble at the interface (Figure 1.4c), if the alkyl chains in **PS3** are not too long and the counter anion (e.g. Cl^-) solubilises the dicationic head in the water phase; or, they may integrate deeper within the membrane (Figure 1.4d) with longer, more hydrophobic alkyl chains and more hydrophobic counter anions (e.g., PF_6^-). Another classical family of PSs consists in metal porphyrins and includes for example **PS4**, **PS5** and **Chla** (Figure 1.6a). **PS4** and **PS5** were immobilised in charged vesicles to study charge recombination²⁵ and transmembrane charge transport,²⁶ respectively. The biological PS **Chla** (Figure 1.6a) acts as a visible-light harvesting unit in PSI and PSII, and was utilised in charged micelles for photocatalytic hydrogen evolution.²⁷

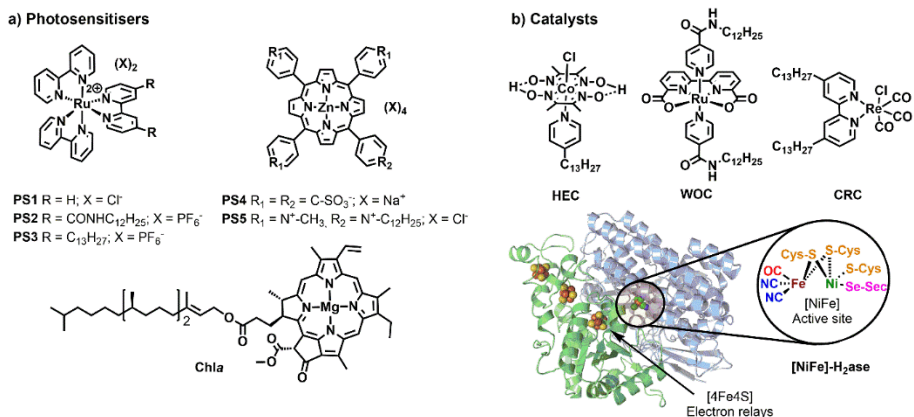


Figure 1.6. Synthetic and biological (a) PSs and (b) catalysts used to build photocatalytic vesicular and micellar systems. X = counterion, HEC = hydrogen evolution catalyst, WOC = water oxidation catalyst, CRC = CO₂ reduction catalyst, H₂ase = crystal structure of oxygen-tolerant [Ni-Fe]-hydrogenase enzyme, obtained from bacterium *Desulfomicrobium baculatum* (pdb: 1CC1).

It should be noted that the integration of the PS into the membrane has often a significant effect on its electronic and photochemical properties. Despite the currently unpredictable effects of the membrane environments on the properties of the integrated components, ligand modifications (e.g. covalent attachment of alkyl groups) can tune the photophysical and redox behaviour of the PSs as well,¹⁸ or that of other active components (see below), making the spectroscopic and electrochemical characterisation of newly synthesised components fundamental to reach an efficient self-assembled system. Last but not least, the primary input in a photocatalytic system is the rate of formation of excited states, or rate of photon absorption. This photochemical input depends not only on the PS concentration, but also on the molar absorption coefficient of the PS at the irradiation wavelength, and on light intensity. The quantum yield of product formation can be calculated by the measured rate of product formation, divided by the rate of photon absorption.

Catalysts for solar fuel production are commonly redox active metal complexes that can accumulate charges (either electrons and/or protons) to facilitate bond-making and bond-breaking reactions such as hydrogen evolution, CO₂ reduction, or water oxidation. Examples for catalysts that have been supported on lipid bilayers and micelles are depicted in Figure 1.6b. Hydrogen evolution was performed with an alkylated cobaloxime-based hydrogen evolution catalyst (**HEC**) in zwitterionic vesicles and with a hydrogenase in charged micelles.^{19,28} An alkylated rhenium CO₂ reduction catalyst (**CRC**) was employed to study photocatalytic CO₂ reduction in zwitterionic vesicles.²⁴ Photocatalytic water oxidation in vesicles was achieved with an alkylated version of a Ru-based water oxidation catalyst (**WOC**).²³ More examples of catalysts, which could be potentially employed upon ligand modification in vesicles, are reported elsewhere.^{6,29}

To select a suitable catalyst, several performance metrics such as catalytic activity, product selectivity, and stability, need to be considered. The catalytic activity is characterised by the turnover number (TON_{Cat}) and turnover frequency (TOF_{Cat}). TOF_{Cat} is a measure of the product generation rate, given as the number of moles of products produced per mole of catalyst in the system and per unit time. The TON_{Cat} at a certain time *t*, is the total number of product molecules generated at that moment per molecule of catalyst initially introduced in the system. While in catalysis under dark conditions, catalyst decomposition often explains why the reaction stops, in photocatalysis the end of a photocatalytic reaction may also be due to PS degradation. For photocatalytic systems it is thus equally important to assess the PS stability. Here, we refer to TON_{PS} and TOF_{PS} when referencing the TON or TOF of the system to the amount of PS initially introduced. It should also be noted that sometimes, pH changes or consumption of the sacrificial reagent may also be involved in the end of the photocatalytic reaction.

A catalyst requires a certain driving force (i.e., redox potential) to generate the catalytically active species. The difference between this catalytic onset potential and the thermodynamic potential (see Equations 1.1-1.6) is known as the overpotential. In an ideal scenario, a high reaction rate is reached at a small overpotential. In a photochemical system, the “applied” potential

corresponds to the redox potential of the reduced or oxidised ground state of the PS, and it should match the overpotential requirement of the catalyst. Particularly important in CO₂ reduction is product selectivity, because co-generation of H₂ and other carbon-based reduction products readily occurs in CO₂-saturated aqueous solutions. Stability is especially challenging in water oxidation catalysis, where organic ligands often degrade under the highly oxidising conditions and evolved O₂.³⁰ The performance of catalysts is commonly assessed in homogeneous solution, but the hydrophobic anchoring groups and the membrane environment will affect the catalytic properties.²⁹

Biological catalysts (enzymes) operate commonly with intrinsically low overpotentials and are therefore efficient model catalysts in semiartificial photocatalytic systems,^{2,10} including semiartificial photocatalytic micellar systems and electrocatalytic bilayer lipid membranes.^{29,31} These excellent catalytic capabilities are mainly due to their evolutionary-optimised architecture in which the protein environment facilitates the catalytic transformation at the active site by controlling substrate access and orientation as well as stabilising transition states of catalytic intermediates. Some examples are hydrogenase ($\text{H}^+ \leftrightarrow \text{H}_2$; Figure 1.6b), formate dehydrogenase ($\text{CO}_2 \leftrightarrow \text{formate}$), carbon monoxide dehydrogenase ($\text{CO}_2 \leftrightarrow \text{CO}$) enzymes, and PSII for light-driven water oxidation.^{1,2,9} Despite their excellent performance, these enzymes are costly to isolate, fragile, and often display O₂-sensitivity, which can make them difficult to handle. Their suitability for the integration in photocatalytic systems also requires consideration of cofactor dependence (e.g. NADH) and substrate affinity. The latter is expressed by the Michaelis-Menten constant (K_M), which is low for high substrate affinity. The use of compartmentalised vesicles allows the encapsulation of enzymes within the vesicles with low substrate affinity and provide them with the required high local concentration of substrate as in living cells. The reader is referred to references^{1,9} for a more detailed discussion on selection criteria for enzymes.

Sacrificial ED and EA reagents are widely used in artificial photosynthesis when studying half-reactions, although the ultimate goal is to use a sustainable source of charge to drive a closed redox cycle.³² They serve as reductive and oxidative equivalents used to quench a photoexcited PS (PS^* , Figure 1.5), or regenerate the PS after reductive or oxidative quenching by a primary quencher. This reduces the possibility for charge recombination as they commonly decompose quickly and irreversibly. The use of sacrificial reagents allows investigating and optimising individual half-reactions such as proton/ CO_2 reduction or water oxidation without the demanding requirement to couple both half reactions with a single charge carrier. The choice of ED and EA is generally based on their redox potentials, rapid photooxidation and reduction in the presence of PS^* and, ideally, producing harmless intermediates and products, although non-innocent decomposition by-products are sometimes generated. Some of the most commonly used ED in aqueous media for light-driven proton and CO_2 reduction are mild reducing agents such as triethanolamine, ethylenediaminetetraacetic acid (EDTA), and ascorbic acid.³² On the other hand, one of the most common EA used in light-driven water oxidation reactions is the strong oxidising agent sodium peroxodisulphate ($Na_2S_2O_8$);⁶ $[Co(NH_3)_5Cl]Cl_2$ has been proposed as well, but its propensity to form catalytically active cobalt oxides is problematic, in particular in the context of the water oxidation reaction. One should note that the conditions used for many photocatalytic water oxidation experiments, i.e. near-neutral pH and $Na_2S_2O_8$ as EA, are drastically different from the conditions in which chemically driven water oxidation catalysts are usually tested, which involves strong concentrations of cerium ammonium nitrate (CAN) and highly acidic solution (pH = 1).

Charge carriers are redox active species capable of transporting reducing or oxidising equivalents between different components of a photocatalytic system (Figure 1.7a). A typical example is the water-soluble, dicationic methyl viologen (MV^{2+}), which can accept one electron to form the blue-coloured cation radical $MV^{\bullet+}$. In some cases, charge carriers can undergo proton-coupled electron transfer (PCET) and carry electrons and protons across lipid membranes; good examples are the membrane-soluble 1-methoxy-*N*-methylphenazinium cation (MMP^+), or the quinones 2,5-

diphenyl-1,4-benzoquinone (**Q_s**) and decylubiquinone (**dQ**).^{26,33} The thermodynamic and kinetic features of charge carriers must also be carefully considered to ensure an efficient unidirectional electron transfer. Furthermore, the chemical stability and solubility of the charge carrier must be high in the relevant redox and protonation states (Figure 1.7a). For example, in presence of O₂ the one-electron reduced species **MV^{•+}** is re-oxidised into **MV²⁺**, which can be problematic in full water-splitting schemes also producing O₂.

The electrostatic charge of a carrier can also be exploited to enhance ET kinetics or minimise charge recombination due to electrostatic repulsion or attraction.²⁵ Other features to consider are whether the reduced or oxidised charge carrier acts innocently, i.e. it exclusively engages in an outer-sphere ET reaction, or non-innocently, i.e. it can undergo side reactions such as a disproportionation reaction (e.g. $2 \text{MV}^{\bullet+} \rightarrow \text{MV}^{2+} + \text{MV}^0$) or reacts with O₂ present in solution.³⁴ The affinity of the charge carrier for the catalyst should also be considered, as it could disrupt catalysis by coordinatively binding to the catalytically active metal centre. Another aspect to consider are changes in the pK_a value due to reduction or oxidation of the charge carrier, which could influence catalysis. Moreover, the effect of membrane environments can tune features of the catalyst such as its redox potentials, which are typically measured electrochemically in bulk organic solutions. In addition to the presented metal-free charge carriers (Figure 1.7a), water-soluble metal-based complexes, such as cationic cobalt tris-bipyridine complex, [Co(bpy)₃]^{2+/3+}, could be conceptually appropriate reductive and oxidative equivalent carriers, however because of the similarity with other synthetic components (e.g. the water oxidation or proton reduction catalyst) they may potentially act undesirably. Other hydrophilic electron relays such as I⁻/IO₃⁻ and Fe³⁺/Fe²⁺ have also been used. Compartmentalised vesicles have also been proposed that use lipophilic charge carriers to transport electrons and protons across vesicle membranes between spatially separated reaction centres. For example, membrane-bound cytochrome MtrCAB proteins (Figure 1.7b) have been proposed as biological molecular wires and membrane-embedded artificial reaction centres, which artificial quinone-porphyrin-carotenoid triads (**Q-P-C**, Figure 1.7c)^{33,35} try to mimic. Overall,

transporting the reductive equivalent from the site of water oxidation to the site of proton or CO₂ reduction requires charge carriers that are metastable in two different oxidation states, and do not react too quickly with the photogenerated products O₂, H₂, and/or reduced form of carbon dioxide.

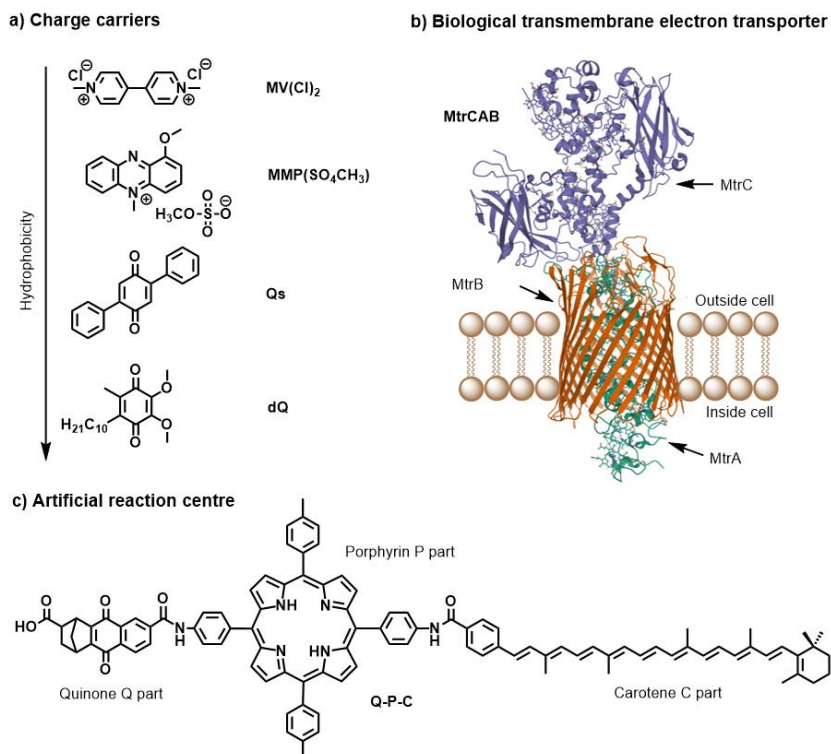


Figure 1.7. Molecular structures of (a) metal-free charge carriers, (b) crystal structure of biological electron transmembrane transporter icosaheme cytochrome protein MtrCAB from bacterium *Shewanella baltica* (pdb: 6R2Q), with cellular lipid bilayers and its three subunits, and (c) artificial reaction centre Q-P-C used to light-induce proton transport across vesicle membranes.^{33,35}

To conclude, not only the position in the membrane, but also the number of electrons exchanged by the different components of the membrane during photocatalysis, should be considered carefully. Overall, natural photosynthesis requires at least eight photons in both photosystems to extract four electrons and protons from two water molecules in PSII, and to deliver these electrons one by one for the two-electron reduction of two

NAD(P)⁺ molecules via Cytochrome b6f (Cyt b6f) to PSI, while protons are passed one by one through the membrane by stepwise rotation of ATPase, thereby generating ATP (Figure 1.1, left). Likewise, there is often a mismatch in the number of electrons (or charges) exchanged by the different components of an artificial photosynthesis system (Figure 1.1, right). Typically, one electron is exchanged between an excited photosensitiser molecule and a charge carrier such as ascorbate or MV²⁺, while two electrons are needed for long-distance charge transporters such as quinones or MMP⁺, two to eight electrons are needed for catalytic fuel production, and four electrons are provided by water oxidation. This discrepancy in principle requires careful analysis of the kinetics of each electron transfer step, to understand how they may integrate in a solar fuel production system.

1.2 The hydrophobic membrane

1.2.1 Properties of the membrane

Natural cell membranes are two-dimensional (2D) flexible liquid crystals that can adjust easily to environmental mechanic stress and provide a fluid “solvent” for membrane proteins as well as high mobility for mass transport within the membrane. Depending on the application, more rigid membranes can also be prepared.^{6,24,26} Most membranes indeed can exist in different phases, typically a liquid-crystalline phase with high lateral diffusion of the lipids, and a gel-like or even “solid” phase, characterised by much lower lateral diffusion properties (Figure 1.8). A membrane with the desired phase, flexibility, and mobility, can be constructed from either pure lipids or from lipid mixtures. In the former case, transition temperatures (T_m) from the gel phase to the liquid crystalline phase are tabulated for most lipids (see Table 1.1).¹⁵ Additives such as cholesterol and lipid mixtures can fine-tune the properties of the membrane. Experimentally, T_m can for example be obtained from fluorescence anisotropy measurements with a membrane-solubilised probe,³⁴ or differential scanning calorimetry.

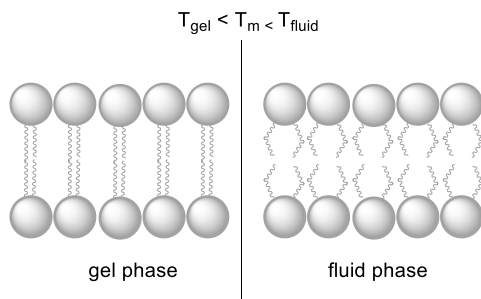


Figure 1.8. A lipid bilayer changes from the rigid gel phase (left) to the mobile fluid phase (right) above the transition temperature (T_m) of the lipid.

Molecularly, the phase of the lipid bilayer is influenced by the number and length of the alkyl chains, their degree of unsaturation, the headgroup structure (i.e. its size, electrical charge, and polarity), and the presence of additives such as other amphiphiles or cholesterol to the membrane. Saturated chains (such as DPPC) allow for closer packing than the less flexible and bulkier unsaturated chains (such as 1,2-dioleoyl-*sn*-glycero-3-phosphocholine, DOPC), and longer chains maximise hydrophobic interactions. These features explain the large variation in gel-to-liquid crystalline transition temperatures T_m between lipids such as DPPC and DOPC. The lateral and transverse diffusion of lipids and active components in the lipid bilayer are influenced by the mobility of the medium and hence the phase of the lipid bilayer. Diffusion coefficients for 2D lateral mobility in liquid crystalline bilayers are on the order of $\mu\text{m}^2\text{s}^{-1}$, while the values in the gel phase are several orders of magnitude lower. The lateral mobility describes the mobility of a lipid molecule (or photoactive component in the membrane) parallel to the water-membrane interface and within one of the monolayers forming the membrane. Transversal diffusion from one monolayer to the other, also called “flip-flop”, requires intermediates states where the hydrophilic head of the molecule is located in the hydrophobic core of the membrane; it is hence a slow process, that takes place within several hours to weeks, depending on the lipid composition and temperature.¹⁵

Table 1.1. Phase transition temperature (T_m) from liquid crystalline to gel phase of selected membrane forming lipids.^{15,34}

Lipids	T_m (°C)
DSPC	55
DPPC	41
SMPC	31
DMPG	23
DOPC	-17
Egg lecithin	-10

Unsaturated lipids in a lipid mixture usually decrease its phase transition temperature T_m and increase the lateral fluidity of a membrane, which is in principle good for electron transfer processes within the membrane. However, they also increase the photochemical membrane instability, as double bonds are prone to oxidation in the presence of light and O_2 , in particular with transition-metal based PSs that can quickly generate long-lived triplet excited states. In the presence of O_2 , these triplet excited states are indeed prone to generate singlet oxygen (1O_2) by energy transfer, or radical oxygen-based species (such as the superoxide ion $O_2^{\cdot-}$) by electron transfer, which in turn can oxidise the unsaturated moieties in the lipid tails into peroxides, alcohols, or conjugated ketones.³⁶ Lipid photooxidation can culminate into C=C double bond breaking and generation of aldehydes that destabilise the membrane and make it leaky, which is counter-productive for compartmentalised photocatalysis. The introduction of unsaturated parts in photocatalytic membranes needs hence to be carefully considered, avoided if possible, and when utilised, the integrity of the membranes should be carefully verified.

The role of membrane fluidity in semi-artificial vesicular systems was investigated in a few examples. Photocatalytic hydrogen evolution in vesicles, containing membrane-bound **PS2** and a homogeneous [**FeFe**]-**H₂ase** subunit mimic catalyst, performed with higher TON of H_2 with low T_m lipids, such as DOPC and DMPC, than with DPPC or 1,2-distearoyl-sn-glycero-3-phosphocholine (DSPC).³⁷ On the other hand, photocatalytic water oxidation in vesicles,²² containing membrane-bound **PS2** and $[Ru(ddd)(4\text{-picoline})_3]$

(ddp = 4-dodecyl-2,6-dipicolinate) catalyst, showed the opposite trend, i.e. lower TON of O₂ were obtained with the low T_m lipid DOPC than with lipids with higher T_m such as DMPC and 1-stearoyl-2-myristoyl-sn-glycero-3-phosphocholine (SMPC). Thus, although basic understanding of the physical-chemical principles underlying photochemistry in unsaturated membrane is available, there has been no thorough investigation of the detailed role of unsaturations in lipids and of T_m on the performances of photocatalytic membranes.

1.2.2 Structural integrity of liposomes

Although liposomes are well-defined supramolecular systems with excellent kinetic stability in solution, photoreactive liposomes sometimes become unstable in the dark or during photocatalysis. For example, they may coalesce into very large assemblies by aggregation, in particular with uncharged lipids; alternatively, the membrane may rupture due to the formation of holes or due to photochemical oxidation of its lipids components; or the membrane may become destabilised by external agents, for example, a detergent, or a photoproduct. These phenomena may be prevented by the following “tricks”:

- a) The bilayer may be strengthened by introducing additives, e.g. 20 percent cholesterol;
- b) Electrostatic repulsion may be embedded by design, e.g. by doping the liposomes with positively or negatively charged lipids to generate charged membrane interfaces. For example, 20% charged lipids were mixed in neutral or zwitterionic lipids,³⁸ or amphiphilic active components with charged head groups were added to the membrane.²⁵
- c) Steric hindrance may be added by introducing polyethylene glycol-containing lipids in the lipid mixture forming the membrane. Here as well, the PEG group prevents the liposomes to aggregate. A typical example is the anionic lipid 1,2-dimyristoyl-sn-glycero-3-phosphoethanolamine-N-[methoxy(polyethylene glycol)-2000] (NaDSPE-PEG2K), which is added (~1 mol%) to for example

zwitterionic lipid membranes based on e.g. 1,2-dimyristoyl-sn-glycero-3-phosphocholine (DMPC).³⁹

1.2.3 Osmotic pressure

Controlling the bulk concentrations of membrane-impermeable solutes, and hence the osmotic pressure of the aqueous solutions on both sides of the liposome membrane, is a crucial consideration when preparing photocatalytic liposomes, especially where the inner aqueous compartment and outer bulk solution do not have the same composition (see section 1.3.1). The osmotic pressure of a solution onto a bilayer membrane expresses the pressure which is required to stop water from diffusing through the lipid bilayer by osmosis. The two solutions on both sides of the membrane may have different or equal osmotic pressures, which will determine the electrochemical and mechanical balance of the membrane (see below). For each solution, the contribution π_i (in Pa) of each solute i to the total osmotic pressure π can in principle be calculated by Equation 1.9.

$$\pi_i = j_i \cdot c \cdot R \cdot T \quad \text{Equation 1.9}$$

In Equation 1.9, j_i is the Van 't Hoff factor of solute i (dimensionless), c is the concentration of the solute (in mol L⁻¹), R is the ideal gas constant (8314.5 Pa K⁻¹ L mol⁻¹), and the temperature T (in K). The Van 't Hoff factor j_i is calculated based on its degree of dissociation α_i , and the number of resulting molecular/ionic species, n_i , obtained upon dissolution of the solute i (Equation 1.10).

$$j_i = 1 + \alpha_i(n_i - 1) \quad \text{Equation 1.10}$$

Equation 1.10 gives, for a simple solution containing a non-dissociating solute such as glucose ($n_i = 1$), $\alpha_i = 0$ and $j_i = 1$. A fully dissociating solute has $\alpha_i = 1$, thus NaCl ($n_i = 2$) yields $j_i = 2$, while MgCl₂ ($n_i = 3$) yields $j_i = 3$. However, for any solute that is dissociating incompletely ($0 < \alpha_i < 1$), such as carboxylic acids, or for the phosphates of a phosphate buffer, it may become difficult to calculate j_i and hence π_i . In addition, Equation 1.9 and 1.10 account for

perfect solutions only, and might deviate from reality when ions have multiple charges, or when concentrations are not low ($>10^{-2}$ mol L⁻¹). Last but not least, buffer solutions might be too complex, or have unknown components, which makes the calculation of its osmotic pressure impossible. In such cases, the total osmotic pressure of a solution can simply be measured experimentally, in osmole per litre (abbreviated as Osm L⁻¹, a non-SI unit), using an osmometer. For example, a 0.125 M ethylenediaminetetraacetic acid buffer at pH = 8 has an osmotic pressure of 374 mOsm.²³ To obtain mechanically stable liposomes, the experimental osmotic pressures of the two solutions on both sides of the liposome membrane, whatever they contain, should be equal.

In a liposome, three scenarios can indeed be distinguished: a hypotonic, a hypertonic, and an isotonic situation (Figure 1.9). In a hypotonic scenario, the solution on the outside of the lipid bilayer has a lower concentration of membrane-impermeable solutes. This scenario results in a net flow of water from the bulk towards the inner aqueous compartment, in turn leading to the swelling of the liposome (Figure 1.9a). In extreme cases, the liposomes may burst, releasing their interior towards the outside. A hypertonic situation describes the opposite scenario, which causes a net flow of water from the inner compartment towards the bulk resulting in liposome shrinkage (Figure 1.9b). For instance, liposomes based on egg yolk phosphatidylcholine with a typical hydrodynamic diameter of 140 – 150 nm as determined by DLS, decreased by 20 nm upon addition of NaOH (to pH >11) to the bulk (outside) solution.⁴⁰ This physical behaviour was assigned to the impermeability of the lipid bilayer towards Na⁺. Finally, in the isotonic situation (Figure 1.9c) the total contribution to the osmotic pressure of all membrane-impermeable solutes in the inner aqueous compartment and in the bulk, are balanced, resulting in a net-zero movement of water, and a time-independent size of the liposomes. A hypothetical dilution of such a liposome sample with pure water would result in a decrease of the bulk concentration of NaCl and hence yield a hypotonic situation and swelling of the liposomes. To conclude, liposomes are very dynamic supramolecular systems and simple dilutions with MilliQ water for example can lead to drastic changes in the size and integrity of the liposomes. In principle,

addition of redox or photoactive components on one side of a liposome, should always be done with isotonic solutions, prepared with an osmometer.

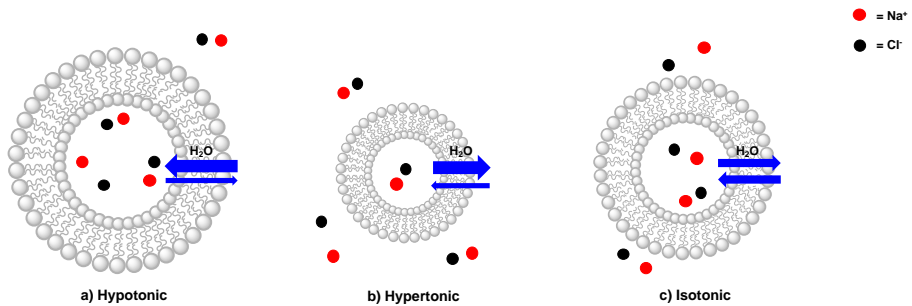


Figure 1.9. Different ions and ion concentrations lead to osmotic pressure, which results in a) a hypotonic, b) hypertonic, or c) isotonic situation. Amount of red and black dots represent relative concentrations.

1.2.4 Membrane permeability and leakage

Membrane permeability: phenomenology. The formation of a lipid bilayer results in the separation of two distinct aqueous interfaces, namely that in contact with the inner aqueous compartment and the bulk solution. Importantly, molecules can diffuse across the lipid bilayer from one interface to the other, but the membrane permeability is different for each molecule and lipid composition. The diffusion rate can be defined by Equations 1.11 and 1.12, derived from Fick's first law.

$$J_i = K_i \cdot A \cdot (C_{i, \text{outside}} - C_{i, \text{inside}}) \quad \text{Equation 1.11}$$

$$K_i = (P \cdot D_i) / d \quad \text{Equation 1.12}$$

In Equations 1.11 and 1.12, J_i is the rate of diffusion of solute i (in mol s^{-1}), K_i is the permeability coefficient of solute i (cm s^{-1}), A is the surface area of the membrane (in cm^2), $C_{i, \text{outside}} - C_{i, \text{inside}}$ is the concentration difference of solute i across the membrane (assuming $C_{i, \text{outside}} > C_{i, \text{inside}}$, in mol cm^{-3}), P is the partition coefficient of the solute in the membrane that may be approximated to that used in $\log P$ measured at n-octanol/water biphasic mixtures, D_i is the 2D diffusion constant of solute i (in $\text{cm}^2 \text{s}^{-1}$), and d is membrane thickness (in cm). As can be observed from Equation 1.11, a high

concentration gradient and a high surface area of the membrane result in a higher rate of diffusion, whereas a thick membrane results in a lower rate of diffusion. The thickness of the membrane depends on the character of the head group, the length of the alkyl tails, and the packing of the lipids.¹⁵ For example, it was demonstrated that the permeability of phospholipid bilayers in their fluidic phase ($T > T_m$) to protons, potassium ions, water, urea, and glycerol, decreases with chain length (from 14 to 24 carbon atoms) for unsaturated lipids; for instance, proton permeation was reduced from $K_i = 1.3 \times 10^{-2} \text{ cm s}^{-1}$ to $4.9 \times 10^{-5} \text{ cm s}^{-1}$, when increasing membrane thickness from 2.0 nm to 3.8 nm.⁴¹

The permeability coefficient (P) varies per molecule and is dependent on the charge, polarity, size, and molecular mass of the molecule in motion. If ΔG is the change in free Gibbs enthalpy (kJ mol^{-1}) involved when moving a solute from the bulk aqueous phase to the hydrophobic core of the membrane, one can estimate whether a molecule can cross the lipid bilayer ($\Delta G \leq 0$) by using $\log P$ as a guideline (Figure 1.10). In general, very hydrophobic molecules dissolve well inside the hydrophobic lipid bilayers and accumulate there, such as DPPC and cholesterol ($\log P \gg 0$, Figure 1.10c). Amphiphilic small molecules characterised by $\log P \approx 0$, which includes gas molecules relevant to artificial photosynthesis (O_2 , CO_2 , N_2 , or H_2), can either accumulate or diffuse across the lipid bilayer (Figure 1.10b). Neutral polar molecules, such as H_2O , can also diffuse through a lipid bilayer albeit much slower than small hydrophobic molecules, because they prefer to be solubilised by water.⁴⁰ On the other hand, hydrophilic, charged molecules such as **PS1** or calcein characterised by a $\log P \ll 0$, are poorly permeable to the lipid membrane because it is too costly to dissolve them in the hydrophobic core of the membrane (Figure 1.10a).^{21,42} Similarly, ions, protons, and electrons, are poorly permeable to the membrane and therefore their transfer across a lipid bilayer has to be facilitated by other means such as membrane channels or ion pumps (see section 1.2.6 for more details). To illustrate these points with some numbers, the permeability coefficients through lecithin-based lipid bilayers are generally in the order of 10^{-3} to $10^{-4} \text{ cm s}^{-1}$ for H_2O , 10^{-11} to $10^{-12} \text{ cm s}^{-1}$ for anions, and 10^{-12} to $10^{-14} \text{ cm s}^{-1}$ for cations that are commonly

utilised such as Na^+ .⁴⁰ In some other cases certain charged molecules, such as the charge carrier cetyl methyl viologen (CMV), have a different mechanism to cross the lipid bilayer: The stable and twofold positively charged form, CMV^{2+} , is water soluble and barely penetrates the lipid bilayer. Likewise, the singly reduced species CMV^+ is still positively charged and anticipated to rest in the aqueous phase. However, upon a disproportionation reaction two singly-charged CMV^+ molecules can generate a CMV^{2+} and a neutral CMV^0 molecule, which can freely diffuse across a lipid bilayer.⁴³

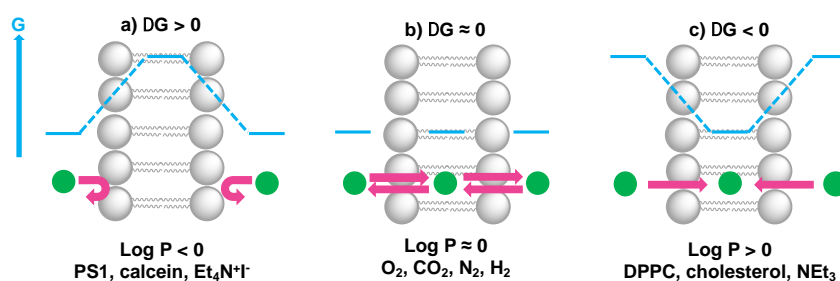


Figure 1.10. The membrane permeability and residence time of ions and molecules depend on their hydrophilicity. When a) $\log P \ll 0$, $\Delta G > 0$, molecules cannot cross or enter the lipid bilayer; when b) $\log P \approx 0$, $\Delta G \approx 0$, molecules can redistribute between the aqueous phase and the hydrophobic core of the lipid bilayer, and cross the membrane; when c) $\log P \gg 0$, $\Delta G < 0$, molecules prefer to reside within the lipid bilayer. Actual $\log P$ values can be found in references^{16,21,42} or can be obtained by using $\log P$ predictors such as miLogP2.2 (<http://www.molinspiration.com>). For example, $\log P = +7.62$ for cholesterol, $\log P = +0.09$ for O_2 , $\log P = +0.02$ for CO_2 , $\log P = +0.02$ for N_2 , and $\log P = +0.16$ for H_2 .

Although membrane leakage has mainly been studied for liposome-based drug delivery, it is also an important aspect in artificial photosynthesis applications, especially when preparing dissymmetrical liposomes for transmembrane electron, proton, or ion transfer (see section 1.2.6). For such systems, the interior of the liposome contains a chemical that is absent from the outside bulk solution, or vice-versa. To demonstrate transmembrane electron- or proton-transfer, both sides of the membrane should not exchange molecules by membrane leakage. For example, transmembrane electron transfer was initially reported for a system containing the charge carrier MV^{2+} (see Figure 1.7a) in the inner aqueous compartment of sodium

dihexadecyl phosphate (DHP) vesicles, whereas the **PS1** and the sacrificial ED (EDTA) were located in the bulk.⁷ However, several studies pointed to the photoredox reaction between photoexcited **PS1** and **MV²⁺** actually occurring in the bulk, due to leakage of both **MV^{•+}** and **PS1** across the DHP bilayer.⁷

As a side note, the membrane permeability of molecules does not depend only on their log P, as water-soluble compounds may also permeate membranes via holes or ruptures in the membrane. The lipid composition, for example, was shown to play an important role in membrane leakage. Liposomes prepared from the unsaturated lipid DOPC ($T_m = -17\text{ °C}$) have a larger release rate at room temperature for water-soluble molecules than liposomes prepared from the saturated lipid DPPC ($T_m = +41\text{ °C}$).⁴² Generally, vesicles prepared from saturated lipids with longer alkyl chain lengths pack more tightly, possess a high gel-to-liquid crystalline transition temperature (T_m), and retain entrapped solutes better than unsaturated lipids and shorter alkyl tail lengths who have a less rigid lipid bilayer assembly. Furthermore, addition of cholesterol to the lipid composition leads to increased lipid bilayer stability and less membrane leakage. Last but not least, liposomes are leakier near their phase transition temperature T_m due to the co-existence of gel-phase and liquid-phase domains within the membrane, which generate grain junction through which polar molecules may diffuse. As a practical consequence, vesicles constructed from DMPC, which has a transition temperature $T_m = +23\text{ °C}$ that is near room temperature, are typically leakier in room-temperature experiments, compared to DPPC-based liposomes which have T_m significantly higher than 20-25 °C (Figure 1.11).⁴⁴ Photocatalytic membranes based on DMPC should hence be studied at lower or higher temperature than room temperature.

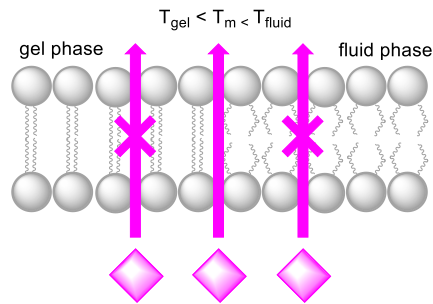


Figure 1.11. Water-soluble substrate (pink diamonds) crosses membranes more easily near the transition temperature T_m due to permeable grain junction between fluid phase and gel phase domains.

Membrane leakage: experimental approaches. Leakage can be quantified experimentally using self-quenching dyes, such as calcein, 5(6)-carboxyfluorescein and sulforhodamine B. A typical membrane leakage experiment consists in encapsulating one of these water-soluble dyes at high concentration inside liposomes, which causes low emission levels due to self-quenching (Figure 1.12). Upon release of the water-soluble dye into the outside bulk solution, i.e., upon membrane leakage, the emission intensity increases because the dye outside the liposome is not self-quenched anymore. At the end of the experiment, a detergent such as Triton-X-100 is added to the liposome sample, resulting in the complete disruption of the liposome, full release of the dye, and subsequent formation of micelles containing both the liposomal lipids, the detergent, and the dye. This point is taken as reference (unquenched) emission with 100% dye leakage. It should be noted that all self-quenching dyes used for such experiments are negatively charged and may self-assemble with positively charged components of the membrane. Currently, there is a lack of cationic self-quenching dyes for membrane leakage experiments.

An alternative method is to use dye-quencher pairs, such as 8-aminonaphthalene-1,3,6-trisulfonic acid with p-xylene-bis-pyridinium bromide (ANTS/DPX), and fluorescent enhancement pairs, like Tb^{3+} and dipicolinic acid (Tb^{3+} /DPA).⁴⁵ For ANTS/DPX, both molecules are co-encapsulated in the vesicle and quench each other; upon disruption of the lipid bilayer by a detergent luminescence increases because quenching

becomes smaller. The latter case involves one of the only positively charged probes used for leakage tests. Here, the weakly luminescent Tb^{3+} ions leak from the interior of the liposome and coordinate to DPA present in the bulk outside solution, leading to the formation of a highly luminescent $[Tb(DPA)_3]$ complex.⁴⁵

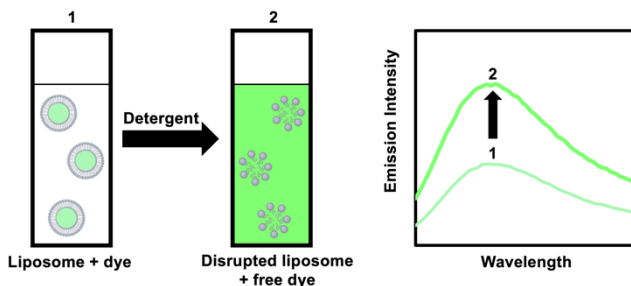


Figure 1.12. Addition of a detergent to a liposome solution with an encapsulated and weakly luminescent dye results in the release of the dye and enhanced emission intensity.

1.2.5 Shape of vesicles

Vesicles exist in different sizes and shapes and their preparation is described in section 1.3.1. Vesicles that are visible with a microscope should have a micrometre diameter and are called “giant” vesicles (Figure 1.13a). Vesicles that are smaller than $1\ \mu\text{m}$ are either called “large” or “small” vesicles (Figure 1.13b). Both types can be unilamellar (only one bilayer) or multilamellar (several bilayers) with multiple membranes forming an onion-like “vesicle within a vesicle”. Liposomes are spherical vesicles made of at least one unilamellar membrane. In principle, the larger the vesicle becomes, the more shapes are possible, which can be seen in the confocal image of membrane-stained giant vesicles in Figure 1.13a. Apart from spheres, ellipsoids, tubes and other shapes have also been described.

The morphology of the lipid bilayer of liposomes depends on the lipid head group, the length of the hydrocarbon tails, the size of the liposomes, the transition temperature of the lipid, and the preparation methodology. Decreasing the temperature of a liposome solution to values below T_m , may result in faceted vesicles (Figure 1.13c) or the creation of open bilayer

fragments (Figure 1.13d) instead of smooth round vesicles, as can be experimentally visualised by cryogenic transmission electron microscopy (CryoTEM, see Figure 1.13b, 1.13c, 1.13d).³⁴ These morphological changes have an effect on photoredox reactions, such as the reduction of CMV by dithionite ($S_2O_4^{2-}$).³⁴ In the case of smooth vesicles, monoexponential reduction kinetics can be observed, whereas the presence of bilayer irregularities and non-vesicular structures can lead to double-exponential reduction kinetics.³⁴ Therefore, in order to ease the study of complex photocatalytic reactions occurring at the membrane-water interface, such as electron, proton, or ion transport across a lipid bilayer,³⁴ one should aim to use regular unilamellar vesicles either in the fluid or the gel phase.

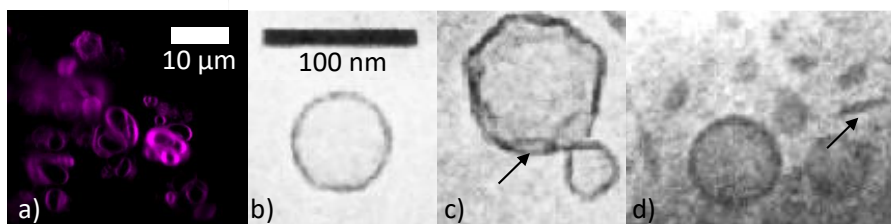


Figure 1.13. a) Confocal microscopy image of a luminescent dye embedded in the lipid bilayer of giant DMPC vesicles. Figure adapted from reference³⁹. CryoTEM images of b) extruded DMPC ($T_m = 23\text{ }^\circ\text{C}$) vesicles vitrified from $40\text{ }^\circ\text{C}$, c) extruded DPPC ($T_m = 41\text{ }^\circ\text{C}$) vesicles vitrified from $25\text{ }^\circ\text{C}$, and d) sonicated DLPA ($T_m = 31\text{ }^\circ\text{C}$) vesicles vitrified from $18\text{ }^\circ\text{C}$. Figures adapted from reference³⁴.

1.2.6 Transport of electrons, protons, and ions across a lipid bilayer

Biological transmembrane electron transfer takes place in cell compartments of photosynthetic and respiratory organelles to allow for redox reactions to occur and to generate an imbalance in electrochemical potential across the membrane. This imbalance is translated into a proton motive force that is ultimately used as an energy source to drive endergonic transformations such as the generation of ATP by the membrane-embedded ATPase. There are also examples for ion transfer that act without proton motive forces, such as simple passive transmembrane protein channels such as gramicidin A, aquaporin, the prokaryotic potassium channels of *streptomyces A*, or even artificial ion channels or transporters. In this chapter, we only consider the

light-induced transport of electrons, protons, and ions across lipid bilayers for artificial photosynthesis.

Electron transfer through a lipid bilayer cannot generally occur by direct tunnelling between reactants on either side of the membrane as the thickness of the hydrophobic core of typically ca. 30-35 Å is too high to allow direct charge transfer at reasonable rate. The electron transfer rate, k , is given by Equation 1.13.

$$k = A \cdot e^{-\beta r} \quad \text{Equation 1.13}$$

In Equation 1.13, A is the exponential prefactor, β the attenuation factor (in Å⁻¹), and r is the distance (in Å). β is typically around 1.0 Å⁻¹,⁴⁶ which would make even an activationless reaction proceed on a time scale as slow as minute to hours. Instead, the electrons are typically carried across the membrane by small molecules, or transferred by hopping in several shorter steps via redox centres located inside the hydrophobic part of the membrane as it occurs in thylakoid membranes.

To mimic natural transmembrane redox processes the following strategies are possible; (a) To incorporate biologic components into the lipid bilayer such as natural reaction centres and membrane-bound electron transfer proteins (Figures 1.14a-c and 1.15a-b); (b) To synthesise transmembrane molecules spanning the lipid bilayer, such as rigid molecular triads or supramolecular assemblies of electron conduits (Figure 1.15c-e); (c) To organise the diffusion of molecular charge carriers embedded within the lipid bilayer of artificial membranes (Figure 1.15b, c, f). Although many examples have been reported,⁷ we only present here a selection of examples to illustrate the three strategies discussed above.

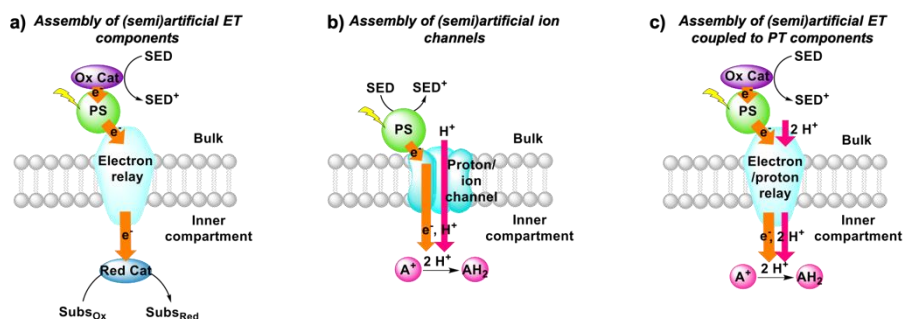


Figure 1.14. General strategies for the development of (semi)artificial liposome systems. Assemblies of a) (semi)artificial electron transfer (ET) components, b) (semi)artificial ET coupled to proton transfer (PT) components across the membrane, and c) (semi)artificial ion channels. Ox. Cat. = oxidation catalyst; Red. Cat. = reduction catalyst; SED = sacrificial electron donor; Subst_{Ox} = oxidised substrate; Subst_{Red} = reduced substrate; A⁺ = electron acceptor; AH₂ = reduced and protonated electron acceptor.

Strategy a is best represented by a semiartificial compartmentalised liposome system (Figure 1.15a) that used the proton-coupled icosahem transmembrane electron transfer protein complex, MtrCAB (analogous to *S. Baltica OS185's* structure shown in Figure 1.7c).⁵ MtrCAB is a cytochrome-type protein complex found in *Shewanella oneidensis* MR-1 bacteria, where it acts as a natural transporter of electrons to external minerals. In the reported system, phosphonated ruthenium(II) tris-bipyridine ($[\text{Ru}(\text{bpy})_2(4,4'-(\text{PO}_3\text{H}_2)_2\text{bpy})]^{2+}$, **RuP**) photosensitised titanium oxide nanoparticles (**RuP-TiO₂**), and carbon nanodots were employed as synthetic light harvesters placed outside the liposome. To demonstrate spectroscopically transmembrane electron transfer with MtrCAB embedded in a synthetic liposome, the redox active dye, reactive red 120 (RR120), was encapsulated inside the liposome and showed the expected bleaching of the band at 539 nm upon photo-reduction. The sacrificial electron donor EDTA regenerated the hole left in the light-harvesting nanoparticles. The rate limiting step was identified as the electron transfer from the light-harvesting nanoparticles to the MtrCAB electron relay.⁵

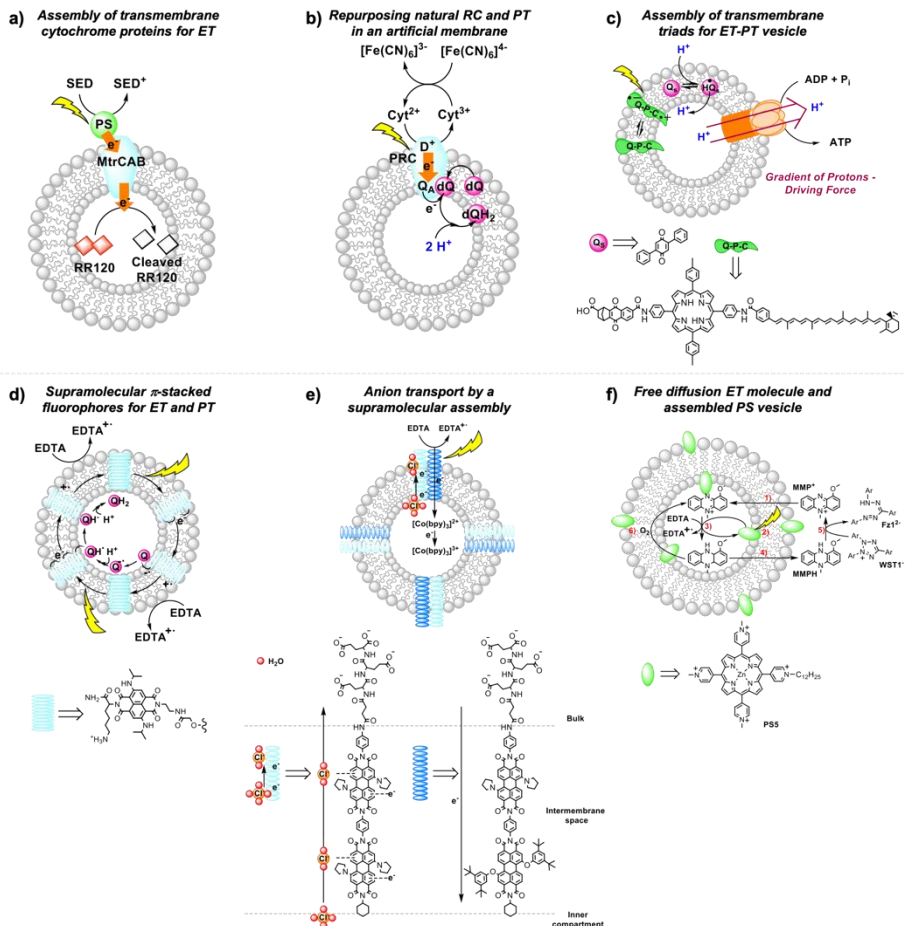


Figure 1.15. Selected examples for proton and electron transfer across lipid bilayers. Assemblies of a) transmembrane cytochrome (MtrCAB) proteins for ET,⁵ b) repurposed natural photosynthetic reaction centres (PRC) and proton transfer components in an artificial membrane⁴⁷, c) transmembrane quinone-porphyrin-carotenoid triad (Q-P-C) for coupled ET-PT across the membrane^{33,35}, d) supramolecular π -stacked fluorophores for coupled ET and PT⁴⁸, e) supramolecular transmembrane rods for electron and anion transport⁴⁹, and f) membrane-embedded PSs combined with a diffusion-based ET molecule²⁶. SED = sacrificial electron donor; Q_s and dQ = membrane-soluble quinone (Figure 1.7), D^+ = donor; Q_A = quinone A from the isolated reaction centre.

In a similar example, a re-purposed photosynthetic reaction centre, isolated from *R. sphaeroides* bacteria, was embedded in the membrane of a giant unilamellar vesicle with the desired physiological orientation by following a

droplet transfer synthetic method (Figure 1.15b).⁴⁷ With this protocol roughly 90% of the photosynthetic reaction centre was facing the aqueous bulk solution and, thus, 90% of the quinone sites (Q_B) were facing the inner space of the lipid bilayer, thus creating an artificial lumen that enabled the generation of a light-driven proton gradient across the membrane. This semiartificial vesicle was used in combination with the water-soluble ED cytochrome c_2 , the natural electron donor to this reaction centre, as well as ferrocyanide ($[Fe(CN)_6]^{4-}$) in the bulk; on the other hand, the quinone on the inner monolayer of the vesicle was used as final EA. Under constant red-light irradiation ($\lambda = 865$ nm) the repurposed reaction centres converted light energy to the energy of a proton gradient across the lipid bilayer at about 0.061 pH min^{-1} , which is equivalent to a proton motive force of 3.6 mV min^{-1} . Hence, the reduction and subsequent protonation of the quinone within the membrane induced a pH gradient in addition to the electrochemical potential.⁴⁷

In strategy b, fully synthetic examples were developed to couple transmembrane electron transfer to transmembrane proton transfer. A prominent example is the synthetic molecular triad (**Q-P-C**, Figure 1.15c) consisting of a naphthoquinone moiety as electron acceptor (**Q**), the PS tetraarylporphyrin (**P**), and a carotenoid as electron donor (**C**). This triad was embedded into a lipid bilayer and transported electrons across a membrane upon light irradiation.³³ Control titration studies showed that the majority of triads were arranged with their **Q** ends facing the aqueous bulk, while the **C** moiety spanned the lipid bilayer towards the inner aqueous compartment. Irradiation of the triad with laser pulses at 430 nm excited the porphyrin group, which results in the formation of a charge separated species Q^-P-C^+ that could be detected by the transient absorbance of the carotenoid radical cation at 930 nm. This biradical was generated with a quantum yield of 0.1 and had a lifetime of 60 ns within the lipid bilayer in the presence of freely diffusing quinones (Q_S), which established a reduction potential near the outer surface of the bilayer and an oxidation potential near its inner surface. In response to that, Q_S accepted an electron from the Q^- part of the triad generating a reduced and anionic quinone that got protonated and hence transferred protons across the bilayer by electron transfer to the oxidised C^+

part of the triad, with an overall quantum yield of 0.004.³³ This process turned over during light irradiation, generating a pH gradient between the inner compartment and the bulk.³³ Ultimately, in a follow-up study, the proton motive force generated by this artificial liposome was coupled to a membrane-bound ATP synthase complex in the same lipid bilayer, which upon irradiation resulted in the synthesis of ATP with an initial quantum yield at low-light irradiation of more than 0.07 for the whole process within the new assembly.³⁵ In another example, p-octiphenyl rods were used to create a helical tetrameric supramolecular assembly with π -stacked blue and red-fluorescent naphthalene diimides spanning the lipid bilayer of a liposome, which also contained freely diffusing quinones as EA (Figure 1.15d). The functionalised liposomes were immersed in an aqueous solution containing EDTA as ED in the bulk. The irradiation of the π -stacked dyes with visible light generated a fast electron transport across the interacting chromophores until the electron was finally accepted by the quinone in the inner aqueous compartment, which was accompanied by proton transfer to the quinone. The long-lived charge separated state across the membrane was hence translated into an oxidation potential near the outer surface of the membrane and a reduction potential near the inner surface, as well as a proton gradient across the membrane.⁴⁸ In a third and last example of coupled electron and ion transmembrane transfer, rigid oligo(p-phenyl-ene)-N,N-perylenediimide rods were embedded in egg yolk phosphatidylcholine based vesicles (Figure 1.15e).⁴⁹ These rods were able to perform photoinduced transmembrane electron transfer from EDTA in the bulk to the electron-accepting charge carrier $[\text{Co}(\text{bpy})_3]^{2+}$ in the inner aqueous phase, while simultaneously transporting Cl^- , OH^- or SO_4^{2-} anions, in the reverse direction. Interestingly, the rods failed to transport cations at all and its selectivity for anion transport was thus proposed to result from anion- π interactions along the π -acidic environments of the oligo-aromatic rods.⁴⁹

Finally, in strategy c the membrane-soluble molecular charge carrier **MMP⁺** was employed for unidirectional transmembrane electron transfer in liposomes. In this system, **PS5** was embedded in the membrane, EDTA was placed in the inner space of the liposome as ED, and 2-(4-iodophenyl)-3-(4-nitrophenyl)-5-(2,4-disulfophenyl)-2H-tetrazolium anion (**WST1⁻**) was finally

added in the exterior aqueous bulk solution as EA (Figure 1.15f).²⁶ In an anaerobic atmosphere, **MMP**⁺ catalytically transported photoelectrons across the membrane without limiting the overall reaction rate. In such conditions late charge recombination of reduced **WST1**⁻ with **ED**⁺, as well as quenching of **PS5**^{*} excited states by the reduced **WST1**⁻ were avoided by their physical separation with the liposomal membrane. However, as soon as oxygen was introduced in the system transmembrane photoelectron transfer stopped occurring, because **MMPH**, the reduced form of **MMP**⁺, reacted with O₂ faster than with **WST1**⁻. This limitation shows how tricky it is to avoid charge recombination even at a late stage of the photocatalytic cycle.

1.3 The water membrane interface

1.3.1 Preparation of liposomes and generation of confined aqueous reaction spaces

Vesicles provide three different reaction spaces: the inner aqueous compartment, the hydrophobic core of the membrane, and the outer aqueous bulk solution. These three spaces can be addressed separately, loaded with different photocatalytic components, and characterised via different experimental techniques. Table A1 (Appendix A) lists these techniques and which information one can obtain from them.

By self-assembly of lipid bilayers into vesicles a high local concentration of reactants can be achieved in the bilayer or by the encapsulation of the substrates in the inner aqueous compartment, even upon dilution of the vesicle solution. As an example, a vesicle with a diameter of 100 nm has an internal volume of approximately 10⁻¹³ μL. Confinement within the vesicle can be important because the local concentration of water soluble substrates and products influences reaction dynamics in water and at the interface of the membrane.^{1,9} Furthermore, the hydrophilic products from water oxidation and CO₂ reduction, such as protons and formate, respectively, might affect membrane stability due to changes of the osmotic pressure. For example, when oxidising two water molecules to one molecule of O₂ that

diffuses away, four protons are generated as well, which changes the pH and osmotic pressure.

For unidirectional electron transfer through membranes, it can be particularly appealing to differentiate the inner and outer reaction spaces in vesicles, for example by loading the interior space of the vesicles with functional molecules or substrate, or by adding after liposome preparation, compounds that will only be present on the outside. Among all methods to prepare liposomes, a standard one is depicted in Figure 1.16.

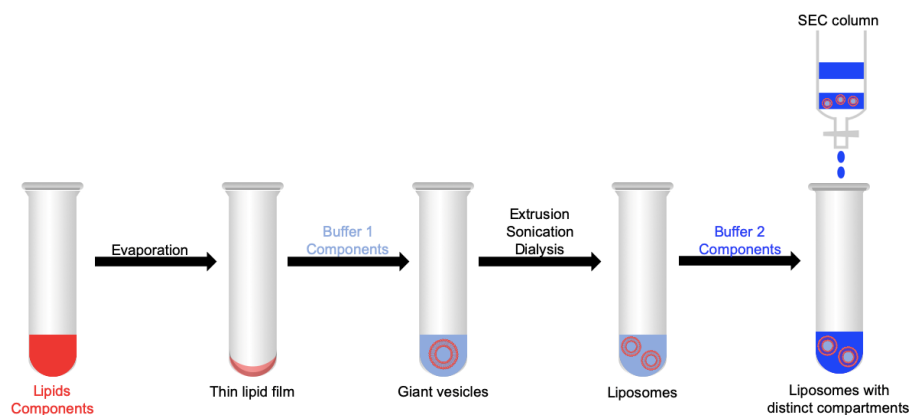


Figure 1.16. Method for the preparation of liposomes with distinct compartments that are functionalised with active components for artificial photosynthesis. SEC = size exclusion chromatography. Membrane soluble components are shown in red, whereas water-soluble components are shown in light or dark blue. Light blue shows Buffer 1, dark blue Buffer 2 (see text).

Firstly, a solution of lipids and membrane-soluble components, such as PSs and catalysts (see section 1.1.3) dissolved in organic solvents, is transferred to a glass tube or flask. Subsequently, the organic solvents are removed under reduced pressure, resulting in the formation of a thin lipid film on the glass wall of the tube or flask. In the next step, the vacuum dried thin lipid film is hydrated using an aqueous buffer containing water-soluble components, such as sacrificial reagents or charge carriers (Buffer 1). Several freeze-thaw cycles (in some cases also sonication) induce the formation of giant multilamellar vesicles (diameter $> 1 \mu\text{m}$). To obtain liposomes (diameter $< 1 \mu\text{m}$), extrusion with a suitable pore size filter, sonication, or

dialysis, can be performed. Extrusion typically provides relatively narrow hydrodynamic diameter distributions characterised by low polydispersity index (PDI) in DLS or cryo-TEM analysis ($PDI < 0.1$). At this stage both sides of the membrane are identical; however, the bulk solution can be replaced by a second and different aqueous buffer solution (Buffer 2) containing water-soluble components that are absent from the interior; using size exclusion chromatography (SEC), it is then possible to isolate the liposomes filled with Buffer 1 from excess Buffer 1. Dissymmetrical liposomes are then obtained, filled with Buffer 1 and surrounded with Buffer 2. As mentioned above, with such liposomes it is critical to use two Buffers 1 and 2 with identical osmotic pressure, as measured by an osmometer. Otherwise, differences in osmotic pressure on both sides of the membrane lead to the uptake or release of water from the inner aqueous compartment, which may make the membrane leaky (see section 1.2.3).

1.3.2 Properties of the interface

Local concentrations at self-assembled lipid membranes. For efficient photocatalysis, managing local concentrations of active components, protons fluxes, and redox potentials, are crucial. Lipid bilayers typically enhance local concentrations when PS and catalyst molecules are co-embedded in the lipid bilayer, resulting in closer proximity of these components, compared to homogeneous solution with identical bulk concentrations. An example was reported for photocatalytic water oxidation (Figure 1.17), where **PS1** and a **non-alkylated WOC** in homogeneous solution was compared with co-embedded **PS2** and **WOC** in DMPC based liposomes, using $\text{Na}_2\text{S}_2\text{O}_8$ as sacrificial EA.²³

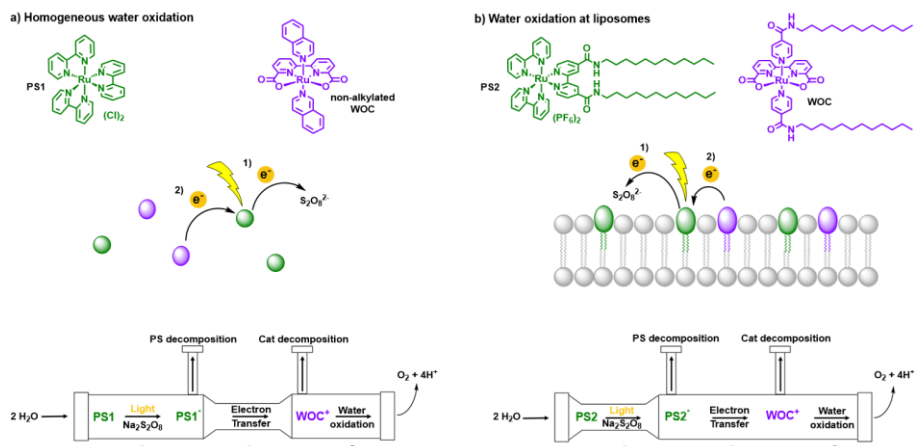


Figure 1.17. Water oxidation in (a) homogeneous solution and at (b) liposomes. (Top) Photosensitisers (green) **PS1** and **PS2** and catalysts (purple) **non-alkylated WOC** and **WOC**. (Middle) Schematic step-by-step electron transfer in homogeneous conditions and at liposomes. (Bottom) Scheme of three rate determining steps (RDS) in photocatalytic water oxidation under homogeneous and liposome conditions. Figure adapted from reference ²³.

The photochemical reaction involved three identified steps in both photocatalytic systems: first, light induced electron transfer between the PS and the EA (rate r_1), second, electron transfer between the oxidised PS and the catalyst (rate r_2), and finally, redox catalysis (rate r_3). In homogeneous conditions, r_1 and r_2 are limited by diffusional processes, which resulted in concentration-dependent electron transfer steps 1 and 2.²³ Due to the high concentration of the EA (mM), the rate-limiting step (RDS) was found to be step 2, as the catalyst concentration was much lower (μM). On the other hand, when PS and the water oxidation catalyst were embedded in the membrane the electron transfer rate between **WOC** and **PS2⁺**, i.e. step 2, became much faster and stopped being rate determining. Instead, step 1 became rate limiting.^{6,23} This specific change in RDS from step 2 to step 1 significantly improved the overall photocatalytic reaction, notably because the PS decomposition was partly prevented by the lower concentration of **PS2⁺**. This form of decomposition is an important limiting factor in water oxidation systems employing ruthenium polypyridine-based PSs.²³ Using UV-Vis spectroscopy, it was found that the rate of oxidative quenching of photoexcited **PS2** by Na₂S₂O₈ in liposomes was at least one order of

magnitude lower than with the homogeneous analogue **PS1** in homogeneous conditions. Namely, **PS2** was either regenerated via electron transfer from the catalyst or decomposed in the oxidised state **PS2⁺**. At decreasing concentrations of **WOC** the formation of **PS2⁺** increased with concomitant decomposition, highlighting that electron transfer from **WOC** to **PS2⁺** and catalytic oxidation of water is fast enough to maintain the concentration of the sensitive **PS2⁺** at concentrations below the detection limit.²³ These results also highlight that the stability of a photocatalytic system highly depends on kinetics, and notably on the synergistic performances of the four components (light, PS, cat, EA) working as a team, and not only on the intrinsic stability (and even photostability) of its individual components.²³

Another surface concentration effect that should be noted is related to protons; proton management is indeed important, as most redox reactions in artificial photosynthesis are coupled to proton transfer (PCET, see for example Equations 1.1-1.6). At lipid bilayer interfaces the protonation-deprotonation dynamics are different than in homogeneous solution. This protonation – deprotonation equilibrium is described by the acidity constant, pK_a . The pK_a of a proton-donating or accepting group at the bilayer-water interface differs from the value in bulk water solutions, essentially due to different surface polarities (dielectric constant), and the electrostatic enhancement or reduction of proton concentration at the bilayer interface due to surface charge changes. For example, while the acidity constants of most lipids are tabulated,¹⁵ it should be noted that pK_a values at a membrane can shift by up to $\Delta pK_a = 2.5$.¹⁵

Ion “belts” around charged membrane surfaces. The effect of counterions on the properties of lipid membranes is often forgotten while they may result in changes in two-dimensional diffusion properties and electron transfer kinetics between membrane-bound species as a result notably of phase transitions. For example, cations with large charge densities such as Ca^{2+} and Li^+ adsorb to zwitterionic lipid membranes, which can induce rigidification of the membrane and a stabilisation of their gel-phase.³⁸ This phenomenon was investigated using NaCl, KCl, and CsCl with liposomes made of mixtures of 1,2-palmitoyl-oleoyl-sn-glycero-3-phosphocholine (POPC) and 1,2-palmitoyl-

oleoyl-sn-glycero-3-phosphoserine (POPS) lipids and doped with the phase sensitive fluorescence probe Laurdan.³⁸ Fluorescence and spectroscopic computational molecular dynamic simulations supported that liposomes made of 4:1 POPC:POPS (i.e. 20% content of anionic lipid) had higher adsorption levels of monovalent cations, in comparison with zwitterionic neutral vesicles. Furthermore, Na⁺ was found to be the strongest cation adsorbed, followed by K⁺ and then Cs⁺. The rigidification of the membranes was explained by the formation of lipid-cation complexes via the coordinating oxygen atoms in carbonyl groups of hydrophilic lipid head groups to the respective cations.

1.3.3 Adsorption of active molecules at the water-membrane interface

Considering the adsorption of active components to membrane surfaces is important both during the construction of photoactive liposomes and during the light-induced chemical reactions itself, electrostatic and hydrophobic interactions play a major role in the overall photocatalytic scenario. In terms of energy, the supramolecular adsorption of molecules onto lipid bilayers can be described in terms of a solvation-desolvation process, where all supramolecular forces describing the interaction between the functional molecule and the membrane have to be considered, i.e., charges and hydrophobicity indeed, but also π - π stacking, dipolar interactions, van der Waals interactions, hydrogen bonding, and ligand coordination to metals. Altogether, these interactions combine into a free Gibbs energy of adsorption of the photoactive molecule to the membrane (ΔG_{ads}) that is composed of an enthalpy (ΔH_{ads}) and an entropy (ΔS_{ads}) term (Equation 1.14, Figure 1.18).

$$\Delta G_{\text{ads}} = \Delta H_{\text{ads}} - T \cdot \Delta S_{\text{ads}} \quad \text{Equation 1.14}$$

Both ΔH_{ads} and ΔS_{ads} have the following contributions:

- a) supramolecular interaction between the functional molecule and lipid membrane

- b) solvation of the functional molecule and its counter anions/cations in the aqueous phase
- c) solvation of the lipid membrane and its counter anions/cations in the aqueous phase
- d) ion pair formation between the counter anions and counter cations, which are released from the membrane upon adsorption.

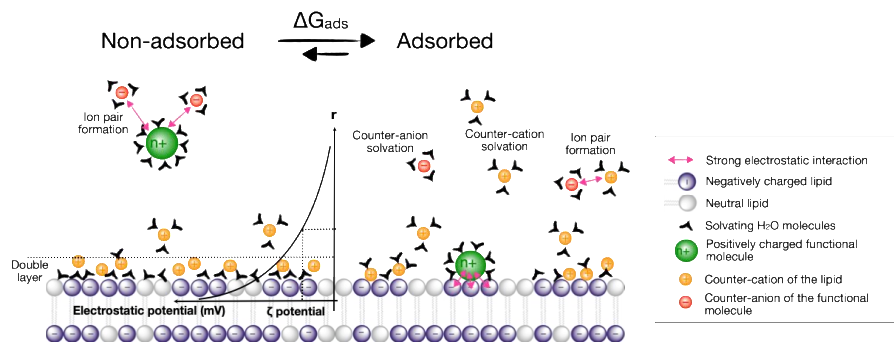


Figure 1.18. Adsorption of charged photoactive molecules (in green) onto a negatively charged membrane (negatively charged lipids in purple). The left side represents the non-adsorbed state, the right side the adsorbed state. Counter anions of the functional molecules (in red) and counter cations of the lipids (in orange) are also exchanged and re-solvated upon adsorption, which plays a major contribution in the free Gibbs energy of adsorption (ΔG_{ads}) of the functional molecule onto the membrane. Black symbols represent (a selection of) the water molecules solvating the charged species, either in the bulk, or at the membrane. Pink double arrows represent electrostatic attraction between charged species in the system. The double layer and evolution of the electrostatic potential and the zeta (ζ) potential are shown as a function of the distance (r) from the membrane.

Negatively charged lipid bilayers are normally surrounded by NH_4^+ , Na^+ or K^+ counter-cations, and positively charged metal complexes bring along anions such as Cl^- or PF_6^- . Upon adsorption of a positively charged functional molecule to the surface of negatively charged lipid bilayers the counter-ions can be exchanged, a process that has thermodynamic consequences. In the exemplary case of the adsorption of one dicationic functional molecule such as $[\text{Ru}(\text{tpy})(\text{bpy})(\text{OH}_2)]^{2+}$ ($\text{tpy} = 2,2':6',2''\text{-terpyridine}$) onto negatively charged DMPG based lipid bilayers involves the desorption of two Na^+ from the bilayer surface.⁵⁰ Depending on the respective ion pairing and solvation energies and entropies, this process can either be endothermic or exergonic due to a

significant energetic contribution from the entropy term of ion release (two equivalents of Na⁺ cations) to the bulk.⁵⁰

1.3.4 Reaction dynamics at water-membrane interfaces

Reaction dynamics differ between vesicles-supported reactions and reactions in homogeneous solutions. In a homogeneous solution, components interact in a three-dimensional manner, whereas in vesicles components are normally immobilised on a two-dimensional lipid bilayer, which forms the platform of the photoreactions. One method to study the effects of reduced dimensionality on reaction kinetics is bimolecular fluorescence quenching with PSs and quenchers attached to the membrane. For three-dimensional bimolecular reactions, fluorescence quenching with excess of quencher molecules will show a normal exponential decay of fluorescence vs. time, with a rate law that is pseudo-first order in quencher concentration [Q]. For reactants diffusing in 2D within the vesicle interface, the fluorescence decay will instead be strongly non-exponential. This can be qualitatively understood by considering the concentration profile of quenchers as a function of distance from excited molecules, $[Q] = f(r)$ (Figure 1.19). At the time of excitation ($t = 0$) the quenchers are randomly distributed in solution and [Q] will be independent on r . The excited PSs that are next to a quencher will react rapidly, and the remaining excited PSs will be the ones with larger distance to the nearest Q. With time, the reaction will consume all quenchers at a short distance, leaving a “concentration hole” around the remaining excited states. At the same time, diffusion of quenchers from the bulk to the vesicle interface will occur to balance the concentration. In a three-dimensional, homogeneous solution, reaction and diffusion rates rapidly equilibrate to set up a steady-state concentration profile of quenchers that then remains for the rest of the reaction, resulting in single-exponential kinetics. When the concentration profile still changes, however, quenching is faster than given by the long-time rate constant. This transient effect in fluorescence quenching is well established⁵¹ and is important at times after excitation $t \ll R^2/D_{\text{PSQ}}$, where R is the intermolecular reaction

distance and D_{PSQ} is the sum of the diffusion coefficients of PS and quencher. For small molecules in a low-viscosity solvent, this is typically at $t < 100$ ps.

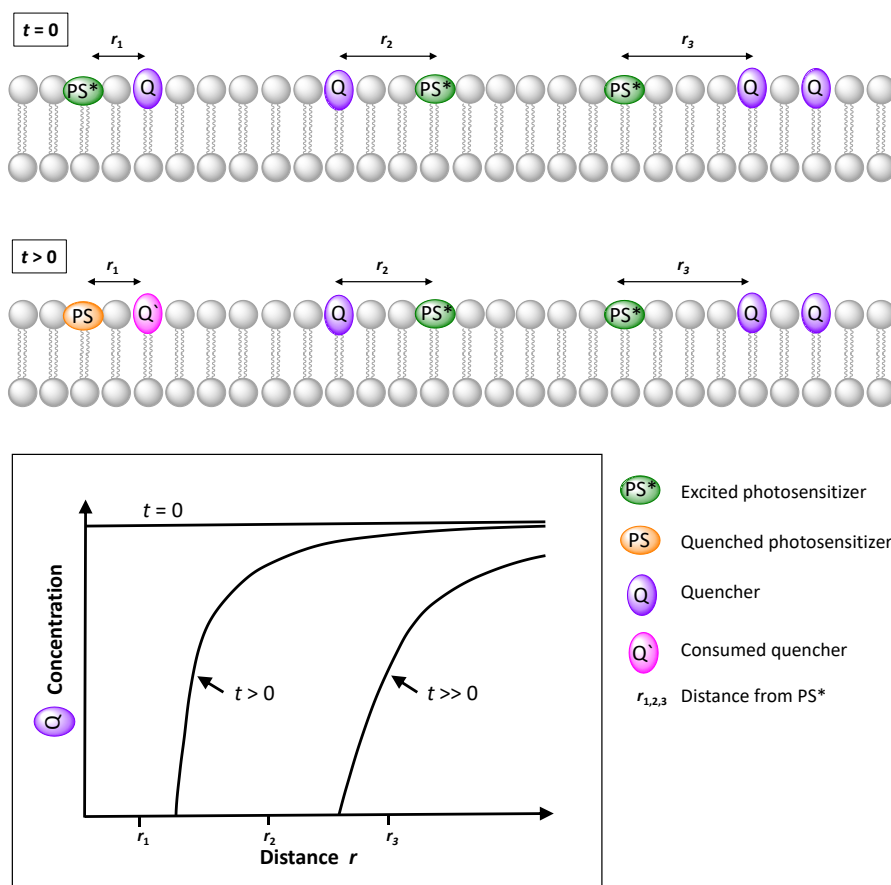


Figure 1.19. Qualitative diffusion-reaction dynamics at lipid bilayer surfaces containing PS and quenchers (Q) at various distances ($r_{1,2,3}$) leads to a time-dependent concentration profile of Q as a function of distance from PS*. For three-dimensional (homogeneous) solution, the concentration profile rapidly becomes constant (qualitatively similar to the profile labelled “ $t > 0$ ”), and the usual pseudo-first order rate constant is obtained. With two-dimensional diffusion instead, the concentration profile keeps evolving and the kinetics is non-exponential. The concentration profiles are qualitative and not mathematically exact.

For diffusion in lower dimensions, such as within a two-dimensional lipid bilayer, diffusion can never keep up with reaction, and the “concentration hole” will keep growing as the reaction proceeds. The fluorescence decay is

then much more complicated, so that numerical fitting of experimental data becomes unfeasible. An approximate solution for the time dependence of the fluorescence intensity in the case of diffusion-controlled, two-dimensional quenching is given in Equation 1.15,⁵² where τ_0 is the lifetime of the PS in the absence of quencher and $[Q]$ is the concentration of quencher. The solution for the case of reaction-control (slower than the diffusion limit) is somewhat more complex.⁵³ For very slow quenching, *i.e.* low reactivity even at contact distance, $[Q]$ near the PSs will be approximately equal to the bulk value, and the quenching kinetics should again be simple and follow a single exponential.

$$\frac{I(t)}{I(t=0)} = \exp\left\{-t/\tau_0 - 7.44[Q]R(D_{PSQ}t)^{\frac{1}{2}} - 2.28[Q]D_{PSQ}t\right\} \quad \text{Equation 1.15}$$

An example where Equation 1.15 was used to study electron transfer at the interface of vesicles is shown in Figure 1.20. The ruthenium PS $[\text{Ru}(\text{dcb})_3]^{4-}$ ($\text{dcb} = 4,4'$ -dicarboxylate-2,2'-bipyridine) was electrostatically associated to egg lecithin vesicles doped with cationic surfactants, and amphiphilic CMV^{2+} as quenchers.⁵⁴ The good agreement with Equation 1.15 suggests that $[\text{Ru}(\text{dcb})_3]^{4-}$ was localised very close to the surface, with negligible diffusion orthogonal to the membrane surface. The diffusion coefficient obtained from a fit to the data was comparable to that of amphiphiles in bilayers, $(6 \pm 2) \times 10^{-11} \text{ m}^2 \text{ s}^{-1}$.⁵⁴ For comparison: diffusion coefficients in homogeneous solution are on the order of $1 \times 10^{-9} \text{ m}^2 \text{ s}^{-1}$.⁵⁵ As a last remark, these kinetic effects are not only important for energy transfer; Equation 1.15 is also valid for electron transfer, *e.g.* the non-fluorescent reactions of for instance an oxidised or reduced PS, in its ground state, with membrane-bound catalysts.

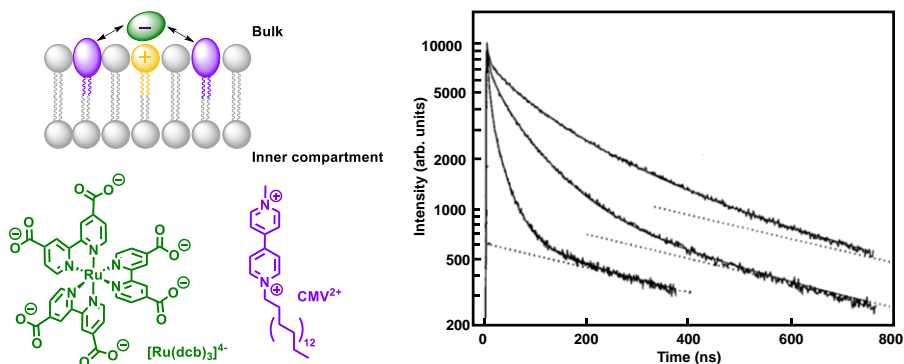


Figure 1.20. Left: Example of homogeneous PS $[\text{Ru}(\text{dcb})_3]^{4-}$ (green) electrostatically associated to egg lecithin vesicles doped with cationic surfactants (yellow), and amphiphilic CMV^{2+} (purple) as membrane-immobilised quencher. Right: Representative time-resolved luminescence decay of $[\text{Ru}(\text{dcb})_3]^{4-}$ in the presence of CMV^{2+} , showing strongly non-exponential behaviour (the dotted line indicates luminescence from a fraction of $[\text{Ru}(\text{dcb})_3]^{4-}$ not bound to the vesicles). Figure adapted from reference⁵⁴.

1.4 Aim and outline of this thesis

Liposomes represent an attractive and under-explored concept that complements traditional semiconductor-based developments and photo-electrochemical cells to drive photocatalysis.^{56–59} In particular, they allow interrogating the coupling of two half-reactions in a single photocatalytic system⁶⁰, and provide a framework for developing innovative solutions to avoid charge recombination and back electron transfer reactions, which are the main challenges of artificial photosynthesis. To achieve such a combined photocatalytic system based on liposomes, it would be necessary that the liposomes fulfil the following requirements (Figure 1.21):

- a) They support an efficient oxidation reaction; i.e. photocatalytic water oxidation
- b) They support an efficient reduction reaction; i.e. photocatalytic carbon dioxide reduction (Chapter 3) or proton reduction (Chapter 4)

- c) They couple the oxidation site and the reduction site using an electron relay that transfers electrons in a unidirectional way from one side to the other
- d) They do not leak even in presence of a gradient of chemicals on both sides of the membrane (Chapter 5), and are able to perform transmembrane electron transfer to avoid charge recombination, for example using a membrane-embedded peptide-photosensitiser conjugate (Chapter 2)
- e) They also allow for proton transfer from the oxidation site to the reduction site; i.e. with a proton channel such as the gramicidin ion channel
- f) The oxidation and reduction liposomes remain separated by a physical membrane that on the one hand avoids the formation of a potentially explosive mixture of the products of the redox half-reactions (H_2 and O_2) and on the other hand allows the protons and the electron relay molecules to move from one photocatalytic site to the other.

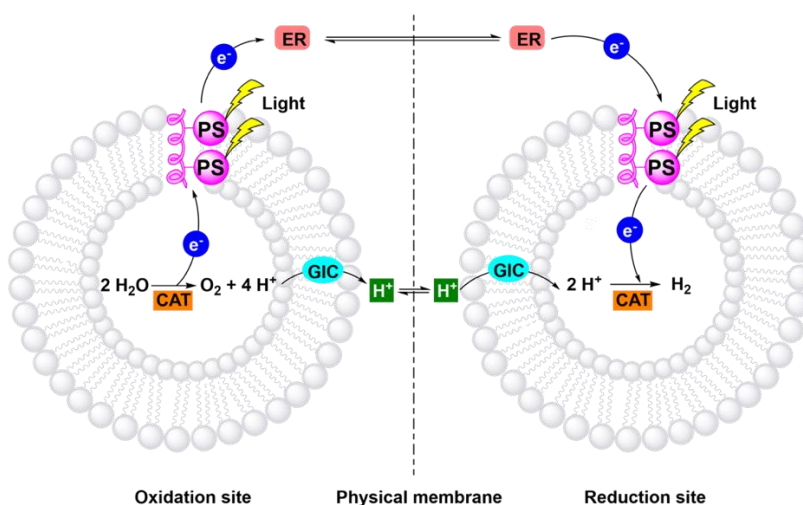


Figure 1.21. Proposed photocatalytic system for artificial water splitting based on liposomes. Electrons (blue) are transferred in a unidirectional way from the oxidation site to the reduction site via an electron relay and across the lipid bilayer via a photoactivatable peptide-photosensitiser conjugate. Protons (green) are transferred in a similar way with a proton channel. A physical membrane separates the oxidation and reduction site in two distinct compartments. CAT = catalyst, ER = electron relay, GIC = gramicidin ion channel, and PS = photosensitiser.

In Chapter 2, we report the preparation of two membrane-embedded metallopeptides, which were designed for driving photoinduced transmembrane electron transfer in liposomes from an electron donor encapsulated within the inner compartment to an electron acceptor located in the bulk. With a membrane leakage assay we studied whether genuine transmembrane electron transfer occurred or whether light-induced leakage of the donor through the membrane resulted in photoelectron transfer on one side of the membrane.

In Chapter 3, we prepared a series of ruthenium-based photosensitisers and rhenium-based catalysts covalently functionalised with alkyl chains of different lengths. These amphiphilic molecules were immobilised on liposomes to perform photocatalytic CO₂ reduction using ascorbate as sacrificial electron donor. We studied the influence of the length of the alkyl chain on the efficiency of liposome immobilisation, on the diffusion kinetics of the photoactive molecules within the lipid bilayer of the liposomes, on the electron transfer rate between the ruthenium photosensitiser and the rhenium catalyst, and on the overall photocatalytic performance of these liposomes.

In Chapter 4, we prepared a new alkylated cobalt polypyridyl catalyst for proton reduction and integrated it in liposomes for photocatalytic H₂ generation. Here, we aimed to maximise the turnover number of hydrogen by changing the concentration of the catalyst and the photosensitiser, the pH, and the lipids, and we looked for the reason why photocatalysis stops working after a few hours.

Though not directly related to the field of artificial photosynthesis, in Chapter 5, we applied a similar membrane leakage assay used in Chapter 2 of this thesis to measure the stability of liposomes during nebulisation. Nebulisation is a common technique for pulmonary drug delivery. To study whether different nebulisation techniques induced drug leakage from the liposomes, we encapsulated the fluorophore calcein inside the liposomes and measured its leakage to the bulk aqueous phase by emission spectroscopy.

Finally, in Chapter 6 a summary of the findings in this thesis is presented, followed by general conclusions, and an outlook. Parts of this thesis have been published^{61–64}, and other parts have been submitted or are being prepared for submission.

1.5 References

- 1 W. Lubitz, H. Ogata, O. Rüdiger and E. Reijerse, *Chem. Rev.*, 2014, **114**, 4081–4148.
- 2 X. Fang, S. Kalathil and E. Reisner, *Chem. Soc. Rev.*, 2020, **49**, 4926–4952.
- 3 I. Rojdestvenski, A. G. Ivanov, M. G. Cottam, A. Borodich, N. P. A. Huner and G. Oquist, *Biophys. J.*, 2002, **82**, 1719–1730.
- 4 B. Daum, D. Nicastro, J. Austin, J. R. McIntosh and W. Kühlbrandt, *Plant Cell*, 2010, **22**, 1299–1312.
- 5 A. Stikane, E. T. Hwang, E. V. Ainsworth, S. E. H. Piper, K. Critchley, J. N. Butt, E. Reisner and L. J. C. Jeuken, *Faraday Discuss.*, 2019, **215**, 26–38.
- 6 M. Hansen, S. Troppmann and B. König, *Chem. Eur. J.*, 2016, **22**, 58–72.
- 7 J. N. Robinson and D. J. Cole-Hamilton, *Chem. Soc. Rev.*, 1991, **20**, 49–94.
- 8 J. Flores, B. M. White, R. J. Brea, J. M. Baskin and N. K. Devaraj, *Chem. Soc. Rev.*, 2020, **49**, 4602–4614.
- 9 F. A. Armstrong and J. Hirst, *Proc. Natl. Acad. Sci.*, 2011, **108**, 14049–14054.
- 10 E. Rideau, R. Dimova, P. Schwille, F. R. Wurm and K. Landfester, *Chem. Soc. Rev.*, 2018, **47**, 8572–8610.
- 11 H.-J. Choi and C. D. Montemagno, *Nano Lett.*, 2005, **5**, 2538–2542.
- 12 M. C. M. van Oers, F. Rutjes and J. C. M. van Hest, *Curr. Opin. Biotechnol.*, 2014, **28**, 10–16.
- 13 D. Hvasanov, J. R. Peterson and P. Thordarson, *Chem. Sci.*, 2013, **4**, 3833–3838.
- 14 T. F. Tadros, *An Introduction to Surfactants*, De Gruyter, 2014.
- 15 D. Marsh, *Handbook of Lipid Bilayers*, CRC Press, 2013.
- 16 A. Leo, C. Hansch and D. Elkins, *Chem. Rev.*, 1971, **71**, 525–616.
- 17 J. N. Israelachvili, *Intermolecular and Surface Forces*, Academic Press, 2011.
- 18 D. M. Arias-Rotondo and J. K. McCusker, *Chem. Soc. Rev.*, 2016, **45**, 5803–5820.
- 19 S. Troppmann and B. König, *Chem. Eur. J.*, 2014, **20**, 14570–14574.
- 20 G. D. Scholes, G. R. Fleming, A. Olaya-Castro and R. van Grondelle, *Nat. Chem.*, 2011, **3**, 763–774.
- 21 C. A. Puckett and J. K. Barton, *J. Am. Chem. Soc.*, 2007, **129**, 46–47.
- 22 M. Hansen, F. Li, L. Sun and B. König, *Chem. Sci.*, 2014, **5**, 2683–2687.
- 23 B. Limburg, J. Wermink, S. S. van Nielsen, R. Kortlever, M. T. M. Koper, E. Bouwman and S. Bonnet, *ACS Catal.*, 2016, **6**, 5968–5977.

- 24 N. Ikuta, S. Y. Takizawa and S. Murata, *Photochem. Photobiol. Sci.*, 2014, **13**, 691–702.
- 25 B. Limburg, E. Bouwman and S. Bonnet, *J. Phys. Chem. B*, 2016, **120**, 6969–6975.
- 26 B. Limburg, E. Bouwman and S. Bonnet, *Chem. Commun.*, 2015, **51**, 17128–17131.
- 27 N. Sugiyama, M. Toyoda and Y. Amao, *Colloids Surf. A Physicochem. Eng. Asp.*, 2006, **284–285**, 384–387.
- 28 Y. Amao and I. Okura, *J. Mol. Catal. Chem.*, 1996, **105**, 125–130.
- 29 F. Franco, S. Fernández and J. Lloret-Fillol, *Curr. Opin. Electrochem.*, 2019, **15**, 109–117.
- 30 P. Garrido-Barros, C. Gimbert-Suriñach, R. Matheu, X. Sala and A. Llobet, *Chem. Soc. Rev.*, 2017, **46**, 6088–6098.
- 31 V. Radu, S. Frielingsdorf, S. D. Evans, O. Lenz and L. J. C. Jeuken, *J. Am. Chem. Soc.*, 2014, **136**, 8512–8515.
- 32 Y. Pellegrin and F. Odobel, *C. R. Chim.*, 2017, **20**, 283–295.
- 33 G. Steinberg-Yfrach, P. A. Liddell, S.-C. Hung, A. L. Moore, D. Gust and T. A. Moore, *Nature*, 1997, **385**, 239–241.
- 34 M. Andersson, L. Hammarström and K. Edwards, *J. Phys. Chem.*, 1995, **99**, 14531–14538.
- 35 G. Steinberg-Yfrach, J.-L. Rigaud, E. N. Durantini, A. L. Moore, D. Gust and T. A. Moore, *Nature*, 1998, **392**, 479–482.
- 36 I. O. L. Bacellar, M. C. Oliveira, L. S. Dantas, E. B. Costa, H. C. Junqueira, W. K. Martins, A. M. Durantini, G. Cosa, P. Di Mascio, M. Wainwright, R. Miotto, R. M. Cordeiro, S. Miyamoto and M. S. Baptista, *J. Am. Chem. Soc.*, 2018, **140**, 9606–9615.
- 37 S. Troppmann, E. Brandes, H. Motschmann, F. Li, M. Wang, L. Sun and B. König, *Eur. J. Inorg. Chem.*, 2016, **2016**, 554–560.
- 38 P. Jurkiewicz, L. Cwiklik, A. Vojtíšková, P. Jungwirth and M. Hof, *Biochim. Biophys. Acta - Biomembr.*, 2012, **1818**, 609–616.
- 39 A. Pannwitz, H. Saaring, N. Beztsinna, X. Li, M. A. Siegler and S. Bonnet, *Chem. Eur. J.*, 2021, **27**, 3013–3018.
- 40 J. Sabin, G. Prieto, J. M. Ruso, R. Hidalgo-Álvarez and F. Sarmiento, *Eur. Phys. J. E*, 2006, **20**, 401–408.
- 41 S. Paula, A. G. Volkov, A. N. van Hoek, T. H. Haines and D. W. Deamer, *Biophys. J.*, 1996, **70**, 339–348.
- 42 B. Maherani, E. Arab-Tehrany, A. Kheiriloom, D. Geny and M. Linder, *Biochimie*, 2013, **95**, 2018–2033.
- 43 L. Hammarström, M. Almgren and T. Norrby, *J. Phys. Chem.*, 1992, **96**, 5017–5024.
- 44 L. M. Hays, J. H. Crowe, W. Wolkers and S. Rudenko, *Cryobiology*, 2001, **42**, 88–102.
- 45 I. D. Johnson, *Molecular Probes Handbook: A Guide to Fluorescent Probes and Labeling Technologies*, Life Technologies Corporation, 2010.

- 46 C. C. Page, C. C. Moser, X. Chen and P. L. Dutton, *Nature*, 1999, **402**, 47–52.
- 47 E. Altamura, F. Milano, R. R. Tangorra, M. Trotta, O. H. Omar, P. Stano and F. Mavelli, *Proc. Natl. Acad. Sci. U. S. A.*, 2017, **114**, 3837–3842.
- 48 S. Bhosale, A. L. Sisson, P. Talukdar, A. Fürstner, N. Banetji, E. Vauthey, G. Bollot, J. Mareda, C. Röger, F. Würthner, N. Sakai and S. Matile, *Science*, 2006, **313**, 84–86.
- 49 A. Perez-Velasco, V. Gorteau and S. Matile, *Angew. Chem. Int. Ed.*, 2008, **47**, 921–923.
- 50 A. Bahreman, M. Rabe, A. Kros, G. Bruylants and S. Bonnet, *Chem. Eur. J.*, 2014, **20**, 7429–7438.
- 51 T. L. Nemzek and W. R. Ware, *J. Chem. Phys.*, 1975, **62**, 477–489.
- 52 C. S. Owen, *J. Chem. Phys.*, 1975, **62**, 3204–3207.
- 53 B. Medhage and M. Almgren, *J. Fluoresc.*, 1992, **2**, 7–21.
- 54 L. Hammarström, T. Norrby, G. Stenhagen, J. Mårtensson, B. Åkermark and M. Almgren, *J. Phys. Chem. B*, 1997, **101**, 7494–7504.
- 55 J. Moldenhauer, M. Meier and D. W. Paul, *J. Electrochem. Soc.*, 2016, **163**, H672–H678.
- 56 Y. Tachibana, L. Vayssieres and J. R. Durrant, *Nat. Photonics*, 2012, **6**, 511–518.
- 57 Gurudayal, D. Sabba, M. H. Kumar, L. H. Wong, J. Barber, M. Grätzel and N. Mathews, *Nano Lett.*, 2015, **15**, 3833–3839.
- 58 F. Li, K. Fan, B. Xu, E. Gabrielsson, Q. Daniel, L. Li and L. Sun, *J. Am. Chem. Soc.*, 2015, **137**, 9153–9159.
- 59 K. P. Sokol, W. E. Robinson, J. Warnan, N. Kornienko, M. M. Nowaczyk, A. Ruff, J. Z. Zhang and E. Reisner, *Nat. Energy*, 2018, **3**, 944–951.
- 60 H. Hu, Z. Wang, L. Cao, L. Zeng, C. Zhang, W. Lin and C. Wang, *Nat. Chem.*, 2021, **13**, 358–366.
- 61 A. Pannwitz, D. M. Klein, S. Rodríguez-Jiménez, C. Casadevall, H. Song, E. Reisner, L. Hammarström and S. Bonnet, *Chem. Soc. Rev.*, 2021, **50**, 4833–4855.
- 62 D. M. Klein, S. Rodríguez-Jiménez, M. E. Hoefnagel, A. Pannwitz, A. Prabhakaran, M. A. Siegler, T. E. Keyes, E. Reisner, A. M. Brouwer and S. Bonnet, *Chem. Eur. J.*, 2021, **27**, 17203–17212.
- 63 D. M. Klein, A. Poortinga, F. M. Verhoeven, D. Bonn, S. Bonnet and C. J. M. van Rijn, *Chem. Phys.*, 2021, **547**, 111192.
- 64 D. M. Klein, L. Passerini, M. Huber and S. Bonnet, *ChemCatChem*, 2022, accepted.

Unidirectional transmembrane photoinduced electron transfer with membrane-embedded metallopeptides

*Unidirectional transmembrane electron transfer is an essential process in natural photosynthetic solar energy conversion, where it plays a key role in separating reaction products and slowing charge recombination. Biomimicking photosynthetic membranes by making use of artificial liposomes to demonstrate transmembrane electron transfer is a challenging strategy; in particular, differentiating genuine transmembrane electron transfer through a molecularly impermeable lipid membrane, from light-induced leakage of molecular electron donors or acceptors through the membrane, followed by photoelectron transfer at the surface of the bilayer, is a complicated task. Here, we report two membrane-embedded metallopeptides, **WALP23-Ru₂** and **WALP23-Re₂**, designed to drive photoinduced transmembrane electron transfer in liposomes. Upon light irradiation, the polycationic peptide **WALP23-Ru₂** seemed to quickly transfer electrons from a donor located in a liposome interior, to an acceptor located on the other side of the membrane. However, a membrane leakage assay demonstrated that the reaction was the result of leakage of the electron donor through the membrane, followed by photoinduced electron transfer on one side of the membrane. In contrast, the neutral peptide **WALP23-Re₂** achieved slower light-induced electron transfer, but without leakage, thereby realizing genuine transmembrane electron transfer. These results highlight the importance of leakage studies for the development of biomimicking artificial photosynthetic systems and the potential of artificial metallopeptides as transmembrane electron transporters.*

This chapter is to be submitted as a full paper: David M. Klein, Xinmeng Li, Aimee L. Boyle, Rianne van der Pol, G. J. Agur Sevink, Albert M. Brouwer, and Sylvestre Bonnet, *in preparation*.

2.1 Introduction

In natural photosynthesis, the efficiency of electron extraction from water in green plants is optimised by embedding all key components of the system, i.e. the oxygen evolving complex, photosystem I, and photosystem II, around the lipid bilayer of the photosynthetic membrane. Unidirectional electron transfer through the membrane is achieved using several redox mediators assembled at fixed positions inside the membrane, as well as a tight, evolutionary-evolved Z-like energy scheme, which prevents non-productive charge recombination.¹ This system allows green plants to use the energy from sunlight and catalytic water oxidation to perform CO₂ reduction and produce sugars via the Calvin cycle. A promising strategy for artificial solar fuel production is to mimic natural photosynthesis using the lipid bilayer of liposomes as a platform for the co-embedding of catalysts and photosensitisers.²⁻⁴ Liposomes are spherical supramolecular assemblies of lipids that define two distinct aqueous compartments, i.e., an inner compartment and the exterior bulk aqueous phase, and one lipophilic phase, i.e., the interior of the membrane. These compartments can be exploited for artificial photosynthetic purposes by separating water-soluble components (i.e. electron donors from electron acceptors, or water oxidation catalysts from water reduction catalysts) to avoid energy-wasting charge recombination reactions. To enable electrons running from one compartment to the other, for example to couple water oxidation with water reduction, it is crucial to be able to transfer electrons across the lipid bilayer. The membrane is, however, an insulator, and it is also too thick (typically 30 – 35 Å) for allowing electron transfer to occur in one single step.^{4,5}

Driving unidirectional photoinduced electron transfer through an insulating lipid membrane is hence recognised as one of the holy grails of artificial photosynthesis. Three main strategies have been considered to achieve it: 1) incorporation of biological components, such as an electron-transfer transmembrane protein, into the lipid bilayer^{6,7}; 2) synthesis of artificial transmembrane molecules spanning the lipid bilayer⁸⁻¹⁰; and 3) use of molecular charge carriers that can diffuse across the membrane¹¹. Still, the

number of liposomal systems that can actually perform transmembrane electron transfer is limited.⁶⁻¹¹ These strategies indeed share many challenges, such as difficult syntheses, problems in controlling the orientation of a dissymmetric molecule relative to a lipid bilayer separating two different aqueous environments, or quenching of the photoinduced electron transfer reaction in the presence of molecular dioxygen. In addition, the mechanistic problem of distinguishing the leakage of redox mediator molecules through the membrane, followed by electron transfer on one side of the membrane, from genuine transmembrane electron transfer across a truly impermeable bilayer, has rarely been discussed.^{2,12,13}

To address these challenges simultaneously, we prepared two new metalloptides, **WALP23-Ru₂** and **WALP23-Re₂**, which are well-defined, air-stable molecules designed to place two identical ruthenium(II) or rhenium(I) photosensitisers at intermediate positions inside a lipid bilayer membrane. Ideally, such a molecule may allow transmembrane electron transfer to occur in three shorter (< 20 Å) steps, rather than one large step of more than 40 Å, which is highly improbable.⁵ We investigated the orientation of the metalloptides within the membrane and their ability to transfer electrons, upon light irradiation, across a lipid bilayer, from an electron donor located in the inner compartment of the liposome, towards an electron acceptor located outside, i.e., in the bulk (Figure 2.1A, pathway I). By using a membrane leakage assay, we were able to distinguish genuine transmembrane electron transfer, which takes place with **WALP23-Re₂**, from transmembrane leakage of the electron donor, which occurs with **WALP23-Ru₂** (Figure 2.1A, pathway II).

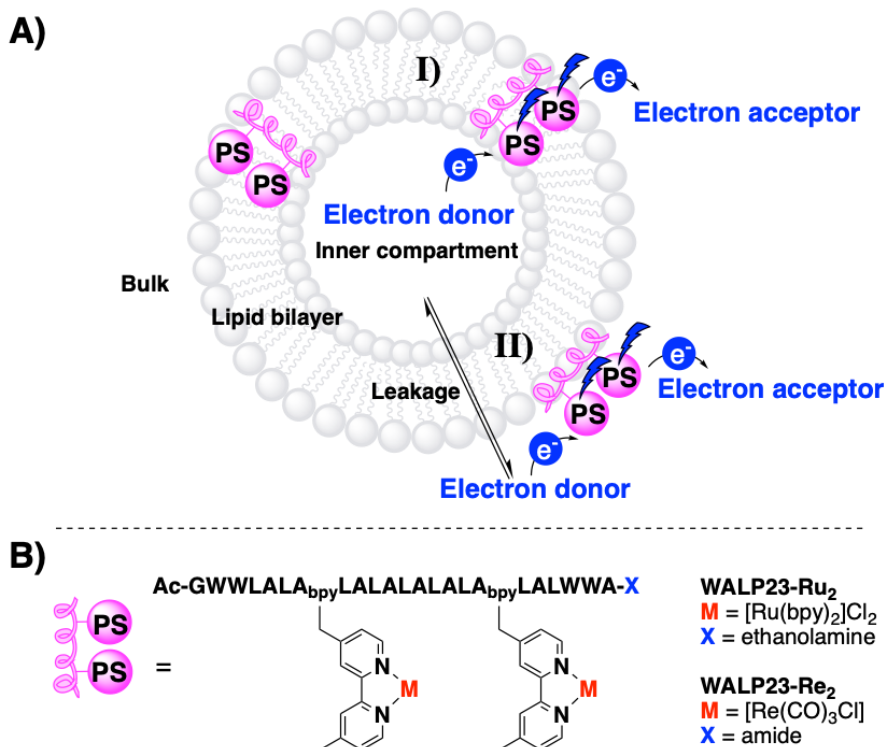


Figure 2.1. Transmembrane electron transfer with metallopeptides in the lipid bilayer. (A) Two pathways for electron transfer are possible; I) electron transfer across the lipid bilayer via a light-activatable metallopeptide from an electron donor in the inner compartment of liposomes to an electron acceptor located in the aqueous bulk, and II) transmembrane leakage of the electron donor to the aqueous bulk resulting in electron transfer via a light-activatable metallopeptide on the same side of the membrane. (B) Molecular structure of the metallopeptides investigated in this study. A = alanine, A_{bpy} = bipyridylalanine, Ac = acetyl, G = glycine, L = leucine, and W = tryptophan.

2.2 Results and Discussion

The molecular structure of the metallopeptides **WALP23-Ru₂** and **WALP23-Re₂** (Figure 2.1B) derives from the WALP_n peptides (Ac-GWWL(AL)_nWWA-X, with Ac = acetyl, G = glycine, W = tryptophan, L = leucine, A = alanine, and X = amide or ethanolamine). WALP_n peptides are hydrophobic α -helical peptides, initially developed by Killian *et al.* as a model for the hydrophobic domains of many transmembrane proteins found in nature.^{14–16} We

envisioned that by incorporating at least two metal centers within the peptide chain of WALPn, photoinduced electron transfer may be achieved by splitting it into several steps; 1) light absorption by the photosensitisers resulting in the formation of an excited state PS^* , 2) reductive quenching of PS^* by the electron donor located near the inner compartment of the liposome, resulting in the formation of reduced photosensitiser (PS^-), 3) oxidative quenching of PS^* by the electron acceptor located near the bulk aqueous phase, resulting in the formation of oxidised photosensitiser (PS^+), and finally 4) charge recombination between PS^- and PS^+ within the membrane, to regenerate the two ground state photosensitisers. Thus, we replaced two alanine residues in the original WALPn peptide sequence by two unnatural amino acids that can chelate metal ions, namely bipyridylalanines (A_{bpy}).^{17,18} Two parameters of the peptide were designed simultaneously: 1) the length of the α -helical part of the peptide (i.e. the amino acids $L(AL)_n$, where the length of one amino acid is assumed to be 0.15 nm in an ideal α -helix) should fit the hydrophobic thickness of the membrane bilayer (2.65 nm for 1,2-dipalmitoyl-*sn*-glycero-3-phosphocholine; DPPC)¹⁵; 2) the distance between the two metal centers should be short enough to allow electron transfer between them to occur; ideally both PS molecules should be on the same side of the α -helix. Based on initial modeling using the YASARA program, we chose to prepare a WALP23 peptide (thus Ac-GWWL(AL)₄WWA-X) with A_{bpy} residues in positions 7 and 17; **WALP23-bpy₂** (Figure B1 and Table B1). We prepared **WALP23-bpy₂** by a combination of automated solid-phase peptide synthesis, with manual peptide synthesis for the coupling of the two A_{bpy} residues. The metallopeptides **WALP23-Ru₂** and **WALP23-Re₂** were then synthesised by reaction of **WALP23-bpy₂** with *cis*-[Ru(bpy)₂Cl₂] and [Re(CO₅)Cl] metal precursors, respectively. The metallopeptides were purified by size-exclusion chromatography and characterised by elemental analysis, HPLC-MS (Figures B2 – B4), and UV-Vis (Figures B5 and B6).

Although both metallopeptides were prepared from the same hydrophobic peptide and hence may seem similar, **WALP23-Ru₂** bears 4 positive charges and 4 chloride counter anions, while **WALP23-Re₂** is neutral. Such different charges are likely to affect the lipophilicity of the peptides, which may in turn

influence their membrane embedding, shape, and/or orientation with respect to the membrane. Molecular dynamics (MD) simulations were performed to study these questions and qualitatively assess whether **WALP23-Ru₂** and **WALP23-Re₂** may retain the reported propensity of WALP23 to insert into the membrane with a perpendicular orientation with respect to the lipid bilayer. The primary goal of the modeling was to investigate the insertion probability of each peptide. 200 ns MD simulations were hence performed by spontaneous aggregation of independent random mixtures containing one metalloprotein molecule, 128 DPPC lipid molecules solvated by water molecules, and in the case of **WALP23-Ru₂**, 4 chloride anions to neutralise the charge of the system. We opted for spontaneous aggregation of the lipid bilayer because the high free energy barrier associated with inserting peptides into a readily formed membrane is known to hamper the observation of spontaneous insertion on the time scales of standard MD.^{19–22} The alternative approach, i.e., the determination of a free energy difference by constrained MD²³, suffers from a lack of clearly defined reaction coordinates, as the propensity of the metal centers for the interface is likely to induce important conformational changes in the WALP23 backbone. Earlier studies have also corroborated that, while the kinetics of insertion may vary with particular force field parameters and simulation techniques, the energetics of partitioning can be reliably extracted by different approaches. We note that, whereas NMR data support an insertion motif for WALP23 of an (antiparallel) dimer²⁴, the (charged) metallic groups at the peptide interface are likely to oppose dimer formation, so only monomers were simulated.

Simulation trajectories were analysed to determine the insertion characteristics of the metalloprotein via its orientational angle (ϑ) and immersion ratio (φ), see Figure 2.2A. Here, ϑ , is defined as the angle between the two metals and the local normal of the lipid membrane, while φ is the ratio between the number of DPPC molecules and the total number of molecules (DPPC, water, and ions) that surround the metalloprotein (within a pre-defined cut-off range of 0.35 nm). Typically, a metalloprotein that would show $\vartheta < 50^\circ$ and $\varphi > 0.5$ could be considered as “transmembrane”, while metalloproteins with $\vartheta > 50^\circ$ and $\varphi > 0.5$ could be considered as

“parallel” to the membrane, typically placed at the water-bilayer interface. In the case of $\varphi < 0.5$, the metallopeptide is surrounded by more water molecules than DPPC molecules, and therefore its orientation with respect to the lipid bilayer was not determined. Furthermore, the mass density profiles of the metallopeptides within the lipid bilayer were analysed to verify whether the configuration was truly transmembrane or parallel (Figures B7, B8, and B9). Figure 2.2B shows that in a majority of the cases, a relatively short 200 ns trajectory was sufficient for the metallopeptide to either bind to or insert into a well-identified lipid bilayer membrane, in agreement with the hydrophobic nature of their WALP23 core. While most peptides were found to bind to the membrane, 2 of the 13 simulated **WALP23-Ru₂** peptides led to transmembrane configurations, while for the more hydrophobic **WALP23-Re₂** peptide the number of transmembrane configurations was significantly higher (5 out of 16, as one **WALP23-Re₂** peptide considered as parallel ($\varphi = 0.58$ and $\vartheta = 60^\circ$) turned out to be in a transmembrane configuration by its mass density profile), see Figures 2.2C and 2.2D. Within the transmembrane configurations, the average distance between the two metal atoms was found to be 2.0 ± 0.3 nm for Ru-Ru and 2.1 ± 0.6 nm for Re-Re (Table B2), which should in theory accommodate electron transfer between them, as electron transfer within biological systems are reported up to 3.5 nm.⁵ Importantly, these results highlight that even when designed to assemble perpendicularly to a lipid bilayer membrane, artificial amphipathic molecules may also assemble in a parallel fashion at the interface with water, as such assembly also offers improved molecular contacts with both hydrophobic and hydrophilic phases.

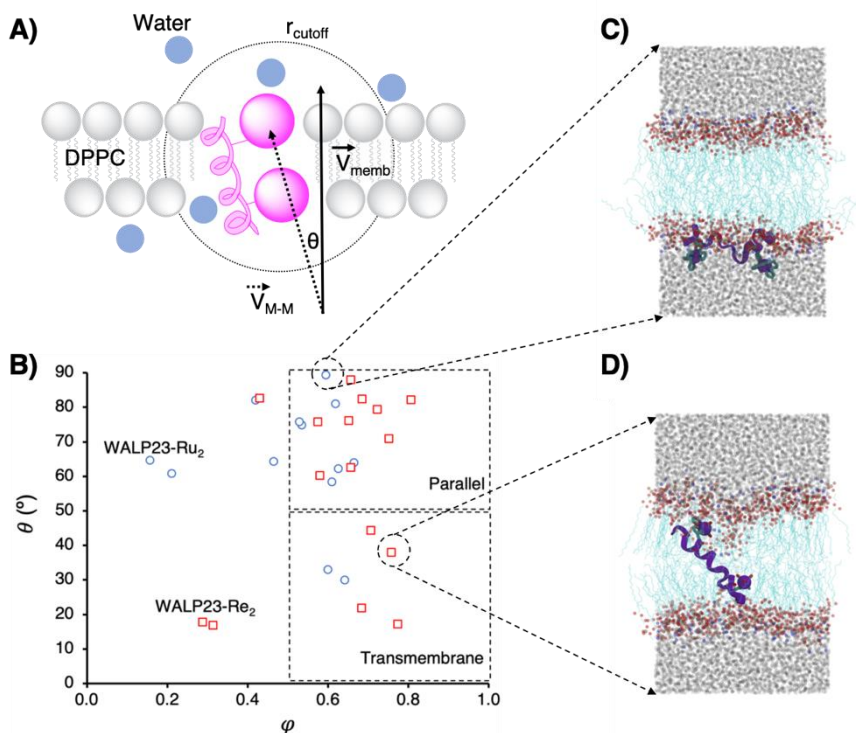


Figure 2.2. Molecular dynamics simulations to study the orientation of the metallopeptides. (A) Illustration of the procedure that was used to determine the orientation of the metallopeptide with respect to the lipid membrane. ϑ is the angle between the metal-metal vector (\vec{V}_{M-M}) and the normal vector of the lipid membrane (\vec{V}_{memb}). r_{cutoff} is the cut-off range. (B) φ and ϑ values of **WALP23-Ru₂** and **WALP23-Re₂** after 200 ns MD simulation time. φ is the ratio between the number of DPPC molecules and the total number of molecules within r_{cutoff} . (C) MD snapshots showing a parallel orientation of **WALP23-Ru₂** with respect to the lipid bilayer and (D) a transmembrane **WALP23-Re₂**.

To determine whether the MD simulations reflect the experimental incorporation of metallopeptides into a DPPC membrane, we prepared metallopeptide-functionalised liposomes. For the preparation of these liposomes, either **WALP23-bpy₂**, **WALP23-Ru₂** or **WALP23-Re₂** (1 mol%) was added to a DPPC formulation containing one percent 1,2-distearoyl-*sn*-glycero-3-phosphoethanolamine N-(carbonyl-methoxypolyethylene glycol-2000) (NaDSPE-PEG2K), which served to prevent liposome aggregation.²⁵ The liposomes were prepared by standard extrusion methods using an NH₄OAc

buffer at a pH of 7.0 and an osmolality of 0.42 Osm (see Appendix B). According to dynamic light scattering the average hydrodynamic diameter of the resulting liposomes was 137 nm for liposomes containing **WALP23-bpy₂**, 136 nm for liposomes containing **WALP23-Ru₂** and 123 nm for liposomes containing **WALP23-Re₂**, and their polydispersity index (PDI) was lower than 0.20, which indicated a uniform size distribution (Table B3). As absorption spectra obtained using UV-Vis spectroscopy suffered from strong scattering due to the presence of the liposomes, photoluminescence excitation and emission spectra were measured to characterise the lowest energy absorption (λ_{abs}) and emission maxima (λ_{em}) of the metallopeptides in the liposome environment. λ_{abs} and λ_{em} were 454 nm and 616 nm, respectively, for **WALP23-Ru₂**, and 366 nm and 562 nm, respectively, for **WALP23-Re₂**, which fits with values typically reported for [Ru(bpy)₃]²⁺ and [Re(bpy)(CO)₃Cl] complexes in lipid membranes (Figure B10).^{26,27} For both metallopeptides, emission from the W amino acids ($\lambda_{\text{em}} = 334$ nm for **WALP23-Ru₂** and 335 nm for **WALP23-Re₂**, was slightly blue-shifted compared to **WALP23-bpy₂** ($\lambda_{\text{em}} = 349$ nm, Figure B11). Time-dependent photoluminescence could be best fitted with biexponential decay rate laws, with lifetimes $\tau_1 = 123$ ns and $\tau_2 = 787$ ns for **WALP23-Ru₂** and $\tau_1 = 8$ ns and $\tau_2 = 103$ ns for **WALP23-Re₂** (Figure B12). Altogether, and also considering that both metallopeptides are insoluble in water, these results strongly indicate that **WALP23-Ru₂** and **WALP23-Re₂** were indeed taken up by the membrane of the liposomes. This assumption was confirmed using confocal microscopy of the **WALP23-Ru₂**-containing multilamellar giant vesicles obtained before extrusion during liposome preparation, which showed red emission ($\lambda_{\text{exc}} = 488$ nm and $\lambda_{\text{em}} = 640 - 680$ nm) coming from the lipid bilayer only (Figure B13).

To perform the transmembrane electron transfer experiments, dissymmetric DPPC:NaDSPE-PEG2K (100:1) liposomes were prepared containing 1 mol% of the metallopeptide in the membrane, the electron donor ethylenediaminetetraacetic acid (EDTA; in the form of HEDTA³⁻ at pH = 8.2) in the aqueous inner compartment of the liposome, and the electron acceptor 2-(4-iodophenyl)-3-(4-nitrophenyl)-5-(2,4-disulfophenyl)-2H-tetrazolium anion (WST1⁻) in the bulk aqueous phase, thus on the outside

(pH = 7.0) of the liposome (Figure 2.3). We chose WST1⁻ as the electron acceptor as lipid membranes are notoriously impermeable to it; this dye is known by biologists to be reduced to formazan (Fz1²⁻) by electrons and protons generated inside living cells only in the presence of a membrane-soluble relay such as the 1-methoxy-*N*-methylphenazinium cation (MMP⁺).^{11,28} When left in the dark for 30 min, the liposomes were stable and did not show any sign of formazan formation. However, upon light irradiation a new absorption band at $\lambda_{\text{max}} = 438 \text{ nm}$ gradually appeared that is characteristic of Fz1²⁻ (Figure 2.3).¹¹ This evolution clearly demonstrated that photoinduced electron transfer had taken place, with a quantum yield of 0.015% for **WALP23-Ru₂** and 0.027% for **WALP23-Re₂** after 1 h of irradiation (see Appendix B for the calculation and Figure B14). Furthermore, the liposome systems were photoactive under both a N₂ atmosphere and an air atmosphere (Figures B15 – B18), which is a significant improvement over systems requiring MMP⁺ as a transmembrane electron transporter for example, which is re-oxidised in the presence of dioxygen.¹¹ Dynamic light scattering measurements showed that the liposomes remained intact during the photoreaction, as the size and polydispersity remained identical before and after 2.5 h light irradiation (Table B4). A control experiment with **WALP23-bpy₂** in the membrane instead of a metallopeptide showed no photoinduced electron transfer, demonstrating that the metal-based photosensitisers were required for light-driven electron transfer (Figure B19). Overall, both membrane-embedded metallopeptides clearly allowed photoinduced electron transfer to occur between the HEDTA³⁻ donor and WST1⁻ acceptor originally located on opposite sides of the membrane.

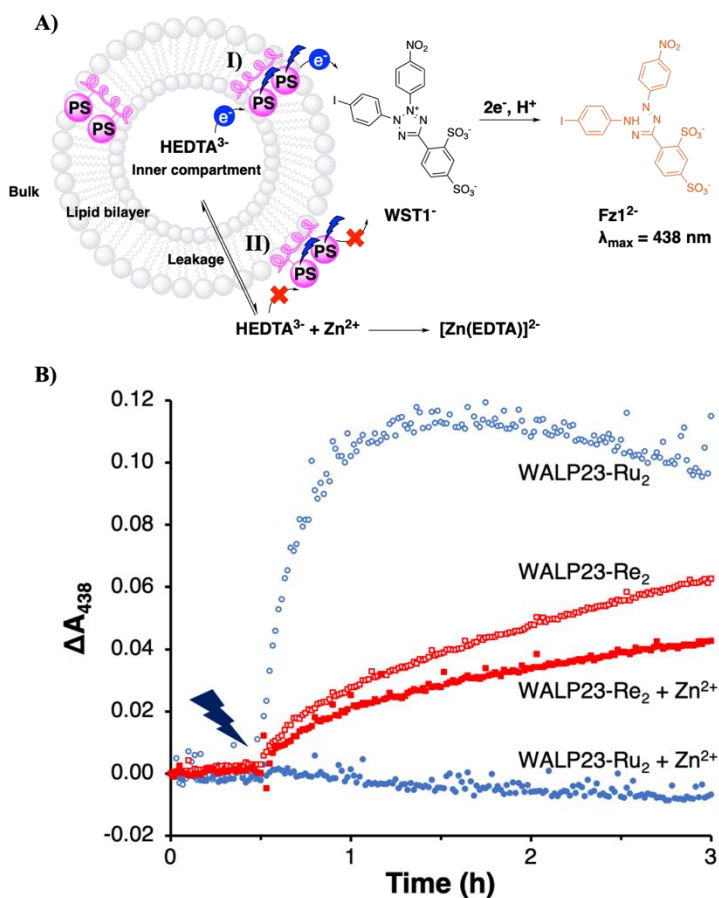


Figure 2.3. Electron transfer studies of the metallopeptides in liposomes. (A) Electron transfer processes initiated by light irradiation; I) transmembrane electron transfer from the sacrificial electron donor HEDTA³⁻ located in the inner compartment of the liposome via a membrane-embedded peptide-photosensitizer conjugate to the sacrificial electron acceptor WST1⁻ located in the bulk forming the colored Fz1²⁻, which can be followed by UV-Vis, and II) externally added Zn²⁺ ions form a complex with HEDTA³⁻, thereby inactivating the electron transfer pathway on the outside of the membrane; (B) The formation of Fz²⁻ as monitored by a change in absorbance ($\lambda_{\max} = 438$ nm) versus irradiation time for liposome systems containing either **WALP23-Ru₂** (blue circles) or **WALP23-Re₂** (red squares) with (closed symbols) or without Zn(OAc)₂ (open symbols). Blue light irradiation ($\lambda_{\text{irr}} = 450$ nm, P = 15.8 mW, $\Phi_0 = 39.1$ nmol/s for **WALP23-Ru₂** and $\lambda_{\text{irr}} = 385$ nm, P = 7.3 mW, $\Phi_0 = 13.1$ nmol/s for **WALP23-Re₂**) was started after 0.5 h in the dark. Experimental conditions: [DPPC] = 2.5 mM, [DSPE-PEG2K] = 25 μ M, [**WALP23-Ru₂** or **WALP23-Re₂**] = 25 μ M, [HEDTA³⁻] = 0.125 M (before SEC column), [WST1⁻] = 0.33 mM, [Zn(OAc)₂] = 0 or 5 mM in 0.1 M NH₄OAc (pH = 7.0, p = 0.42 Osm). The measurements were performed at 25 °C under an air atmosphere.

At this stage, however, it became essential to distinguish unambiguously between genuine transmembrane electron transfer, and leakage of the donor through the membrane, followed by photoinduced electron transfer on one side of the membrane (Figure 2.3A). In order to distinguish between these two mechanisms, an excess of Zn^{2+} ions was added on the outside of the liposomes before light irradiation, keeping the same osmolality as the inner solution using NH_4OAc . Zn^{2+} ions chemically bind to HEDTA^{3-} molecules to form the complex $[\text{Zn}(\text{EDTA})]^{2-}$. By doing so, the electron donor ability of HEDTA^{3-} molecules that may have remained outside the liposomes after liposome purification, or that may have leaked through the membrane during the photoreaction, is inactivated.¹¹ Hence, addition of Zn^{2+} enables the differentiation of true transmembrane electron transfer by excitation of the transmembrane metallopeptide, from leakage of HEDTA^{3-} through the membrane followed by photoinduced electron transfer to WST1^- on the outside of the membrane. For liposomes containing the **WALP23-Ru₂** metallopeptide the photoinduced electron transfer observed in the absence of Zn^{2+} ions was fully quenched when Zn^{2+} was added, while those containing **WALP23-Re₂** conserved their ability to transfer electrons (at a slightly lower rate, Figure 2.3B). Additional control experiments were realised using mononuclear photosensitisers $[\text{Ru}(\text{bpy})_2(\text{bpy}-(\text{C}_{15})_2)]\text{Cl}_2$ ($\text{bpy} = 2,2'$ -bipyridine; $\text{bpy}-(\text{C}_{15})_2 = 4,4'$ -di-pentadecane-2,2'-bipyridine) or $[\text{Re}(\text{bpy}-(\text{C}_{15}))(\text{CO})_3\text{Cl}]$ instead of the metallopeptides, which distribute on both leaflets of the bilayer and are not physically coupled to each other as in **WALP23-Ru₂** or **WALP23-Re₂** (Figures B20 and B21).²⁷ All other conditions being identical, these experiments showed much slower electron transfer compared to membranes functionalised with the metallopeptides, which were deactivated upon addition of free Zn^{2+} ions on the outside of the liposomes (Figure B22). These controls demonstrate that the mechanical link and close distance between the two metals in the metallopeptide play a crucial role in their transmembrane electron transfer abilities.

To investigate in more detail why **WALP23-Ru₂** showed formation of Fz1^{2-} in absence of Zn^{2+} ions, while it was unable to do so in the presence of Zn^{2+} ions, whereas electron transfer with **WALP23-Re₂** was more or less insensitive to zinc addition, we quantified HEDTA^{3-} leakage through the membrane using a

murexide-based titration experiment.¹¹ Murexide is a purple dye that becomes orange upon binding to Cu^{2+} , but cannot compete with copper chelation by HEDTA^{3-} . Addition of an excess of murexide to liposomes kept in the dark or irradiated with light, followed by dropwise titration with known amounts of Cu^{2+} , allowed the quantification of the amount of HEDTA^{3-} in the outside aqueous phase (Table B5). The concentration of HEDTA^{3-} outside the liposomes was found to be low (0.0 – 0.2 mM) for liposomes containing either **WALP23-Ru₂** or **WALP23-Re₂** metallopeptides. This result indicated that i) purification of the asymmetric liposomes using size-exclusion chromatography was successful at removing HEDTA^{3-} located on the outside of the liposomes, and ii) leakage of HEDTA^{3-} through the membrane did not occur in the dark. In contrast, for irradiated liposomes containing **WALP23-Ru₂** in the membrane, the amount of HEDTA^{3-} outside the liposomes increased significantly (from 0.0 – 0.2 mM to 0.2 – 0.4 mM) upon irradiation. Similar results were obtained upon irradiation of liposomes containing **WALP23-Re₂** in the membrane (from 0.0 – 0.2 mM to 0.4 – 0.6 mM HEDTA^{3-} outside the liposomes). In both cases, the amount of HEDTA^{3-} was much smaller than the amount of Zn^{2+} ions (5 mM) present, thus all HEDTA^{3-} molecules located on the outside of the liposomes were inactivated as electron donors. Considering that with **WALP23-Ru₂** photoinduced electron transfer was fully inactivated in the presence of Zn^{2+} ions, the photoinduced electron transfer occurring in absence of Zn^{2+} ions can essentially be attributed to light-induced leakage of HEDTA^{3-} , followed by photosensitised electron transfer at the liposome surface from donor to acceptor molecules both located outside the liposomes. It is likely that such a process is sensitised *via* **WALP23-Ru₂** molecules assembled parallel to the lipid membrane. Another hypothesis is that light-induced leakage of Zn^{2+} from the bulk to the inner compartment of the liposomes resulted in the inactivation of the inner HEDTA^{3-} molecules. In contrast, for **WALP23-Re₂** electron transfer still occurred after addition of Zn^{2+} ions, which could only take place from HEDTA^{3-} molecules protected from Zn^{2+} ions, hence inside the liposomes, towards WST1^- outside the liposomes. Control liposomes containing mononuclear photosensitisers ($[\text{Ru}(\text{bpy})_2(\text{bpy}-(\text{C}_{15})_2)]\text{Cl}_2$ or $[\text{Re}(\text{bpy}-(\text{C}_{15})(\text{CO})_3\text{Cl})]$) showed, both in the dark and after light irradiation, the same concentration of HEDTA^{3-} (0.4 – 0.6 mM) outside the liposomes. It was

hence photoinduced electron transfer on one side of the membrane that occurred for these liposomes, rather than transmembrane photoinduced electron transfer, which again highlights the importance of the mechanical link between the two metal centers in the metallopeptides to trigger true transmembrane electron transfer. Overall, **WALP23-Re₂** is one of the few known artificial molecules capable of triggering true transmembrane electron transfer.

2.3 Conclusion

To conclude, metallopeptides built by attaching two neutral rhenium(I) photosensitiser molecules on a WALP23 peptide are capable of performing unidirectional transmembrane electron transfer under an air atmosphere. In such studies, careful examination of the concentration of the encapsulated electron donor, both before and after light irradiation, and both inside and outside the membrane, is crucial to differentiate genuine transmembrane electron transfer, as obtained with **WALP23-Re₂**, from light-induced leakage of the electron donor, as observed with **WALP23-Ru₂**. In addition, the high modularity of solid-state peptide synthesis allows for imagining a range of metallopeptides with different lengths, and different numbers and relative positions of the metal centers in the membrane, which may lead to optimised transmembrane electron transfer rates without a need for major variations in the synthetic procedure of the “wire”. Ultimately, a better fundamental understanding of these systems will be required before fully artificial photosynthetic systems can be developed, where biomimetic transmembrane electron transfer allows for coupling catalytic water oxidation and proton or CO₂ reduction.

2.4 References

- 1 D. Gust and T.A. Moore, *Science*, 1989, **244**, 35–41.
- 2 J. N. Robinson and D. J. Cole-Hamilton, *Chem. Soc. Rev.*, 1991, **20**, 49–94.
- 3 M. Hansen, S. Troppmann and B. König, *Chem. Eur. J.*, 2016, **22**, 58–72.
- 4 A. Pannwitz, D. M. Klein, S. Rodríguez-Jiménez, C. Casadevall, H. Song, E.

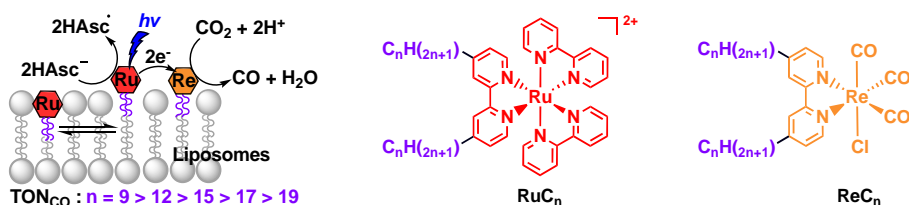
- Reisner, L. Hammarström and S. Bonnet, *Chem. Soc. Rev.*, 2021, **50**, 4833–4855.
- 5 C. C. Moser, J. M. Keske, K. Warncke, R. S. Farid and P. L. Dutton, *Nature*, 1992, **355**, 796–802.
- 6 E. Altamura, F. Milano, R. R. Tangorra, M. Trotta, O. H. Omar, P. Stano and F. Mavelli, *Proc. Natl. Acad. Sci. U. S. A.*, 2017, **114**, 3837–3842.
- 7 A. Stikane, E. T. Hwang, E. V. Ainsworth, S. E. H. Piper, K. Critchley, J. N. Butt, E. Reisner and L. J. C. Jeuken, *Faraday Discuss.*, 2019, **215**, 26–38.
- 8 G. Steinberg-Yfrach, P. A. Liddell, S.-C. Hung, A. L. Moore, D. Gust and T. A. Moore, *Nature*, 1997, **385**, 239–241.
- 9 S. Bhosale, A. L. Sisson, P. Talukdar, A. Fürstenberg, N. Banetji, E. Vauthey, G. Bollot, J. Mareda, C. Röger, F. Würthner, N. Sakai and S. Matile, *Science*, 2006, **313**, 84–86.
- 10 A. Perez-Velasco, V. Gorteau and S. Matile, *Angew. Chem. Int. Ed.*, 2008, **47**, 921–923.
- 11 B. Limburg, E. Bouwman and S. Bonnet, *Chem. Commun.*, 2015, **51**, 17128–17131.
- 12 L. Hammarström, M. Almgren, J. Lind, G. Merenyi, T. Norrby and B. Åkermark, *J. Phys. Chem.*, 1993, **97**, 10083–10091.
- 13 L. Hammarström and M. Almgren, *J. Chem. Sci.*, 1993, **105**, 539–554.
- 14 J. A. Killian, I. Salemink, M. R. R. de Planque, G. Lindblom, R. E. Koeppe and D. V Greathouse, *Biochemistry*, 1996, **35**, 1037–1045.
- 15 M. R. R. de Planque and J. A. Killian, *Mol. Membr. Biol.*, 2003, **20**, 271–284.
- 16 J. A. Killian and T. K. M. Nyholm, *Curr. Opin. Struct. Biol.*, 2006, **16**, 473–479.
- 17 K. J. Kise and B. E. Bowler, *Inorg. Chem.*, 2002, **41**, 379–386.
- 18 I. Gamba, I. Salvadó, G. Rama, M. Bertazzon, M. I. Sánchez, V. M. Sánchez-Pedregal, J. Martínez-Costas, R. F. Brissos, P. Gamez, J. L. Mascareñas, M. Vázquez López and M. E. Vázquez, *Chem. Eur. J.*, 2013, **19**, 13369–13375.
- 19 S. Esteban-Martín and J. Salgado, *Biophys. J.*, 2007, **92**, 903–912.
- 20 J. P. Ulmschneider, J. C. Smith, S. H. White and M. B. Ulmschneider, *J. Am. Chem. Soc.*, 2011, **133**, 15487–15495.
- 21 T. Bereau, W. F. D. Bennett, J. Pfaendtner, M. Deserno and M. Karttunen, *J. Chem. Phys.*, 2015, **143**, 243127.
- 22 I. Kabelka and R. Vácha, *Biophys. J.*, 2018, **115**, 1045–1054.
- 23 T. Kim and W. Im, *Biophys. J.*, 2010, **99**, 175–183.
- 24 L. Monticelli, D. P. Tieleman and P. F. J. Fuchs, *Biophys. J.*, 2010, **99**, 1455–1464.
- 25 B. Limburg, J. Wermink, S. S. van Nielen, R. Kortlever, M. T. M. Koper, E. Bouwman and S. Bonnet, *ACS Catal.*, 2016, **6**, 5968–5977.
- 26 N. Ikuta, S. Y. Takizawa and S. Murata, *Photochem. Photobiol. Sci.*, 2014, **13**, 691–702.
- 27 D. M. Klein, S. Rodríguez-Jiménez, M. E. Hoefnagel, A. Pannwitz, A. Prabhakaran, M. A. Siegler, T. E. Keyes, E. Reisner, A. M. Brouwer and S. Bonnet, *Chem. Eur. J.*, 2021, **27**, 17203–17212.

Chapter 2

- 28 M. Ishiyama, M. Shiga, K. Sasamoto, M. Mizoguchi and P. He, *Chem. Pharm. Bull.*, 1993, **41**, 1118–1122.

Influence of the alkyl chain length of liposome-supported photosensitisers and catalysts for photocatalytic CO₂ reduction

Covalent functionalisation with alkyl tails is a common method for supporting molecular catalysts and photosensitisers onto lipid bilayers, but the influence of the alkyl chain length on the photocatalytic performances of the resulting liposomes is not well understood. In this work, we first prepared a series of rhenium-based CO₂-reduction catalysts [Re(4,4'-(C_nH_{2n+1})₂-bpy)(CO)₃Cl] (**ReC_n**; 4,4'-(C_nH_{2n+1})₂-bpy = 4,4'-dialkyl-2,2'-bipyridine) and ruthenium-based photosensitisers [Ru(bpy)₂(4,4'-(C_nH_{2n+1})₂-bpy)](PF₆)₂ (**RuC_n**) with different alkyl chain lengths (n = 0, 9, 12, 15, 17, and 19). We then prepared a series of PEGylated DPPC liposomes containing **RuC_n** and **ReC_n**, hereafter noted **C_n**, to perform photocatalytic CO₂ reduction in the presence of sodium ascorbate. The photocatalytic performance of the **C_n** liposomes was found to depend on the alkyl tail length, as the turnover number for CO (TON) was inversely correlated to the alkyl chain length, with a more than fivefold higher CO production (TON = 14.5) for the **C₉** liposomes, compared to **C₁₉** (TON = 2.8). Based on immobilisation efficiency quantification, diffusion kinetics, and time-resolved spectroscopy, we identified the main reason for this trend: two types of membrane-bound **RuC_n** species can be found in the membrane, either deeply buried in the bilayer and diffusing slowly, or less buried with much faster diffusion kinetics. Our data suggest that the higher photocatalytic performance of the **C₉** system is due to the higher fraction of the more mobile and less buried molecular species, which leads to enhanced electron transfer kinetics between **RuC₉** and **ReC₉**.



This chapter has been published as a full paper: David M. Klein, Santiago Rodríguez-Jiménez, Marlene E. Hoefnagel, Andrea Pannwitz, Amrutha Prabhakaran, Maxime A. Siegler, Tia E. Keyes, Erwin Reisner, Albert M. Brouwer, and Sylvestre Bonnet, *Chemistry – A European Journal* **2021**, 27, 17203-17212.

3.1 Introduction

Artificial photosynthesis has recognised potential to produce fuels in a sustainable way from earth-abundant resources such as water, carbon dioxide (CO₂), and sunlight.¹ In an artificial photosynthetic system, two half-reactions, such as water oxidation and CO₂ reduction, have to be combined, which requires control of light harvesting by photosensitisers, electron relays, and electron transfer to and from catalysts.¹ In natural photosynthesis, the efficiency and directionality of electron transfer is maximised by compartmentalisation, which consists in embedding the key components of the system, i.e., the oxygen evolving complex, photosystem I and II, and natural electron relays, within the lipid bilayer of the thylakoid membrane. A promising approach for artificial photosynthesis is to use lipid-based supramolecular assemblies, such as liposomes, as artificial mimics of thylakoid membranes. Photocatalytic liposomes represent a versatile platform for the co-embedding of catalysts and photosensitisers, as they are easy to prepare, allow one to solubilise apolar compounds in water, and can even facilitate charge separation.¹⁻³ In addition, they offer a unique way to compartmentalise molecular catalysts and photosensitisers in an aqueous environment, by keeping both types of molecules close to the water-bilayer interface and close to each other, thereby enhancing electron transfer rates.¹⁻³

A common way to immobilise photochemically or catalytically active metal complexes onto the lipid bilayer of liposomes is by increasing their lipophilicity via functionalisation with alkyl tails. When a metal-containing complex is hydrophilic enough, the resulting alkyl-functionalised molecule *a priori* resembles an amphiphile, which allows it to self-assemble within the liposome bilayer. On the other hand, the metal head group of such amphiphiles bears the catalytically active centre; it should hence be close enough to the bulk water phase in order to be able to accept electrons and protons from the bulk aqueous environment. Such an immobilisation strategy has been employed by different groups in the context of solar fuels; for example, photocatalytic water oxidation with liposomes was

demonstrated using alkylated Ru-based water oxidation catalysts and photosensitisers bearing C₁₂ tails^{4,5}; hydrogen evolution was achieved using a C₁₂-alkylated cobaloxime-based hydrogen evolution catalyst and a C₁₂-alkylated Ru photosensitiser⁶; and a C₁₃-alkylated rhenium-based CO₂ reduction catalyst was used in combination with a C₁₃-alkylated Ru-based photosensitiser⁷. These studies focussed primarily on optimising the photocatalytic reaction by choosing the most efficient photosensitiser and catalyst; varying the fluidity of the lipid bilayer using unsaturated or saturated lipids; changing the light intensity and the concentrations of the catalysts, photosensitisers, and electron mediators; and overall comparing the photocatalytic mechanism on liposomes with that observed in homogeneous conditions. All studies concur that the photocatalytic mechanism on liposomes is strongly influenced by the confinement of the photosensitiser and catalyst to the same two-dimensional medium. However, so far, the alkyl chain length of such amphiphilic photosensitisers and catalysts seems to have been chosen according to synthetic availability or simply by chance, while the influence of the alkyl chain length on the photocatalytic performance of these systems has not been studied. Changing the alkyl chain length of an amphiphilic metal complex might modify the efficacy of membrane functionalisation or the location of the molecule within the lipid membrane. For example, a study by Ohba *et al.*⁸ showed that the yields for chemically-driven water oxidation on liposomes could be enhanced by varying the length of the linker between ruthenium and the cholesterol group of a membrane-embedded water oxidation catalyst. Overall, the concentration and position of the photochemically and catalytically active molecules in the membrane are known to influence their photocatalytic or electron transfer properties; they should hence play a critical role in photocatalysis. Last but not least, as time-resolved spectroscopy studies in photocatalytic liposome are scarce, our understanding of their supramolecular photochemistry remains limited.

To address these knowledge gaps, we prepared here a series of rhenium-based CO₂-reduction catalysts [Re(bpy-(4,4'-C_n)₂)(CO)₃Cl] (**ReC_n**; (bpy-(4,4'-C_n)₂ = 4,4'-di-X-2,2'-bipyridine; X = C_nH_{2n+1} with n = 0, 9, 12, 15, 17, and 19) and a series of ruthenium-based photosensitisers [Ru(bpy)₂(bpy-(4,4'-

$C_n)_2]](PF_6)_2$ (RuC_n ; $n = 0, 9, 12, 15, 17,$ and 19) and used them for photocatalytic CO_2 reduction on PEGylated DPPC liposomes (hereafter noted C_n). The choice of this type of ruthenium photosensitisers was based on their known ability, both in terms of redox potential in the ground state and energy in the excited state, to fuel CO_2 reduction catalysed with rhenium catalysts.^{7,9–12} The choice of the rhenium catalyst was based on the synthetic rationale that once prepared for the series of Ru-based photosensitiser, the series of bisalkylated 2,2'-bipyridine ligands with different chain lengths could be coordinated also to rhenium to make, in one step, a series of CO_2 reduction catalyst molecules with different chain lengths. In addition, the $[Re(bpy)(CO)_3Cl]$ catalyst discovered by Lehn and co-workers¹² is one of the most studied CO_2 -reduction catalysts, for which much information is available in the literature, for example about its CO_2 reduction mechanism. It must be noted, however, that the supramolecular properties of both types of molecules and their assembly in lipid membranes were expected to be different because of the neutral charge of the rhenium catalysts, compared to the dicationic nature of the ruthenium photosensitisers. In this work, we studied the photocatalytic performance of liposomes containing both molecules for CO_2 reduction using ascorbate ($HAsc^-$) as electron donor (Figure 3.1).

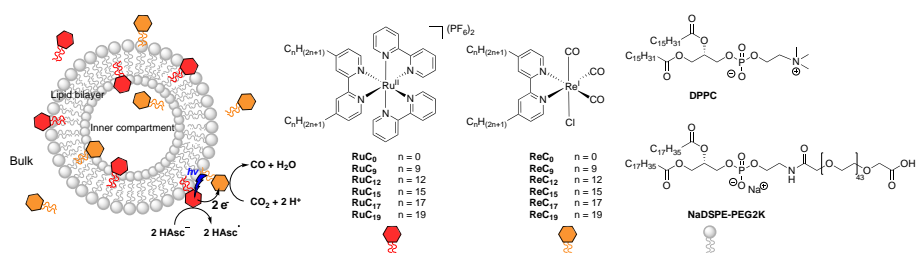


Figure 3.1. Formulae and naming of the ruthenium photosensitisers (red), rhenium catalysts (orange), and lipids (grey) used for photocatalytic CO_2 reduction on liposomes.

To understand the obtained photocatalytic results, we quantified the number of complexes that were actually immobilised on the liposome using inductively-coupled plasma mass-spectrometry (ICP-MS), and performed time-resolved spectroscopic and two-dimensional diffusion studies to assess the influence of the chain length on the electron transfer and molecular

diffusion in the membrane. We unravelled the existence of two types of photosensitiser species, one deeply embedded in the membrane that diffuses slowly and represents a dead-end for electron transfer and hence photocatalysis; and another one diffusing faster in the membrane leading to improved electron transfer. This fast-diffusing species must be located closer to the aqueous phase and plays therefore a major role in photocatalysis.

3.2 Results and Discussion

Synthesis and preparation of liposomes. A series of bis-alkylated ruthenium tris-bipyridine RuC_n and bis-alkylated rhenium tris(carbonyl) complexes ReC_n (Figure 3.1) were synthesised and characterised as described in the experimental part (see Appendix C). Then a series of liposome samples were prepared containing either one or both metal complexes with the same alkyl chain length; for example, the photocatalytic C_9 liposome system contained RuC_9 and ReC_9 . For liposome preparation, the metal complexes were mixed with the respective lipid (either DMPC (1,2-dimyristoyl-*sn*-glycero-3-phosphocholine), DPPC (1,2-dipalmitoyl-*sn*-glycero-3-phosphocholine), or DSPC (1,2-distearoyl-*sn*-glycero-3-phosphocholine)) in organic solvents. 1,2-distearoyl-*sn*-glycero-3-phosphoethanolamine.

N-(carbonyl-methoxypolyethylene glycol-2000) (NaDSPE-PEG2K) was added to the liposome formulation, which is known to stabilise liposome suspensions by avoiding aggregation.⁴ Thorough evaporation of the organic solvent and hydration with a phosphate buffered solution (0.1 M, pH = 7.7), several freeze-thawing cycles, and standard extrusion through a 0.2 μm polycarbonate filter, afforded the liposomes (lipid:NaDSPE-PEG2K: RuC_n : ReC_n in a typical ratio of 100:1.0:X:Y with X = 0.0 or 0.4 and Y = 0.0 or 0.4). The liposome samples containing one or both metal complexes were characterised by dynamic light scattering to obtain the average diameter (Z_{ave}) and the polydispersity index (PDI) of the liposomes and by spectroscopic techniques to obtain the absorption maximum (λ_{abs}) and emission maximum (λ_{em}) of the metal complexes in the liposomes (see Tables C1, C2, C3, and C4 in Appendix C). Z_{ave} was typically found to be 120 – 140 nm for DMPC liposomes, 140 – 150 nm for DPPC liposomes, and 150 – 170 nm

for DSPC liposomes, with PDI values below 0.20 that indicated a uniform size distribution. The absorption and emission maxima for the ruthenium complexes (**RuC₉** – **RuC₁₉**, $\lambda_{\text{abs}} = 424 - 465$ nm and $\lambda_{\text{em}} = 625 - 634$ nm) and the emission maxima for the rhenium complexes (**ReC₉** – **ReC₁₉**, $\lambda_{\text{em}} = 510 - 554$ nm) immobilised on liposomes (Table C1 and Figure C1 for two representative examples) were comparable to literature values for **RuC₁₃** and **ReC₁₃** immobilised on DPPC vesicles.⁷ λ_{abs} could not be determined for the rhenium complexes by UV-Vis spectroscopy due to lipid scattering in the region where rhenium absorbs ($\lambda_{\text{abs}} = 380$ nm in chloroform). Liposomes containing both metal complexes showed similar emission maxima for the ruthenium complexes ($\lambda_{\text{em}} = 607 - 632$ nm) and for the rhenium complexes ($\lambda_{\text{em}} = 555 - 556$ nm) immobilised on liposomes (Table C2), thus demonstrating that the spectroscopic features of the photosensitiser as well as of the catalyst are retained after incorporation into the liposome.

Influence of alkyl chain length on photocatalytic CO₂ reduction.

Photocatalytic CO₂ reduction experiments were conducted with DPPC:NaDSPE-PEG2K:**RuC_n**:**ReC_n** (100:1.0:0.4:0.4) liposomes in CO₂-saturated aqueous phosphate solutions at pH 6.3 containing sodium ascorbate (NaHAsc, 0.1 M) as sacrificial electron donor (Figure 3.2 and Table C5). The gaseous products (CO and H₂) from photocatalytic reduction of aqueous CO₂ were quantified by gas chromatography, and the possible formation of formate in the aqueous phase was also monitored by IR and ¹H NMR spectroscopy. Three hours of UV- and blue light filtered simulated solar light irradiation were employed ($\lambda > 455$ nm, AM 1.5G, 100 mW cm⁻²) to avoid photoexcitation of the Re(I) catalyst. CO evolved as the major product, with minor amounts of H₂ in all six photocatalytic **RuC_n**-**ReC_n** liposome systems, as reported in other rhenium-based CO₂-reduction catalytic systems that pointed already to the excellent selectivity of these catalysts.^{7,11,13} The CO selectivity ranged between 97 – 99% for the **C₉**-**C₁₉** systems and 94% for the **C₀** system. Strikingly, a clear trend was observed: the photochemical performances of the photocatalytic liposomes were inversely correlated to the alkyl chain length, with the turnover number ($\text{TON} = n_{\text{product}}/n_{\text{Re-catalyst}}$) and photocatalytic turnover number ($\text{PTON} = 2 \times n_{\text{product}}/n_{\text{Ru-photosensitiser}}$; the factor

2 accounts for the fact that 2 molecules of photosensitiser must turnover once for the formation of one CO molecule) decreasing regularly from the **C₉** to the **C₁₉** system (Figure 3.2, Table C5, and C6, which give both η_{immob} -corrected and uncorrected TON and PTON, see below). The same trend was also observed for the turnover frequency (TOF = TON/time) and photocatalytic turnover frequency (PTOF = PTON/time). The **C₉** and **C₁₂** liposomes were hence the most active in reducing CO₂ to CO (81 – 109 nmol CO, TON = 10.8 – 14.5, PTON = 21.6 – 29.0, TOF = 4.3 – 5.7 h⁻¹, and PTOF = 8.7 – 11.3 h⁻¹), whereas the **C₁₅**, **C₁₇**, and **C₁₉** systems were much less active (21 – 41 nmol CO, TON = 2.8 – 5.5, PTON = 5.5 – 10.9, TOF = 1.1 – 2.0 h⁻¹, and PTOF = 2.3 – 3.9 h⁻¹). In all systems, a decrease in the TOF was observed after one hour, indicating that the systems were decomposing during irradiation, most probably due to the degradation of **RuC_n** as reported for the **C₁₃** system,⁷ although the possible decomposition of **ReC_n** could not be discarded either on the basis of previous reports.^{9,11}

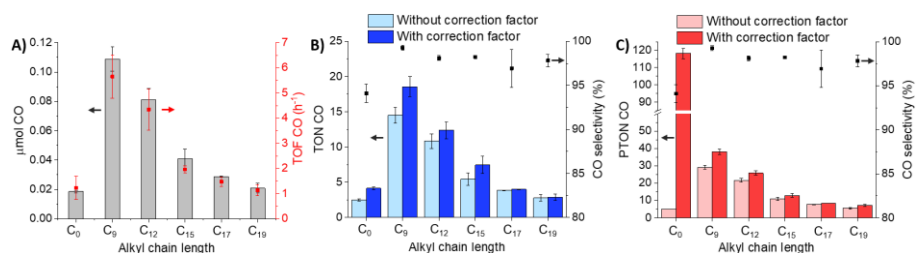


Figure 3.2. Photocatalytic activity after three hours of simulated solar light irradiation ($\lambda > 455$ nm, AM 1.5G, 100 mW cm⁻²) as a function of alkyl chain length for DPPC liposomes containing **ReC_n-RuC_n** with same *n*: (A) evolved μmol of CO and uncorrected TOF CO; (B) (light blue) uncorrected and (dark blue) corrected TON CO and CO selectivity; (C) (light red) uncorrected and (dark red) corrected turnover number of CO produced per mol of photosensitiser (PTON CO) and CO selectivity. The TONs and TOFs were obtained after 3 h and 1 h, respectively. The applied correction factor (η_{immob}) can be found in Figure 3.4 and Table C9. Experimental conditions: [DPPC] = 625 μM , [DSPE-PEG2K] = 6.25 μM , [**ReC_n**] = 2.5 μM and [**RuC_n**] = 2.5 μM ; CO₂-saturated 0.1 M NaH₂PO₄ and 0.1 M NaHAsc aqueous solution (3 mL, pH \approx 6.3) at 25 °C. Bulk concentrations [**ReC_n**] and [**RuC_n**] indicate theoretical concentrations (before extrusion). Experiments were performed in triplicates.

For the most active system (**C₉**), the internal quantum yield for CO formation (Φ_{CO})¹⁴ was calculated on the basis of the number of photons absorbed by

RuC₉ (see Equation C1 in Appendix C). In this calculation, Φ_{CO} was $0.048 \pm 0.026\%$ during the first hour of monochromatic visible light irradiation ($\lambda = 455 \text{ nm}$). This value corresponded to a lower rate of CO production ($0.04 \mu\text{mol h}^{-1}$, TON = 11 after 2 h) compared to the **C₁₃** system published by Murata et al⁷ ($3.1 \mu\text{mol h}^{-1}$, TON = 52 after 2 h). Such lower rate is probably a consequence of the lower concentration of the active components in our **C₉** system (0.4 mol% **RuC₉** and **ReC₉** in the membrane, 2.5 μM bulk concentration, 10^{-3} M local concentration for each complex), compared to the **C₁₃** system of Murata et al⁷ ($\approx 3.5 \text{ mol}\%$ **RuC₁₃** and **ReC₁₃** in the membrane, 40 μM bulk concentration, 10^{-2} M local concentration for each complex), which could lead to slower electron transfer between Ru and Re and/or more charge recombination, altogether decreasing the photocatalytic performance of the system. The **C₀** system in our study exhibited a particularly low activity (19 nmol CO, TON = 2.5, PTON = 5.0, TOF = 1.2 h^{-1} , and PTOF = 2.5 h^{-1}), but for such a system the **RuC₀** photosensitiser is hardly embedded in the membrane due to its low lipophilicity, while 62% of the **ReC₀** catalyst is embedded in the lipid bilayer, thus preventing efficient electron transfer (see section on immobilisation efficiency). Overall, our results not only highlight that alkyl chains are indeed required to immobilise both metal complexes onto photocatalytic liposomes, but they also strikingly demonstrate that a too long alkyl chain length is detrimental towards the photocatalytic performance of the system, and that shorter alkyl tails (**C₉** and **C₁₂**) give much better photocatalytic results.

Control experiments were performed to verify a few basic assumptions in this system. First, dynamic light scattering measurements were carried out to monitor the changes in size of the liposomes before and after photocatalysis. The average size of $150 \pm 16 \text{ nm}$ obtained before irradiation, and $161 \pm 15 \text{ nm}$ obtained after three hours irradiation (Table C3, Appendix C), were very similar, indicating that the liposomes remained essentially intact during photocatalysis. Second, UV-filtered but blue light-containing beam ($\lambda > 400 \text{ nm}$) led to analogous photocatalytic performances compared to the above conditions where UV and blue filters were used (Figures C2 and C3). These results suggest that the main path for photocatalytic CO₂

reduction, even when the light beam contains blue light capable of exciting the rhenium complex, is photoexcitation of the **RuC_n** photosensitiser, followed by reductive quenching by ascorbate, and further electron transfer from the reduced **RuC_n⁻** photosensitiser species to the **ReC_n** catalyst, as proposed by Murata and co-workers.⁷ Third, experiments performed with the **C₉** system in absence of one of the components (Table C7) confirmed that neither CO nor H₂ evolved when **RuC₉**, NaHAsc, or visible light irradiation were absent. In the absence of **ReC₉**, only 0.2 ± 0.1 nmol of CO was detected, compared to 108.9 ± 8.3 nmol of CO when all components were present. This small amount of CO was probably produced by **RuC₉** or unidentified photodegraded by-products, as suggested previously.^{10,15-19} Fourth, isotopic labelling experiments using ¹³CO₂ confirmed that ¹³CO evolved as the only photocatalytic CO₂ reduction product, and no other CO₂ reduction products such as formate were detected after three-hour experiments using IR and ¹H NMR spectroscopy (Figures C4 and C5). Overall, all controls point to the well-behaved performance of this system: the catalysis really takes place at the surface of the liposome with membrane-embedded species, which remain stable during irradiation.

Understanding the tail-dependent photocatalytic behaviour. The more than five-fold difference in TON between **C₉** and **C₁₉** systems is worth mentioning, as elongating the alkyl chains may be conceptualised as a way to enhance membrane embedding of the functional molecules, thereby enhancing photocatalytic properties. Importantly, the lower photocatalytic activity observed with longer alkyl chains could not be explained by a change in the redox potentials of the complexes from **C₉** up to **C₁₉**. These redox potentials indeed hardly differed when alkyl chain lengths varied (i.e. Ru^{2+/+} = -1.76 V for **RuC₉** and -1.70 V for **RuC₁₅**, Re^{+/0} = -1.83 V for **ReC₉** and -1.83 V for **ReC₁₅**, measured in acetonitrile, and referenced versus Fc^{+/0}, Figures C6, C7, C8, and Table C8), even if the irreversibility of the **RuC₁₇** and **RuC₁₉** complexes in such conditions prevented reliable measurement of redox potentials. Thus, we turned to other methods, i.e., immobilisation efficiency quantification, transient absorption spectroscopy, and membrane diffusion measurements, to look for reasons behind the photocatalytic trend observed in Figure 3.2.

Immobilisation efficiency of ruthenium and rhenium complexes on liposomes. Liposome preparation contains many steps (Figure 3.3) including multiple hand-made filtrations through an extrusion filter, which may adsorb significant amounts of functional molecules depending on their solubility, their interaction with the filter material, or the pressure generated by the operator, as well as multiple cooling and heating steps, which are also potential sources of irreproducibility. Overall, the quantitative embedding of amphiphilic molecules in the membrane might be questioned. We hence engaged into measuring to what extent the alkyl tail length may influence the real efficiency of liposome immobilisation. Of course, preliminary confocal microscopy of **RuC₁₂**-containing multilamellar giant liposomes obtained before extrusion showed red emission ($\lambda_{\text{exc}} = 488 \text{ nm}$ and $\lambda_{\text{em}} = 640 - 680 \text{ nm}$) coming only from the lipid bilayer (Figure C9), suggesting qualitatively that **RuC₁₂** was in majority taken up by the lipid bilayer itself. However, this technique was not quantitative, and it could not be used to study the photocatalytic liposomes obtained after extrusion and used for CO₂ reduction, as their hydrodynamic diameter ($Z_{\text{ave}} < 200 \text{ nm}$) was significantly lower than the ultimate resolution of optical microscopy ($\sim 250\text{-}400 \text{ nm}$ depending on wavelength).²⁰

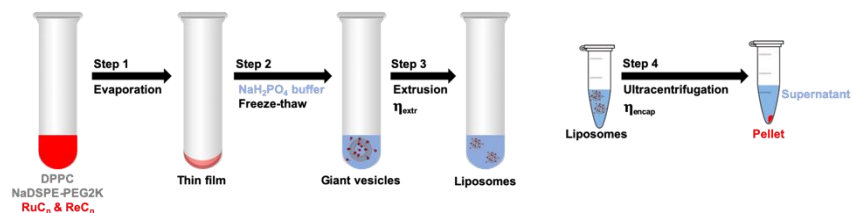


Figure 3.3. Stepwise preparation of photocatalytic liposomes and definition of the extrusion efficiency (η_{extr}) and encapsulation efficiency (η_{encap} , see main text).

Therefore, we used a more quantitative assay to address the immobilisation efficacy, which consisted in ultracentrifugating (at 100.4 kG) the metal-functionalised liposomes, and measuring the amount of metal complex in the supernatant after ultracentrifugation, either by UV-Vis spectroscopy or by ICP-MS. In this assay we considered a metal complex as “immobilised” in the liposome, if after ultracentrifugation it ended up in the centrifuged lipid pellet, and hence disappeared from the supernatant. As a note, we could not

distinguish whether the complex was entrapped in the inner aqueous compartment of the liposome, or really located inside the hydrophobic pocket of the lipid bilayer, as both cases led to entrapment in the lipid pellet. On the other hand, all molecules located in the outside bulk aqueous solution ended up in the supernatant and were hence considered as “non-immobilised”.

This assay was realised in a first attempt by UV-Vis spectroscopy using liposomes containing a single type of metal complex (**RuC_n** or **ReC_n**). It showed that UV-Vis spectroscopy was not a suitable technique for quantification of the amount of liposome-immobilised metal complexes: before ultracentrifugation light scattering by the liposomes is significant in the blue and near-UV region of the spectrum where for example **RuC₁₂** (Figure C10) and **ReC₁₂** (Figure C11) absorb. The quantification of the initial amount of metal complex was hence not reproducible. As a consequence, we turned to ICP-MS analysis, with which it is possible to quantitatively and accurately determine the metal content (Ru and Re) of the liposome samples before extrusion, between extrusion and ultracentrifugation, or that of the supernatant after ultracentrifugation (see Figure 3.3). It is hence possible to measure experimentally the immobilisation efficiency (η_{immob}), defined as the amount of complex effectively present in the liposome, divided by the amount of complex introduced in the liposome formulation. Two phenomena during liposome preparation can lead to an immobilisation efficiency η_{immob} lower than unity (Equation 3.1): first, extrusion may lead to adsorption of some of the metal complex onto the extrusion filter (Figure C12), which lowers the quantity of metal complex effectively present in the extruded sample, compared to the amount theoretically introduced. We defined η_{extr} as the extrusion efficiency (step 3 in Figure 3.3) and quantified it by measuring the amount of Ru and Re effectively found in the liposome sample by ICP-MS after extrusion but before ultracentrifugation, and divided it by the theoretical amount of Ru and Re introduced in the liposome formulation (Equation 3.2). Second, depending on its total hydrophobicity, the amphiphilic complexes effectively present in the extruded sample may be distributed between the aqueous phase (interior or exterior) and the

hydrophobic environment of the membrane, rather than fully embedded in the membrane. In principle, higher alkyl chain lengths will increase lipophilicity and hence the amount of complex embedded in the lipid bilayer; but the extent of such embedding is usually not addressed and might have been over-evaluated in previous work, as it will depend on the hydrophilicity of the metal head as well. We hence defined the encapsulation efficiency, η_{encap} , as the molar fraction of metal complex entrapped in the lipid pellet obtained after ultracentrifugation, divided by the total amount of complex present in the extruded sample (before ultracentrifugation, step 4 in Figure 3.3).²¹ η_{encap} is given by Equation 3.3. The final yield of complex immobilisation (η_{immob}) is the product of the extrusion yield η_{extr} with the encapsulation yield η_{encap} (Equation 3.1).

$$\eta_{\text{immob}} = \eta_{\text{extr}} \times \eta_{\text{encap}} \quad \text{Equation 3.1}$$

$$\eta_{\text{extr}} = \frac{[\text{metal}]_{\text{liposomes}}}{[\text{metal}]_{\text{giant vesicles}}} \times 100\% \quad \text{Equation 3.2}$$

$$\eta_{\text{encap}} = \left(1 - \left(\frac{[\text{metal}]_{\text{supernatant}}}{[\text{metal}]_{\text{liposomes}}} \right) \right) \times 100\% \quad \text{Equation 3.3}$$

The experimental values of η_{extr} , η_{encap} , and η_{immob} for photocatalytic liposome formulations containing both metal complexes (DPPC:NaDSPE-PEG2K:RuC_n:ReC_n in a ratio of 100:1.0:0.4:0.4) are shown in Figure 3.4 and Table C9. Interestingly, η_{extr} was high for RuC₀ and ReC₀ (> 95%) but moderately high (> 75%) for RuC_n and ReC_n with n > 9. Thus, a considerable amount of compound was lost during extrusion, as visually observed by a yellowish-orange deposit on the polycarbonate filter (Figure C12). These losses were essentially independent of the alkyl chain length. We attribute the significant error bars in η_{extr} (especially for ReC₉, ReC₁₂, and ReC₁₅) to the complexity of the extrusion procedure (e.g., tricky temperature control, minute variations of the manual pressure during extrusion, or different amounts of time between the different steps of multiple extrusion) and to the dynamics of such a supramolecular system. The low η_{encap} value for RuC₀ (< 5%) and the moderate η_{encap} for ReC₀ (62%) demonstrate the crucial role of alkyl tails for the immobilisation of such complexes in lipid bilayers. In both

cases the supernatant was very colourful and the liposome pellet was colourless (Figure C13, left) in contrast to for example C_9 liposomes for which the supernatant was poorly coloured compared to the lipid pellet (Figure C13, right). In contrast, for RuC_n and ReC_n , η_{encap} was close to 100% in all $n \geq 9$ cases. Thus, with these particular metal-containing heads the alkyl chain length did not affect η_{encap} significantly, as long as alkyl tails were present ($n \geq 9$), and all molecules that did not stay in the extrusion filter effectively ended up immobilised within the membrane. Most importantly, the variation of η_{immob} with n did not provide an explanation for the trend observed in Figure 3.2: the most hydrophobic RuC_n and ReC_n complexes were rather efficiently immobilised in the liposomes, hence the lower photocatalytic efficacy of the C_{17} and C_{19} liposomes could not be explained by a lower immobilisation efficacy of its molecular components in the membrane. It should be noted, however, that the losses during immobilisation, which are essentially due to the losses during extrusion, are crucial to correctly calculate turnover numbers and turnover frequencies in photocatalytic experiments with liposomes (e.g. TON and PTON). Without such corrections the PS or catalyst concentration will be over evaluated and hence the (P)TONs and (P)TOFs systematically underestimated.

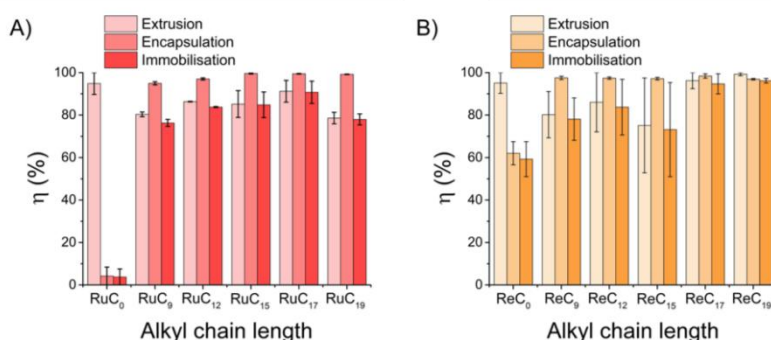


Figure 3.4. Evolution of the extrusion (η_{extr}), encapsulation (η_{encap}), and immobilisation (η_{immob}) efficiencies versus alkyl chain length for DPPC liposomes containing RuC_n and ReC_n with the same n . A) and B) show the data for ruthenium and rhenium, respectively. Experimental conditions before extrusion: [DPPC] = 6.25 mM, [NaDSPE-PEG2K] = 62.5 μ M, [ReC_n] = 25 μ M and [RuC_n] = 25 μ M in 0.1 M NaH_2PO_4 buffer. Efficiencies are indicated as an average from two independent liposome preparations; error bars correspond to the average deviation from the mean.

Transient absorption spectroscopy study. As the lower photocatalytic activity of the liposomes containing the more hydrophobic amphiphiles could not be explained by problems during liposome preparation, we analysed two liposome systems in more detail using transient absorption (TA) spectroscopy, focusing on the ones containing the shortest (**C**₉) and longest (**C**₁₉) tails in the series. In these TA experiments, we followed the quenching of the key photoreduced intermediate in the membrane, **RuC**_n⁻ (similar to [Ru(bpy)₃]⁺, reported at $\lambda_{\text{max}} \approx 505$ nm, $\epsilon_{505\text{nm}} = 1.2 \times 10^4 \text{ M}^{-1}\text{cm}^{-1}$ in acetonitrile²²), by the catalyst **ReC**_n present at either 0.0, 0.4, or 1.6 mol% in the membrane. **RuC**_n⁻ is obtained by the reductive quenching of the membrane-embedded excited state **RuC**_n^{*} (0.4 mol%) in presence of 0.1 M NaHAsc in the bulk aqueous phase. Under these conditions, **RuC**_n⁻ was formed within the first 40 ns (together with the ascorbate radical HAsc[•]) and its concentration kept increasing over at least 2 μs (Figure C14).⁷ Its decay was monitored for up to 10 ms, as the clear signature peak of **RuC**_n⁻ near 505 nm was still visible after a very long time of 2 ms (Figure C15). The decay of **RuC**_n⁻ with and without **ReC**_n is shown in Figure 3.5 and Figure C16.

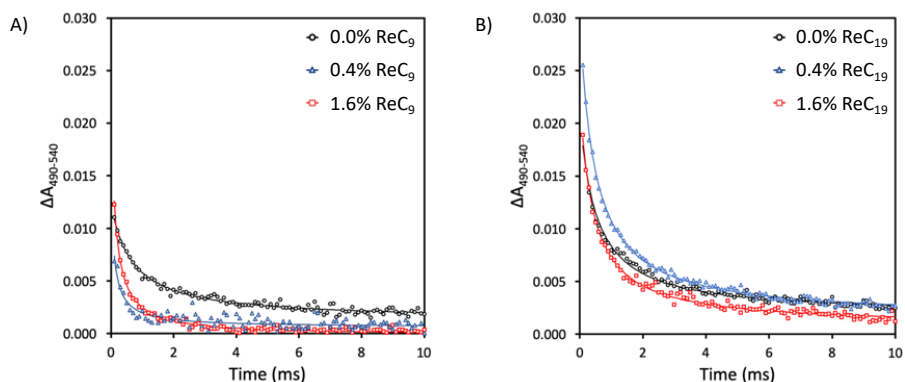


Figure 3.5. TA kinetic traces of photocatalytic DPPC liposomes containing 1 mol% NaDSPE-PEG2K, 0.4 mol% **RuC**_n and varying amounts of **ReC**_n (A: n = 9, B: n = 19), after laser excitation ($\lambda_{\text{exc}} = 450$ nm, 3.5 mJ per pulse) on a 10 ms timescale (timestep = 0.1 ms). The values for absorption were averaged between 490 – 540 nm. Experimental conditions: [DPPC] = 6.25 mM, [NaDSPE-PEG2K] = 62.5 μM , [**RuC**_n] = 25 μM , and [**ReC**_n] = 0, 25 or 100 μM in CO₂-saturated 0.1 M NaHAsc aqueous solution. Bulk concentrations [**ReC**_n] and [**RuC**_n] indicate theoretical concentrations (before extrusion).

The TA signature of RuC_n^- decayed in time following a non-exponential rate law. In the simplest model, in the absence of quencher ReC_n , such a decay is a result of second-order charge recombination of RuC_n^- and HAsc^\bullet with rate constant k_{CR} , both having identical initial concentration c_0 because they were formed together. The time-dependent concentration $c(t)$ of the RuC_n^- intermediate is then given by Equation 3.4 (see Appendix C for mathematical derivation). The data obtained could not be fitted using this simple model, probably because of the disproportionation reaction of HAsc^\bullet , which lowered the effective amount of HAsc^\bullet near the membrane and hence resulted in an excess of RuC_n^- remaining at long time scales (Figure 3.5A, black curve).²³ If the excess of unreacted RuC_n^- (c_∞) was included in the model (Equation 3.4), then the decay data could be fitted pretty well (Equation 3.5).

$$c(t) = \frac{c_0}{1 + k_{\text{CR}}c_0t} \quad \text{Equation 3.4}$$

$$c(t) = \frac{c_0}{1 + k_{\text{CR}}c_0t} + c_\infty \quad \text{Equation 3.5}$$

$$c(t) = \frac{k_{\text{Q}}c_0}{k_{\text{Q}}e^{k_{\text{Q}}t} + k_{\text{CR}}c_0(e^{k_{\text{Q}}t} - 1)} \quad \text{Equation 3.6}$$

In the presence of 0.4 mol% of the ReC_n quencher, the decay of the RuC_n^- absorption was faster, which can be described as a combination of first order quenching k_{Q} and second order charge recombination k_{CR} according to Equation 3.6.²⁴ The fit with Equation 3.6, however, showed a strong interdependence of the values of the fitted rate constants and the fit was not improved in comparison to Equation 3.5. In Figure 3.5, the blue and red decay curves show data fitting using Equation 3.5 (for fitting parameters see Table C10). Figure 3.5A shows a clear quenching of RuC_9^- by an increasing concentration of ReC_9 . The residual absorbance at longer times decreased significantly in comparison to the data obtained in absence of ReC_9 in the membrane, which can be interpreted as the result of all RuC_9^- disappearing due to electron transfer to the ReC_9 . By contrast, the TA data obtained with ReC_{19} (Figure 3.5B) demonstrated that RuC_{19}^- was also quenched by the presence of the Re catalyst, but to a much smaller extent. Overall, these spectroscopic data strongly suggested that electron transfer from RuC_n^- to ReC_n was significantly faster in the case of the C_9 system than with the C_{19}

system. This observation would correlate with the lower photocatalytic performances of the liposome-embedded system with longer alkyl chains, if we assume that the redox and catalytic properties of the metal head of the amphiphilic complexes are independent from the chain length, which seems reasonable. To further investigate why the alkyl chain length strongly influenced the ability of these membrane-embedded molecules to transfer electrons, we went further into studying the mobility of the molecules in the membrane.

Lateral mobility of membrane-bound RuC_n. The rate of lateral diffusion of membrane-bound Ru and Re species will impact their collision frequency, which may impact intermolecular electron transfer kinetics. To investigate this hypothesis, we probed the diffusivity of the emissive **RuC_n** photosensitiser complexes in a model pore-supported lipid bilayer. In this experimental setup previously reported by some of us,^{25,26} and coined “microcavity supported lipid bilayers” (MSLBs), the lipid bilayer is supported across aqueous-filled micron-diameter pore arrays, shown schematically in Figure C17. The lateral mobility of emissive molecules situated in the membranes located above the pores, because of the aqueous interface at both leaflets, was shown to be very similar to that observed in liposomes of the same composition.^{27,28} The micron dimensions of the cavities and the good stability of the supported lipid membranes make this model highly amenable to study lateral diffusion by fluorescence correlation spectroscopy.²⁹ Due to experimental limitations it was not possible to obtain two-dimensional diffusion data for the **ReC₉** and **ReC₁₉** catalysts, so only the ruthenium photosensitisers were probed.

MSLBs comprised of DPPC:NaDSPE-PEG2K:**RuC_n** in a ratio 100:1:4·10⁻⁴ were hence prepared on polydimethylsiloxane pore arrays supports by Langmuir-Blodgett deposition followed by fusion of vesicles reconstituted with the complexes. The emission lifetime images (Figure C17) show pore array with supported membrane labelled with DOPE-ATTO 655, which confirmed the formation of the bilayer. Autocorrelation functions (ACFs) from ruthenium emission were collected across 20 – 30 cavities per sample and averaged to obtain diffusion values. The diffusion coefficients of the **RuC_n** molecules were

calculated by fitting the ACF using the two-component model given in Appendix C (method section); the resulting data for the **RuC₉** and **RuC₁₉** complexes is given in Table 3.1. For comparison, the ACF was also collected for the free **RuC₁₉** complex in bulk acetonitrile and this data fit to a three-dimensional diffusion to obtain a typical bulk diffusion coefficient of $199 \mu\text{m}^2\text{s}^{-1}$ (Figure C17).

Table 3.1. ACF data of **RuC_n** in MSLBs consisting of DPPC:NaDSPE-PEG2K.

Complex	D ₁ ($\mu\text{m}^2\text{s}^{-1}$)	D ₂ ($\mu\text{m}^2\text{s}^{-1}$)	A ₁ (%)	A ₂ (%)	α_1	α_2
RuC₉	82 ± 7	0.3 ± 0.9	82	18	1.12 ± 0.07	0.64 ± 0.01
RuC₁₉	50 ± 2	0.4 ± 0.8	56	44	1.20 ± 0.05	0.98 ± 0.02

Figure 3.6 shows representative plots of fluorescence fluctuations (time-traces) and the corresponding ACFs obtained for **RuC_n** in MSLBs comprised of DPPC:NaDSPE-PEG2K:**RuC_n**. Interestingly, in both cases the ACFs showed two diffusing components from membrane-bound **RuC_n**: a slow one and a fast one. The two-dimensional diffusion coefficients of the slow-moving component for **RuC₉** and **RuC₁₉** were $0.3 \pm 0.9 \mu\text{m}^2\text{s}^{-1}$ and $0.4 \pm 0.8 \mu\text{m}^2\text{s}^{-1}$, respectively, which are identical within experimental error. These values are also consistent with the fluidity of a typical DPPC:NaDSPE-PEG2K bilayer at room temperature: the transition temperature of $41 \text{ }^\circ\text{C}$ for DPPC has been shown to be only modestly mitigated by the presence of 1 mol% NaDSPE-PEG2K,³⁰ so that the membrane is in the gel phase at room temperature, leading to typical two-dimensional diffusion coefficients below $1 \mu\text{m}^2\text{s}^{-1}$. By contrast, the diffusion values for the fast-moving component were $82 \pm 7 \mu\text{m}^2\text{s}^{-1}$ and $49 \pm 2 \mu\text{m}^2\text{s}^{-1}$ for **RuC₉** and **RuC₁₉**, respectively, which is on the one hand significantly faster than that of lipid probes fully embedded in the hydrophobic core of the membrane, but on the other hand much slower than the value measured for diffusion in bulk solution. The fast-moving components are hence tentatively attributed to **RuC_n** molecules that are clearly associated with the bilayer, but not deeply embedded into it. Alternatively, the fast-diffusing complexes may be associated with domains originating from NaDSPE-PEG2K.³¹ As noted previously, fast super-diffusion can be observed at the membrane interface upon modification with PEG.³² Super-diffusion is characterised by an anomalous factor (α) greater than 1

and such an α value was noted here. For the slow diffusion component, α is effectively 1 for **RuC₁₉**, indicating free Brownian diffusion, but α is below 1 for **RuC₉**, which may indicate some self-aggregation of the complex in the membrane, which would also be consistent with the time trace in Figure 3.6A that shows some clustered peaks.

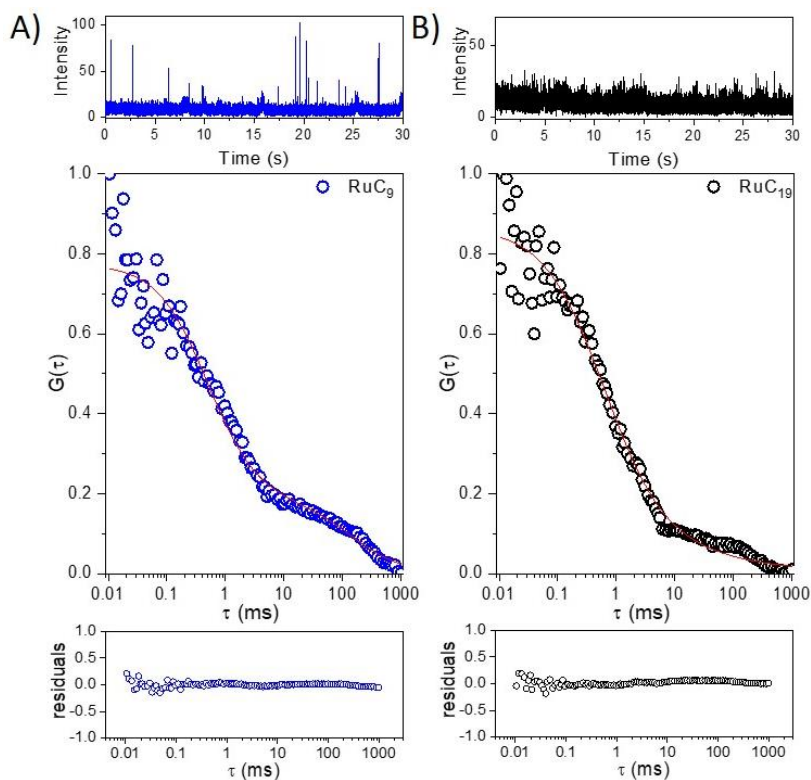


Figure 3.6. Representative intensity-time trace (top) and ACF (bottom) data measured over a single microcavity of MSLBs comprised of DPPC:NaDSPE-PEG2K:**RuC_n** in a ratio of 100:1:10⁻⁴ for (a) **RuC₉**, and (b) **RuC₁₉**. The fit ACF to the two-component model is shown as the red line and bottom shows the residuals, that indicate the quality of the fit to the two-dimensional model of diffusion. Experimental conditions: [DPPC] = 1.36 mM, [NaDSPE-PEG2K] = 13.6 μM, and [**RuC_n**] = 40 nM in phosphate buffer saline (pH = 7.7). Bulk concentration [**RuC_n**] indicates theoretical concentration (before extrusion).

Critically, the relative contribution or amplitude of the fast- and slow-diffusing components was found to vary with alkyl chain length. 82% of **RuC₉** constituted the fast component (D_1) in contrast to 56% for **RuC₁₉**. The

diffusion values for the fast component varied hence with the mass of the molecule, while the slow component did not. The latter observation was consistent with complexes that are well-embedded in the bilayer and essentially follow the diffusion rate of other lipids of the membranes; it hence directly reflects, as discussed above, the typical viscosity of a gel phase membrane at room temperature. However, the higher amplitude of the fast-diffusing component observed for **RuC₉**, correlates well with the higher photocatalytic performances of the **C₉** liposome system and faster electron transfer rate observed by TA spectroscopy, compared to the **C₁₉** system. The coexistence of two different types of membrane-embedded **RuC_n** species with two different diffusion coefficients, is, to our knowledge, unprecedented. It suggests that the fast-diffusing **RuC_n** molecules at the liposome interface participate primarily in the photocatalytic process, and that the higher proportion of fully-embedded and slowly-diffusing molecules obtained with more hydrophobic amphiphiles (here **RuC₁₉**, but also probably **ReC₁₉**) is responsible for the lowering of the electron transfer rates and the overall lower yields for photocatalytic CO₂ reduction in DPPC liposomes (Figure 3.7). It may even be that **RuC₁₉** species are just too slow-diffusing to have any significant collision frequency for efficient electron transfer, i.e., that they are photocatalytically “dead”. In other words, when all redox and excited state properties of photosensitisers and catalysts are equal it is the lateral diffusion of the molecules within the lipid bilayer that determines the final efficacy of photocatalysis, so that shorter alkyl chains are actually better than longer ones. As a side note it is very difficult, on the basis of available experimental evidence, to be definitive about the orientation of particularly the fast-diffusing species with respect to the membrane. The diffusion coefficient of the slow-diffusing component is very similar to what would be expected for a gel phase lipid bilayer, which suggests that this fraction of the complex is incorporated into the membrane in a manner similar to the amphiphilic lipids, with the metal head group oriented close to the zwitterionic lipid head group at the aqueous interface, and the alkyl tail embedded into the hydrophobic core of the membrane. By contrast, the fast component may be lying along the membrane interface, i.e., be poorly embedded, or may be associated with PEG domains at the membrane interface. Also, the comparative roles of the relative orientation versus the

rate of diffusion of ReC_n and RuC_n are impossible to assess at this stage. More experiments and/or calculations would be needed draw a conclusion on this point.

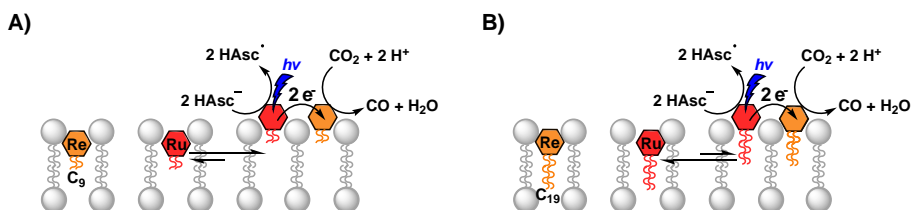


Figure 3.7. Proposed model for photocatalytic CO_2 reduction in DPPC lipid bilayers for a) the C_9 system, where the amphiphilic RuC_9 molecules in the membrane are less hydrophobic and hence primarily located near the water-membrane interface, where they diffuse faster and perform faster electron transfer to ReC_9 ; and b) the C_{19} system, where the amphiphilic RuC_{19} molecules are more hydrophobic and hence primarily deeply buried inside the hydrophobic core of the membrane, where they diffuse slower and perform slower electron transfer to ReC_{19} . Note: the real orientation of the alkyl tail is unknown and the drawing is not supposed to represent their real orientation in the membrane.

3.3 Conclusion

In this work, we observed that the photocatalytic performance of liposomes functionalised with amphiphilic ruthenium photosensitisers and CO_2 -reducing rhenium catalysts is inversely correlated to the alkyl chain length of the amphiphilic molecules embedded in the membrane. In addition, we observed for the first time two co-existing types of amphiphilic ruthenium molecules RuC_n in these lipid bilayers: one slow-diffusing and deeply buried in the membrane, and another one diffusing much faster at the membrane-water interface, and prone to participate in electron transfer processes. Photocatalytic CO_2 reduction on liposomes hence requires careful optimisation of the alkyl chain length: no tail is detrimental to the immobilisation on the membrane, but chains that are too long lead to a larger fraction of deeply buried, slow-diffusing molecular species, leading to less efficient electron transfer and low photocatalytic performances. Overall, this work appears as an essential step towards increasing our fundamental understanding of the supramolecular- and photo-chemistry of amphiphilic

functional molecules inserted in lipid bilayers, which will be essential for the development of more efficient biomimetic systems for artificial photosynthesis.

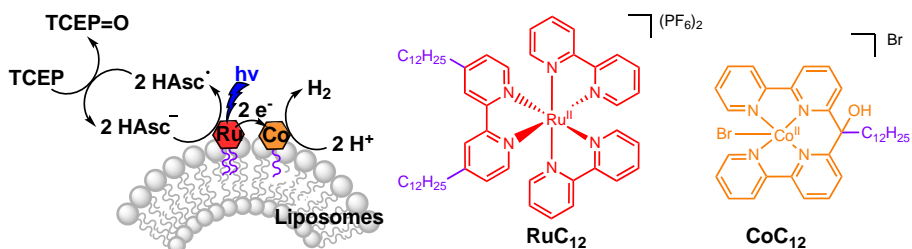
3.4 References

- 1 A. Pannwitz, D. M. Klein, S. Rodríguez-Jiménez, C. Casadevall, H. Song, E. Reisner, L. Hammarström and S. Bonnet, *Chem. Soc. Rev.*, 2021, **50**, 4833–4855.
- 2 M. Hansen, S. Troppmann and B. König, *Chem. Eur. J.*, 2016, **22**, 58–72.
- 3 J. N. Robinson and D. J. Cole-Hamilton, *Chem. Soc. Rev.*, 1991, **20**, 49–94.
- 4 B. Limburg, J. Wermink, S. S. van Nielen, R. Kortlever, M. T. M. Koper, E. Bouwman and S. Bonnet, *ACS Catal.*, 2016, **6**, 5968–5977.
- 5 M. Hansen, F. Li, L. Sun and B. König, *Chem. Sci.*, 2014, **5**, 2683–2687.
- 6 S. Troppmann and B. König, *Chem. Eur. J.*, 2014, **20**, 14570–14574.
- 7 N. Ikuta, S. Y. Takizawa and S. Murata, *Photochem. Photobiol. Sci.*, 2014, **13**, 691–702.
- 8 T. Koshiyama, N. Kanda, K. Iwata, M. Honjo, S. Asada, T. Hatae, Y. Tsuji, M. Yoshida, M. Okamura, R. Kuga, S. Masaoka and M. Ohba, *Dalt. Trans.*, 2015, **44**, 15126–15129.
- 9 J. Hawecker, J.-M. Lehn and R. Ziessel, *Helv. Chim. Acta*, 1986, **69**, 1990–2012.
- 10 J. Hawecker, J.-M. Lehn and R. Ziessel, *J. Chem. Soc. Chem. Commun.*, 1985, 56–58.
- 11 G. Sahara and O. Ishitani, *Inorg. Chem.*, 2015, **54**, 5096–5104.
- 12 J. Hawecker, J.-M. Lehn and R. Ziessel, *J. Chem. Soc. Chem. Commun.*, 1984, 328–330.
- 13 A. Nakada, K. Koike, K. Maeda and O. Ishitani, *Green Chem.*, 2016, **18**, 139–143.
- 14 J. Bonin, M. Robert and M. Routier, *J. Am. Chem. Soc.*, 2014, **136**, 16768–16771.
- 15 A. Nakada, K. Koike, T. Nakashima, T. Morimoto and O. Ishitani, *Inorg. Chem.*, 2015, **54**, 1800–1807.
- 16 J. L. Grant, K. Goswami, L. O. Spreer, J. W. Otvos and M. Calvin, *J. Chem. Soc. Dalt. Trans.*, 1987, 2105–2109.
- 17 A. Call, M. Cibian, K. Yamamoto, T. Nakazono, K. Yamauchi and K. Sakai, *ACS Catal.*, 2019, **9**, 4867–4874.
- 18 P. L. Cheung, C. W. Machan, A. Y. S. Malkhasian, J. Agarwal and C. P. Kubiak, *Inorg. Chem.*, 2016, **55**, 3192–3198.
- 19 Z. Guo, G. Chen, C. Cometto, B. Ma, H. Zhao, T. Groizard, L. Chen, H. Fan, W.-L. Man, S.-M. Yiu, K.-C. Lau, T.-C. Lau and M. Robert, *Nat. Catal.*, 2019, **2**,

- 801–808.
- 20 A.-L. Robson, P. C. Dastoor, J. Flynn, W. Palmer, A. Martin, D. W. Smith, A. Woldu and S. Hua, *Front. Pharmacol.*, 2018, **9**, 80.
- 21 S. Bonnet, B. Limburg, J. D. Meeldijk, R. J. M. Klein Gebbink and J. A. Killian, *J. Am. Chem. Soc.*, 2011, **133**, 252–261.
- 22 R. S. Khnayzer, V. S. Thoi, M. Nippe, A. E. King, J. W. Jurss, K. A. El Roz, J. R. Long, C. J. Chang and F. N. Castellano, *Energy Environ. Sci.*, 2014, **7**, 1477–1488.
- 23 Y. Pellegrin and F. Odobel, *C. R. Chim.*, 2017, **20**, 283–295.
- 24 B. Limburg, E. Bouwman and S. Bonnet, *J. Phys. Chem. B*, 2016, **120**, 6969–6975.
- 25 G. B. Berselli, N. K. Sarangi, S. Ramadurai, P. V Murphy and T. E. Keyes, *ACS Appl. Bio Mater.*, 2019, **2**, 3404–3417.
- 26 S. Ramadurai, A. Kohut, N. K. Sarangi, O. Zholobko, V. A. Baulin, A. Voronov and T. E. Keyes, *J. Colloid Interface Sci.*, 2019, **542**, 483–494.
- 27 G. B. Berselli, A. V Gimenez, A. O’Connor and T. E. Keyes, *ACS Appl. Mater. Interfaces*, 2021, **13**, 29158–29169.
- 28 G. B. Berselli, N. K. Sarangi, A. V Gimenez, P. V Murphy and T. E. Keyes, *Chem. Commun.*, 2020, **56**, 11251–11254.
- 29 H. Basit, V. Gaul, S. Maher, R. J. Forster and T. E. Keyes, *Analyst*, 2015, **140**, 3012–3018.
- 30 L. M. Ickenstein, M. C. Sandström, L. D. Mayer and K. Edwards, *Biochim. Biophys. Acta - Biomembr.*, 2006, **1758**, 171–180.
- 31 K. Hashizaki, H. Taguchi, C. Itoh, H. Sakai, M. Abe, Y. Saito and N. Ogawa, *Chem. Pharm. Bull.*, 2003, **51**, 815–820.
- 32 T. Tabarin, A. Martin, R. J. Forster and T. E. Keyes, *Soft Matter*, 2012, **8**, 8743–8751.

A stable alkylated cobalt catalyst for photocatalytic H₂ generation in liposomes

Photocatalytic proton reduction is a promising way to produce dihydrogen (H₂) in a clean and sustainable manner, and mimicking nature by immobilising proton reduction catalysts and photosensitisers on liposomes is an attractive approach for biomimetic solar fuel production in aqueous solvents. Current photocatalytic proton reduction systems on liposomes are, however, limited by the stability of the catalyst. To overcome this problem, we synthesised a new alkylated cobalt(II) polypyridyl complex (**CoC₁₂**), immobilised it on the lipid bilayer of liposomes, and studied its performance in a photocatalytic system containing an alkylated ruthenium photosensitiser (**RuC₁₂**) and a 1:1 mixture of sodium ascorbate and tris-2-carboxyethylphosphine hydrochloride as sacrificial electron donors. Several parameters (concentration of **CoC₁₂** and **RuC₁₂**, pH, membrane composition) were changed to optimise the turnover number for H₂ production. Overall, **CoC₁₂** was found to be photostable and the optimised turnover number (161) was limited only by the decomposition of the ruthenium-based photosensitiser.



This chapter has been accepted as a full paper: David M. Klein, Leonardo Passerini, Martina Huber and Sylvestre Bonnet, *ChemCatChem* **2022**, accepted.

4.1. Introduction

Photocatalytic water splitting into dioxygen (O_2) and dihydrogen (H_2) is a promising approach to store sunlight in chemical bonds (H_2), and hence a potential green solution to solve the current energy crisis.¹ Photocatalytic water splitting consists of two half-reactions, i.e. water oxidation and proton reduction. A common way to investigate these half reactions is by studying three-component systems containing a catalyst (i.e. a water oxidation catalyst or a proton reduction catalyst), a photosensitiser, and an electron acceptor (for water oxidation) or an electron donor (for proton reduction).² In nature, such light-driven half-reactions occur in the presence of a lipid membrane, i.e., the thylakoid membrane in plants, which enables precise spatial organisation of the catalysts, light-harvesting molecules, and electron transporters. Overall, compartmentalisation of the different half-reactions in or around lipid membranes minimises charge recombination and other undesired side reactions.³ Mimicking nature with artificially constructed lipid-based photocatalytic liposomes is therefore an appealing strategy for biomimetic solar fuel production.³⁻⁵ Liposomes are spherical supramolecular assemblies of lipids that define two aqueous phases, i.e. an inner compartment and the exterior bulk aqueous phase, and one hydrophobic phase, i.e., the interior of the lipid bilayer. As a consequence, liposomes can be exploited for solubilising both polar as well as nonpolar molecules in an aqueous solution. With liposomes, catalysts and photosensitisers, which are only soluble in purely organic solvents or in a mixture of water and organic solvents,⁶⁻⁹ can also be studied in aqueous conditions.

Up to now, the number of published liposome systems that are capable of performing photocatalytic half-reactions, such as water oxidation^{10,11}, proton reduction¹²⁻¹⁵, or carbon dioxide reduction¹⁶⁻¹⁸, is limited. For liposome-based proton reduction, the two only catalysts studied so far, i.e., an amphiphilic cobaloxime complex and an [Fe-Fe] hydrogenase mimic, decomposed during photocatalysis, which limited the photoreaction.^{12,13,15} To restore photocatalytic activity, it was either required to add free ligand in the case of the cobaloxime complex, or to add more catalyst in the case of

the [Fe-Fe] hydrogenase mimic.^{12,13,15} Therefore, a more stable catalyst is required that would allow for running photocatalytic proton reduction on liposomes for a longer time. Co(II) polypyridyl complexes are good catalyst candidates, as they are known to be photostable, exhibit good photocatalytic performance for proton reduction in aqueous media, and because cobalt is an earth-abundant metal.^{19–23}

We hence prepared the alkylated cobalt polypyridyl complex **CoC₁₂** (Figure 4.1), immobilised it on liposomes, and studied its photocatalytic performance in the presence of a known alkylated ruthenium-based photosensitiser (**RuC₁₂**)¹⁷ in the membrane, and of a mixture of sodium ascorbate (NaHAsc) and tris-2-carboxyethylphosphine hydrochloride (TCEP) in the aqueous phase as sacrificial electron donors (Figure 4.1). In such conditions, it is usually assumed that after reductive quenching of the excited photosensitiser **RuC₁₂**^{*} by HAsc⁻, TCEP is capable of recycling the 1-electron oxidised ascorbate radical (HAsc[•]) back to HAsc⁻, which is known to enhance photocatalytic hydrogen production.²⁴ We varied the concentrations of the proton reduction catalyst **CoC₁₂** and of the photosensitiser **RuC₁₂**, the pH of the solution, and the lipid composition of the liposomes, to optimise this system. Finally, we investigated whether, in optimised conditions, decomposition of the catalyst, or decomposition of the photosensitiser, limited H₂ production.

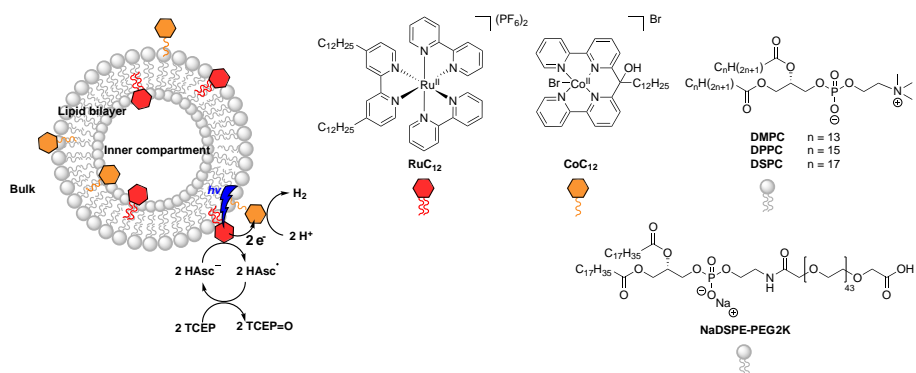


Figure 4.1. Formulae and naming of the alkyl-tail functionalised ruthenium photosensitiser (**RuC₁₂**, red), of the alkyl-tail functionalised cobalt catalyst (**CoC₁₂**, orange), and of the lipids (grey) used for photocatalytic H₂ evolution on liposomes.

4.2. Results and Discussion

4.2.1. Catalyst synthesis and preparation of photocatalytic liposomes

The amphiphilic derivative **RuC₁₂** of the well-known photosensitiser [Ru(bpy)₃]²⁺ was prepared by bis-alkylation of one of the bipyridine ligands with C₁₂H₂₅ chains, following literature procedures.¹⁷ The new cobalt catalyst **CoC₁₂** is based on a homogeneous catalyst developed by Alberto and co-workers.^{20,24,25} It was prepared by the alkylation of the easily accessible di([2,2-bipyridin]6-yl)methanone with one C₁₂H₂₅ chain in a two-step process, and it was characterised by TLC, NMR, mass spectrometry, and elemental analysis, as described in the experimental part. The oxidation state of the cobalt centre was estimated using Evans' method in MeOD at 20 °C.²⁶ An effective magnetic moment was found to be 4.28 μ_B, which is in agreement with the presence of one high-spin Co(II) centre with three unpaired electrons.²⁷ Indeed, this observation was further confirmed by EPR measurements, which showed a broad EPR feature that is typical for a high spin Co(II) species (Figure D1, see Appendix D). Furthermore, the redox potentials of **CoC₁₂** in acetonitrile (Figure D2), *i.e.*, -1.24 and -1.54 V vs. Fc/Fc⁺, are in agreement with that of similar complexes reported in literature.²⁸ Thus, the reduced **RuC₁₂⁻** (Ru^{2+/+} = -1.70 V vs Fc/Fc⁺ in acetonitrile)¹⁷, formed after reductive quenching of the excited photosensitiser **RuC₁₂^{*}** by HAsc⁻, is thermodynamically speaking capable of reducing twice **CoC₁₂**.

Functionalised liposomes for photocatalytic H₂ evolution were prepared by mixing the two metal complexes with either 1,2-dimyristoyl-*sn*-glycero-3-phosphocholine (DMPC), 1,2-dipalmitoyl-*sn*-glycero-3-phosphocholine (DPPC), or 1,2-distearoyl-*sn*-glycero-3-phosphocholine (DSPC), in organic solvents. 1,2-distearoyl-*sn*-glycero-3-phosphoethanolamine N-(carboxymethoxypolyethylene glycol-2000) (NaDSPE-PEG2K) was added (1 mol%) to the liposome formulation, as it is known to stabilise liposome suspensions by avoiding aggregation.¹¹ Thorough evaporation of the organic solvents and hydration with an aqueous solution containing an equimolar mixture of the electron donors NaHAsc (0.1 M) and TCEP (0.1 M) at pH 3, 4, 5, or 6, several

freeze-thawing cycles, and standard extrusion through a 0.2 μm polycarbonate filter, afforded photocatalytic liposomes characterised by the formula lipid:NaDSPE-PEG2K:**RuC₁₂**:**CoC₁₂** 100:1:X:Y, where lipid is DMPC, DPPC, or DSPC, X = 0.5 or 1 mol%, and Y = 0.02, 0.1, 0.5, or 1 mol%. The liposome samples were characterised by dynamic light scattering, which afforded their average diameter (Z_{ave}) and polydispersity index (PDI). Z_{ave} was typically found to be 145 – 205 nm and PDI values were below 0.20, which indicated a uniform size distribution (Table D1). As a note, bulk concentrations of 50 μM (**RuC₁₂**) and 5 μM (**CoC₁₂**) in 178 nm diameter DPPC liposomes correspond to local concentrations of 12 and 1.2 mM in the volume of the lipid bilayer, respectively (see Appendix D): due to the small ratio of the bilayer, compared to the bulk volume of the sample, supporting the photosensitiser and catalyst on the bilayers increases their concentrations by a factor ~ 240 .

4.2.2. Photocatalytic H₂ reduction.

Photocatalytic H₂ evolution experiments were conducted by shining blue light ($\lambda_{\text{irr}} = 450 \text{ nm}$, $P = 10.6 \text{ mW}$) on the photocatalytic liposomes in argon-saturated aqueous solutions. The formation of the product H₂ in the gas phase above the irradiated solution was measured by a Clark H₂ sensor, which was integrated within an in-house assembled set-up.²⁹ Prior to irradiation, each liposome solution was left in the dark for 1 h, which in all cases did not result in any H₂ formation. Then, the solution was irradiated with blue light for 19 h.

The photocatalytic performances of all tested photocatalytic liposome solutions are summarised in Table 4.1. Here, TON is the turnover number (defined as $\text{TON} = n_{\text{H}_2}/n_{\text{CoC}_{12}}$) and PTON the photocatalytic turnover number (defined as $\text{PTON} = 2 \times n_{\text{H}_2}/n_{\text{RuC}_{12}}$; the factor 2 accounts for the fact that 2 molecules of photosensitiser must turnover once for the formation of one H₂ molecule). The (photocatalytic) turnover frequency ((P)TOF) is defined as the maximum number of (P)TON per unit time at the highest rate of H₂ production. In order to optimise the photocatalytic performance of the **CoC₁₂-RuC₁₂** liposomal system, we varied the concentrations of **CoC₁₂** (1, 5,

25, and 50 μM) and of **RuC₁₂** (25 and 50 μM), the pH of the solution (3 – 6), and the type of lipid in the membrane (DMPC, DPPC, or DSPC), which influences its fluidity at the temperature used for photocatalysis (298 K). All other parameters (i.e. the light intensity and the concentration of the electron donors) were kept constant. Dynamic light scattering measurements were carried out to monitor changes in the size of the liposomes when running photocatalysis. In all cases except at pH = 6 (see below), the hydrodynamic radius after irradiation did not differ much (< 10 nm) compared with that before irradiation, suggesting that the photocatalytic liposomes remained essentially intact in such conditions (Table D1). Control experiments performed in absence of one of each component (Table 4.1, Figure D3) confirmed that no H₂ evolved when any one of them were absent from the catalytic mixture. Notably, no photocatalytic activity was observed in absence of TCEP, although many hydrogen evolution systems based on ruthenium-based photosensitisers and cobalt-based catalysts are reported to operate with solely HAsc⁻ as sacrificial electron donor.³⁰

As a note, as shown in Table 4.1 and Figure 4.2 the margin of error is larger with photocatalytic liposomes than that observed in homogeneous conditions. We attribute these experimental variations to the large number of steps necessary to prepare liposome samples. For example, liposome preparation includes many freeze/thawing cycles, which may take place at different rates; extrusion requires pressure, which is applied by hand. Lastly, the time between the preparation of the liposomes and the start of the photocatalytic experiment, is likely to be different for each sample. Even when no obvious signs of aggregation can be seen experimentally by DLS, it still might occur in the dark, slightly changing the photocatalytic results compared to samples which were used directly after preparation. All in all, analysing trends based on a single replicate is impossible, and reproducing at least three independent experiments is a must for studying photocatalytic liposomes.

Table 4.1. Photocatalytic H₂ generation with liposomes prepared from mixtures of a lipid (DMPC, DPPC, or DSPC), NaDSPE-PEG2K, NaHAsc, TCEP, RuC₁₂, and CoC₁₂, upon blue light irradiation.^[a]

Lipid	[NaHAsc]	[TCEP]	[RuC ₁₂]	[CoC ₁₂]	pH	n H ₂ ^[b,c]	TON ^[d]	TOF ^[d]	PTON ^[e]	PTOF ^[d]
DPPC	0.1 M	0.1 M	50 μM	50 μM	5.0	6.8 ± 3.2	39 ± 18	8.4 ± 2.2	78 ± 36	17 ± 4
DPPC	0.1 M	0.1 M	50 μM	25 μM	5.0	7.1 ± 2.2	81 ± 25	19 ± 5	81 ± 25	19 ± 5
DPPC	0.1 M	0.1 M	50 μM	5 μM	5.0	1.9 ± 0.8	107 ± 46	25 ± 8	21 ± 9	4.9 ± 1.6
DPPC	0.1 M	0.1 M	50 μM	1 μM	5.0	0.3 ± 0.3	n.d. ^[e]	n.d. ^[e]	n.d. ^[e]	n.d. ^[e]
DPPC	0.1 M	0.1 M	50 μM	5 μM	3.0	1.6 ± 1.2	92 ± 69	43 ± 1	18 ± 14	8.5 ± 0.2
DPPC	0.1 M	0.1 M	50 μM	5 μM	4.0	2.8 ± 0.7	161 ± 41	86 ± 22	32 ± 8	17 ± 4
DPPC	0.1 M	0.1 M	50 μM	5 μM	6.0	2.6 ± 0.6	149 ± 34	16 ± 3	30 ± 7	3.1 ± 0.6
DPPC	0.1 M	0.1 M	25 μM	5 μM	5.0	1.0 ± 0.7	58 ± 43	7.0 ± 0.7	23 ± 17	2.8 ± 0.3
DMPC	0.1 M	0.1 M	50 μM	5 μM	4.0	1.2 ± 0.5	68 ± 27	74 ± 35	14 ± 5	15 ± 7
DSPC	0.1 M	0.1 M	50 μM	5 μM	4.0	1.5 ± 0.9	87 ± 51	25 ± 5	17 ± 10	5.1 ± 1.0
DPPC	0.1 M	0.1 M	50 μM	-	5.0	0.4	-	-	5	2.9
DPPC	0.1 M	0.1 M	-	25 μM	5.0	-	-	-	-	-
DPPC	0.1 M	-	50 μM	25 μM	5.0	0.4	5	1.9	5	1.9
DPPC	-	0.1 M	50 μM	25 μM	5.0	-	-	-	-	-

^[a] Bulk concentrations: [lipid] = 5 mM, [NaDSPE-PEG2K] = 50 μM, $t_{\text{irr}} = 19$ h, $\lambda_{\text{irr}} = 450$ nm, $P = 10.6$ mW, photon flux (Φ_0) = 13.7 nmol/s (see Appendix D for the derivation and Figure D4). Conditions: argon-saturated solutions, volume 3.5 mL, temperature 25 °C. The values and standard deviations are derived from the average of three replicate experiments. Control experiments were performed once. ^[b] in μmol. ^[c] at $t = 20$ h. ^[d] in h⁻¹. ^[e] The error on the measurement was too high to determine these values, because the amount of H₂ generated was near the detection limit of the sensor.

Varying the concentration of CoC₁₂ and RuC₁₂. When the amount of catalyst CoC₁₂ in the DPPC membrane was decreased (50, 25, 5, 1 μM) at constant photosensitiser concentration (50 μM), the TON and TOF increased (Figure 4.2), from 39 ± 18 and 8.4 ± 2.2 h⁻¹, respectively, for 50 μM CoC₁₂, up to 107 ± 46 and 25 ± 8 h⁻¹, respectively, for 5 μM CoC₁₂. Unfortunately, the TON could not be determined when the concentration of CoC₁₂ was lowered down to 1 μM, because in such conditions the amount of H₂ produced (0.3 ± 0.3 μmol) became very low, within the range of the signal noise of the H₂ detector. Still, the productivity and rate of the catalyst improved when its concentration was decreased down to 5 μM, suggesting that high concentrations of the cobalt catalyst in the membrane are detrimental to the overall photocatalytic process.

On the other hand, the PTON and PTOF both decreased when the amount of CoC₁₂ in the DPPC membrane was lowered, from 78 ± 36 and 17 ± 4 h⁻¹, respectively, for 50 μM CoC₁₂, down to 21 ± 9 and 4.9 ± 1.6 h⁻¹, respectively, for 5 μM CoC₁₂. These results clearly indicate that the stability of the

photosensitiser is limiting the photocatalytic system. Decreasing the concentration of the photosensitiser RuC_{12} from $50 \mu\text{M}$ to $25 \mu\text{M}$ also leads to a less efficient photocatalytic system, as almost half the amount of hydrogen was produced ($\text{TON} = 58 \pm 43$), while the maximum hydrogen production rate became 2-3 times slower ($\text{TOF} = 7.0 \pm 0.7 \text{ h}^{-1}$ and $\text{PTOF} = 2.8 \pm 0.3 \text{ h}^{-1}$). The PTON remained constant within experimental errors (from 21 ± 9 to 23 ± 17), while we would have expected the same H_2 production, hence a doubled PTON , if the catalyst would decompose. Based on these data, it was decided to keep a photosensitiser concentration of $50 \mu\text{M}$ in the membrane during further optimisation. In addition, most probably the rate-determining step of the photocatalytic system as a whole, involves the photosensitiser molecule.

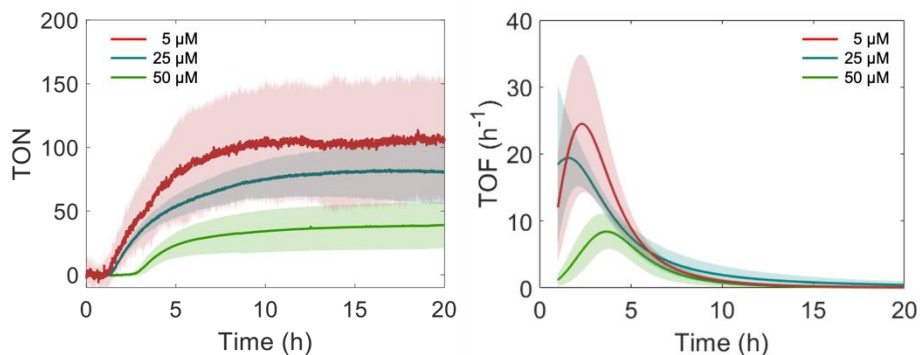


Figure 4.2. Photocatalytic activity of liposomes consisting of DPPC:NaDSPE-PEG2K: RuC_{12} : CoC_{12} with varying catalyst concentration $[\text{CoC}_{12}]$. The samples were left in the dark for 1 h and then irradiated with blue light for 19 h. Each curve is the average of the data of three replicates and includes the standard deviation (shaded area). Experimental conditions: $[\text{DPPC}] = 5 \text{ mM}$, $[\text{NaDSPE-PEG2K}] = 50 \mu\text{M}$, $[\text{RuC}_{12}] = 50 \mu\text{M}$; argon-saturated 0.1 M NaHAsc and 0.1 M TCEP aqueous solution, volume 3.5 mL , temperature $25 \text{ }^\circ\text{C}$, $\lambda_{\text{irr}} = 450 \text{ nm}$, $P = 10.6 \text{ mW}$, $\Phi_0 = 13.7 \text{ nmol/s}$. Bulk concentrations $[\text{RuC}_{12}]$ and $[\text{CoC}_{12}]$ indicate theoretical concentrations assuming no losses during liposome preparation.

Varying the pH. As the next step, we investigated whether the pH of the solution may have an effect on photocatalysis. Typically, higher proton concentrations make proton reduction catalysts faster, until catalyst decomposition or protonation of the electron donor start to take place. As a note, in all experiments the pH of the liposome solution did not change much (< 0.5) upon light irradiation for 19 h (Table D1). With this system, the highest

photocatalytic performance was obtained at pH 4.0 (Figure 4.3). In more acidic conditions (pH = 3.0), the lower concentration of the ascorbate electron donor HAsc^- ($\text{pK}_a = 4.0$, $\text{H}_2\text{Asc} \rightarrow \text{H}^+ + \text{HAsc}^-$)^{2,31} is likely to negatively influence photocatalysis. In less acidic conditions (pH = 6.0), aggregation of the liposomes occurred, as observed by dynamic light scattering after photocatalysis (Table D1). It is unclear how such aggregation influences the photocatalytic mechanism, but clearly, the photocatalytic rate of the DPPC liposomes at pH 6 was lower (TOF = $16 \pm 3 \text{ h}^{-1}$ compared to TOF = $86 \pm 22 \text{ h}^{-1}$ at pH 4), while the system was still active after 19 h light irradiation, suggesting a higher stability. Overall, the photocatalytic rate was maximal at pH 4, which we hence considered as the optimal condition for this system.

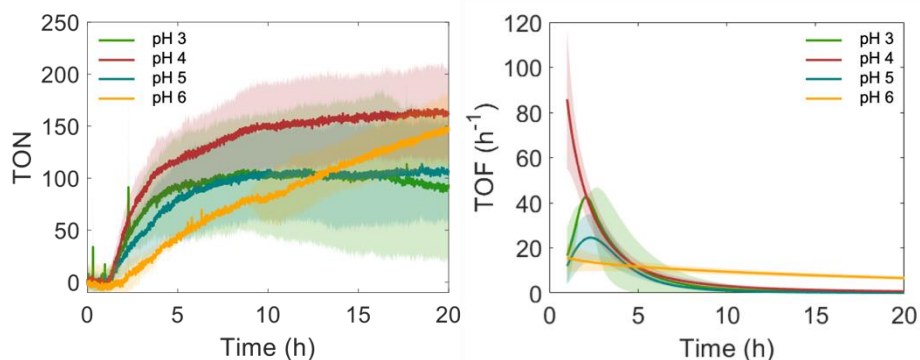


Figure 4.3. Photocatalytic activity of DPPC:NaDSPE-PEG2K:RuC₁₂:CoC₁₂ 100:1:1:0.1 liposomes at varying pH. The samples were left in the dark for 1 h and then irradiated with blue light for 19 h. Each curve is the average of three replicates and includes the standard deviation (shaded area). Experimental conditions: [DPPC] = 5 mM, [NaDSPE-PEG2K] = 50 μM , [RuC₁₂] = 50 μM , and [CoC₁₂] = 5 μM ; argon-saturated 0.1 M NaHAsc and 0.1 M TCEP aqueous solution, volume 3.5 mL, temperature 25 °C, $\lambda_{\text{irr}} = 450 \text{ nm}$, $P = 10.6 \text{ mW}$, $\Phi_0 = 13.7 \text{ nmol/s}$. Bulk concentrations [RuC₁₂] and [CoC₁₂] indicate theoretical concentrations assuming no losses during liposome preparation.

Varying the lipid. To investigate the influence of the phospholipid on photocatalysis, we embedded CoC₁₂ (5 μM) and RuC₁₂ (50 μM) in three different membranes prepared from the saturated lipids DMPC, DPPC, or DSPC. We did not include unsaturated lipids such as 1,2-dioleoyl-*sn*-glycero-3-phosphocholine (DOPC) in this study, because their membrane has been reported to be photochemically unstable.³ A membrane can exist in different phases, such as the liquid crystalline phase, which results in a more flexible

and mobile membrane, or the gel phase, a more rigid membrane. The phase transition temperature T_m , at which the membrane goes from the gel phase to the liquid crystalline phase, increases from DMPC ($T_m = 23\text{ }^\circ\text{C}$) to DPPC ($T_m = 41\text{ }^\circ\text{C}$) and DSPC ($T_m = 55\text{ }^\circ\text{C}$). There is currently no fundamental understanding about which phase of the membrane is better for photocatalysis; in some cases photocatalysis occurs better in the gel phase, in other cases better in the liquid crystalline phase.³ In our experiments run at $25\text{ }^\circ\text{C}$, both DPPC and DSPC membranes were in the gel phase, while DMPC was near the transition temperature. According to our data, the nature of the lipid had a dramatic effect on the TON; **CoC₁₂** and **RuC₁₂** were much more active in a DPPC membrane (TON = 161 ± 41) than in a DMPC (TON = 68 ± 27) or DSPC membrane (TON = 87 ± 51) (Figure 4.4). Thus, for this particular photocatalytic system, a rigid and stable DPPC membrane was preferred over a mobile DMPC membrane, but the membrane should not be too rigid (DSPC).

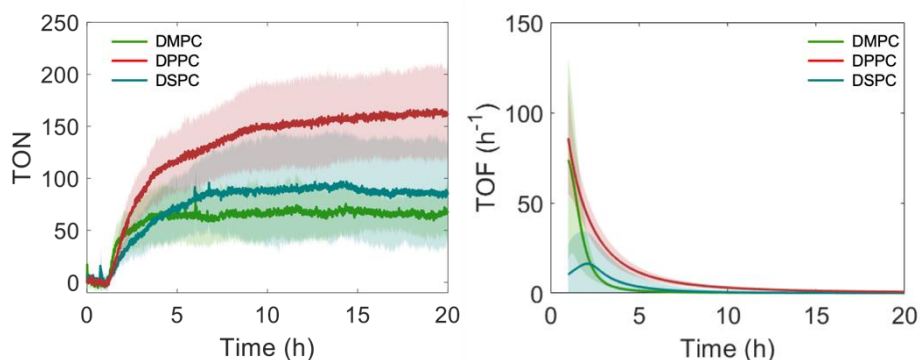


Figure 4.4. Photocatalytic activity of liposomes consisting of lipid:NaDSPE-PEG2K:**RuC₁₂**:**CoC₁₂** 100:1:1:0.1, where lipid is either DMPC, DPPC, or DSPC. The samples were left in the dark for 1 h and afterwards irradiated with a blue light for 19 h. Each curve is the average of three replicates and includes the standard deviation (shaded area). Experimental conditions: [DMPC, DPPC, or DSPC] = 5 mM, [NaDSPE-PEG2K] = 50 μM , [**RuC₁₂**] = 50 μM , and [**CoC₁₂**] = 5 μM ; argon-saturated 0.1 M NaHAsc and 0.1 M TCEP aqueous solution, volume 3.5 mL, pH = 4.0, temperature $25\text{ }^\circ\text{C}$, $\lambda_{\text{irr}} = 450\text{ nm}$, $P = 10.6\text{ mW}$, $\Phi_0 = 13.7\text{ nmol/s}$. Bulk concentrations [**RuC₁₂**] and [**CoC₁₂**] indicate theoretical concentrations assuming no losses during liposome preparation.

Stability of the system. As determined by the experiments described above, under fully optimised conditions (DPPC lipid, 5 μM **CoC₁₂**, 50 μM **RuC₁₂**, pH

4), the TON was equal to 161 ± 41 with a quantum yield of 2.9% after 1 h of irradiation (see Appendix D for the calculation), which is comparable to our knowledge to the highest TON reported for H₂ evolution on photocatalytic liposomes with purely molecular catalysts and photosensitisers.¹² On the other hand, with **CoC₁₂** it was not required to add excess ligand during irradiation to reach such H₂ production, which is an advantage. Still, after the first hour of light irradiation, H₂ generation slowed down and after 19 h of irradiation no significant H₂ production was observed anymore, which was a sign of decomposition of at least one of the components of the photocatalytic system. To obtain some insight into the reasons for the limitations of photocatalysis, we added either an additional equivalent of fresh photosensitiser (**RuC₁₂**), or an equivalent of fresh catalyst (**CoC₁₂**), to the reaction mixture after a first photocatalytic run. In previous work¹³, such replenishment of active molecules had been made by adding freshly-prepared liposomes containing solely the photosensitiser, to the irradiated reaction mixture. In such conditions, dilution of the reaction mixture may occur, and migration of the photosensitiser molecules from the freshly added liposomes to the irradiated, catalyst-containing vesicles, was not 100% sure. To avoid these effects, here we prepared a thin film of either **RuC₁₂** or **CoC₁₂** in a glass pressure-resistant tube, added the irradiated liposome reaction mixture to this flask, and heated the solution for 1 h at 50 °C while gently vortex-mixing the solution every 15 min. By doing so, we aimed at maximising the insertion of the photosensitiser molecules, from the thin film into the irradiated liposomes. Upon resuming light irradiation, we observed that the addition of extra **RuC₁₂** prolonged the photocatalytic activity by a supplemental TON = 75, whereas the addition of extra **CoC₁₂** did not lead to any extra H₂ production (Figure 4.5A). This experiment demonstrated that the stability of **RuC₁₂** clearly limited H₂ evolution during the first photocatalytic run. UV-Vis spectroscopy further demonstrated that the characteristic ³MLCT absorption band of **RuC₁₂**, observed between 410 and 470 nm, had almost completely disappeared after 19 h of irradiation of the photocatalytic liposomes (Figure 4.5B). An increase in absorption was observed between 500 and 700 nm that is typical for a $[\text{Ru}(\text{bpy})_2(\text{H}_2\text{O})_2]^{2+}$ decomposition product.³² Such a species is probably formed after photolabilisation of either a bpy-C₁₂ ligand or a bpy ligand, which was

reported as a decomposition pathway in acidic aqueous conditions.^{16,33} Overall these experiments demonstrated that the disappearance of the catalytic activity is due to photosensitiser decomposition, and that the cobalt catalyst was not, in such conditions, the factor limiting H₂ production.

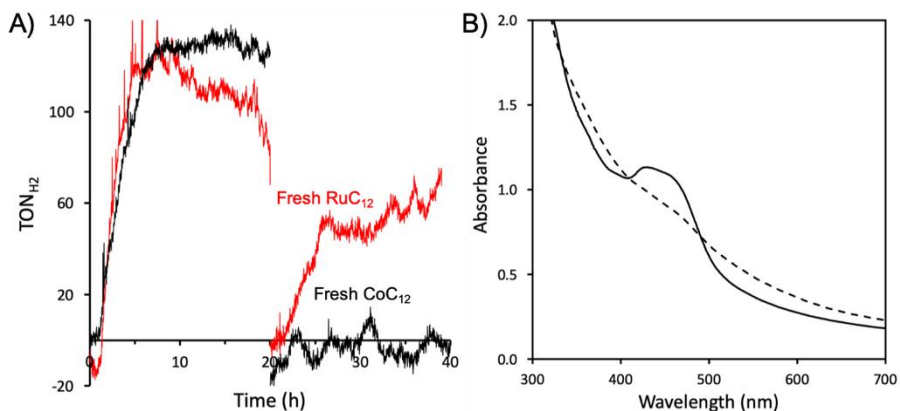


Figure 4.5. (A) Repetitive photocatalytic proton reduction using a liposome mixture consisting of 5 mM DPPC, 50 μM NaDSPE-PEG2K, 50 μM RuC₁₂, 5 μM CoC₁₂ in argon-saturated 0.1 M NaHAsc and 0.1 M TCEP aqueous solution (3.5 mL, pH = 4.0) at 25 °C. The samples were left in the dark for 1 h and afterwards irradiated with blue light ($\lambda_{\text{irr}} = 450 \text{ nm}$, $P = 10.6 \text{ mW}$, $\Phi_0 = 13.7 \text{ nmol/s}$) for 19 h. Afterwards, additional 50 μM RuC₁₂ (red curve) or 5 μM CoC₁₂ (black curve) was added to the reaction mixture and photocatalysis was started again. Bulk concentrations [RuC₁₂] and [CoC₁₂] indicate theoretical concentrations assuming no losses during liposome preparation. (B) UV-Vis spectrum of the reaction solution before irradiation (solid line) and after irradiation (dashed line).

Mechanistic considerations. According to Reisner, Hammarström et al,^[18] in a 0.1 M NaHCO₃ buffer containing 0.1 M NaHAsc the photosensitiser RuC₁₇ (an analogue of RuC₁₂ with 17 carbon atoms per alkyl chain instead of 12) in DMPC:NaDSPE-PEG2K 100:1 liposomes was statically quenched into RuC₁₇⁻. The quantum yield of this process was low (0.06), suggesting a low cage escape yield in this system. This effect was attributed to the adsorption of ascorbate to the membrane, which was rendered positively charged by the presence of the cationic metal complex, thereby leading to an overcrowded membrane and slow diffusion of the photogenerated ascorbate radical HAsc[•]. With liposomes containing RuC₁₂ and CoC₁₂, in absence of TCEP no

reaction took place, so that we assume that in such conditions charge recombination occurred even more quickly. In presence of high concentrations of TCEP, however, the ascorbate radical may be reduced faster by TCEP, thereby allowing **RuC₁₂⁻** to further transfer its electron to the cobalt catalyst and driving H₂ evolution. To test the validity of this hypothesis cyclic voltammetry and differential pulse voltammetry (DPV) analysis was performed for **CoC₁₂** (Figure D2). In homogeneous acetonitrile solution, the two first reductions of the hydrogen evolution catalyst were observed at -1.24 V vs Fc/Fc⁺ for the Co^{2+/+} couple, and -1.54 V vs Fc/Fc⁺ for Co⁺⁰. According to these data, the reduced photosensitiser **RuC₁₂⁻** (Ru^{2+/+} = -1.70 V vs Fc/Fc⁺ in acetonitrile¹⁷) is, at least thermodynamically speaking, capable of reducing the catalyst twice, which may trigger hydrogen evolution. On the other hand, the driving force of the second reduction (160 mV) may be insufficient to drive the photocatalytic system at appreciable rates, so that more kinetic studies would be necessary to confirm this mechanism. It should finally be noted that in photocatalytic liposomes oxidative quenching should not be ruled out as it often is in homogeneous conditions, due to the much higher local concentration of the photocatalytic species trapped in the membrane.

In our system, photocatalysis is probably self-inhibited due to the accumulation of HAsc⁻ at the liposomal surface due to favourable electrostatic interactions with the positively charged **RuC₁₂** and **CoC₁₂**, which potentially leads to fast charge recombination between the reduced **RuC₁₂⁻** and HAsc[•].¹⁸ The addition of an excess of TCEP (0.1 M) compared to **RuC₁₂** (50 μM), most probably ensures that the reaction between TCEP and HAsc[•] is faster than the charge recombination process, thus ensuring that **RuC₁₂⁻** can react with **CoC₁₂**.

4.3. Conclusion

In conclusion, we demonstrated that **CoC₁₂** is a robust catalyst for photocatalytic proton reduction on liposomes using **RuC₁₂** as photosensitiser. The best photocatalytic activity was observed with a 1:10 ratio of **CoC₁₂** to **RuC₁₂** embedded in DPPC liposomes under fully aqueous conditions with the sacrificial electron donors HAsc⁻ and TCEP at a pH of 4. In this system, decomposition of the photosensitiser **RuC₁₂** was the factor limiting the photocatalytic production of H₂. Finding a suitable, earth-abundant, alternative to **RuC₁₂** will be required to define the boundaries of **CoC₁₂** as a catalyst for sustainable photocatalytic hydrogen production on liposomes.

4.4 Experimental

4.4.1 General

General methods. ¹H NMR and ¹³C NMR spectra were recorded on a Bruker AV400 MHz spectrometer. Chemical shift values (δ) are reported in ppm relative to the solvent. Electrospray ionisation mass spectrometry (ESI-MS) spectra were measured with a ThermoFischer Scientific MSQ Plus electrospray ionisation mass spectrometer with a 17 – 2000 *m/z* detection range and a resolution of approximately 0.5 *m/z*. TLC-MS was measured on a Plate Express device coupled to an Advion Expression-L Compact Mass Spectrometer with ESI probe (3.5 kV; 250 °C) using as eluent methanol:water:formic acid 90:10:0.1 with a flow of 200 $\mu\text{L min}^{-1}$. High-resolution mass spectrometry (HRMS) was measured via direct injection on a Thermo Finnagan LTQ Orbitrap with electrospray ionisation. Elemental analysis was performed by Mikroanalytisches Laboratorium Kolbe in Oberhausen, Germany. UV-Vis absorption spectra were measured on a Varian Cary60 spectrophotometer equipped with a single cell Peltier temperature controller at 25 °C using a 3 mL cuvette. Cyclic voltammetry and differential pulse voltammetry were performed using a previously reported set-up.¹⁷

EPR spectroscopy. CoC_{12} was dissolved in acetonitrile and transferred into a 4 mm outer diameter EPR tube. Continuous wave EPR at X-Band (9.5 GHz) was performed on a Bruker ELEXSYS E680 (Bruker, Rheinstetten, Germany) spectrometer equipped with a TE_{102} cavity and an ESR900 cryostat (Oxford Instrument). Low temperature was achieved with a constant helium flow. The parameters were the following: modulation amplitude 10 G, modulation frequency 100 kHz, power 20 mW, total measurement time 7 min. Simulations were performed on MatLab using Easyspin version 5.2.33.³⁴

Materials and reagents. Chemical reagents and solvents were purchased from commercial suppliers and were used without further purification. NaHAsc ($\geq 99\%$) and TCEP were purchased from Merck. The lipids DMPC, DPPC, and DSPC were purchased as dry powders from Avanti Polar Lipids and stored at $-20\text{ }^{\circ}\text{C}$. NaDSPE-PEG2K was purchased as a dry powder from Lipoid and stored at $-20\text{ }^{\circ}\text{C}$. The Avanti Mini-Extruder including polycarbonate extrusion filter (pore size = $0.2\text{ }\mu\text{m}$, diameter = 19 mm) and filter supports (10 mm) was purchased from Avanti Polar Lipids. di([2,2-bipyridin]6-yl)methanone and RuC_{12} were synthesised according to literature.^{17,35} $\text{K}_3[\text{Fe}(\text{C}_2\text{O}_4)_3]\cdot 3\text{H}_2\text{O}$ for actinometry was prepared following a literature procedure, kept in the dark, and used within 1 week after preparation.³⁶

Preparation of liposomes for photocatalysis. DMPC, DPPC, or DSPC lipids in chloroform (2.0 mL of a 30.6 mM solution), NaDSPE-PEG2K in chloroform (1.0 mL of a 0.613 mM solution), RuC_{12} in chloroform (1.0 mL of a 0.613 mM or 0.306 mM solution), and CoC_{12} in methanol (1.0 mL of a 0.613 mM, 0.306 mM, 0.0613 mM, or 0.0123 mM solution) were added in a glass pressure-resistant tube. The organic solvents were evaporated under reduced pressure and the resulting lipid film was dried for at least 1 h in *vacuo* to remove residual solvent. The film was then hydrated with a sodium ascorbate (0.1 M) and TCEP (0.1 M) solution (3.5 mL) at pH = 3 – 6, where the pH was adjusted by the addition of 37% HCl to reach pH 3, or by the addition of 1.0 M NaOH to reach pH 4 – 6. Each lipid suspension was subjected to 10 freeze-thaw cycles between liquid N_2 and a $50\text{ }^{\circ}\text{C}$ water bath. Subsequently, the vesicles were extruded 11x with an Avanti Polar Lipids mini-extruder

through a 0.2 μm polycarbonate membrane at 10 $^{\circ}\text{C}$ above the phase transition temperature of the lipid. Assuming no losses during preparation, the resulting liposomes consist of lipid:NaDSPE-PEG2K:**RuC₁₂**:**CoC₁₂**; for example, in the ratio 100:1.0:1.0:0.1 with expected bulk concentrations of 17.5 mM lipid, 0.175 mM NaDSPE-PEG2K, 0.175 mM **RuC₁₂**, and 0.0175 mM **CoC₁₂**. Liposome samples were stored at RT in the dark and used within one week. For photocatalytic H₂ evolution experiments, the liposome solutions were diluted 3.5x with the same aqueous solution as that used for liposome preparation. The size distribution of the hydrodynamic diameter (Z_{ave}) and the polydispersity index (PDI) were measured at 25 $^{\circ}\text{C}$ by dynamic light scattering with a Zetasizer Nano-S from Malvern operating at 632.8 nm with a scattering angle of 173 $^{\circ}$.

Photocatalytic H₂ evolution. Photocatalytic H₂ evolution was performed using an in-house setup that has been described elsewhere.²⁹ Here, photocatalytic H₂ production was measured by a Clark hydrogen electrode every five seconds (Unisense H2-NP). The Clark hydrogen electrode was calibrated by a five-time injection of a known amount of high-purity H₂ into the fully deaerated (30 min degassing with argon) thermostated (298 K) photochemical reactor (total volume 25.0 mL) containing milli-Q water (3.5 mL). The calibration was adapted with the pressure change using Logger software, affording direct reading of the volume of H₂ (μL) produced in the gas phase of the reactor. For the photocatalytic H₂ evolution experiments, the thermostated photochemical reactor (25 $^{\circ}\text{C}$) was charged with the liposome solution (3.5 mL) and a stirring bar and afterwards the system was closed with one rubber septum and two silicon septa. The Clark hydrogen electrode used for measuring the H₂ concentration in the gas phase and two needles (a long one reaching the solution and a short one) were inserted through the septa. The solution was stirred (750 rpm) and degassed by bubbling argon for 30 min. After removal of the needles required for degassing, the data recording was started; first for 1 h (dark measurement), followed by 19 h during light irradiation (light measurement). The irradiation source was an OSRAM Opto Semiconductors LD W5SM LED ($\lambda_{\text{irr}} = 450 \text{ nm}$, $P = 10.6 \text{ mW}$, $\Phi_0 = 13.7 \text{ nmol/s}$) equipped with water cooling.

Stability experiments. For the stability experiments, a thin film of either **RuC₁₂** (1.0 mL of a 0.175 mM solution) or **CoC₁₂** (1 mL of a 0.0175 mM solution) was prepared in a glass pressure-resistant tube, using the same methodology as for the preparation of liposomes. The thin film was hydrated with the liposome-containing reaction mixture (3.5 mL) that had been irradiated once for a 19 h photocatalytic H₂ evolution experiment. The liposome solution was then heated for 1 h at 50 °C and every 15 min mixed by vortexing for a few seconds to ensure that most of the thin film of **RuC₁₂** or **CoC₁₂** became solubilised. Afterwards, the solution was transferred back to the photocatalytic set-up and a new H₂ evolution experiment was started, identical to the first one.

Data analysis. The (photocatalytic) turnover number ((P)TON) of the photocatalytic H₂ evolution was calculated from the H₂ production data by 1) converting the produced H₂ in μL to μmol using the molar volume constant (1 mol of ideal gas equals to 22.4 L) and converting μmol to (P)TON by dividing the H₂ production by the catalyst concentration or photosensitiser concentration, respectively; 2) reducing the amount of data of PTON vs time from 14400 data points to 2400 using Origin 9.1 software (data manipulation: reduce by group); 3) data fitting and averaging of three replicate experiments using MATLAB R2020b software to obtain the maximum (P)TON and its standard deviation.

The maximum (photocatalytic) turnover frequency ((P)TOF) of photocatalytic H₂ evolution was obtained using Origin 9.1 software by 1) nonlinear curve fitting of the time evolution of the μmol of H₂ evolved, starting at $t = 1$ h (category: Growth/Sigmoidal, function: logistic Fit); 2) calculating the first derivative of the H₂ evolution rate = $f(t)$ using mathematics (differentiate) and; 3) averaging three replicate experiments using MATLAB R2020b software to obtain the maximum (P)TOF and its standard deviation.²⁹

4.4.2 Syntheses

Synthesis of 1,1-di([2,2'-bipyridin]-6-yl)tridecan-1-ol. A three-neck round-bottom flask was charged with a solution of dodecylmagnesium bromide

(0.50 mL of a 1.0 M solution in diethyl ether, 0.50 mmol) in dry and degassed THF (10 mL). The reaction mixture was cooled to 0 °C and stirred under N₂ atmosphere. A solution of di([2,2'-bipyridin]-6-yl)methanone (100 mg, 0.296 mmol) in dry and degassed THF (25 mL, RT) was added drop-wise to the cooled Grignard solution. The resulting solution was stirred for 5 h and then quenched with water (50 mL) at RT. The organic layer was extracted with chloroform (3 x 50 mL). The combined organic layers were dried over MgSO₄, and the solvents were evaporated under reduced pressure. The crude product was purified via column chromatography (dry-loaded with celite) on silica gel (hexane/acetone = 5:2). The solvents were removed under reduced pressure and the remaining solids were dried *in vacuo*. 1,1-di([2,2'-bipyridin]-6-yl)tridecan-1-ol was obtained as a white solid (yield: 92 mg, 0.18 mmol, 61%). *R_f* = 0.1 (hexane:acetone 5:2). TLC-MS (ESI) *m/z* found (calcd): 509.1 (509.72, [M+H]⁺), 531.1, (531.70, [M+Na]⁺). ¹H NMR (400 MHz, CDCl₃): δ = 8.67 (dq, *J* = 4.8, 1.3 Hz, 2H), 8.49 (dt, *J* = 8.0, 1.1 Hz, 2H), 8.28 (dd, *J* = 7.7, 1.0 Hz, 2H), 7.93 (dd, *J* = 7.9, 1.0 Hz, 2H), 7.86 (td, *J* = 7.7, 1.8 Hz, 2H), 7.79 (t, *J* = 7.8 Hz, 2H), 7.32 (ddd, *J* = 7.5, 4.8, 1.2 Hz, 2H), 6.69 (s, 1H), 2.49 (m, 2H), 1.54 (m, 2H), 1.22 (m, 48H), 0.87 (t, *J* = 6.8 Hz, 7H). ¹³C NMR (101 MHz, CDCl₃): δ = 163.09 (C_q), 156.09 (C_q), 153.92 (C_q), 149.29 (CH), 137.84 (CH), 137.02 (CH), 123.85 (CH), 121.35 (CH), 121.13 (CH), 119.32 (CH), 78.71 (C_q), 63.13 (CH₂), 42.44 (CH₂), 32.93 (CH₂), 32.04 (CH₂), 32.02 (CH₂), 30.12 (CH₂), 29.82 (CH₂), 29.78 (CH₂), 29.76 (CH₂), 29.74 (CH₂), 29.72 (CH₂), 29.68 (CH₂), 29.56 (CH₂), 29.48 (CH₂), 29.47 (CH₂), 29.45 (CH₂), 25.88 (CH₂), 23.81 (CH₂), 22.81 (CH₂), 22.79 (CH₂), 14.24 (CH₃). LC-MS (ESI) *m/z* found (calcd): 509.4 (509.72, [M+H]⁺), 531.4 (531.70, [M+Na]⁺).

Synthesis of CoC₁₂. Cobalt(II) dibromide (13 mg, 0.061 mmol) and 1,1-di([2,2'-bipyridin]-6-yl)tridecan-1-ol (30 mg, 0.059 mmol) were dissolved in methanol (5.0 mL). The reaction mixture was stirred for 4 h under ambient conditions (air, RT). Afterwards, the reaction mixture was concentrated under reduced pressure to 1 mL. Precipitation occurred after addition of diethyl ether (15 mL). The precipitates were collected by filtration and washed with diethyl ether (3 x 5 mL) to obtain CoC₁₂ as a brown solid (yield: 30 mg, 0.041 mmol, 69%). *R_f* = 0.3 (hexane:acetone 5:2). ¹H NMR (400 MHz, MeOD): δ = 82.13, 67.11, 50.34, 32.37, 18.54, 9.48, 8.74, 8.44, 8.00, 2.30,

1.75, 1.44, 1.26, 1.04, 0.87. LC-MS (ESI) m/z found (calcd): 647.8 (647.55, $[M-Br]^+$). HR-MS (ESI) m/z found (calcd): 566.24501 (566.24504, $[2M-4Br-2H]^{2+}$), 680.23723 (680.23790, $[M-2Br+CF_3COO]^+$). Elemental analysis calcd (%) for $C_{33}H_{40}Br_2CoN_4O$: C 54.49, H 5.54, N 7.70; found: C 54.79, H 5.91, N 8.01.

4.5 References

- 1 T. R. Cook, D. K. Dogutan, S. Y. Reece, Y. Surendranath, T. S. Teets and D. G. Nocera, *Chem. Rev.*, 2010, **110**, 6474–6502.
- 2 Y. Pellegrin and F. Odobel, *C. R. Chim.*, 2017, **20**, 283–295.
- 3 A. Pannwitz, D. M. Klein, S. Rodríguez-Jiménez, C. Casadevall, H. Song, E. Reisner, L. Hammarström and S. Bonnet, *Chem. Soc. Rev.*, 2021, **50**, 4833–4855.
- 4 J. N. Robinson and D. J. Cole-Hamilton, *Chem. Soc. Rev.*, 1991, **20**, 49–94.
- 5 M. Hansen, S. Troppmann and B. König, *Chem. Eur. J.*, 2016, **22**, 58–72.
- 6 P. Du and R. Eisenberg, *Energy Environ. Sci.*, 2012, **5**, 6012–6021.
- 7 M. D. Kärkäs, O. Verho, E. V. Johnston and B. Åkermark, *Chem. Rev.*, 2014, **114**, 11863–12001.
- 8 J. D. Blakemore, R. H. Crabtree and G. W. Brudvig, *Chem. Rev.*, 2015, **115**, 12974–13005.
- 9 B. Zhang and L. Sun, *Chem. Soc. Rev.*, 2019, **48**, 2216–2264.
- 10 M. Hansen, F. Li, L. Sun and B. König, *Chem. Sci.*, 2014, **5**, 2683–2687.
- 11 B. Limburg, J. Wermink, S. S. van Nielsen, R. Kortlever, M. T. M. Koper, E. Bouwman and S. Bonnet, *ACS Catal.*, 2016, **6**, 5968–5977.
- 12 S. Troppmann and B. König, *Chem. Eur. J.*, 2014, **20**, 14570–14574.
- 13 S. Troppmann, E. Brandes, H. Motschmann, F. Li, M. Wang, L. Sun and B. König, *Eur. J. Inorg. Chem.*, 2016, **2016**, 554–560.
- 14 S. Troppmann and B. König, *ChemistrySelect*, 2016, **1**, 1405–1409.
- 15 R. Becker, T. Bouwens, E. C. F. Schippers, T. van Gelderen, M. Hilbers, S. Woutersen and J. N. H. Reek, *Chem. Eur. J.*, 2019, **25**, 13921–13929.
- 16 N. Ikuta, S. Y. Takizawa and S. Murata, *Photochem. Photobiol. Sci.*, 2014, **13**, 691–702.
- 17 D. M. Klein, S. Rodríguez-Jiménez, M. E. Hoefnagel, A. Pannwitz, A. Prabhakaran, M. A. Siegler, T. E. Keyes, E. Reisner, A. M. Brouwer and S. Bonnet, *Chem. Eur. J.*, 2021, **27**, 17203–17212.
- 18 S. Rodríguez-Jiménez, H. Song, E. Lam, D. Wright, A. Pannwitz, S. A. Bonke, J. J. Baumberg, S. Bonnet, L. Hammarström and E. Reisner, *J. Am. Chem. Soc.*, 2022, **144**, 21, 9399–9412.
- 19 J. P. Bigi, T. E. Hanna, W. H. Harman, A. Chang and C. J. Chang, *Chem. Commun.*, 2010, **46**, 958–960.

- 20 M. Guttentag, A. Rodenberg, C. Bachmann, A. Senn, P. Hamm and R. Alberto, *Dalton Trans.*, 2013, **42**, 334–337.
- 21 R. S. Khnayzer, V. S. Thoi, M. Nippe, A. E. King, J. W. Jurss, K. A. El Roz, J. R. Long, C. J. Chang and F. N. Castellano, *Energy Environ. Sci.*, 2014, **7**, 1477–1488.
- 22 S. Schnidrig, C. Bachmann, P. Müller, N. Weder, B. Spingler, E. Joliat-Wick, M. Mosberger, J. Windisch, R. Alberto and B. Probst, *ChemSusChem*, 2017, **10**, 4570–4580.
- 23 N. Queyriaux, E. Giannoudis, C. D. Windle, S. Roy, J. Pécaut, A. G. Coutsolelos, V. Artero and M. Chavarot-Kerlidou, *Sustain. Energy Fuels*, 2018, **2**, 553–557.
- 24 C. Bachmann, B. Probst, M. Guttentag and R. Alberto, *Chem. Commun.*, 2014, **50**, 6737–6739.
- 25 C. Bachmann, B. Probst, M. Oberholzer, T. Fox and R. Alberto, *Chem. Sci.*, 2016, **7**, 436–445.
- 26 D. F. Evans, *J. Chem. Soc.*, 1959, 2003–2005.
- 27 G. A. Bain and J. F. Berry, *J. Chem. Educ.*, 2008, **85**, 532.
- 28 P. Müller, B. Probst, B. Spingler, O. Blacque and R. Alberto, *Helv. Chim. Acta*, 2022, **105**, e202100237.
- 29 C. Liu, D. van den Bos, B. den Hartog, D. van der Meij, A. Ramakrishnan and S. Bonnet, *Angew. Chem. Int. Ed.*, 2021, **60**, 13463–13469.
- 30 F. Droghetti, F. Lucarini, A. Molinari, A. Ruggi and M. Natali, *Dalton Trans.*, 2022, **51**, 28, 10658–10673.
- 31 C. Creutz, *Inorg. Chem.*, 1981, **20**, 4449–4452.
- 32 B. Durham, S. R. Wilson, D. J. Hodgson and T. J. Meyer, *J. Am. Chem. Soc.*, 1980, **102**, 600–607.
- 33 J. van Houten and R. J. Watts, *Inorg. Chem.*, 1978, **17**, 3381–3385.
- 34 S. Stoll and A. Schweiger, *J. Magn. Reson.*, 2006, **178**, 42–55.
- 35 H. Nierengarten, J. Rojo, E. Leize, J.-M. Lehn and A. van Dorsseleer, *Eur. J. Inorg. Chem.*, 2002, **2002**, 573–579.
- 36 C. G. Hatchard, C. A. Parker and E. J. Bowen, *Proc. R. Soc. Lond. Ser. Math. Phys. Sci.*, 1956, **235**, 518–536.

Degradation of lipid-based drug delivery formulations during nebulisation

Encapsulating pharmaceuticals in protective lipid-based nanoparticles, and nebulising them towards the target area in the body offers a range of clinical advantages. However, the process of nebulisation might possibly damage sensitive nanoparticle structures, such as liposomes, resulting in loss of active pharmaceutical ingredients. We compare this loss for two types of lung inhalation devices: high-frequency piezo-actuated vibrating mesh nebulisers and non-actuated continuous jet nebulisers. We find that vibrating mesh nebulisers cause model liposomes to release more than ten times as much encapsulated material as the continuous jet nebulisers, because the energies involved in nebulisation are much larger. This result highlights the importance of applying a mild nebulisation technology when administering shear-sensitive drug formulations such as lipid nanoparticle-based drugs to the lungs.

This chapter has been published as a communication: David M. Klein, Albert Poortinga, Frank M. Verhoeven, Daniel Bonn, Sylvestre Bonnet, and Cees J. M. van Rijn, *Chemical Physics* **2021**, 547, 111192.

5.1 Introduction

The nebulisation route has some advantages over other administration routes for active pharmaceutical ingredients that specifically target the lung area. The intended therapeutic action in the lung can be triggered faster, unpleasant intravenous injections can be prevented, and also a smaller drug quantity is required, as the drug is delivered directly to its intended site of action. This mode of administration typically results in lower systemic side-effects in comparison to oral or intravenous administration. Side-effects can be further suppressed by encapsulating the drug inside liposomes or lipid nanoparticles (LNPs).^{1,2} Indeed, entrapping drugs in 'conventional' liposomes has proven advantages such as targeted drug delivery to specific tissues, and prevention against drug degradation.¹ Such protection is appealing for drug and vaccine makers,^{3,4} for example in the case of RNA drugs, which are vulnerable to RNase degradation.^{3,5} In addition, the use of LNPs facilitates cellular uptake of the drug with a high efficacy.² LNPs can be seen as a new generation of liposomes, specifically formulated for an efficient delivery of various active pharmaceutical ingredients, and are characterised by having a smaller internal aqueous content than liposomes.¹ However, in the process of converting the lipid based nanoparticle drug formulations into aerosol droplets (nebulisation), the nanoparticles may get damaged due to shear degradation, resulting in loss of the originally entrapped active pharmaceutical ingredients, in particular in case of hydrophilic materials.⁶ This is due to a high shear stress being exerted on the nanoparticles, leading to breakage. The development of lipid-based nanoparticle carriers for inhalation is therefore focused on increasing the strength and rigidity of the nanoparticles with the aim of reducing the detrimental effect of shear stress on nanoparticle stability and maximising its deposition rate and efficacy of the formulation in the 'deep lung'. An example of a lipid based nanoparticle drug formulation success is the recently FDA approved nebulisable liposome formulation of the antibiotic Amikacin, the success of which is attributed to the combined development of a shear-stress resistant nanoparticle formulation of cholesterol-enriched dipalmitoyl-phosphatidylcholine (DPPC-CH) with a liposome size around 300 nm and a PARI eFlow vibrating mesh

nebulisation device.⁷ In this communication we investigate a novel facile and fast nebulisation method with a continuous jet atomisation device to nebulise formulations at a throughput well over 1 mL/min with a minimum amount of shear stress enabling a large window to formulate lipid based nanoparticle drug carriers (Figure 5.1).

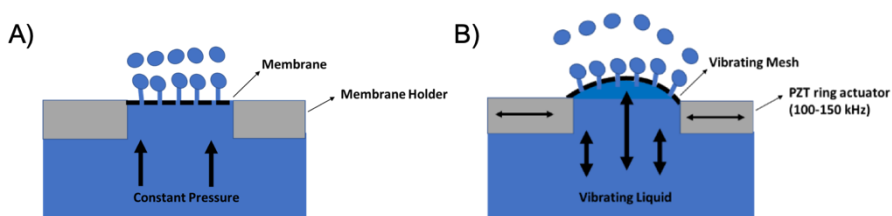


Figure 5.1. Methods of nebulizing used in this study. (A) Continuous atomisation. The nanoparticle formulation is pressed at a constant pressure through a rigid membrane enabling Rayleigh breakup. (B) Vibrating mesh technology. A flexible mesh mounted on a piezo ring actuator is stretching and vibrating. These vibrations are also present in the nanoparticle formulation and are dissipated by heat generation of the liquid.

5.2 Materials and methods

Preparation of liposome formulations. The osmolarity of aqueous solutions was measured on a Micro-Osmometer Autocal Type 13 from Roebing. Calcein was obtained from Carl Roth and used as received. 1,2-dipalmitoyl-sn-glycero-3-phosphocholine (DPPC) and cholesterol (CH) were purchased from Avanti Polar Lipids and sodium N-(carboxymethylpolyethylene glycol-2000)-1,2-distearoyl-sn-glycero-3-phosphoethanol-amine (NaDSPE-PEG2K) from Lipoid. All were stored as solids at $-20\text{ }^{\circ}\text{C}$. Liposomes were prepared as follows.^{8,9} The lipids were dissolved in chloroform at the desired ratio (DPPC 100, DPPC-CH 50:50, and DPPC-NaDSPE-PEG2K 100:1) in a pressure resistant glass tube. Chloroform was evaporated by rotary evaporation and the resulting lipid film was dried in vacuum overnight to remove residual solvent. The film was then hydrated with a NaH_2PO_4 buffer (1 mL, 0.1 M, pH = 7.7, p = 661 mOsm) containing calcein (70 mM), followed by 5 freeze-thaw cycles between liquid N_2 and a $50\text{ }^{\circ}\text{C}$ water bath. Subsequently, the vesicles were extruded 11 times with an Avanti Polar Lipids mini-extruder through a 100

nm polycarbonate membrane at 55 °C. After extrusion, the liposomes were separated from the non-encapsulated calcein using a SEC column (GE Healthcare cartridge) equilibrated with NaH₂PO₄ buffer (0.1 M, pH = 7.7, p = 663 mOsm, osmolarity adjusted by adding NaCl). The orange/brown non-fluorescence band containing the liposomes was obtained until free calcein eluted, as visualised by UV light. These liposome stock solutions (final bulk lipid concentration 5 mM, assuming no losses) were analysed the same day with dynamic light scattering (DLS) and calcein luminescence. DLS was performed at 25 °C on a Zetasizer Nano-S from Malvern operating at 632.8 nm with a scattering angle of 173°.

Calcein leakage testing. To a 1 mL cuvette was added 0.04 mL liposome stock solution and an isotonic 0.96 mL NaH₂PO₄ buffer (0.1 M, pH = 7.7, p = 663 mOsm). A luminescence measurement was carried out on a Horiba Aqualog spectrometer at RT using 495 nm as excitation wavelength. The emission intensity of calcein was recorded at 519 nm. The maximum luminescence intensity of calcein at 519 nm of the sample was determined by addition of TritonX100 (10 mM, 5 µL, 16 days equilibration time), which resulted in the destruction of the liposomes and subsequent release of all calcein into the bulk aqueous solution. The percentage of release of encapsulated calcein (%) was calculated by dividing the fluorescence intensity at a given time, by the final, maximum fluorescence intensity obtained after TritonX100 addition.

Nebulisers. The nebulisers used in this study are shown in Figure 5.2 and all produce drop size distributions (2-6 µm) suitable for inhalation. Nebuliser A (www.pocketair.com.tw) has a flow rate of 0.4 mL/min, nebuliser B (www.pari.com) of 0.5 mL/min and nebuliser C (www.medspray.com) of 1.5 mL/min. Nebuliser A and nebuliser B were filled with 2 mL of liposome formulation and Nebuliser C with 1 mL of liposome formulation. 1 mL of the formulation was nebulised. The nebulised formulation was collected by spraying into a 50 mL centrifuge tube. The degree of calcein leakage inside the collected fluid was measured as described above. The 1 mL liposome formulation that remained in the reservoir of nebuliser A and B at the end of each nebulisation experiment was also analysed for calcein release.

Nebulisation was undertaken within 2 h of preparation of the liposome formulation.



Figure 5.2. Nebulisers used in this study. (A) Pocket air, vibrating mesh nebuliser, (B) PARI eFlow, vibrating mesh nebuliser, and (C) Continuous jet nebuliser operated with a syringe.

Estimating the energy dissipation of the actuated nebulisers. To estimate the dissipation of the actuated mesh nebulisers water was sprayed for 1 min and the temperature increase of the mesh and reservoir was measured using a Flir C3 infrared camera. The measured temperature increase per second was multiplied with the heat capacity of water and divided by the flow rate to obtain a value for the so-called energy density (in J/g): the amount of energy added to the sprayed product.

5.3 Results and Discussion

To ensure that the results apply to different lipid formulations, we prepared three different types of liposomes, i.e. DPPC, DPPC-CH (50:50), and DPPC-NaDSPE-PEG2K (100:1), encapsulating calcein in their inner aqueous compartment as a model of a negatively charged drug. Calcein can be used for testing membrane leakage¹⁰; it is a self-quenching fluorophore that shows low fluorescence at high concentration inside the liposome (70 mM), but increased fluorescence at lower concentration, for example when it leaks outside the liposome into the bulk. Destroying the liposome membrane by adding the surfactant TritonX100 afforded a maximum fluorescence intensity F_{\max} , which allowed to quantify the relative fraction of drug released before full membrane disruption, X (in %), by dividing the fluorescence intensity F (before or after nebulisation) by F_{\max} . Figure 5.3 depicts the hydrodynamic

size distributions of the calcein-encapsulating DPPC, DPPC-CH, and DPPC-NaDSPE-PEG2K liposome formulations in phosphate buffer 1 h after preparation, as determined by DLS. Significant aggregation of the pure DPPC (Figure 5.3A) and DPPC-CH formulations (Figure 5.3B) was observed, whereas the 1% PEGylated DPPC formulation (stealth liposomes) did not aggregate at all, as characterised by a low polydispersity index ($PDI < 0.1$, Figure 5.3C). The characterisation of these size distributions is given in Table 5.1 with the volume average size (Z_{ave}) and the PDI defined based on the square of the relative standard deviation.

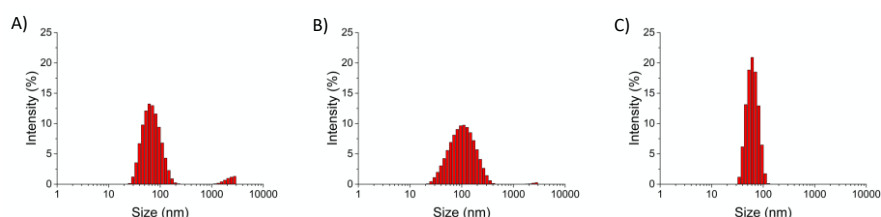


Figure 5.3. Hydrodynamic size distributions of calcein-encapsulated liposome formulations (A) DPPC, (B) DPPC-CH 1:1, and (C) DPPC-NaDSPE-PEG2K 100:1.

Table 5.1. Characterisation of the liposomes by DLS.

Liposome formulation	Z_{ave} (nm)	PDI
DPPC	136	0.23
DPPC-CH	181	0.24
DPPC-NaDSPE-PEG2K	119	0.05

In a second step, the relative calcein leakage of each formulation was quantified by measuring the fluorescence intensity F at the maximum emission (519 nm) of calcein, either directly after preparation, 1 h after preparation, or after nebulisation, and dividing it by the maximum emission intensity F_{max} when 100% of calcein was released by TritonX100-induced destruction of the liposome membrane. While storage of the liposomes for 1 h did not lead to measurable calcein leakage (variation $< 0.1\%$), all liposome formulations released calcein after nebulisation (Table 5.2). However, clear differences in calcein leakage were observed, depending on the type of nebuliser. The actuated mesh nebulisers caused a lot of calcein leakage

outside the liposome (13 – 16% with the pocket air and 32 – 37% with Pari eFlow), while the continuous jet nebuliser caused a negligible drug leakage (2.3 – 4.6% with Medspray). These results confirmed that it is the nebulisation procedure that induced drug release outside the liposome, and not thermal leakage of the membrane. Secondly, they highlight the difficulty of nebulising drug-encapsulating liposomes for example for delivery to the lungs: the energy used to generate the droplets locally tears the lipid membrane, thus leading to unwanted drug release before the liposomes have reached their target. Another potential issue is the heat generated in the reservoir by the vibrating mesh nebuliser, which as observed here may also lead to up to 24% of calcein leakage. Thermal effects on membrane leakage have been reviewed recently.¹¹

Table 5.2. Calcein release after nebulisation.

Experiment ^a	Liposome formulation		
	DPPC	DPPC-CH	DPPC-NaDSPE-PEG2K
Pocket air mist	15 ± 1%	13 ± 1%	16 ± 3%
Pocket air reservoir	14 ± 1%	13 ± 3%	4.8 ± 0.9%
Pari eFlow mist	37 ± 2%	32 ± 1%	34 ± 9%
Pari eFlow reservoir	24 ± 1%	23 ± <1%	6.6 ± 2.1%
Medspray mist	4.6 ± 0.7%	2.3 ± 0.3%	2.6 ± 2.6%

^a all experiments were performed in duplicate.

In order to explain the high leakage observed during nebulisation using mesh nebulisers we determined the energy density dissipated in the solution during nebulisation. The energy density is a parameter that is commonly used to compare emulsification effects.¹² For the non-actuated mesh nebuliser, the energy density is proportional to the applied pressure, which is estimated to be 20 bar giving an energy density of 2 J/g. For the actuated vibrating mesh nebulisers, we calculated the energy density to be in the order of 30 – 60 J/g based on the temperature rise (≈ 2 °C per 30 seconds for the Pocket air and $\approx 3 - 4$ °C per 30 seconds for the Pari eFlow) of the liquid in the reservoir after nebulisation. In the actuated-mesh nebulisers droplets are produced by the action of high frequency pressure waves with a

frequency in the range of 100 – 150 kHz. On the other hand the use of high frequency ultrasound waves is also a well-known technique to break or disrupt liposomes.¹³ It has been reported that the decrease in liposome size is proportional to the energy density.¹⁴ Using a frequency in the order of 100 kHz it was found that the average liposome size decreased with about ten percent at an energy density of 50 J/g. This makes it conceivable that pressure waves used in the actuated-mesh nebulisers cause the liposome membrane to deform and potentially disrupt, leading to a substantial loss of encapsulated calcein. Interestingly this assumption is now experimentally verified, as indeed a substantial leakage of calcein was found in the reservoir of the vibrating mesh nebulisers after nebulisation (5 – 14% with the pocket air and 7 – 24% with the Pari eFlow, see Table 5.2). In the syringe ‘reservoir’ of the Rayleigh jet nebuliser no leakage of calcein was found after nebulisation.

Liposomes and mechanical rigidity. DPPC liposomes are characterised by hydrogen saturated acyl chains, a high gel-to-liquid phase transition temperature (41.4 °C), and hence a high packing density at room temperature. Such characteristics lead to a gel-like, mechanically rigid, and stress-insensitive liposomes. Indeed, in absence of nebulisation, none of the formulation used here leaked significant amounts of calcein within 1 h. It is generally accepted that adding cholesterol (CH) make lipid membranes based on saturated acyl chains (e.g. DPPC) more fluid and lipid packing tighter, resulting in less leaky membranes. The addition of PEGylated phospholipids has been reported to weaken liposomes slightly, because PEGylated phospholipids have a higher exchange rate with the aqueous phase.¹⁵ In absence of nebulisation, none of these additives led to significant changes of the membrane leakage, as pure DPPC membranes were found already very tight at room temperature (< 0.1% leakage within 1 h). Upon “hard” nebulisation using the vibrating mesh nebuliser, adding cholesterol to the DPPC formulation had minimal effects on reducing calcein leakage. Addition of PEGylated lipids did increase the amount of calcein release, especially when passing the pores of the vibrating mesh, considering that the PEGylated lipids remained well preserved within the reservoirs of the vibrating mesh nebulisers during nebulisation. This effect is reminiscent from

the effect of air bubbles on the leakage of 1,2-dioleoyl-sn-glycero-3-phosphocholine (DOPC) liposomes, which was increased in presence of PEGylated lipids in the membrane.¹⁶ Upon “soft” nebulisation using the Rayleigh jet nebuliser, both additives slightly reduced calcein release, which remained much lower than when nebulisation was performed using the vibrating mesh nebulisers.

5.4 Conclusion

In conclusion, we have put forward an efficacious Rayleigh jet inhalation technology that causes less unwanted leakage of encapsulated drugs outside the liposomes during nebulisation, and this is regardless of the liposome composition. This nebulising technology therefore enables nebulising liposomes with a minimal escape of hydrophilic or large encapsulated drug molecules, such as DNA, RNA, proteins, peptides, antibodies, etc. while offering improved freedom in the formulation of lipid drug delivery systems.

5.5 References

- 1 G. Bozzuto and A. Molinari, *Int. J. Nanomedicine*, 2015, **10**, 975–999.
- 2 L. Sercombe, T. Veerati, F. Moheimani, S. Y. Wu, A. K. Sood and S. Hua, *Front. Pharmacol.*, 2015, **6**, 286.
- 3 A. Alshehri, A. Grabowska and S. Stolnik, *Sci. Rep.*, 2018, **8**, 3748.
- 4 G. Chauhan, M. J. Madou, S. Kalra, V. Chopra, D. Ghosh and S. O. Martinez-Chapa, *ACS Nano*, 2020, **14**, 7760–7782.
- 5 Y. X. Hui, G. Pengbo, W. Wu-Cheng and L. W. Ho, *Curr. Pharm. Des.*, 2015, **21**, 3140–3147.
- 6 D. Cipolla, I. Gonda and H.-K. Chan, *Ther. Deliv.*, 2013, **4**, 1047–1072.
- 7 M. S. Niederman, J. Alder, M. Bassetti, F. Boateng, B. Cao, K. Corkery, R. Dhand, K. S. Kaye, R. Lawatscheck, P. McLeroth, D. P. Nicolau, C. Wang, G. C. Wood, R. G. Wunderink and J. Chastre, *Lancet Infect. Dis.*, 2020, **20**, 330–340.
- 8 A. Pannwitz, H. Saaring, N. Beztsinna, X. Li, M. A. Siegler and S. Bonnet, *Chem. Eur. J.*, 2021, **27**, 3013–3018.

- 9 A. Pannwitz, D. M. Klein, S. Rodríguez-Jiménez, C. Casadevall, H. Song, E. Reisner, L. Hammarström and S. Bonnet, *Chem. Soc. Rev.*, 2021, **50**, 4833–4855.
- 10 B. Maherani, E. Arab-Tehrany, A. Kheiriloomoo, D. Geny and M. Linder, *Biochimie*, 2013, **95**, 2018–2033.
- 11 Z. Al-Ahmady and K. Kostarelos, *Chem. Rev.*, 2016, **116**, 3883–3918.
- 12 C. J. M. van Rijn, *Nano and Micro Engineered Membrane Technology*, Elsevier, 2004.
- 13 T. Yamaguchi, M. Nomura, T. Matsuoka and S. Koda, *Chem. Phys. Lipids*, 2009, **160**, 58–62.
- 14 M. De Cuyper, A. Crabbe, J. Cocquyt, P. van der Meeren, F. Martins and M. H. A. Santana, *Phys. Chem. Chem. Phys.*, 2004, **6**, 1487–1492.
- 15 S. Rex, J. Bian, J. R. Silvius and M. Lafleur, *Biochim. Biophys. Acta - Biomembr.*, 2002, **1558**, 211–221.
- 16 T. Fujie and M. Yoshimoto, *Soft Matter*, 2019, **15**, 9537–9546.

Summary, conclusions and outlook

6.1 Summary of this thesis

Artificial photosynthesis has recognised potential to produce green and sustainable fuels from earth-abundant resources such as water, carbon dioxide (CO₂), and sunlight. In an artificial photosynthetic system, two half-reactions, such as water oxidation and proton reduction or CO₂ reduction, have to be combined. To achieve such a system, it is crucial to have: a) efficient light-harvesting by the photosensitiser, b) stable catalysts for the oxidation and the reduction reaction, c) unidirectional proton and electron transport between the oxidation and the reduction site, ideally by a recyclable electron relay, d) efficient charge separation, and e) a strong, photostable membrane that does not leak molecular components. In natural photosynthesis, these requirements are achieved altogether using compartmentalisation, which consists in embedding the key components of the system, i.e. for green plants the oxygen evolving complex, photosystem I and II, and the natural electron relays, around the lipid bilayer of the thylakoid membrane. The use of spherical lipid membranes (such as liposomes) as biological mimics of the thylakoid membrane is a promising approach to confine half-reactions, facilitate charge separation, and avoid charge recombination and other undesired side-reactions. In the research described in this thesis, it was attempted to realise a full artificial photosynthetic system based on liposomes and several of the key intermediate steps were achieved: 1) unidirectional electron transfer across a liposomal membrane from an electron donor encapsulated in the interior of the liposome to an electron acceptor located outside (**Chapter 2**), and 2) photocatalytic reduction of CO₂ (**Chapter 3**) and of protons (**Chapter 4**) at the surface of liposomes. Special attention was paid in **Chapter 2** and **Chapter 5** to the question of the (photo)stability of the membrane and light-induced leakage, an aspect which has received little to no attention in previous studies.

In **Chapter 2**, we report the preparation of two membrane-embedded metallopeptides (**WALP23-Ru₂** and **WALP23-Re₂**), which were designed for driving photoinduced transmembrane electron transfer in liposomes from an

electron donor encapsulated within the inner compartment to an electron acceptor located in the outside. Upon light irradiation, **WALP23-Ru₂** seemed to quickly drive transmembrane electron transfer. A membrane leakage assay, however, demonstrated that the observed photoreaction was the result of light-induced leakage of the electron donor through the membrane, followed by photoinduced electron transfer on one side of the membrane. This observation was further supported by the addition of Zn²⁺ ions to the outside bulk solution, which quenched the photoreaction by inactivating the electron donor molecules that leaked through the membrane. Furthermore, molecular dynamics simulations showed that the metallopeptides not only assembled in the expected transmembrane orientation relative to the membrane, but also in a parallel configuration on one side of the lipid bilayer. On the other hand, **WALP23-Re₂** also achieved electron transfer upon light irradiation, but in this case electron transfer was still occurring after the addition of Zn²⁺ ions to the bulk aqueous phase. Thus, **WALP23-Re₂** is one of the rare molecules capable of realising genuine transmembrane electron transfer, whereas **WALP23-Ru₂** cannot. This work highlights the potential of artificial metallopeptides as transmembrane electron transporters and the importance of performing leakage studies for the development of artificial photosynthetic systems based on liposomes.

In **Chapter 3**, the synthesis of a series of rhenium-based CO₂-reduction catalysts [Re(4,4'-(C_nH_{2n+1})₂-bpy)(CO)₃Cl] (**ReC_n**; 4,4'-(C_nH_{2n+1})₂-bpy = 4,4'-dialkyl-2,2'-bipyridine) and ruthenium-based photosensitisers [Ru(bpy)₂(4,4'-(C_nH_{2n+1})₂-bpy)](PF₆)₂ (**RuC_n**) with different alkyl chain lengths (n = 0, 9, 12, 15, 17, and 19) was described. **ReC_n** and **RuC_n** were immobilised on PEGylated DPPC liposomes (**C_n**) to perform photocatalytic CO₂ reduction in the presence of NaHAsc and TCEP as sacrificial electron donors. The photocatalytic performance of the **C_n** liposomes was found to dramatically depend on the alkyl chain length, as the turnover number for CO production decreased when the alkyl chain length increased from **C₉** to **C₁₉**. This trend was analysed by quantification of the percentage of **RuC_n** and **ReC_n** immobilised within the liposomes using ICP-MS, by electron transfer rate measurements using time-resolved spectroscopy, and by lateral diffusion measurements using fluorescence lifetime correlation spectroscopy. The

ICP-MS measurements demonstrated that the length of the alkyl chain did not have an important effect on the immobilisation efficiency of **RuC_n** and **ReC_n**. The time-resolved spectroscopy measurements, however, revealed that electrons were indeed transferred faster between **RuC₉** and **ReC₉** than between **RuC₁₉** and **ReC₁₉**, which supported the observed photocatalytic trend. Finally, the lateral diffusion measurements demonstrated that the ruthenium complexes exist as a mixture of two sub-populations in the membrane: a slow one and a fast one. The higher contribution of the fast-diffusing component for the **C₉** system, compared to the **C₁₉** system, correlated well with the faster electron transfer rate between Ru and Re complexes observed in the former case. Overall, this work represents a significant advance in the fundamental understanding of supramolecular assemblies of catalysts and photosensitisers immobilised on lipid membranes: longer alkyl chains lengths are detrimental to liposome-supported photocatalysis, as it makes molecules too hydrophobic and buries them in the core of the membrane, where they lose their ability to diffuse and transfer their electrons intermolecularly.

In **Chapter 4**, the synthesis of a new alkylated cobalt polypyridyl complex **CoC₁₂** was described. **CoC₁₂** was studied as a proton reduction catalyst for liposome-supported photocatalytic hydrogen generation in combination with the alkylated ruthenium photosensitiser **RuC₁₂** described in **Chapter 3** and NaHAsc and TCEP as sacrificial electron donors. After optimising the system by varying the membrane concentration of **CoC₁₂** and **RuC₁₂**, the pH, and the lipid composition, a maximum turnover number for hydrogen production of 161 was achieved, which is as high as the best photocatalytic liposome systems published in the literature to date. However, stability studies demonstrated that the photocatalytic activity for this system could be restored, after a first completed photocatalytic run, by the addition of fresh **RuC₁₂**. Addition of fresh **CoC₁₂** did not lead to any further H₂ production, showing that the decomposition of **RuC₁₂** was the factor limiting H₂ production. Previous work on liposome-supported photocatalytic proton reduction¹⁻³ were limited by the stability of the catalyst rather than the stability of the photosensitiser. Thus, this work represents an important development towards a liposome-supported photocatalytic water splitting

system entirely based on earth-abundant elements, provided that the ruthenium trisbipyridine photosensitiser can be replaced by a photosensitiser that is both more stable and based on earth-abundant elements.

Finally, **Chapter 5** was not related to artificial photosynthesis, but describes a collaboration with the University of Amsterdam. In this work, a membrane leakage assay similar to that used in **Chapter 2** was used to measure the stability of liposome membranes towards content leakage during nebulisation, a common technique for pulmonary drug delivery. As a drug mimic, the self-quenching fluorophore calcein was encapsulated in the interior aqueous core of the liposome, and its leakage to the bulk aqueous phase, which was induced by nebulisation using different devices, was monitored using emission spectroscopy. The vibrating mesh nebulisers released more than ten times as much encapsulated material as the continuous jet nebulisers, because the energies involved in the nebulisation process are much larger. All in all, this work provides an excellent methodology to assess whether a given liposomal formulation is suitable for studies where membrane leakage should be avoided (**Chapter 2**). It also demonstrates that apparently stable liposomes may become unstable upon applying external stress such as mechanical nebulisers.

6.2 General conclusions and outlook

Based on the work described in this thesis, a full artificial photosynthetic system could in principle be realised by combining liposomes performing an oxidation reaction (i.e. water oxidation) with liposomes performing a reduction reaction (i.e. CO₂ reduction or proton reduction). Recently, a first complete artificial photosynthetic system based on liposomes was established that was capable of performing photocatalytic water splitting.⁴ In this system, metal-organic frameworks (MOFs) for photocatalytic water oxidation located in the interior aqueous phase of the liposome and MOFs for photocatalytic proton reduction located in the lipid bilayer of the liposome were coupled using two electron relays: a Fe³⁺/Fe²⁺ redox couple in

the interior aqueous phase, and a tetrachlorobenzoquinone/tetrachlorobenzohydrosemiquinone (TCBQ/TCBQH) redox couple embedded in the lipid membrane of the liposome.⁴ In spite of the innovative character of this system, its efficiency turned out to be limited by the accumulation of the electron relays in the reductive form (Fe^{2+} and TCBQH), which recombined with oxidative species on the water oxidation site (i.e. $[\text{Ru}(\text{bpy})_3]^{3+}$), which represents a form of late charge recombination.⁴ To achieve more efficient and longer-standing photocatalysis, it would make sense to physically separate the oxidation side from the reduction side of the system. For example, it would be possible to separate physically oxidative liposomes from reductive liposomes by a nanofiltration membrane.^{5,6} Such a physical membrane would allow small molecules, such as protons and electron transporter molecules, to move from one photocatalytic site to the other, while the liposomes cannot. Moreover, it would avoid the formation of a potentially explosive mixture of the products of both half-reactions (i.e. O_2 and H_2), as well as avoid spending energy to separate them.

An additional way to avoid charge recombination is by the spatial separation of the catalyst, the photosensitiser, and the electron relays; for example by encapsulating the catalyst in the interior of the liposome, putting the photosensitiser in the lipid membrane (**Chapter 2**), and leaving the electron relay on the outside of the liposome, provided that both water-soluble molecules (catalyst and electron relay in this case) cannot leak through the membrane. To test whether a certain liposome formulation is leaky and thus not usable for performing unidirectional transmembrane electron transfer, a general leakage assay screening can be performed either using the fluorophore calcein (**Chapter 5**), or a more selective reagent to look more specifically for leakage of the sacrificial electron donor or acceptor under study. Similar to the copper murexide assay used to probe EDTA leakage (**Chapter 2**), leakage of the electron donor ascorbic acid (used in **Chapter 3** and **Chapter 4**) could be studied by complexometry using iodide in the presence of starch. After all ascorbic acid reacts with iodine to form dehydroascorbic acid and iodide, excess iodine is free to react with starch, forming a blue-black starch-iodine complex.⁷ Similar assays should be developed for studying the leakage of water-soluble catalysts encapsulated

in the inner compartment of a liposome; for instance by measuring, either by ICP-MS or UV-Vis spectroscopy, the metal content of the supernatant after ultracentrifugation of the liposomes, before and after photocatalysis (using the methodology from **Chapter 3**).

Before assembling a full photosynthetic system, it is useful to screen catalysts and photosensitisers in a straightforward manner for their photocatalytic performance on liposomes. For this, sacrificial electron donors and acceptors are widely used to study the redox half-reactions (oxidation and reduction) individually. Replacing the sacrificial electron donors and acceptors by a reversible electron relay, however, remains one of the biggest challenges in artificial photosynthesis. The ideal electron relay should be recyclable, stable to air, soluble in water, insoluble in lipid membranes in both its oxidised and reduced form, and have appropriate redox properties to couple the oxidation site and the reduction site. In natural photosynthesis, charge separation is achieved via a Z-scheme energy-storage architecture using several electron transporters, such as plastoquinone, plastocyanin, and ferredoxin. Quinones or its derivatives are, therefore, good candidates as reversible electron relays and have already been used as recyclable electron relays for photocatalytic proton reduction.⁸ Alternative electron relays, already used in dye sensitised solar cells, include: a) inorganic redox couples; i.e. I^-/I^{3-} and Br^-/Br^{3-} , b) organic compounds; i.e. 2,2,6,6-tetramethyl-1-piperidinyloxy, phenothiazine, tetraphenyldiamine, and thiolate/disulphide, c) metal complexes based on Fe^{3+}/Fe^{2+} , Co^{3+}/Co^{2+} , or Cu^{2+}/Cu^+ .⁹ Furthermore, inspired by natural photosynthesis, and instead of using just one electron relay, several redox couples could be coupled, such as the Fe^{3+}/Fe^{2+} redox couple and the TCBQ/TCBQH couple.⁴ When using reversible electron relay(s), however, mixtures of its/their oxidised and reduced forms will be required, which will put the problem of charge recombination central.

In this thesis, we have embedded photosensitisers and catalysts for CO_2 reduction (**Chapter 3**) and proton reduction (**Chapter 4**) in the lipid membrane of the liposomes by engineering the hydrophobic interactions. An alternative functionalisation method would be to make the catalysts and photosensitisers fully water-soluble (i.e. by chemical modification of the

ligand by either addition of charged or polar side groups) and encapsulate them into the interior aqueous phase of the liposome. Provided that transmembrane electron transfer can be achieved (**Chapter 2**), it is then possible to drive electrons produced by an oxidising catalyst inside liposomes performing water oxidation towards the bulk via an electron relay, and from there to have them reach a reducing catalyst in another liposome performing proton reduction or CO₂ reduction (Figure 1.21). Another and potentially simpler option is to immobilise photosensitisers and catalysts on the same side of the lipid membrane and to separate the oxidation reaction and the reduction reaction by a physical membrane (Figure 6.1). In such a system, the physical membrane represents a barrier for late charge recombination reactions between the oxidative and the reductive side, considering that the liposomes cannot pass through the pores of the membrane. In both systems proposed, we will need to understand in details the kinetics of electron transfer at the interface between the lipid bilayer and the aqueous solution, which remains a challenge.

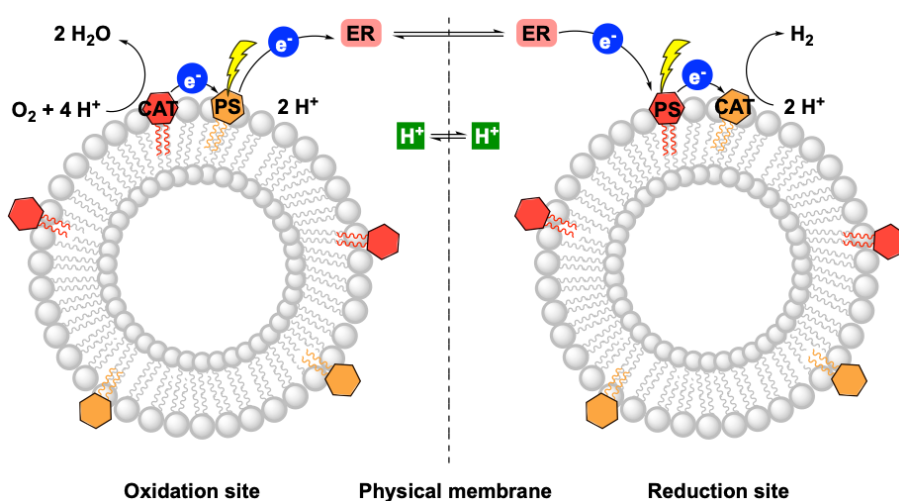


Figure 6.1. Proposed photocatalytic system for artificial water splitting based on liposomes. Electrons (blue) are transferred in a unidirectional way from the oxidation site to the reduction site via an electron relay. A physical membrane separates the oxidation and reduction site in two distinct compartments and allows only the molecular ER and the protons (green) to move from one site to the other. CAT = catalyst, ER = electron relay, and PS = photosensitiser.

Finally, all photosensitisers used in this work rely on expensive, non-abundant metals such as Ru and Re. It is highly desirable to explore earth-abundant alternatives for the development of more sustainable and cheaper liposome-supported photocatalytic systems. Several (metal-free) porphyrins^{10,11}, organic dyes^{12,13}, and metal complexes^{14,15} based on first row transition metals, have already been reported as photosensitisers for homogeneous water oxidation, proton reduction, or CO₂ reduction. They could be modified chemically by the introduction of an alkyl tail or charged groups, to generalise the approach developed in this thesis to systems exclusively composed of earth-abundant elements.

6.3 References

- 1 S. Troppmann and B. König, *Chem. Eur. J.*, 2014, **20**, 14570–14574.
- 2 S. Troppmann, E. Brandes, H. Motschmann, F. Li, M. Wang, L. Sun and B. König, *Eur. J. Inorg. Chem.*, 2016, **2016**, 554–560.
- 3 R. Becker, T. Bouwens, E. C. F. Schippers, T. van Gelderen, M. Hilbers, S. Woutersen and J. N. H. Reek, *Chem. Eur. J.*, 2019, **25**, 13921–13929.
- 4 H. Hu, Z. Wang, L. Cao, L. Zeng, C. Zhang, W. Lin and C. Wang, *Nat. Chem.*, 2021, **13**, 358–366.
- 5 H. P. Dijkstra, G. P. M. van Klink and G. van Koten, *Acc. Chem. Res.*, 2002, **35**, 798–810.
- 6 A. W. Mohammad, Y. H. Teow, W. L. Ang, Y. T. Chung, D. L. Oatley-Radcliffe and N. Hilal, *Desalination*, 2015, **356**, 226–254.
- 7 W. Saenger, *Naturwissenschaften*, 1984, **71**, 31–36.
- 8 A. Rodenberg, M. Oraziotti, M. Mosberger, C. Bachmann, B. Probst, R. Alberto and P. Hamm, *ChemPhysChem*, 2016, **17**, 1321–1328.
- 9 K. S. Srivishnu, S. Prasanthkumar and L. Giribabu, *Mater. Adv.*, 2021, **2**, 1229–1247.
- 10 A. M. Manke, K. Geisel, A. Fetzner and P. Kurz, *Phys. Chem. Chem. Phys.*, 2014, **16**, 12029–12042.
- 11 J. R. Swierk, D. D. Méndez-Hernández, N. S. McCool, P. Liddell, Y. Terazono, I. Pahk, J. J. Tomlin, N. V. Oster, T. A. Moore, A. L. Moore, D. Gust and T. E. Mallouk, *Proc. Natl. Acad. Sci.*, 2015, **112**, 1681–1686.
- 12 R. Gueret, L. Poulard, M. Oshinowo, J. Chauvin, M. Dahmane, G. Dupeyre, P. P. Lainé, J. Fortage and M.-N. Collomb, *ACS Catal.*, 2018, **8**, 3792–3802.
- 13 C.-F. Leung and T.-C. Lau, *Energy Fuels*, 2021, **35**, 18888–18899.
- 14 S.-P. Luo, E. Mejía, A. Friedrich, A. Pazidis, H. Junge, A.-E. Surkus, R. Jackstell, S. Denurra, S. Gladiali, S. Lochbrunner and M. Beller, *Angew. Chem. Int. Ed.*,

Chapter 6

- 2013, **52**, 419–423.
- 15 H. Yuan, B. Cheng, J. Lei, L. Jiang and Z. Han, *Nat. Commun.*, 2021, **12**, 1835.

Supporting information of Chapter 1

A.1. Experimental methods for studying photocatalytic vesicles

Table A1. Experimental techniques for the preparation, characterisation, and study of photocatalytic self-assembled membranes.

Experimental techniques	Information obtained	Reference(s)
Nuclear Magnetic Resonance (NMR)	<ul style="list-style-type: none"> – Nature and purity of membrane-embedded components – Stability of liposomes and membrane-embedded components – Photoproduct analysis and quantification (e.g. formate from CO₂ reduction)* – Position and diffusion of membrane-embedded components (Magic Angle Spinning NMR, MAS NMR) 	1–5
Fourier Transform / Attenuated Total Reflectance Infrared Spectroscopy (FT/ATR-IR)	<ul style="list-style-type: none"> – Confirm presence/immobilisation of membrane components* – Lipid membrane phase transitions 	6–9
Mass Spectrometry (MS, native and LC-MS, HPLC-MS)	<ul style="list-style-type: none"> – Characterisation of the membrane-immobilised components – Determination of reaction products and decomposition by-products of the membrane (lipid degradation) 	10
Cryo Transmission Electron Microscopy (TEM), Cryo Scanning Electron Microscopy (SEM), Energy Dispersive X-ray Spectroscopy (EDX)	<ul style="list-style-type: none"> – Morphology and size of liposomes (cryo TEM, SEM) – Characterisation and quantification of metal-based membrane components (EDX) – Stability studies 	11–13
Electron Paramagnetic Resonance (EPR)	<ul style="list-style-type: none"> – Determination of the physical properties (phase transition, fluidity) of a membrane – Determination of the pH at membranes – Study of oxygen transport in membranes (spin labels) – Study of oxidation of lipids in membranes 	14–16

Appendix A

	– Characterisation of paramagnetic membrane-embedded components	
X-ray Photoelectron Spectroscopy (XPS)	– Characterisation and quantification of metal-based membrane components*	17, 18
UV-Vis spectroscopy	– Characterisation of electronic absorption properties of membrane-immobilised components – Characterisation of the filter effect – Stability of liposomes and membrane-embedded components	12, 19–32
Fluorescence/emission spectroscopy	– Characterisation of excited state energy of membrane-embedded components – Stability of liposomes and membrane-embedded components – Transition temperature of heterogenous mixture of lipids/molecules	6, 10, 11, 21, 22, 24, 26–28, 32–35
Time-resolved absorption or emission spectroscopy	– Determination of excited state lifetime of membrane-embedded photoactive components – Analysis of the binding of immobilised components within the liposome assembly – Nature and kinetics of reactive intermediate species during photocatalysis (mechanism)	11, 20, 22, 24, 28, 30, 32, 33, 36, 37
Single-molecule fluorescence microscopy	– Determination of the lipid lateral diffusion in membranes	38
Differential Scanning Calorimetry (DSC) and fluorescence anisotropy	– Determination of the membrane transition temperature	11, 39
Dynamic and static light scattering	– Hydrodynamic diameter of liposomes – Surface charge of liposomes / zeta (ζ) potential – Stability of liposomes and membrane-embedded components	6, 12, 19, 23, 25–29, 32, 34, 40, 41
Nanoparticle tracking analysis	– Concentration and size distribution of liposomes	19
Atomic Force Microscopy (AFM)	– Analysis of the surface of liposomes	13, 42
Inductively Coupled Plasma - Mass Spectrometry (ICP-MS), Atomic Emission Spectroscopy (ICP-AES), Optical Emission Spectroscopy (ICP-OES)	– Quantification of metal content (synthetic molecules and enzymes)	23, 43, 44
Confocal microscopy	– Assessment of membrane-embedding of luminescent components (only in giant unilamellar vesicles)	1, 13, 32, 34, 35

Extrusion kit (syringes, polycarbonate extrusion filters, etc.)	– Prepare monodispersed liposome solutions	6, 10, 11, 21–23, 25, 29, 32–34, 40, 41, 45
Cyclic voltammetry	– Electrochemical characterisation of lipid membrane-embedded components (quantification, stability, activity)*	8, 37, 46–49
Sonicator, ultrasonicator	– Preparation of small unilamellar liposomes	6, 11, 12, 20, 24, 26–28, 45
Rotary evaporator and liquid N ₂ Dewar	– Preparation of liposomes (before hydration/self-assembly) and storage	12, 21–23, 25, 32, 34, 45
Column chromatography (e.g. size exclusion gel filtration, affinity columns, desalting column, etc.)	– Purification of proteo-liposomes or liposomes after self-assembly with newly immobilised synthetic components	6, 10, 19, 20, 22, 23, 25, 26, 32, 34, 41, 45
Light source (e.g. LED 450 nm for [Ru(bpy) ₃] ²⁺ ; sunlight simulator λ > 400 nm, Xe lamp, 100 mW cm ⁻² , AM 1.5G)	– Light irradiation for photocatalytic experiments	12, 21, 22, 24–28, 30–32, 35, 37
Fluorescence O ₂ probe or Clarke electrode	– Quantification of O ₂	12
Gas Chromatography (GC)	– Product analyses and quantification (gaseous product e.g. H ₂ , O ₂ , CO)	12, 26–28, 30, 31
Ion Chromatography (IC)	– Product analyses and quantification (charged ions e.g. formate)*	5
Osmometer	– Determination of osmolarity of buffer solution containing components (for preparing asymmetric liposomes)	12, 25

* Universal method, mainly used in homogeneous or heterogeneous systems.

A.2. References

- 1 D. K. Weber, M.-A. Sani, M. T. Downton, F. Separovic, F. R. Keene and J. G. Collins, *J. Am. Chem. Soc.*, 2016, **138**, 15267–15277.
- 2 C. Ader, R. Schneider, K. Seidel, M. Etzkorn and M. Baldus, *Biochem. Soc. Trans.*, 2007, **35**, 991–995.
- 3 H. A. Scheidt and D. Huster, *Acta Pharmacol. Sin.*, 2008, **29**, 35–49.
- 4 S. F. Rowe, G. Le Gall, E. V. Ainsworth, J. A. Davies, C. W. J. Lockwood, L. Shi, A. Elliston, I. N. Roberts, K. W. Waldron, D. J. Richardson, T. A. Clarke, L. J. C. Jeuken, E. Reisner and J. N. Butt, *ACS Catal.*, 2017, **7**, 7558–7566.
- 5 Q. Wang, J. Warnan, S. Rodríguez-Jiménez, J. J. Leung, S. Kalathil, V. Andrei, K. Domen and E. Reisner, *Nat. Energy*, 2020, **5**, 703–710.
- 6 L. M. Hays, J. H. Crowe, W. Wolkers and S. Rudenko, *Cryobiology*, 2001, **42**,

- 88–102.
- 7 A. F. A. Aisha, A. M. S. A. Majid and Z. Ismail, *BMC Biotechnol.*, 2014, **14**, 23.
- 8 N. Kornienko, K. H. Ly, W. E. Robinson, N. Heidary, J. Z. Zhang and E. Reisner, *Acc. Chem. Res.*, 2019, **52**, 1439–1448.
- 9 X. Fang, K. P. Sokol, N. Heidary, T. A. Kandiel, J. Z. Zhang and E. Reisner, *Nano Lett.*, 2019, **19**, 1844–1850.
- 10 I. O. L. Bacellar, M. C. Oliveira, L. S. Dantas, E. B. Costa, H. C. Junqueira, W. K. Martins, A. M. Durantini, G. Cosa, P. Di Mascio, M. Wainwright, R. Miotto, R. M. Cordeiro, S. Miyamoto and M. S. Baptista, *J. Am. Chem. Soc.*, 2018, **140**, 9606–9615.
- 11 M. Andersson, L. Hammarström and K. Edwards, *J. Phys. Chem.*, 1995, **99**, 14531–14538.
- 12 B. Limburg, J. Wermink, S. S. van Nielen, R. Kortlever, M. T. M. Koper, E. Bouwman and S. Bonnet, *ACS Catal.*, 2016, **6**, 5968–5977.
- 13 B. Ruozi, D. Belletti, A. Tombesi, G. Tosi, L. Bondioli, F. Forni and M. A. Vandelli, *Int. J. Nanomedicine*, 2011, **6**, 557–563.
- 14 M. A. Voinov, I. Rivera-Rivera and A. I. Smirnov, *Biophys. J.*, 2013, **104**, 106–116.
- 15 A. Ligeza, A. N. Tikhonov, J. S. Hyde and W. K. Subczynski, *Biochim. Biophys. Acta - Bioenerg.*, 1998, **1365**, 453–463.
- 16 S. P. Gabbita, D. A. Butterfield, K. Hensley, W. Shaw and J. M. Carney, *Free Radic. Biol. Med.*, 1997, **23**, 191–201.
- 17 M. K. Baumann, E. Amstad, A. Mashaghi, M. Textor and E. Reimhult, *Biointerphases*, 2010, **5**, 114–119.
- 18 K. Eleršič, J. I. Pavlič, A. Iglič, A. Vesel and M. Mozetič, *Chem. Phys. Lipids*, 2012, **165**, 120–124.
- 19 A. Stikane, E. T. Hwang, E. V. Ainsworth, S. E. H. Piper, K. Critchley, J. N. Butt, E. Reisner and L. J. C. Jeuken, *Faraday Discuss.*, 2019, **215**, 26–38.
- 20 L. Hammarström, H. Berglund and M. Almgren, *J. Phys. Chem.*, 1994, **98**, 9588–9593.
- 21 A. Perez-Velasco, V. Gorteau and S. Matile, *Angew. Chemie Int. Ed.*, 2008, **47**, 921–923.
- 22 S. Bhosale, A. L. Sisson, P. Talukdar, A. Fürstenberg, N. Banetji, E. Vauthey, G. Bollot, J. Mareda, C. Röger, F. Würthner, N. Sakai and S. Matile, *Science*, 2006, **313**, 84–86.
- 23 A. Bahreman, M. Rabe, A. Kros, G. Bruylants and S. Bonnet, *Chem. Eur. J.*, 2014, **20**, 7429–7438.
- 24 L. Hammarström, T. Norrby, G. Stenhagen, J. Mårtensson, B. Åkermark and M. Almgren, *J. Phys. Chem. B*, 1997, **101**, 7494–7504.
- 25 B. Limburg, E. Bouwman and S. Bonnet, *Chem. Commun.*, 2015, **51**, 17128–17131.
- 26 S. Troppmann and B. König, *Chem. Eur. J.*, 2014, **20**, 14570–14574.
- 27 M. Hansen, F. Li, L. Sun and B. König, *Chem. Sci.*, 2014, **5**, 2683–2687.
- 28 N. Ikuta, S. Y. Takizawa and S. Murata, *Photochem. Photobiol. Sci.*, 2014, **13**,

- 691–702.
- 29 B. Limburg, E. Bouwman and S. Bonnet, *J. Phys. Chem. B*, 2016, **120**, 6969–6975.
- 30 Y. Amao and I. Okura, *J. Mol. Catal. A Chem.*, 1996, **105**, 125–130.
- 31 N. Sugiyama, M. Toyoda and Y. Amao, *Colloids Surf A Physicochem. Eng. Asp.*, 2006, **284–285**, 384–387.
- 32 A. Pannwitz, H. Saaring, N. Beztinna, X. Li, M. A. Siegler and S. Bonnet, *Chem. Eur. J.*, 2021, **27**, 3013–3018.
- 33 P. Jurkiewicz, L. Cwiklik, A. Vojtišková, P. Jungwirth and M. Hof, *Biochim. Biophys. Acta - Biomembr.*, 2012, **1818**, 609–616.
- 34 B. Maherani, E. Arab-Tehrany, A. Kheirrolomoom, D. Geny and M. Linder, *Biochimie*, 2013, **95**, 2018–2033.
- 35 E. Altamura, F. Milano, R. R. Tangorra, M. Trotta, O. H. Omar, P. Stano and F. Mavelli, *Proc. Natl. Acad. Sci. U. S. A.*, 2017, **114**, 3837–3842.
- 36 M. J. Llansola-Portoles, D. Gust, T. A. Moore and A. L. Moore, *C. R. Chim.*, 2017, **20**, 296–313.
- 37 R. Becker, T. Bouwens, E. C. F. Schippers, T. van Gelderen, M. Hilbers, S. Woutersen and J. N. H. Reek, *Chem. Eur. J.*, 2019, **25**, 13921–13929.
- 38 M. J. Murcia, S. Garg and C. A. Naumann, in *Methods in Membrane Lipids*, ed. A. M. Dopico, Humana Press, Totowa, NJ, 2007, pp. 277–294.
- 39 S. H. C. Askes, P. Brodie, G. Bruylants and S. Bonnet, *J. Phys. Chem. B*, 2017, **121**, 780–786.
- 40 J. Sabín, G. Prieto, J. M. Ruso, R. Hidalgo-Álvarez and F. Sarmiento, *Eur. Phys. J. E*, 2006, **20**, 401–408.
- 41 S. Paula, A. G. Volkov, A. N. van Hoek, T. H. Haines and D. W. Deamer, *Biophys. J.*, 1996, **70**, 339–348.
- 42 J. Flores, B. M. White, R. J. Brea, J. M. Baskin and N. K. Devaraj, *Chem. Soc. Rev.*, 2020, **49**, 4602–4614.
- 43 I. S. Dovydenko, Y. A. Laricheva, K. V. Korchagina, A. E. Grigoryeva, E. I. Ryabchikova, N. B. Kompankov, D. P. Pischur, A. L. Gushchin, E. K. Apartsin and M. N. Sokolov, *J. Phys. Chem. B*, 2019, **123**, 8829–8837.
- 44 C. Verdiá-Báguena, A. Alcaraz, V. M. Aguilera, A. M. Cioran, S. Tachikawa, H. Nakamura, F. Teixidor and C. Viñas, *Chem. Commun.*, 2014, **50**, 6700–6703.
- 45 A. Akbarzadeh, R. Rezaei-Sadabady, S. Davaran, S. W. Joo, N. Zarghami, Y. Hanifehpour, M. Samiei, M. Kouhi and K. Nejati-Koshki, *Nanoscale Res. Lett.*, 2013, **8**, 102.
- 46 G. R. Heath, M. Li, H. Rong, V. Radu, S. Frielingsdorf, O. Lenz, J. N. Butt and L. J. C. Jeuken, *Adv. Funct. Mater.*, 2017, **27**, 1606265.
- 47 L. N. Pelster and S. D. Minteer, *ACS Catal.*, 2016, **6**, 4995–4999.
- 48 T. Laftoglou and L. J. C. Jeuken, *Chem. Commun.*, 2017, **53**, 3801–3809.
- 49 Ó. Gutiérrez-Sanz, P. Natale, I. Márquez, M. C. Marques, S. Zacarias, M. Pita, I. A. C. Pereira, I. López-Montero, A. L. De Lacey and M. Vélez, *Angew. Chemie Int. Ed.*, 2016, **55**, 6216–6220.

Supporting information of Chapter 2

B. 1. Material and methods

Materials and reagents: All reagents were obtained from Sigma-Aldrich and used as received unless stated otherwise. Fmoc-L-Ala-Wang TentaGel S resin was obtained from Iris Biotech GmbH. DPPC was obtained from Avanti Polar Lipids and stored at $-20\text{ }^{\circ}\text{C}$. NaDSPE-PEG2K was purchased from Lipoid and stored at $-20\text{ }^{\circ}\text{C}$. 4-(bromomethyl)-4'-methyl-2,2'-bipyridine (97%) was obtained from TCI chemicals. Copper(II) nitrate hemi(pentahydrate) was obtained from Riedel-de Haën. $[\text{Re}(\text{bpy}-(\text{C}_{15})(\text{CO})_3\text{Cl})]$ (**ReC₁₅**, $\text{bpy}-(\text{C}_{15})_2 = 4,4'$ -di-pentadecane-2,2'-bipyridine) was available in our group from previous work.¹ Fmoc-protected amino acids: alanine, glycine, leucine, Boc-protected tryptophan, and N-(9H-Fluoren-9-ylmethoxycarbonyloxy)succinimide were obtained from NovaBioChem. DMF (peptide synthesis grade), piperidine, acetic anhydride, pyridine, TFA, and MeCN were purchased from Biosolve. DIPEA and Oxyma were obtained from Carl Roth. DCM and Et₂O were supplied by Honeywell. Sephadex LH-20 was purchased from VWR International B.V. The Avanti Mini-Extruder including polycarbonate extrusion filter (pore size = 200 nm, diameter 19 mm) and filter supports (10 mm) was purchased from Avanti Polar Lipids. Phosphate buffer (1 L, 0.1 M, pH = 7.8) was prepared by dissolving NaH₂PO₄·2H₂O (12 g) in Milli-Q water (500 mL), adjusting the pH with NaOH ($\approx 90\text{ mL}$, 1 M), and diluting further with Milli-Q water up to 1 L. K₃[Fe(C₂O₄)₃]·3H₂O for actinometry was prepared following a literature procedure², kept in the dark, and used within 24 h after preparation.

Instrumentation: ¹H and ¹³C NMR spectra were recorded on a Bruker AV-400 MHz spectrometer. Chemical shift values (δ) are indicated in ppm relative to tetramethylsilane, measured using a residual solvent peak. HRMS was measured via direct injection on a Thermo Finnigan LTQ Orbitrap with

electrospray ionisation. UV-Vis absorption spectra were measured on a Varian Cary60 spectrophotometer equipped with a single cell Peltier temperature controller at 25 °C using a 3 mL cuvette. Emission spectra were measured on a FLS900 spectrometer from Edinburgh Instruments Ltd. in a 3 mL cuvette at 22 °C using 380 nm as excitation source for Re and 450 nm as excitation source for Ru complexes. Luminescence lifetimes were measured using an in-house assembled setup.³ The emission intensity versus time was modelled by a biexponential decay using Glotaran.⁴ The osmolarity of aqueous solutions was measured on a Micro-Osmometer Autocal Type 13 from Roebing. The size distribution of the hydrodynamic diameter (Z_{ave}) and the polydispersity index (PDI) of liposomes were measured at 25 °C on a Zetasizer Nano-S from Malvern operating at 632.8 nm with a scattering angle of 173°. Elemental analysis was performed by Mikroanalytisches Laboratorium Kolbe in Oberhausen, Germany. LED optical power was measured by OPHIR Nova-display laser power meter.

B. 2. Peptide design (preliminary studies)

The x, y, z coordinates of α -helical WALPn peptides (acetyl-GWWL(AL)_nWWA-amide, with G = glycine, W = tryptophan, A = alanine, and L = leucine) were initially generated using PyMol. YASARA (Yet Another Scientific Artificial Reality Application) was then used as a modelling program to replace two alanine amino acids by two unnatural bipyridyl alanine amino acids (A_{bpy}) at the desired positions within the peptide sequence.⁵ Coordination of the metal to the A_{bpy} fragments was achieved by manually inserting a bond between the nitrogen atoms of the A_{bpy} fragments and the metal. We initially used Ca^{2+} as the coordinated metal center instead of Ru^{2+} or Re^+ , because YASARA is not able to model Ru^{2+} or Re^+ . We also added two extra bipyridine (bpy) ligands to Ca^{2+} ; to make it resemble the photosensitiser $[Ru(bpy)_3]^{2+}$. The generated structures were optimised by energy minimisation (using the YASARA force field) and analysed with YASARA to evaluate the Ca-Ca distance.

We chose to synthesise **WALP23-M₂** with the A_{bpy} in positions 7 and 17 (Figure B1, Table B1). By positioning the A_{bpy} at these intermediate positions, the length of the hydrophobic central part (L(AL)₄ = 2.55 nm; length ≈ 0.15 nm per amino acid in an ideal α-helix) matched well with the expected hydrophobic thickness of the lipid bilayer (DPPC bilayer = 2.65 nm)⁶. Furthermore, of all the peptide molecules considered, it has the shortest Ca-Ca distance, which will be important for its electron transfer purposes. Moreover, **WALP23-M₂** with the A_{bpy} in positions 7 and 17 is nearly-symmetrical, e.g. the location of the metals is at the same position from either end of the peptide. Finally, a shorter peptide (WALP23-M₂) would be easier to synthesise than a longer peptide (WALP27-M₂), because the overall yield obtained after solid-phase peptide synthesis (Section B.3) will decrease with every amino acid added to the peptide sequence (i.e. 98% yield at every coupling step would result in a maximum yield of $0.98^{23} \times 100\% = 62.8\%$ for WALP23-M₂ and $0.98^{27} = 58.0\%$ for WALP27-M₂).

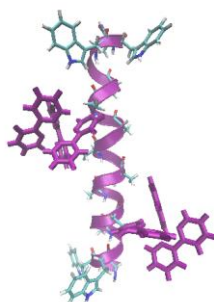


Figure B1. Molecular model of **WALP23-Ca₂** with A₇ and A₁₇ substituted by A_{bpy}.

Table B1. Chemical design of metallopeptides that were considered for this work.

WALPn-M ₂ (A _x and A _y) ^[a]	Peptide length (nm) ^[b]	Ca-Ca distance (nm)	Symmetrical
WALP23-M ₂ (A ₅ and A ₁₉)	3.45	2.1	Yes
WALP23-M ₂ (A ₇ and A ₁₇)	3.45	1.6	Yes
WALP25-M ₂ (A ₅ and A ₂₁)	3.75	3.0	Yes
WALP25-M ₂ (A ₇ and A ₂₁)	3.75	2.4	No
WALP27-M ₂ (A ₅ and A ₂₃)	4.05	3.4	Yes
WALP27-M ₂ (A ₇ and A ₂₁)	4.05	1.9	Yes
WALP27-M ₂ (A ₉ and A ₁₉)	4.05	1.9	Yes

^[a] n equals the number of amino acids within the WALPn peptide and A_x and A_y are the locations of the alanine amino acid residues that were substituted by bipyridyl alanine. ^[b] It is assumed that each amino acid has a length of 0.15 nm in an ideal α-helix.⁷

Fmoc-A_{bpy}: (S)-1-carboxy-2-(4'-methyl-[2,2'-bipyridin]-4-yl)ethan-1-amium chloride (103 mg, 0.35 mmol) was dissolved in a sodium bicarbonate solution (126 mg, 1.19 mmol, 2 mL). To this solution was added dropwise a dioxane solution containing N-(9H-Fluoren-9-ylmethoxycarbonyloxy)succinimide (138 mg, 0.41 mmol, 2 mL). The reaction mixture was stirred at room temperature for 2.5 h. Afterwards, Et₂O (20 mL) was added to the mixture and the mixture was extracted with water (3 x 20 mL). The combined aqueous layers were cooled down to 0 °C and concentrated HCl (≈ 1 mL, 37%) was then added until pH < 2, resulting in the formation of a pink precipitate. The aqueous layers were divided over 4 corning tubes (15 mL) and centrifuged (Jouan Br4i centrifuge, 4000 rpm, 20 min, RT). After removal of the supernatant, the pellets were redissolved in MeOH. After removal of MeOH under reduced pressure and vacuum drying, the product **Fmoc-A_{bpy}** was obtained as a pink-purple powder (75 mg, 0.16 mmol, 45%). ¹H NMR (400 MHz, DMSO-d₆): δ = 8.55 (d, *J* = 5.0 Hz, 1H), 8.49 (d, *J* = 4.9 Hz, 1H), 8.33 (s, 1H), 8.20 (s, 1H), 7.85 (d, *J* = 7.6 Hz, 2H), 7.80 (s, 1H), 7.57 (dd, *J* = 15.1, 7.5 Hz, 2H), 7.36 (m, 3H), 7.22 (m, 3H), 4.28 (t, *J* = 11.5 Hz, 1H), 4.16 (m, 3H), 3.20 (dd, *J* = 13.9, 4.3 Hz, 1H), 2.99 (t, *J* = 13.7, 10.6 Hz, 1H), 2.39 (s, 3H). ¹H NMR (400 MHz, MeOD): δ = 8.73 (d, *J* = 5.2 Hz, 1H), 8.56 (d, *J* = 5.8 Hz, 1H), 8.37 (d, *J* = 8.4 Hz, 2H), 7.81 (m, 1H), 7.69, (m, 4H), 7.46 (m, 2H), 7.33 (m, 3H), 7.18 (m, 2H), 4.69 (m, 1H), 4.28 (m, 2H), 4.03 (t, *J* = 7.2 Hz, 1H), 3.58 (dd, *J* = 14.1, 4.9 Hz, 1H), 3.25 (m, 1H), 2.53 (s, 3H). ¹³C NMR (75 MHz, MeOD): δ = 173.88 (C_q), 172.79 (C_q), 160.20 (C_q), 159.99 (C_q), 158.27 (C_q), 154.37 (C_q), 149.10 (C_q), 148.92 (C_q), 148.02 (CH), 146.19 (C_q), 144.84 (C_q), 144.35 (C_q), 142.33 (CH), 129.08 (CH), 128.81 (CH), 128.38 (CH), 128.12 (CH), 128.05 (CH), 127.90 (CH), 126.08 (CH), 125.36 (CH), 124.86 (CH), 120.90 (CH), 120.73 (CH), 67.84 (CH₂), 55.11 (CH), 48.18 (CH₂), 37.89 (CH), 22.17 (CH₃). HRMS (ESI) *m/z* found (calcd): 480.19139 (480.19178, [M+H]⁺), 494.20695 (494.20743, [M+CH₃]⁺, methyl ester instead of carboxylic acid).

WALP23-bpy₂: Solid-phase peptide synthesis was performed using a Liberty Blue microwave assisted automated peptide synthesiser for the coupling of the natural amino acids (A, W, L, and G). For the coupling of the unnatural amino acid **A_{bpy}**, we performed a manual coupling, see below. Synthesis was performed on the solid-phase, at a 0.1 mmol scale, using Fmoc-L-Ala-Wang

TentaGel resin (90 μm , 0.20 – 0.25 mmol/g) as the solid support. Fmoc deprotection was achieved using 20% piperidine in DMF, and coupling was facilitated with DIC as activator and Oxyma as base using a double deprotection, double coupling procedure. Peptide synthesis was performed twice; the first batch was cleaved with ethanolamine and used for the synthesis of **WALP23-Ru₂**, whereas the second batch was cleaved with TFA and used for the synthesis of **WALP23-Re₂**.

The synthesis of **WALP23-bpy₂** was started by the automated synthesis of LALWWA-resin (**Pep1**). Afterwards, the contents of the reaction vessel were transferred to a 10 mL syringe with a filter and washed with DMF (3 x 5 mL). In the next step, a solution of **Fmoc-A_{bpy}** (52.7 mg, 0.11 mmol), HCTU (45.5 mg, 0.11 mmol), and DIPEA (0.11 mmol, 0.019 mL) in DMF (2 mL) was added to the syringe containing LALWWA-resin and left to react on a rocking platform at RT for 24 h. The reaction mixture was washed with DMF (3 x 5 mL), resulting in a color change of the resin from yellow to purple. **Fmoc-A_{bpy}LALWWA-resin (Pep2)** was added back to the reaction vessel of the peptide synthesiser and the sequence LALALALAL was coupled to it, resulting in a yellow residue, due to the deprotection of the Fmoc group of **Fmoc-A_{bpy}**, which was responsible for the purple color. Afterwards, the contents of the reaction vessel were transferred to a 10 mL syringe with a filter and washed three times with DMF (3 x 5 mL). In the next step, a solution of **Fmoc-A_{bpy}** (52.7 mg, 0.11 mmol), HCTU (45.5 mg, 0.11 mmol), and DIPEA (0.11 mmol, 0.019 mL) in DMF (2 mL) was added to the syringe containing LALALALALA_{bpy}LALWWA-resin (**Pep3**) and left to react on a rocking platform at RT for 24 h. The reaction mixture was washed with DMF (3 x 5 mL), resulting again in a color change of the resin from yellow to purple. **Fmoc-A_{bpy}LALALALALA_{bpy}LALWWA-resin (Pep4)** was added back to the reaction vessel of the peptide synthesiser and the sequence GWWLAL was coupled to it, resulting in a yellow residue. The resin-bound peptide was suspended in DMF (5 mL), transferred to a 10 mL syringe with a filter, and washed with DMF (3 x 5 mL). Afterwards, acetic anhydride (10 drops) and pyridine (11-12 drops) in DMF (5 mL) were added to the syringe and the mixture was left to react on a rocking platform at RT for 1 h to acetylate the N-terminus of the peptide. Then, the syringe was drained and washed with DMF (3 x 5 mL) and

with DCM (3 x 5 mL). At this stage, two methods of cleavage, previously reported for WALP23^{7,11}, were performed for two different batches of **WALP23-bpy₂**; either with 1) ethanolamine or 2) TFA, as described below:

1) Ethanolamine (0.8 mL) and DCM (4.2 mL) were added to the resin and left to react on a rocking platform at RT for 48 h to facilitate peptide cleavage. The solution was filtered and the resin was washed with DCM (10 mL), TFE (5 mL), a mixture of DCM/TFE (1:1, 5 mL), and finally with DCM again (10 mL). The solutions were combined and solvents were evaporated until only ethanolamine was left. Afterwards, a minimum amount of DCM (1 mL) was added and the solution was transferred to a 50 mL conical tube. Water (35 mL) was added and the solution was left in the fridge (4 °C) for 2.5 h, resulting in a suspension. Centrifugation (Thermo IEC CL10 centrifuge, 30 min, 4000 rpm, RT) of the suspension led to a yellowish precipitate. After freeze-drying for 1 day, **WALP23-bpy₂** with **X** = ethanolamine (151.4 mg, 52.5%) was obtained as a white solid that was characterised and, due to its very high hydrophobicity, used without further purification.

2) TFA (3 mL), water (5 drops), and TIPS (6 drops) were added to the resin and left to react on a rocking platform at RT for 3 h to cleave the peptide. The reaction mixture was drained into ice-cold Et₂O (30 mL) resulting in a suspension. Centrifugation (Thermo IEC CL10 centrifuge, 10 min, 4000 rpm, RT) of the suspension led to a yellowish-brown precipitate. The precipitate was redissolved in a mixture of tert-butanol (2 mL) and water (6 mL). After freeze-drying for 1 day, **WALP23-bpy₂** with **X** = NH₂ (41.6 mg, 14.6%) was obtained as a white solid that was characterised and, due to its very high hydrophobicity, used without further purification.

All intermediate peptides were analysed by LC-MS to monitor the progress of peptide synthesis using the following protocol. After finishing a peptide fragment by either solid-phase or manual synthesis, a test cleavage was performed by transferring a few mg of the resin to a 5 mL syringe with filter. The resin was washed with DCM (3 x 2 mL) and afterwards TFA (1 mL), TIPS (2 drops), and water (2 drops) were added. After cleavage (2 h on a rocking platform), the contents of the syringe were added into 20 mL ice-cold Et₂O

and after centrifugation (Thermo IEC CL10 centrifuge, 10 min, 4000 rpm, RT) a solid would remain on the bottom of the centrifuge tube. The supernatant was removed and the residue was typically dissolved in a mixture of H₂O:CH₃CN:tBuOH (1:1:1) for LC-MS analysis on either a C₁₈ column (**Pep1** and **Pep2**) or a diphenyl column (**Pep3**, **Pep4** and **WALP23-bpy₂**), depending on the hydrophobicity of the peptide. In case no precipitation was observed after centrifugation, all solvents were evaporated under a stream of N₂, resulting in a solid residue that was dissolved and analysed as described above.

LC-MS (ESI) *m/z* found (calcd) for **Pep1**: 759.33 (759.42, [M+H]⁺). LC-MS (ESI) *m/z* found (calcd) for **Pep2**: 1220.53 (1220.59, [M+H]⁺). LC-MS (ESI) *m/z* found (calcd) for **Pep3**: 924.75 (925.05, [M+2H]²⁺, 1847.67 (1849.10, [M+H]⁺). LC-MS (ESI) *m/z* found (calcd) for **Pep4**: 1155.6 (1155.64, [M+2H]²⁺, 1177.2 (1176.15, [M+ACN+2H]²⁺). LC-MS (ESI-TOF) *m/z* found (calcd) for **WALP23-bpy₂** with **X** = NH₂: 952.9425 (952.87, [M+3H]³⁺), 1428.8895 (1428.80, [M+2H]²⁺). HRMS (ESI) *m/z* found (calcd) for **WALP23-bpy₂** with **X** = NH₂: 952.87025 (952.87092, [M+3H]³⁺), 1428.80237 (1428.80274, [M+2H]²⁺).

WALP23-Ru₂: DMF and EtOH were dried overnight on molecular sieves (3 – 5Å) and degassed for 15 min with N₂ before use. **WALP23-bpy₂** with **X** = ethanolamine (70.0 mg, 0.024 mmol) and *cis*-[Ru(bpy)₂Cl₂] · 2 H₂O (52.0 mg, 0.100 mmol) were dissolved in a mixture of DMF (2 mL) and EtOH (2 mL). The reaction mixture was heated at 85 °C for 7 days under N₂. Afterwards, the reaction mixture was concentrated under reduced pressure by co-evaporation with toluene (3 x 20 mL). The crude product was purified by size exclusion chromatography (Sephadex LH-20 as packing material) using MeOH as the eluent. The orange band, which was red phosphorescent under UV-light, was collected. After evaporation under reduced pressure, the product was obtained as a red solid (55.4 mg, 0.014 mmol, 59%). Elemental analysis for C₁₉₃H₂₄₄N₄₀O₂₅Ru₂Cl₄ · 4 H₂O: (calcd.): C, 58.83; H, 6.45; N, 14.22; (exp.): C, 58.93; H, 6.57; N, 14.23. LC-MS (ESI-TOF) *m/z* found (calcd) for **WALP23-Ru₂**: 929.0564 (927.93, [M-4Cl-OH]⁴⁺), 1238.4000 (1236.91, [M-4Cl-OH-H]³⁺). LC-MS on a diphenyl column (ESI) *m/z* found (calcd) for **WALP23-Ru₂**: 928.67 (927.93, [M-4Cl-OH]⁴⁺), 1237.75 (1236.91, [M-4Cl-OH-H]³⁺,

1856.08 (1854.35, $[M-4Cl-OH-2H]^{2+}$). UV-Vis (MeOH): λ_{max} (ϵ): 454 nm ($1.59 \times 10^4 \text{ mol}^{-1}\text{dm}^3\text{cm}^{-1}$).

WALP23-Re₂: **WALP23-bpy₂** with **X** = NH₂ (17.6 mg, 6.2 μmol) and [Re(CO₅)Cl] (15.9 mg, 44 μmol) were dissolved in dry toluene (5 mL) and refluxed for 24 h under N₂. The formed precipitate was collected by filtration, washed with toluene (3 x 10 mL), and dried on vacuum overnight. Afterwards, the precipitate was purified by size-exclusion chromatography (Sephadex LH-20 as packing material) using acetone as eluent. The yellowish band, which was yellowish-orange phosphorescent under UV-light, was collected. After evaporation under reduced pressure, the product was obtained as a yellowish brown solid (9.6 mg, 2.8 μmol , 45%). Elemental analysis for C₁₅₇H₂₀₇Cl₂N₃₁O₃₁Re₂ · 2 H₂O: (calcd.): C, 53.82; H, 6.07; N, 12.39; (exp.): C, 53.72; H, 6.06; N, 12.37. LC-MS (ESI-TOF) *m/z* found (calcd) for **WALP23-Re₂**: 1160.2767 (1159.84, $[M-2Cl+2ACN]^{3+}$, 1428.8831 (1428.80, $[M-2[Re(CO)_3Cl]+2H]^{2+}$, unreacted starting material or degradation due to the conditions necessary for dissolving the sample; H₂O:ACN:tBuOH 1:1:1 with few drops of FA), 1739.9296 (1739.76, $[M-2Cl+2ACN]^{2+}$. UV-Vis (CHCl₃): λ_{max} (ϵ): 380 nm ($3.97 \times 10^3 \text{ mol}^{-1}\text{dm}^3\text{cm}^{-1}$).

RuC₁₅: The crude product [Ru(bpy)₂(bpy-(C₁₅)₂)]Cl₂ · x NaCl (258.4 mg, 0.243 mmol, 56.2% yield) was obtained as described in literature¹. To remove excess salts, the crude product (61.0 mg, 0.057 mmol) was purified by size-exclusion chromatography (Sephadex LH-20 as packing material) using methanol as eluent. After evaporation under reduced pressure, the product was obtained as a red solid (34.8 mg, 0.033 mmol). *R_f* = 0.1 (SiO₂, acetone:water:brine (8:4:1)). ¹H NMR (400 MHz, CD₃OD): δ = 8.71 (d, *J* = 8.2 Hz, 4H), 8.63 (d, *J* = 1.9 Hz, 2H), 8.11 (tt, *J* = 8.0, 1.5 Hz, 4H), 7.82 (td, *J* = 5.7, 1.8 Hz, 4H), 7.63 (d, *J* = 5.8 Hz, 2H), 7.49 (dq, *J* = 7.0, 5.5, 1.3 Hz, 4H), 7.34 (dd, *J* = 5.9, 1.7 Hz, 2H), 2.85 (t, *J* = 7.8 Hz, 4H), 1.73 (q., *J* = 8.0 Hz, 4H), 1.28 (m, 48H), 0.89 (t, *J* = 6.6 Hz, 6H). ¹³C NMR (100 MHz, CD₃OD): δ = 158.62 (C_q), 158.58 (C_q), 158.17 (C_q), 156.55 (C_q), 152.63 (CH), 152.49 (CH), 151.87 (CH), 139.05 (CH), 128.87 (CH), 125.62 (CH), 36.24 (CH₂), 33.07 (CH₂), 31.35 (CH₂), 30.79 (CH₂), 30.75 (CH₂), 30.72 (CH₂), 30.61 (CH₂), 30.47 (CH₂), 30.44 (CH₂), 30.41 (CH₂), 23.74 (CH₂), 14.46 (CH₃). Elemental analysis for C₆₀H₈₄N₆Cl₂Ru · x

NaCl (before size-exclusion chromatography): (calcd.): C, 67.90; H, 7.98; N, 7.92; (exp.): C, 44.76; H, 7.40; N, 5.12. Elemental analysis for $C_{60}H_{84}N_6Cl_2Ru + 1 H_2O$ (after size-exclusion chromatography): (calcd.): C, 66.77; H, 8.03; N, 7.79; (exp.): C, 66.98; H, 8.12; N, 7.79. HRMS (ESI) m/z found (calcd): 495.29007 (495.29032, $[RuC_{15}-2Cl]^{2+}$).

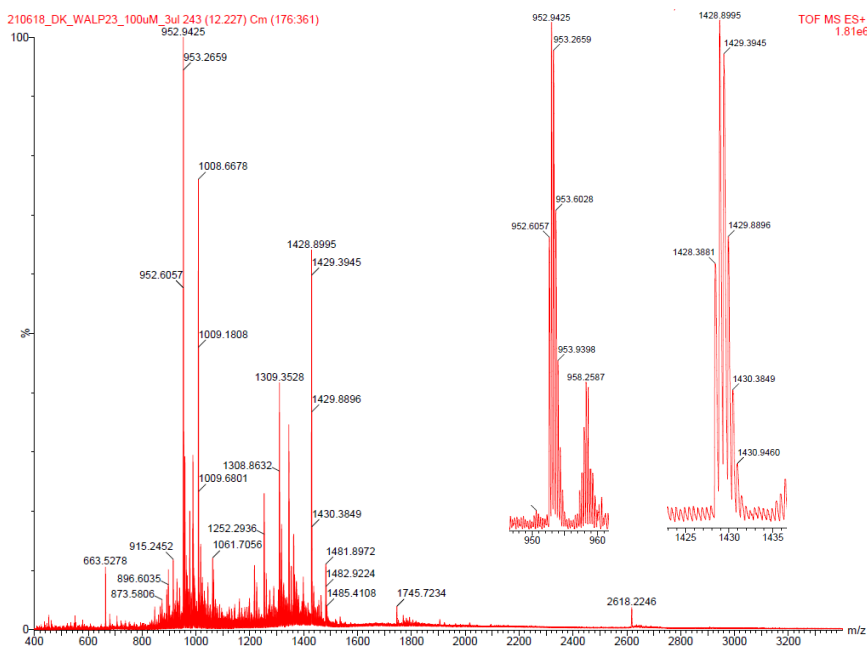


Figure B2. ESI-TOF spectrum of WALP23-bpy₂.

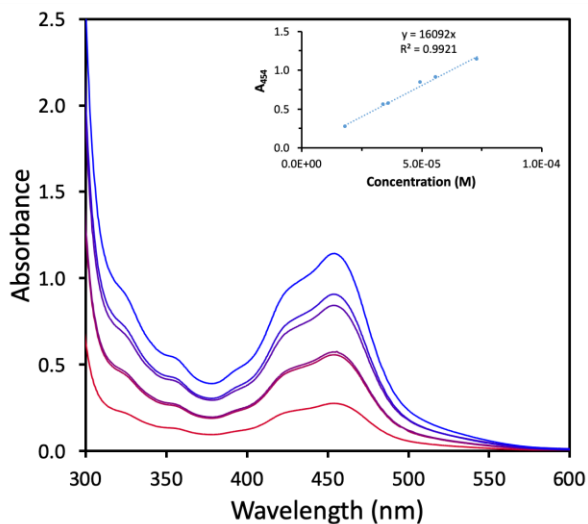


Figure B5. UV-Vis spectra of six samples of **WALP23-Ru₂** with different concentrations, measured in 3 mL MeOH in a cuvette ($l = 1$ cm) at 298 K. Inset: determination of the molar absorption coefficient of **WALP23-Ru₂**; $\epsilon = 1.61 \times 10^4 \text{ M}^{-1} \text{ cm}^{-1}$ at $\lambda = 454$ nm. For $[\text{Ru}(\text{bpy})_3\text{Cl}_2]$, $\epsilon = 1.46 \times 10^4 \text{ M}^{-1} \text{ cm}^{-1}$ at $\lambda = 453$ nm in MeOH.¹²

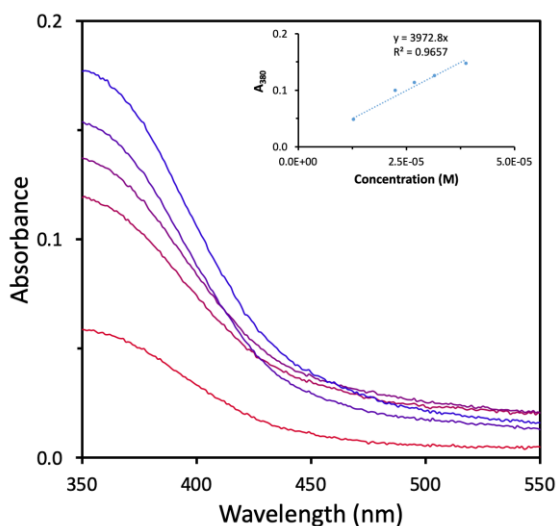


Figure B6. UV-Vis spectra of five samples of **WALP23-Re₂** at different concentrations, measured in 3 mL CHCl_3 in a cuvette ($l = 1$ cm) at 298 K. Inset: determination of the molar absorption coefficient of **WALP23-Re₂**; $\epsilon = 3.97 \times 10^3 \text{ M}^{-1} \text{ cm}^{-1}$ at $\lambda = 380$ nm. For $[\text{Re}(\text{dmb})(\text{CO})_3\text{Cl}]$ ($\text{dmb} = 4,4'$ -dimethyl-2,2'-bipyridine), $\epsilon = 3.5 \times 10^3 \text{ M}^{-1} \text{ cm}^{-1}$ at $\lambda = 383$ nm in CHCl_3 .¹³

B. 4. Molecular Dynamics

Computational methods: All MD simulations were performed using Gromacs 2018¹⁴ with periodic boundary conditions applied along all Cartesian dimensions. Both metal peptide complexes were treated with the AMBER99SB force field.¹⁵ We adopted two different methods to incorporate the metal complex residue. The Ru-complex residue was optimised using DFT calculations (B3LYP/def2-TZVP level), and the atomic point-charge parameters were obtained according to the charge model 5 (CM5).¹⁶ Following a bonded model approach, six Ru–N bonds were added to keep about 0.21 nm coordination distance between Ru and N. The Lennard-Jones non-bonded parameters of Ru were taken from Brandt’s work.¹⁷ The Re-complex residue was parameterised using the MCPB.py tool¹⁸ with B3LYP/6-31G(d)-LanL2DZ level DFT calculations. All the DFT calculations were performed using the Gaussian16 software.¹⁹ The force field parameters of DPPC were obtained from Lyubartsev’s work,²⁰ which are compatible with the Amber force fields. For water molecules, the TIP3P model was used.²¹

For each system, we sequentially performed energy minimisation, NVT and NPT relaxation simulation, and NPT production simulation (100 ns anisotropic pressure coupling and another 100 ns semi-isotropic pressure coupling). The target temperature and pressure are set to 300 K and 1 Bar. The velocity-rescale thermostat was used with a coupling constant of 0.1 ps.²² Anisotropic pressure coupling was applied using the Berendsen scheme with a coupling constant of 1.0 ps.²³ In semi-isotropic pressure coupling simulations, a Parrinello-Rahman barostat with a coupling constant of 2.0 ps was also used.^{24,25} Bond lengths were constrained using the LINCS algorithm and simulations were run with a 2.0 fs time step. The van der Waals interactions were calculated using a cut-off of 1.0 nm, with the potential energy shifted to be zero at the cut-off. The electrostatic interactions were calculated using the PME method.²⁶

Spontaneous aggregation simulation. We performed spontaneous aggregation simulations on two systems: 1 molecule of **WALP23-Ru₂** or 1

molecule of **WALP23-Re₂** and 128 DPPC lipid molecules for the membrane. Both systems were solvated by water molecules in a cubic box (about 7.0 nm edge length) and the overall charge of the system containing **WALP23-Ru₂** was neutralised by the addition of 4 Cl⁻ ions.

Our simulation protocol was adapted from previous research.²⁷ After energy minimisation, 10 ps NVT and 40 ps NPT (isotropic pressure control) simulations were conducted with position constraints on the heavy atoms of the metalloprotein. A consequential 100 ns production NPT simulation allowed the system to evolve freely under anisotropic pressure coupling. At the end, an extra 100 ns NPT simulation using semi-isotropic pressure coupling was performed to further equilibrate the formed membrane. As the semi-isotropic pressure coupling in Gromacs is suitable for membranes that align with their normal vectors along the z-axis, the membrane formed from the anisotropic simulation had to be oriented accordingly before the last 100 ns NPT simulation.

To guarantee the randomness, in each simulation instance the lipid molecules were inserted into the box via the *gmx insert-molecules* command, using a unique seed. We note that sometimes the anisotropic pressure coupling led to “unsuccessful” simulations, in which the simulation box became over-stretched, and we discarded such results. We obtained a total of 13 successful trajectories of **WALP23-Ru₂** and 16 of **WALP23-Re₂** showing the formation of a proper lipid membrane, and we visually checked the trans-membrane status of the metalloprotein in addition to the automated analysis. The total simulation time for all proper cases was 5.8 μs.

The immersion ratio (φ , see main text) and the angle between the metal-metal vector and the normal vector of the lipid membrane (ϑ , see main text) were derived from the final orientation of the molecules in the system at the last frame of each MD simulation trajectory. To calculate φ , we used the following equation:

$$\varphi = \frac{N_{DPPC}}{N_{total}} \quad \text{Equation B1}$$

In Equation B1, N_{DPPC} are the amount of non-hydrogen atoms from DPPC molecules and N_{total} are the total amount of non-hydrogen atoms from DPPC, water, and/or Cl^- ions that surround the metal residue of the metallopeptide within a cut-off range of 0.35 nm. To calculate the angle between the metal-metal vector and the normal vector of the lipid membrane (ϑ , see main text), we used the following equation:

$$\cos(\theta) = \frac{\vec{V}_{memb} \vec{V}_{M-M}}{|\vec{V}_{memb}| |\vec{V}_{M-M}|} \quad \text{Equation B2}$$

In Equation B2, \vec{V}_{memb} is the normal vector of the lipid membrane and \vec{V}_{M-M} is the vector joining the two metals centers (Ru-Ru or Re-Re) of the metallopeptides.

Mass density profiles. The mass density of grouped atoms was determined along the z-axis, which in all simulations is defined as the normal vector of the lipid membrane (\vec{V}_{memb}). The atom groups are defined as shown in Figure B7. The densities are centered on the last carbon beads of both tails of the DPPC lipids, since on average this can be defined as the center of the bilayer. The density plots were obtained with Gromacs, using the *gmx density* command, from the last 20 ns of the simulations that formed bilayers, and they were averaged over 1000 frames (Figure B8 and Figure B9).

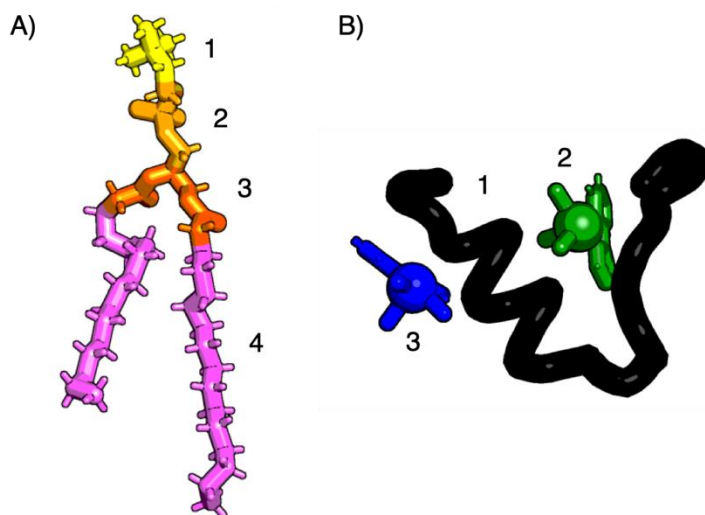


Figure B7. The grouping used for the mass density profiles. (A) A schematic representation of the DPPC lipid. The groups are choline (1), phosphor oxygen (2), glycerol groups (3), and the hydrophobic tails (4). (B) A schematic representation of the WALP23-peptide with the metal atoms including its ligands (three bipyridines in the case of **WALP23-Ru₂**, and one bipyridine, three CO, and one Cl in the case of **WALP23-Re₂**). Here the groups are defined as WALP23-peptide (1), one metal atom including its ligands (2), and the other metal atom including its ligands (3).

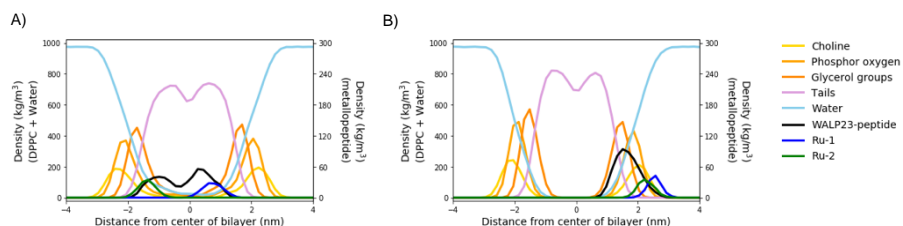


Figure B8. Representative mass density profiles of DPPC, water, and the metalloprotein **WALP23-Ru₂**. In the transmembrane configuration (A) **WALP23-Ru₂** is located within the hydrophobic region of the lipid bilayer (tails). In the parallel configuration (B) **WALP23-Ru₂** is located on one side of the lipid bilayer at the lipid-water interface (choline, phosphor oxygen, and glycerol groups).

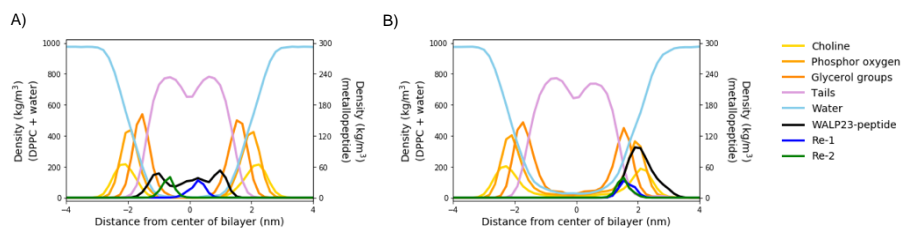


Figure B9. Representative mass density profiles of DPPC, water, and the metallopeptide **WALP23-Re₂**. In the transmembrane configuration (A) **WALP23-Re₂** is located within the hydrophobic region of the lipid bilayer (tails). In the parallel configuration (B) **WALP23-Re₂** is located on one side of the lipid bilayer at the lipid-water interface (choline, phosphor oxygen, and glycerol groups).

The metal-metal distance. The distances between the metal atoms (Re or Ru) were calculated with Gromacs using the *gmx distance* command. For each transmembrane peptide the distance was averaged over the last 20 ns of the simulation with 1000 frames, resulting in the distances given in Table B2 and an average distance of 1.999 ± 0.300 for Ru-Ru and 2.090 ± 0.584 for Re-Re.

Table B2. Distances between both metal atoms in all transmembrane configurations of the WALP23-peptide MD model in a DPPC membrane.

Metallopeptide	Distance (nm)	Standard dev (nm)
WALP23-Ru ₂	2.299	0.159
WALP23-Ru ₂	1.698	0.204
WALP23-Re ₂	1.026	0.055
WALP23-Re ₂	2.710	0.101
WALP23-Re ₂	2.501	0.077
WALP23-Re ₂	2.211	0.084
WALP23-Re ₂	2.002	0.061
WALP23-Ru ₂ average	1.999	0.300
WALP23-Re ₂ average	2.090	0.584

B. 5. Liposome characterisation

Preparation of liposomes for characterisation: DPPC lipids in chloroform, NaDSPE-PEG2K in chloroform, and one of the (metallo)peptides in chloroform (**WALP23-bpy₂** and **WALP23-Re₂**) or methanol (**WALP23-Ru₂**) were added to a pressure resistant tube. The organic solvents were evaporated under reduced pressure and the resulting film was dried for at least 1 h in *vacuo* to remove residual solvent. The film was then hydrated with NH₄OAc buffer (1 mL, pH = 7.0, p = 0.42 Osm), followed by 10 freeze-thaw cycles between liquid N₂ and a 50 °C water bath. Subsequently, the vesicles were extruded 11× with an Avanti Polar Lipids mini-extruder through a 0.2 µm polycarbonate membrane at 55 °C. Assuming no losses during preparation, the resulting liposome stock solutions consisted of DPPC:NaDSPE-PEG2K:(metallo)peptide in the ratio 100:1:1 with bulk concentrations of 12.5 mM DPPC, 0.125 mM NaDSPE-PEG2K, and 0.125 mM (metallo)peptide. Liposome samples were stored at RT and used within two days. The liposome solutions were analysed the same day with DLS and the next day with UV-Vis, emission, and time-resolved fluorescence spectroscopy. For the spectroscopy experiments, the liposome stock solutions were diluted 5× with NH₄OAc.

Preparation of giant vesicles for confocal microscopy: DPPC lipids in chloroform and **WALP23-Ru₂** in methanol were added to a pressure resistant tube. The organic solvents were evaporated under reduced pressure and the resulting film was dried for at least 1 h in *vacuo* to remove residual solvent. The film was then hydrated with NaH₂PO₄ buffer (1 mL, 0.1 M, pH = 7.8, p = 0.43 Osm), followed by 3 freeze-thaw cycles between liquid N₂ and a 50 °C water bath. Assuming no losses during preparation, the resulting giant vesicles solution consist of DPPC:**WALP23-Ru₂** in the ratio 100:0.4 with bulk concentrations of 25 mM DPPC and 0.1 mM **WALP23-Ru₂**. For confocal microscopy, 150 µL of NaH₂PO₄ buffer (0.1 M, pH = 7.8, p = 0.43 Osm) and 50 µL of giant vesicles solution was added to one of the wells of a chambered coverslip with 8 wells (µ-slide 8 well glass bottom from Ibidi). Confocal microscopy images were taken on a Nikon Eclipse Ti microscope with 20×

objective (0.75 NA, 1.00 WD) and confocal imaging with 488 nm laser and 640 – 680 nm detection wavelength. Images were processed with the Fiji version of Image J2.

Table B3. Z_{ave} and PDI (polydispersity index) of liposomes prepared from DPPC, NaDSPE-PEG2K, and (metallo)peptide in a ratio of 100:1:1, which were used for characterisation studies.

Sample ^[a]	Z_{ave} (nm) ^[b]	PDI ^[b]
WALP23-bpy ₂	137.0	0.089
WALP23-Ru ₂	135.6	0.077
WALP23-Re ₂	123.0	0.091

^[a] Experimental conditions: [DPPC] = 12.5 mM, [NaDSPE-PEG2K] = 0.125 mM, [WALP23-bpy₂, WALP23-Ru₂ or WALP23-Re₂] = 0.125 mM. ^[b] The liposome size is considered to be uniformly distributed when PDI < 0.2.

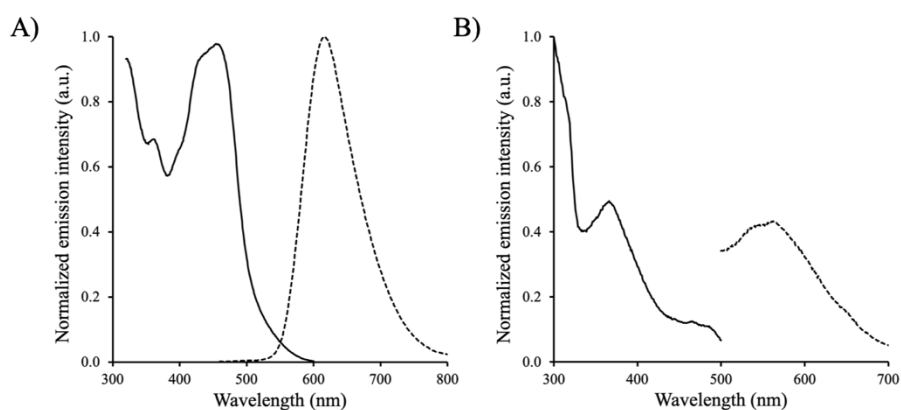


Figure B10. The excitation (solid line, λ_{em} = 620 nm for Ru and 550 nm for Re) and emission spectrum (dashed line, λ_{exc} = 450 nm for Ru and 380 nm for Re) of (A) **WALP23-Ru₂** and (B) **WALP23-Re₂** embedded within DPPC liposomes. Experimental conditions: [DPPC] = 2.5 mM, [NaDSPE-PEG2K] = 25 μ M, [WALP23-Ru₂ or WALP23-Re₂] = 25 μ M in 0.1 M NH₄OAc (pH = 7.0) under an Ar atmosphere. Excitation spectra were measured instead of absorption spectra, because lipid scattering obscured UV-Vis absorption bands.

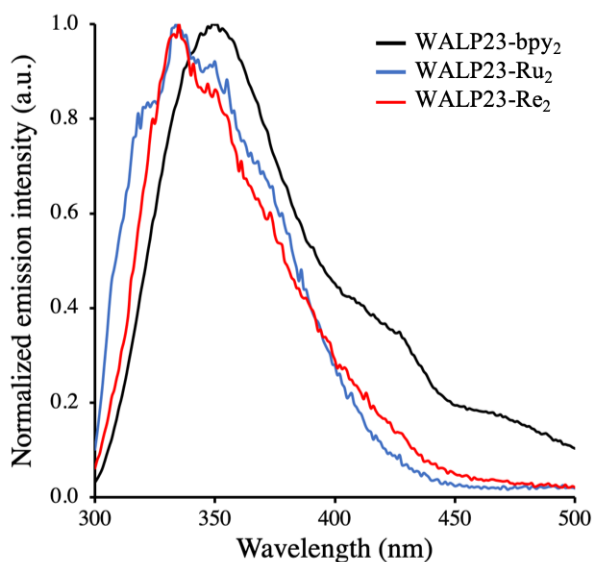


Figure B11. The emission spectrum ($\lambda_{\text{exc}} = 280$ nm) of the tryptophan (W) amino acids of **WALP23-bpy₂**, **WALP23-Ru₂** **WALP23-Re₂** embedded within DPPC liposomes. Experimental conditions: [DPPC] = 2.5 mM, [NaDSPE-PEG2K] = 25 μ M, [**WALP23-bpy₂**, **WALP23-Ru₂** or **WALP23-Re₂**] = 25 μ M in 0.1 M NH_4OAc (pH = 7.0) under an air atmosphere.

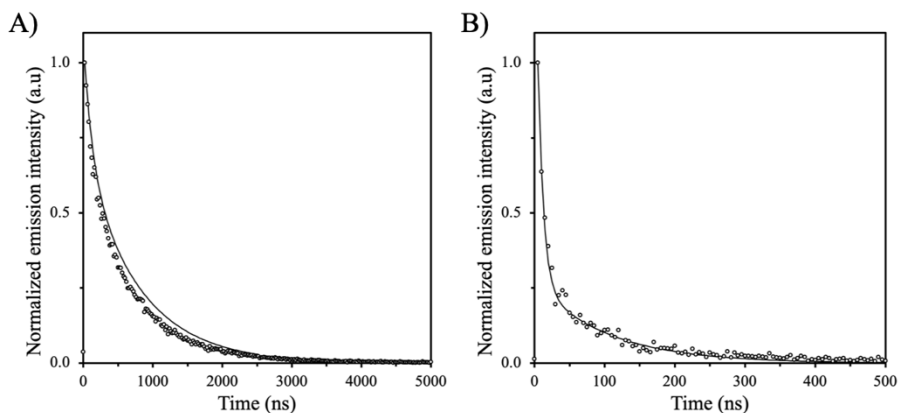


Figure B12. Normalised photoluminescence decays of (A) **WALP23-Ru₂** ($\lambda_{\text{exc}} = 450$ nm, 3.5 mJ/pulse, $\lambda_{\text{em}} = 616$ nm) or (B) **WALP23-Re₂** ($\lambda_{\text{exc}} = 380$ nm, 3.5 mJ/pulse, $\lambda_{\text{em}} = 562$ nm) embedded within DPPC liposomes. The data (circles) were fitted by a biexponential decay (solid line) using Glotaran; yielding for **WALP23-Ru₂** $\tau_1 = 123$ ns and $\tau_2 = 787$ ns and for **WALP23-Re₂** $\tau_1 = 8$ ns and $\tau_2 = 103$ ns. Experimental conditions: [DPPC] = 2.5 mM, [NaDSPE-PEG2K] = 25 μ M, [**WALP23-Ru₂** or **WALP23-Re₂**] = 25 μ M in 0.1 M NH_4OAc (pH = 7.0) under an Ar atmosphere.

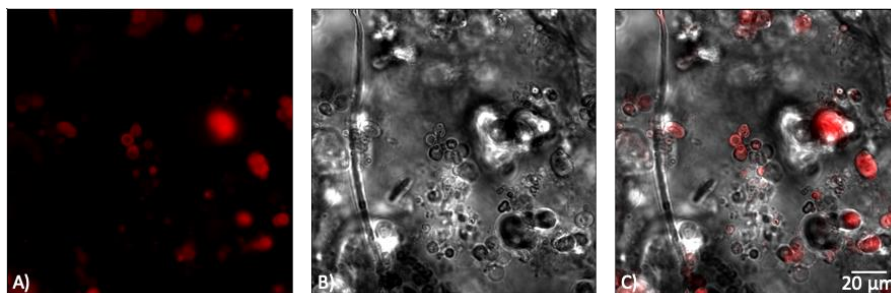


Figure B13. Confocal microscopy of DPPC giant vesicles containing 0.4% **WALP23-Ru₂** in NaH₂PO₄ buffer (0.1 M, pH = 7.8, p = 0.43 Osm). Figure B13A is the fluorescence image, Figure B13B is the transmission image, and Figure B13C is the overlay. Images were taken with a Nikon Ti2 microscope at 80x total zoom, 488 nm excitation, and 640 – 680 nm emission.

B. 6. Photoirradiation experiments

Preparation of asymmetric liposomes for irradiation experiments: DPPC lipids in chloroform, NaDSPE-PEG2K in chloroform, and one of the (metallo)peptides or one of the mononuclear metal complexes in either methanol (**WALP23-Ru₂** and **RuC₁₅**) or chloroform (**WALP23-bpy₂**, **WALP23-Re₂**, or **ReC₁₅**) were added to a pressure-resistant tube. The organic solvents were evaporated under reduced pressure and the resulting film was dried for at least 1 h in *vacuo* to remove residual solvent. The film was then hydrated with a Na₃HEDTA buffer (2 mL, 0.125 M, pH = 8.2, p = 0.42 Osm), followed by 10 freeze-thaw cycles between liquid N₂ and a 50 °C water bath. Subsequently, the vesicles were extruded 11× with an Avanti Polar Lipids mini-extruder through a 0.2 μm polycarbonate membrane at 55 °C. After extrusion, the liposomes were purified over a size-exclusion column (GE Healthcare Illustra™ NAP™-25 size exclusion chromatography cartridges) using an isotonic NH₄OAc buffer (pH = 7.0, p = 0.42 Osm). The liposome fraction was then separated from the Na₃HEDTA fraction (Na₃HEDTA eluted from 3.6 mL and further, as visualised by complexometry as described elsewhere²⁸). Assuming no losses during preparation, the resulting liposome stock solutions consisted of DPPC:NaDSPE-PEG2K:(metallo)peptide or metal complex in the ratio 100:1:1 with bulk concentrations of 12.5 mM DPPC, 0.125 mM NaDSPE-PEG2K, and 0.125 mM (metallo)peptide or metal

complex. Liposome samples were stored at RT and used the same day. For irradiation experiments, the liposome stock solutions were diluted 5× (see below). DLS was performed on the liposome stock solutions as well as on the diluted liposome samples after irradiation and the irradiation experiments were followed by UV-Vis spectroscopy.

Photoreactions studied by UV-Vis: A cuvette (3 mL) was filled with a mixture of the asymmetric liposome solution (2.5 mM DPPC, 25 μ M NaDSPE-PEG2K, and 25 μ M (metallo)peptide or metal complex), a solution of WST1⁻ (0.33 mM) in NH₄OAc buffer (pH = 7.0, ρ = 0.42 Osm), and/or a solution of ZnSO₄ or Zn(OAc)₂ (5 mM) in NH₄OAc buffer (pH = 7.0, ρ = 0.42 Osm). When mixing these solutions, it was critical to make sure all solutions were at the same osmolality of 0.42 Osm, to avoid osmotic stress on the membrane and the associated leakage of Na₃HEDTA encapsulated inside the liposomes. Each sample was deaerated by gently bubbling N₂ through the solution for 15 min under constant stirring. A blue LED (λ_{irr} = 410 or 385 nm for Re and λ_{irr} = 450 nm for Ru obtained from OSRAM Opto Semiconductors) with water cooling was then fitted to the top of the cuvette. The time evolution of the absorbance of the solution was recorded horizontally (optical pathway 1 cm) on a Varian Cary60 spectrophotometer at 25 °C under constant stirring, first in the dark for 30 min, then under light irradiation for 2.5 h (vertical beam, optical pathway 3 cm). The cuvette contained a small hole in the top, which was either left open to air or used to purge the system under N₂ depending on the experimental conditions.

Actinometry: The photon fluxes (in mol/s) of the different LEDs (λ = 385, 410, and 450 nm) used in this work were determined by ferrioxalate actinometry using a standard protocol.^{2,29,30} In short, the cuvette used for the photoreactions was charged with a solution of freshly prepared K₃[Fe(C₂O₄)₃]·3H₂O (3 mL, 150 mM in 0.05 M H₂SO₄). The reaction mixture was stirred for 2 min, followed by irradiation (vertical beam, optical pathway 3 cm) with one of the LEDs for a given time (Figure B14). Afterwards, a fraction of the irradiated solution (1 mL) was transferred to a vial containing a solution of 1,10-phenanthroline (2 mL, 5.55 mM in water), a buffer solution (0.5 mL from a solution prepared from 36.03 g glacial acetic acid, 25.57 g

Na₂SO₄ in 100 mL water and 240 mL 1 M NaOH), and water (1.5 mL). The resulting [Fe(phen)₃]²⁺ (phen = 1,10-phenanthroline) solution (3 mL) was transferred to a cuvette and its absorption spectrum measured by UV-Vis spectroscopy. The absorbance at 510 nm was used to calculate (using the molar absorption coefficient $\epsilon = 11110 \text{ M}^{-1} \text{ cm}^{-1}$ in water for [Fe(phen)₃]²⁺²⁹) how much Fe²⁺ was formed during irradiation for a given time ($\frac{dn_{\text{Fe}^{2+}}}{dt}$), which is the slope in Figure B14. The following equation was then used to calculate the photon flux (Φ_0) of the respective LED:

$$\frac{dn_{\text{Fe}^{2+}}}{dt} = \Phi_0 (1 - 10^{-A_{\text{ref}}}) \varphi_{\text{ref}} \quad \text{Equation B3}$$

In Equations B3, $(1 - 10^{-A_{\text{ref}}})$ is the probability of photon absorption by the solution and φ_{ref} is the known quantum yield of the ferrioxalate actinometer for the generation of Fe²⁺ at the irradiated wavelength.^{2,30} In this particular system, A_{ref} equals $A'_{\text{ref}} \times 3$ (as the vertical beam has an optical pathway of 3 cm), where A'_{ref} is the absorption of the non-irradiated solution of K₃[Fe(C₂O₄)₃]·3H₂O (3 mL, 150 mM in 0.05 M H₂SO₄) at the irradiation wavelength of the LED, measured with a 1 cm pathlength cuvette.³¹ Using Equation B3, Φ_0 was 13.1 nmol/s for the 385 nm LED (P = 7.3 mW), 30.4 nmol/s for the 410 nm LED (P = 8.9 mW), and 39.1 nmol/s for the 450 nm LED (P = 15.8 mW).

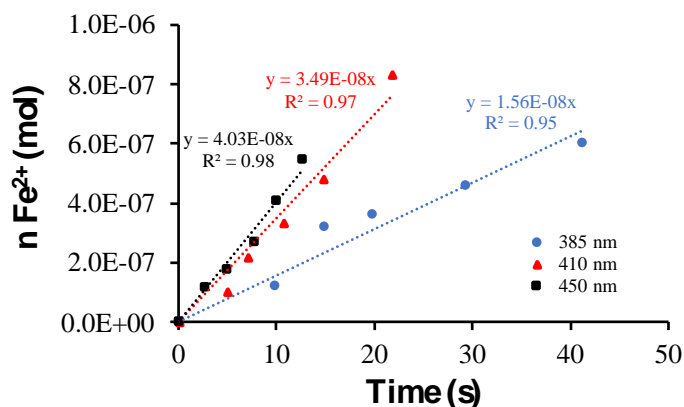


Figure B14. Ferrioxalate actinometry was performed to determine Φ_0 of the used LEDs within the photoirradiation setup.

Transmembrane photoelectron transfer quantum yield determination: The quantum yield (QY) of the photoinduced electron transfer from EDTA to WST1⁻ through the DPPC membrane functionalised with 1 mol% of a light-activatable metallopeptide was obtained using the following equation:

$$QY = \frac{\# \text{ photoinduced electron transfer}}{\# \text{ photons absorbed by photoactive molecule}} = \frac{k_e n_e}{\Phi_0 (1 - 10^{-A_{\text{ref}}})} \quad \text{Equation B4}$$

In Equation B4, k_e is the rate of electron transfer in s^{-1} and n_e is the number of electrons transferred from EDTA to WST1⁻ in nmol, Φ_0 the photon flux of the LED in nmol/s (see section on actinometry), and $(1 - 10^{-A_{\text{ref}}})$ equals the probability of photon absorption by the liposome solution at the irradiation wavelength. The difference in absorption at 438 nm (the molar absorption coefficient $\epsilon = 37000 \text{ M}^{-1} \text{ cm}^{-1}$ at 438 nm for Fz1²⁻ in water³²) after a chosen irradiation time ($t = 1 \text{ h}$) was used to calculate the amount of formazan produced, hence $k_e \times n_e$, taking into account that two electrons must be transferred for the formation of one Fz1²⁻ molecule. In this particular system, A_{ref} was not measured experimentally but calculated using the molar absorption coefficients of **WALP23-Ru₂** ($\epsilon = 1.59 \times 10^4 \text{ M}^{-1} \text{ cm}^{-1}$ at $\lambda = 450 \text{ nm}$ in MeOH) and **WALP23-Re₂** ($\epsilon = 3.70 \times 10^3 \text{ M}^{-1} \text{ cm}^{-1}$ at $\lambda = 385 \text{ nm}$ in CHCl₃), a pathlength of 3 cm, and the bulk concentration (25 μM) of the metallopeptide, because the absorption measured experimentally has a significant lipid scattering deviation from the Beer-Lambert law generated by the liposomes, in particular in the near-UV domain.¹ Using these values, the QY for electron transfer was determined to be 1.5×10^{-4} for **WALP23-Ru₂** and 2.7×10^{-4} for **WALP23-Re₂** after 1 h of irradiation.

Table B4. Z_{ave} and PDI of liposomes prepared from DPPC, NaDSPE-PEG2K, and (metallo)peptide or metal complex in a ratio of 100:1:1, which were used for the irradiation experiments.

Sample ^[a]	Z_{ave} (nm) ^[b]	PDI ^[b]
WALP23-Ru ₂ stock before irradiation ^[c]	135.6 ± 0.8	0.066 ± 0.015
WALP23-Ru ₂ after irradiation (no Zn) ^[c]	134.3 ± 4.9	0.107 ± 0.038
WALP23-Ru ₂ after irradiation (Zn(OAc) ₂) ^[c]	137.3 ± 3.3	0.116 ± 0.036
WALP23-Ru ₂ after irradiation (ZnSO ₄)	138.0	0.123
WALP23-Re ₂ stock before irradiation ^[c]	123.9 ± 0.5	0.132 ± 0.005
WALP23-Re ₂ after irradiation (no Zn) ^[c]	120.0 ± 1.0	0.126 ± 0.012
WALP23-Re ₂ after irradiation (Zn(OAc) ₂) ^[c]	121.5 ± 1.0	0.147 ± 0.004
WALP23-bpy ₂ stock before irradiation	162.7	0.116
RuC ₁₅ stock before irradiation	148.1	0.123
RuC ₁₅ after irradiation (no Zn)	145.3	0.114
RuC ₁₅ after irradiation (ZnSO ₄)	146.9	0.119
ReC ₁₅ stock before irradiation	117.0	0.125
ReC ₁₅ after irradiation (no Zn)	114.8	0.103
ReC ₁₅ after irradiation (Zn(OAc) ₂)	116.3	0.116

^[a] Experimental conditions for liposome stock solutions: [DPPC] = 12.5 mM, [NaDSPE-PEG2K] = 125 μM, [WALP23-Ru₂ or WALP23-Re₂] = 125 μM, [HEDTA³⁻] = 0.125 M (before SEC column) in 0.1 M NH₄OAc (pH = 7.0, p = 0.42 Osm). Experimental condition for diluted liposomes solutions after irradiation: [DPPC] = 2.5 mM, [NaDSPE-PEG2K] = 25 μM, [WALP23-Ru₂ or WALP23-Re₂] = 25 μM, [HEDTA³⁻] = 0.125 M (before SEC column), [WST1⁻] = 0.33 mM, and with or without [Zn(OAc)₂ or ZnSO₄] = 5 mM in 0.1 M NH₄OAc (pH = 7.0, p = 0.42 Osm). ^[b] The liposome size is considered to be uniformly distributed when PDI < 0.2. ^[c] Samples were prepared in duplicate (to perform the photoreaction experiments under air and under N₂). The errors correspond to the average deviation from the mean.

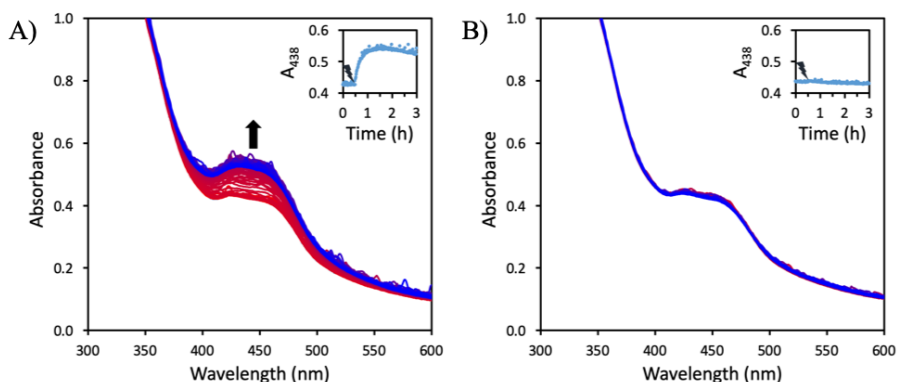


Figure B15. The change in absorbance due to the conversion of $WST1^-$ versus irradiation time for liposomes prepared from DPPC:NaDSPE-PEG2K:WALP23-Ru₂ (100:1:1) in absence (A) or in presence (B) of added Zn(OAc)₂ (5 mM). Experimental conditions: [DPPC] = 2.5 mM, [NaDSPE-PEG2K] = 25 μM, [WALP23-Ru₂] = 25 μM, [HEDTA³⁻] = 0.125 M (before SEC column), [WST1⁻] = 0.33 mM, [Zn(OAc)₂] = 0 or 5 mM in 0.1 M NH₄OAc (pH = 7.0), under an air atmosphere, and blue light irradiation (λ_{irr} = 450 nm, P = 15.8 mW, Φ_0 = 39.1 nmol/s).

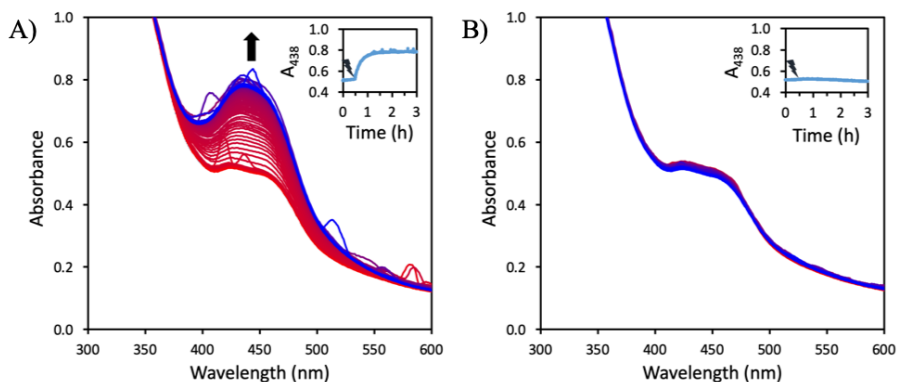


Figure B16. The change in absorbance due to the conversion of $WST1^-$ versus irradiation time for liposomes prepared from DPPC:NaDSPE-PEG2K:WALP23-Ru₂ (100:1:1) in absence (A) or in presence (B) of added Zn(OAc)₂ (5 mM). Experimental conditions: [DPPC] = 2.5 mM, [NaDSPE-PEG2K] = 25 μM, [WALP23-Ru₂] = 25 μM, [HEDTA³⁻] = 0.125 M (before SEC column), [WST1⁻] = 0.33 mM, [Zn(OAc)₂] = 0 or 5 mM in 0.1 M NH₄OAc (pH = 7.0), under a N₂ atmosphere, and blue light irradiation (λ_{irr} = 450 nm, P = 15.8 mW, Φ_0 = 39.1 nmol/s).

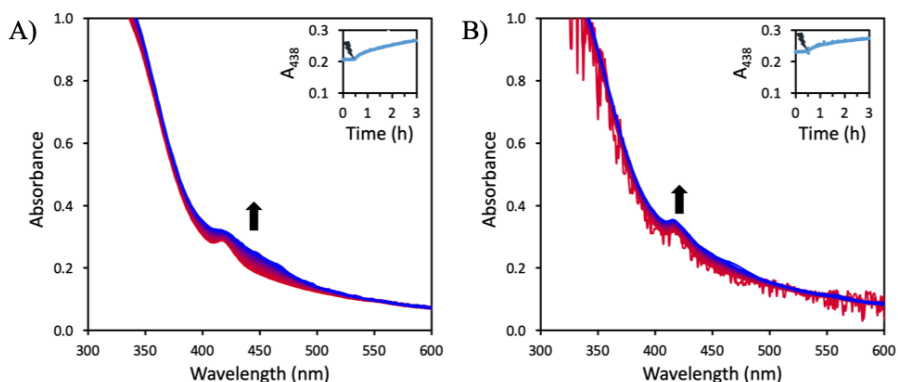


Figure B17. The change in absorbance due to the conversion of $WST1^-$ versus irradiation time for liposomes prepared from DPPC:NaDSPE-PEG2K:WALP23-Re₂ (100:1:1) in absence (A) or in presence (B) of added $Zn(OAc)_2$ (5 mM). Experimental conditions: [DPPC] = 2.5 mM, [NaDSPE-PEG2K] = 25 μ M, [WALP23-Re₂] = 25 μ M, [HEDTA³⁻] = 0.125 M (before SEC column), [$WST1^-$] = 0.33 mM, [$Zn(OAc)_2$] = 0 or 5 mM in 0.1 M NH_4OAc (pH = 7.0), under an air atmosphere, and blue light irradiation (λ_{irr} = 385 nm, P = 7.3 mW, Φ_0 = 13.1 nmol/s).

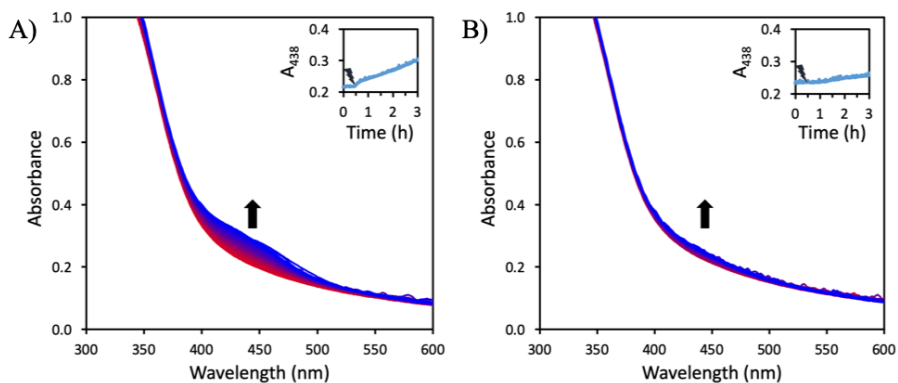


Figure B18. The change in absorbance due to the conversion of $WST1^-$ versus irradiation time for liposomes prepared from DPPC:NaDSPE-PEG2K:WALP23-Re₂ (100:1:1) in absence (A) or in presence (B) of added $Zn(OAc)_2$ (5 mM). Experimental conditions: [DPPC] = 2.5 mM, [NaDSPE-PEG2K] = 25 μ M, [WALP23-Re₂] = 25 μ M, [HEDTA³⁻] = 0.125 M (before SEC column), [$WST1^-$] = 0.33 mM, [$Zn(OAc)_2$] = 0 or 5 mM in 0.1 M NH_4OAc (pH = 7.0), under a N_2 atmosphere, and blue light irradiation (λ_{irr} = 410 nm, P = 8.9 mW, Φ_0 = 30.4 nmol/s).

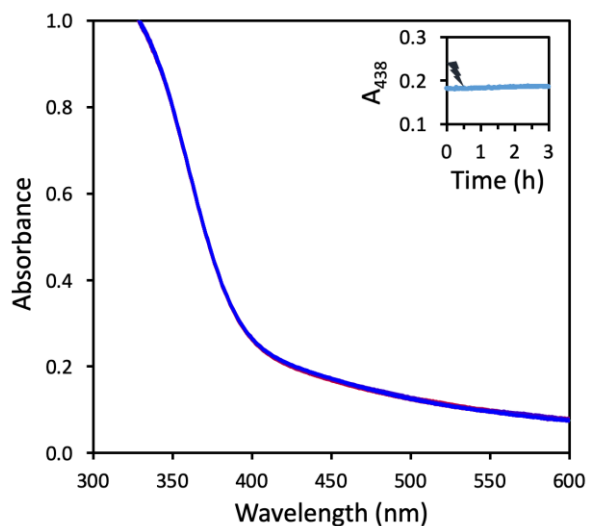


Figure B19. The change in absorbance due to the conversion of $WST1^-$ versus irradiation time for liposomes prepared from DPPC:NaDSPE-PEG2K:WALP23-bpy₂ (100:1:1) in absence of added $Zn(OAc)_2$. Experimental conditions: [DPPC] = 2.5 mM, [NaDSPE-PEG2K] = 25 μ M, [WALP23-bpy₂] = 25 μ M, [HEDTA³⁻] = 0.125 M (before SEC column), [$WST1^-$] = 0.33 mM in 0.1 M NH_4OAc (pH = 7.0), under a N_2 atmosphere, and blue light irradiation (λ_{irr} = 410 nm, P = 8.9 mW, Φ_0 = 30.4 nmol/s).

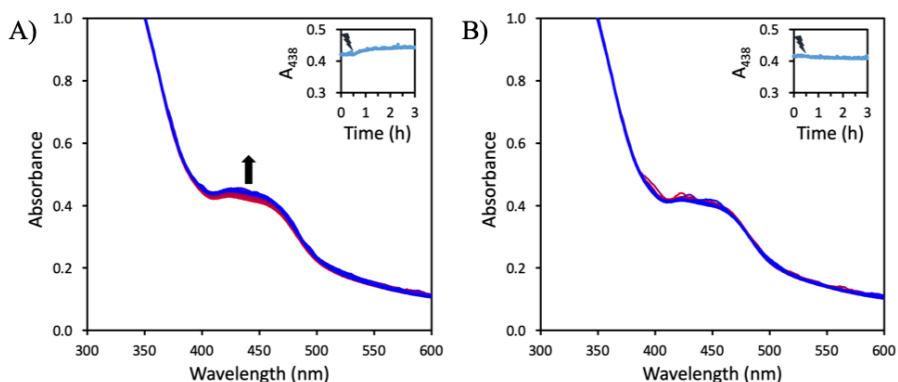


Figure B20. The change in absorbance due to the conversion of $WST1^-$ versus irradiation time for liposomes prepared from DPPC:NaDSPE-PEG2K:RuC₁₅ (100:1:1) in absence (A) or in presence (B) of $Zn(OAc)_2$ (5 mM). Experimental conditions: [DPPC] = 2.5 mM, [NaDSPE-PEG2K] = 25 μ M, [RuC₁₅] = 25 μ M, [HEDTA³⁻] = 0.125 M (before SEC column), [$WST1^-$] = 0.33 mM, [$ZnSO_4$] = 0 or 5 mM in 0.1 M NH_4OAc (pH = 7.0), under a N_2 atmosphere, and blue light irradiation (λ_{irr} = 450 nm, P = 15.8 mW, Φ_0 = 39.1 nmol/s).

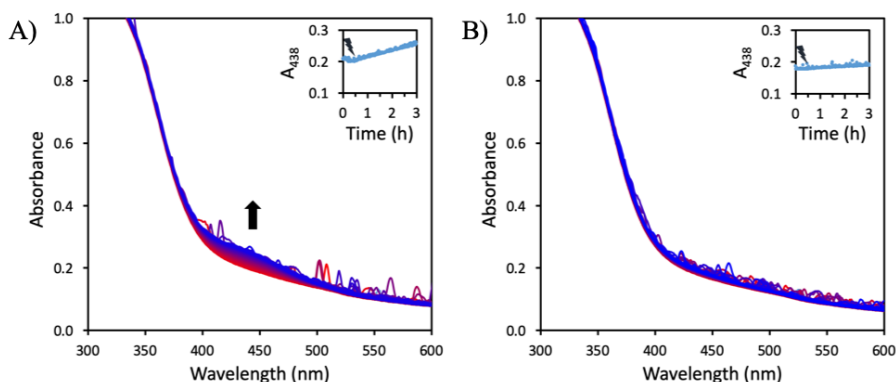


Figure B21. The change in absorbance due to the conversion of WST1⁻ versus irradiation time for liposomes prepared from DPPC:NaDSPE-PEG2K:ReC₁₅ (100:1:1) in absence (A) or in presence (B) of added Zn(OAc)₂ (5 mM). Experimental conditions: [DPPC] = 2.5 mM, [NaDSPE-PEG2K] = 25 μM, [ReC₁₅] = 25 μM, [HEDTA³⁻] = 0.125 M (before SEC column), [WST1⁻] = 0.33 mM, [Zn(OAc)₂] = 0 or 5 mM in 0.1 M NH₄OAc (pH = 7.0), under a N₂ atmosphere, and blue light irradiation ($\lambda_{\text{irr}} = 410$ nm, P = 8.9 mW, $\Phi_0 = 39.1$ nmol/s).

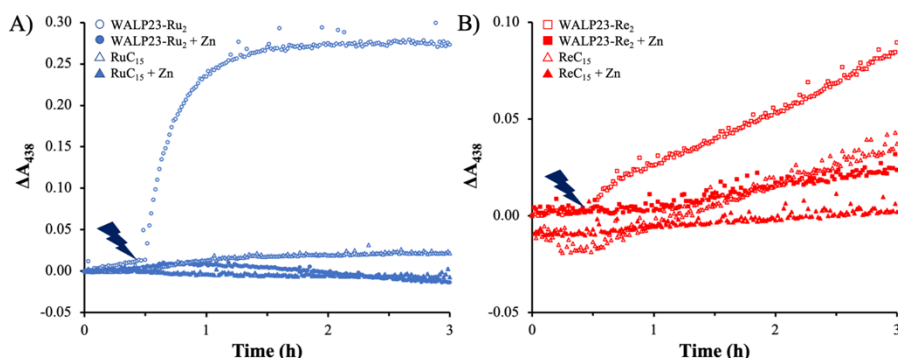
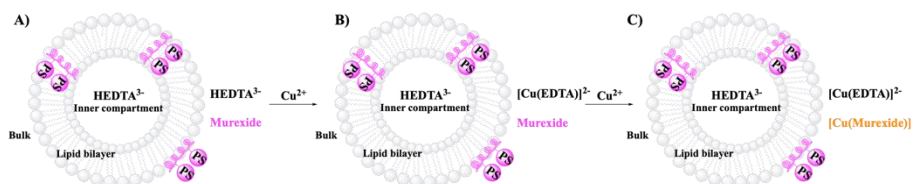


Figure B22. The formation of Fz²⁻ as monitored by a change in absorbance ($\lambda_{\text{max}} = 438$ nm) versus irradiation time for liposome systems containing WALP23-Ru₂ or RuC₁₅ (A) or WALP23-Re₂ or ReC₁₅ (B) with (open symbols) or without Zn (closed symbols). The data are based on the insets of Figures B16, B18, B20, and B21. Experimental conditions: [DPPC] = 2.5 mM, [NaDSPE-PEG2K] = 25 μM, [WALP23-Ru₂, RuC₁₅, WALP23-Re₂ or ReC₁₅] = 25 μM, [HEDTA³⁻] = 0.125 M (before SEC column), [WST1⁻] = 0.33 mM, [Zn(OAc)₂ or ZnSO₄] = 0 or 5 mM in 0.1 M NH₄OAc (pH = 7.0), under a N₂ atmosphere, and blue light irradiation ($\lambda_{\text{irr}} = 450$ nm, P = 15.8 mW, $\Phi_0 = 39.1$ nmol/s for WALP23-Ru₂ and RuC₁₅, $\lambda_{\text{irr}} = 410$ nm, P = 8.9 mW, $\Phi_0 = 30.4$ nmol/s for WALP23-Re₂ and ReC₁₅).

B. 7. Leakage studies

Protocol to determine the concentration of HEDTA³⁻ in liposome samples:

The concentration of HEDTA³⁻ (both outside the liposomes, and in the whole sample) was determined by complexometry as described earlier.²⁸ In this work, we determined the concentration of HEDTA³⁻ for three different cases: a) directly after liposome preparation; b) 3 h after liposome preparation, keeping the samples in the dark; and c) after irradiation experiments (0.5 h dark and 2.5 h light irradiation). In short, a cuvette (3 mL) was equipped with either 0.1 mL liposome stock solution (0.125 mM (metallo)peptide or metal complex) for case a and b, or 0.5 mL liposome solution (0.025 mM (metallo)peptide or metal complex) for case c. Afterwards an aqueous solution of NH₄OAc (pH = 7.0, p = 0.42 mOsm) was added to reach a total volume of 2.9 mL. Finally, a solution of murexide (9 mg of 250:1 K₂SO₄:murexide) in 0.1 mL NaOH (0.1 M) was added, resulting in bulk concentrations of 0.4167 mM DPPC, 4.167 μM NaDSPE-PEG2K, and 4.167 μM (metallo)peptide or metal complex respectively (30× dilution compared to the liposome stock solution). The murexide/liposome solution was titrated with an aqueous solution of Cu(NO₃)₂ (10 mM, 2 μL per addition), and a UV-Vis spectrum was recorded after each addition. The amount of HEDTA³⁻ present in the aqueous bulk was determined as follows; when addition of one further drop of the copper solution led to a decrease in the absorbance at 525 nm (free murexide), it meant that all the HEDTA³⁻ in the aqueous bulk was bound to Cu²⁺ and therefore that [Cu(murexide)] (λ = 468 nm) was formed (see Scheme B2). In a second step, the liposomes were destroyed by the addition of 5 μL 10% w/v% triton-X100, leading to a further increase in the absorbance at 525 nm, due to the release of HEDTA³⁻ from the inner compartment of the liposome to the bulk, leading to a competitive complexation of copper. The Cu(NO₃)₂ titration of the murexide/destroyed liposome solutions was resumed (10 mM, 2 μL per addition). When addition of one drop of the copper solution led to a second decrease in the absorbance at 525 nm, all HEDTA³⁻ (bulk + inner compartment) was bound to Cu²⁺, which provided the total amount of HEDTA³⁻ in the sample.



Scheme B2. Titration of HEDTA³⁻ in asymmetric liposome samples using murexide and Cu²⁺. **(A)** At the start of the experiment, the solution is purple ($\lambda = 525$ nm) due to the presence of unbound murexide. **(B)** Cu²⁺ will first react with HEDTA³⁻ to form [Cu(EDTA)]²⁻; the solution is still purple due to the presence of unbound murexide. **(C)** Addition of excess Cu²⁺ compared to HEDTA³⁻ leads to the reaction between Cu²⁺ and murexide. The newly formed [Cu(murexide)] is orange ($\lambda = 468$ nm), leading to a decrease of the absorption at 525 nm, which is detected.

Table B5. Concentration of HEDTA³⁻ in the bulk aqueous phase, C_{outside} , and the total amount of HEDTA³⁻ present in the liposome sample after liposome disruption following addition of triton-X100, C_{total} , as determined by murexide titration following the absorbance at 525 nm.

Sample	C_{outside} (mM) ^[a]	C_{total} (mM) ^[a]
WALP23-Ru ₂ t = 0 h	0.0 – 0.2	0.4 – 0.6
WALP23-Ru ₂ t = 3 h, dark	0.0 – 0.2	0.4 – 0.6
WALP23-Ru ₂ t = 3 h, light	0.2 – 0.4	0.4 – 0.6
WALP23-Re ₂ t = 0 h	0.0 – 0.2	1.4 – 1.6
WALP23-Re ₂ t = 3 h, dark	0.0 – 0.2	1.4 – 1.6
WALP23-Re ₂ t = 3 h, light	0.4 – 0.6	1.4 – 1.6
RuC ₁₅ before reaction ^[b]	0.4 – 0.6	2.0 – 2.2
RuC ₁₅ after reaction	0.4 – 0.6	2.0 – 2.2
ReC ₁₅ before reaction ^[b]	0.4 – 0.6	1.8 – 2.0
ReC ₁₅ after reaction	0.4 – 0.6	2.2 – 2.4
WALP23-bpy ₂ before reaction ^[b]	0.0 – 0.1	0.9 – 1.0
WALP23-bpy ₂ after reaction	n.d.	n.d.

^[a] The concentrations of HEDTA³⁻ given are the ones for the liposome stock solution; thus, the concentration of HEDTA³⁻ determined by murexide titration was multiplied by 30 to take into account the dilution factor. A range is given for the concentrations; the first number corresponds to the amount of Cu²⁺ that was added without observing a change in the absorption at 525 nm, and the last number corresponds to the amount of Cu²⁺ that was needed to induce a decrease in the absorption at 525 nm. ^[b] Determined within 3 h after liposome preparation to minimise passive leakage of HEDTA³⁻ across the lipid bilayer.

B. 8. References

- 1 D. M. Klein, S. Rodríguez-Jiménez, M. E. Hoefnagel, A. Pannwitz, A. Prabhakaran, M. A. Siegler, T. E. Keyes, E. Reisner, A. M. Brouwer and S. Bonnet, *Chem. Eur. J.*, 2021, **27**, 17203–17212.
- 2 C. G. Hatchard, C. A. Parker and E. J. Bowen, *Proc. R. Soc. Lond. Ser. Math. Phys. Sci.*, 1956, **235**, 518–536.
- 3 M. W. H. Hoorens, M. Medved', A. D. Laurent, M. Di Donato, S. Fanetti, L. Slappendel, M. Hilbers, B. L. Feringa, W. J. Buma and W. Szymanski, *Nat. Commun.*, 2019, **10**, 2390.
- 4 J. J. Snellenburg, S. Laptенок, R. Seger, K. M. Mullen and I. H. M. van Stokkum, *J. Stat. Softw.*, 2012, **49**, 1–22.
- 5 E. Krieger and G. Vriend, *Bioinformatics*, 2014, **30**, 2981–2982.
- 6 M. R. R. de Planque and J. A. Killian, *Mol. Membr. Biol.*, 2003, **20**, 271–284.
- 7 J. A. Killian, I. Salemink, M. R. R. de Planque, G. Lindblom, R. E. Koeppe and D. V. Greathouse, *Biochemistry*, 1996, **35**, 1037–1045.
- 8 K. J. Kise and B. E. Bowler, *Tetrahedron Asymmetry*, 1998, **9**, 3319–3324.
- 9 J. E. Collins, J. J. S. Lamba, J. C. Love, J. E. McAlvin, C. Ng, B. P. Peters, X. Wu and C. L. Fraser, *Inorg. Chem.*, 1999, **38**, 2020–2024.
- 10 K. J. Kise and B. E. Bowler, *Inorg. Chem.*, 2002, **41**, 379–386.
- 11 D. V. Greathouse, R. L. Goforth, T. Crawford, P. C. A. van der Wel and J. A. Killian, *J. Pept. Res.*, 2001, **57**, 519–527.
- 12 A. Juris, V. Balzani, F. Barigelletti, S. Campagna, P. Belser and A. von Zelewsky, *Coord. Chem. Rev.*, 1988, **84**, 85–277.
- 13 N. Ikuta, S. Y. Takizawa and S. Murata, *Photochem. Photobiol. Sci.*, 2014, **13**, 691–702.
- 14 M. J. Abraham, T. Murtola, R. Schulz, S. Páll, J. C. Smith, B. Hess and E. Lindahl, *SoftwareX*, 2015, **1–2**, 19–25.
- 15 E. J. Sorin and V. S. Pande, *Biophys. J.*, 2005, **88**, 2472–2493.
- 16 A. V. Marenich, S. V. Jerome, C. J. Cramer and D. G. Truhlar, *J. Chem. Theory Comput.*, 2012, **8**, 527–541.
- 17 P. Brandt, T. Norrby, B. Åkermark and P.-O. Norrby, *Inorg. Chem.*, 1998, **37**, 4120–4127.
- 18 P. Li and K. M. Merz, *J. Chem. Inf. Model.*, 2016, **56**, 599–604.
- 19 M. J. Frisch, G. W. Trucks, H. B. Schlegel, G. E. Scuseria, M. A. Robb, J. R. Cheeseman, G. Scalmani, V. Barone, G. A. Petersson, H. Nakatsuji, X. Li, M. Caricato, A. V. Marenich, J. Bloino, B. G. Janesko, R. Gomperts, B. Mennucci, H. P. Hratchian, J. V. Ortiz, A. F. Izmaylov, J. L. Sonnenberg, D. Williams-Young, F. Ding, F. Lipparini, F. Egidi, J. Goings, B. Peng, A. Petrone, T. Henderson, D. Ranasinghe, V. G. Zakrzewski, J. Gao, N. Rega, G. Zheng, W.

- Liang, M. Hada, M. Ehara, K. Toyota, R. Fukuda, J. Hasegawa, M. Ishida, T. Nakajima, Y. Honda, O. Kitao, H. Nakai, T. Vreven, K. Throssell, J. A. Montgomery Jr., J. E. Peralta, F. Ogliaro, M. J. Bearpark, J. J. Heyd, E. N. Brothers, K. N. Kudin, V. N. Staroverov, T. A. Keith, R. Kobayashi, J. Normand, K. Raghavachari, A. P. Rendell, J. C. Burant, S. S. Iyengar, J. Tomasi, M. Cossi, J. M. Millam, M. Klene, C. Adamo, R. Cammi, J. W. Ochterski, R. L. Martin, K. Morokuma, O. Farkas, J. B. Foresman and D. J. Fox, Gaussian, Inc., Wallingford CT, 2016.
- 20 J. P. M. Jämbeck and A. P. Lyubartsev, *J. Phys. Chem. B*, 2012, **116**, 3164–3179.
- 21 W. L. Jorgensen, J. Chandrasekhar, J. D. Madura, R. W. Impey and M. L. Klein, *J. Chem. Phys.*, 1983, **79**, 926–935.
- 22 G. Bussi, D. Donadio and M. Parrinello, *J. Chem. Phys.*, 2007, **126**, 014101.
- 23 H. J. C. Berendsen, J. P. M. Postma, W. F. van Gunsteren, A. DiNola and J. R. Haak, *J. Chem. Phys.*, 1984, **81**, 3684–3690.
- 24 M. Parrinello and A. Rahman, *J. Appl. Phys.*, 1981, **52**, 7182–7190.
- 25 S. Nosé and M. L. Klein, *Mol. Phys.*, 1983, **50**, 1055–1076.
- 26 U. Essmann, L. Perera, M. L. Berkowitz, T. Darden, H. Lee and L. G. Pedersen, *J. Chem. Phys.*, 1995, **103**, 8577–8593.
- 27 A. Pannwitz, H. Saaring, N. Beztsinna, X. Li, M. A. Siegler and S. Bonnet, *Chem. Eur. J.*, 2021, **27**, 3013–3018.
- 28 B. Limburg, E. Bouwman and S. Bonnet, *Chem. Commun.*, 2015, **51**, 17128–17131.
- 29 J. N. Demas, W. D. Bowman, E. F. Zalewski and R. A. Velapoldi, *J. Phys. Chem.*, 1981, **85**, 2766–2771.
- 30 B. Limburg, E. Bouwman and S. Bonnet, *ACS Catal.*, 2016, **6**, 5273–5284.
- 31 A. Bahreman, M. Rabe, A. Kros, G. Bruylants and S. Bonnet, *Chem. Eur. J.*, 2014, **20**, 7429–7438.
- 32 M. Ishiyama, M. Shiga, K. Sasamoto, M. Mizoguchi and P. He, *Chem. Pharm. Bull.*, 1993, **41**, 1118–1122.

Supporting information for Chapter 3

C. 1. Methods

General methods. ^1H NMR and ^{13}C NMR spectra were recorded on a Bruker AV400 MHz spectrometer and ^{19}F NMR spectra on a Bruker AV500 MHz spectrometer. Chemical shift values (δ) are reported in ppm relative to the solvent. Electrospray ionisation mass spectrometry (ESI-MS) spectra were measured with a ThermoFischer Scientific MSQ Plus electrospray ionisation mass spectrometer with a 17 – 2000 m/z detection range and a resolution of approximately 0.5 m/z . High-resolution mass spectrometry (HRMS) was measured via direct injection on a Thermo Finnagan LTQ Orbitrap with electrospray ionisation. Elemental analysis was performed by Mikroanalytisches Laboratorium Kolbe in Oberhausen, Germany. UV-Vis absorption spectra were measured on a Varian Cary60 spectrophotometer equipped with a single cell Peltier temperature controller at 25 °C using either a 3 mL cuvette for standard solutions or a 0.6 mL cuvette for liposome solutions. Emission spectra were measured on a FLS900 spectrometer from Edinburgh Instruments Ltd. in a 3 mL cuvette at 22 °C using 380 nm as excitation source for the rhenium complexes and 450 nm as excitation source for the ruthenium complexes. Luminescence lifetimes were measured for rhenium complexes using the set-up for transient absorption spectroscopy described below, using an excitation wavelength of 380 nm. Instead of detecting the transmitted probe light, the spontaneous emission generated by the laser pulse was observed at different delay times determined by the electronically controlled detector gate (gate width = 5 ns), and the intensity versus time was modelled by a monoexponential decay using Glotaran.¹ Confocal microscopy images were taken on a Nikon Eclipse Ti microscope with 20x objective (0.75 NA, 1.00 WD) and confocal imaging with 488 nm laser and 640 – 680 nm detection wavelength. Images were processed with the Fiji version of ImageJ2.

Preparation of liposomes for immobilisation studies and photocatalysis.

DMPC, DPPC, or DSPC lipids in chloroform, NaDSPE-PEG2K in chloroform, **RuC_n** in methanol, and/or **ReC_n** in chloroform were added in a pressure resistant tube. The organic solvents were evaporated under reduced pressure and the resulting lipid film was dried for at least 1 hour in *vacuo* to remove residual solvent. The film was then hydrated with NaH₂PO₄ buffer (4 mL, 0.1 M, pH = 7.7) with or without sodium ascorbate (0.1 M), followed by 10 freeze-thaw cycles in liquid N₂ and 50 °C water bath. Subsequently, the vesicles were extruded 11x with an Avanti Polar Lipids mini-extruder through a 0.2 µm polycarbonate membrane at 10 °C above the phase transition temperature of the lipid. Assuming no losses during preparation, the resulting liposomes consist of lipid:NaDSPE-PEG2K:**RuC_n**:**ReC_n** in the ratio 100:1.0:0.4:0.4 with expected bulk concentrations of 6.25 mM lipid, 0.625 mM NaDSPE-PEG2K, and 0.025 mM **RuC_n** and 0.025 mM **ReC_n**. Liposome samples were stored at RT and used within one week. For photocatalytic CO₂ reduction experiments, the liposome solutions were diluted ten-fold with the same buffer as that used for liposome preparation. The size distribution of the hydrodynamic diameter (Z_{ave}) and the polydispersity index (PDI) were measured at 25 °C by dynamic light scattering with a Zetasizer Nano-S from Malvern operating at 632.8 nm with a scattering angle of 173°; at this wavelength neither **RuC_n** nor **ReC_n** absorb light significantly.

Photocatalysis measurements. Before photocatalysis, the liposome-containing solution obtained right after extrusion (0.3 mL) was diluted 10-fold using an aqueous solution containing 0.1 M phosphate buffer and 0.1 M sodium ascorbate. It was then purged in triplicates for 20 min with CO₂, or N₂ for control experiments, containing in both cases 2% methane as internal standard for gas chromatography. After purging, the vials were kept in a water bath at 25 °C and irradiated for 3 h using a Newport Oriel Xenon 150 W solar light simulator (100 mW cm⁻², AM1.5G containing infrared water and ultraviolet ($\lambda > 455$ or 400 nm) filters).

Product quantification. The amount of produced H₂ and CO was monitored by headspace gas analysis using a Shimadzu Tracera GC-2010 Plus with a barrier discharge ionisation detector. The GC-2010 Plus was equipped with a

ShinCarbon micro-ST column (0.53 mm diameter) kept at 40 °C using helium carrier gas. Aliquots of 50 μL of the headspace gas were removed from the sealed photocatalytic vials using a gastight syringe (Hamilton) for gas chromatography analysis at hourly time intervals. Each different photocatalytic experiment was performed in triplicate, unless stated otherwise. Data are presented as mean \pm standard error of the mean. The mean values and standard errors of the mean were calculated from the number of repeats of independent experiments.

Isotopic labelling experiment. Photocatalysis experiment with $^{13}\text{CO}_2$ as the headspace gas was performed. After three hours of simulated light irradiation, the vial headspace was transferred to an evacuated gas infrared cell (SpecAc, 10 cm path length, equipped with KBr windows) and a high-resolution transmission spectrum was collected on a Thermo Scientific Nicolet iS50 FT-IR spectrometer. To check whether formate had formed, an aliquot of the aqueous phase, together with a D_2O solution of trimethylsilylpropanoic acid as internal standard, was measured by ^1H NMR on a Bruker 400 MHz NMR spectrometer at room temperature.

Quantum yield measurements. One-millilitre solutions containing DPPC liposomes made of **ReC₉** and **RuC₉** (bulk concentration = 25 μM) were irradiated with monochromatic light ($\lambda = 455 \text{ nm}$), using two different light intensities ($I_1 = 10.5 \text{ mW cm}^{-2}$, and $I_2 = 13.5 \text{ mW cm}^{-2}$), produced by a solar simulator (LOT LSN 254) equipped with a monochromator (LOT MSH 300). Duplicate experiments were performed for each light intensity and the averaged values of the produced mol of CO were utilised to determine the Φ_{CO} using Equation C1:

$$\Phi_{\text{CO}} (\%) = \frac{2 n_{\text{CO}} N_{\text{A}} h c}{t_{\text{irr}} \lambda I A P} \cdot 100 \quad \text{Equation C1}$$

where n_{CO} is the moles of photogenerated CO gas ($n_{\text{CO},1} = 2.12 \times 10^{-8} \text{ mol}$ and $n_{\text{CO},2} = 1.20 \times 10^{-8} \text{ mol}$), N_{A} is the Avogadro constant in mol^{-1} , h is the Planck constant in J s, c the speed of light in m s^{-1} , t_{irr} is the irradiation time (3600 s), λ is the monochromatic light wavelength in m, I the light intensity in J s^{-1}

m^{-2} , and A is the irradiation cross-section ($1 \times 10^{-4} m^2$). P is the probability of absorbing a photon by the photosensitiser, i.e. $1 - 10^{-(Abs@454nm)}$, where due to the high scattering of the DPPC liposomes the absorbance used (0.252) was calculated employing the bulk concentration (25 μM), the molar absorption coefficient ($1.32 \times 10^4 M^{-1} cm^{-1}$), and the immobilisation correction factor ($\eta_{immob} = 0.764$) of photosensitiser **RuC₉**.

Protocol for cyclic voltammetry (CV) and differential pulse voltammetry (DPV). CV and DPV were recorded with an Autolab Pgstat 10 potentiostat controlled by GPES4 software in a customised glass cell, equipped with a 1 mM solution of **RuC_n** or **ReC_n** and 0.1 M Bu₄NPF₆ in 6 mL dry acetonitrile or dichloromethane. The solution was stirred and degassed with argon for 15 minutes before each measurement. At the end of each measurement, 5 mg (0.03 mmol) ferrocene was added as an internal reference. A glassy carbon working electrode, a Ag/AgCl reference electrode, and a platinum counter electrode were employed to obtain spectra typically from $-2.0 V$ to $1.6 V$, with a scan rate of 100 mV/s (CV) or 50 mV/s (DPV).

Protocol for studying immobilisation efficiency of metal complexes on liposomes. For the immobilisation efficiency tests, liposome samples (0.6 mL) were loaded in specialised safe-lock Eppendorfs (Thermo Scientific X100 Tube PA Microtubes, 1.5 mL) and placed within adapters from Beranek Laborgeräte (catalogue number 11044). Subsequently, the liposomes were spinned down by ultracentrifugation on a Beckman Coulter Optima XE-90 Ultracentrifuge, using a Ti70 rotor at 36000 rpm (max. 100.4 kG) and 4 °C. Afterwards, the supernatant was separated from the pellet containing liposomes and immobilised metal complexes. Both the liposome stock sample before ultracentrifugation, as well as the supernatant were subsequently studied by UV-Vis spectroscopy and ICP-MS analysis.

Protocol for ICP-MS analysis. The supernatant samples for ICP-MS were prepared by digesting 100 μL supernatant sample in 100 μL nitric acid (65%) in a 10 mL plastic tube overnight. Then 9.8 mL MilliQ water was added. The solutions still containing liposomes were prepared by adding 100 μL liposome sample to 80 μL 37% HCl and 120 μL 65% HNO₃ in a glass tube with

a glass marble on top and digesting for 48 hours at 90°C in the oven. After 48 hours the water had evaporated and 10 mL MilliQ water was added. The ruthenium and rhenium content of the samples were subsequently measured in triplicate using a NexION 2000 ICP mass spectrometer, a SC2 DX auto sampler, and Syngistix software from Perkin Elmer.

Nanosecond transient absorption spectroscopy. Nanosecond transient absorption was measured using an in-house assembled setup in which transient (ΔA) spectra were recorded as a function of delay time with respect to a laser pulse exciting the solution.² The excitation pulses at 450 nm (3.5 mJ/pulse; ca. 5 ns full width at half maximum) were generated using a tunable Nd:YAG-laser system (NT342B, Ekspla). The laser system was operated at a repetition rate of 5 Hz. The probe light, running at 10 Hz, was generated by a high-stability short arc xenon flash lamp (FX-1160, Excelitas Technologies) with a modified PS302 controller (EG&G). The probe light was split in a signal and a reference beam with a 50/50 beam splitter and focused on the entrance slit of a spectrograph (SpectraPro-150, Princeton Instruments). The probe beam ($A = 1 \text{ mm}^2$) was passed through the sample cell and orthogonally overlapped with the excitation beam on a $1 \text{ mm} \times 1 \text{ cm}$ area. The excitation power was recorded by measuring the excitation power at the back of an empty sample holder. The reference beam was used to normalise the signal for fluctuations in the flash lamp spectral intensity. Both beams were recorded simultaneously using a gated intensified CCD camera (PI-MAX3, Princeton Instruments) with an adjustable gate (gate width = 20 ns). The timing of the excitation pulse, the flash lamp, and the gate of the camera was achieved with a delay generator (DG645, Stanford Research Systems, Inc.). The setup was controlled by an in-house written program (LabView). Spectra were averaged from 490 to 540 nm (RuC_n^- absorption) and the ΔA_{av} values as a function of time were fitted with Equation 3.5 using Igor Pro version 8 (Wavemetrics).

Microcavity Support. The micropore array substrates for fluorescence correlation spectroscopy were prepared in polydimethylsiloxane (PDMS) as described previously.³ First, mica sheets were cut in to 1 cm^2 area and glued to a cover glass slide. $\sim 20 \text{ }\mu\text{L}$ of ethanolic solution of 0.1% of $4.61 \text{ }\mu\text{m}$

polystyrene spheres was drop cast onto the flat mica sheet and after evaporation, PDMS was poured over the array of spheres, and cured at 90 °C for 1 h. On cooling, the PDMS was gently peeled off to create a thin chamber of identical dimensions of mica sheet thickness. The pores were generated by dissolving PS sphere from the PDMS substrate by immersion and sonication in tetrahydrofuran for 15 min. The substrates were then left to dry overnight. The PDMS substrates were then plasma cleaned using oxygen plasma for 5 min to make the surface hydrophilic and the microcavities were buffer filled by sonication and stored inside buffer prior to applying the bilayer.

Preparation of microcavity supported lipid bilayers. The lipid bilayers were prepared on the PDMS substrate containing 2 μm sized cavities through Langmuir-Blodgett technique followed by vesicle fusion methods.³ The proximal lipid monolayer was transferred by Langmuir-Blodgett technique (KSV Nema) in the air-water interface. The lipid solution was left to evaporate for about 10 min at the sub-phase surface (MilliQ water, pH 7.4) and the lipid monolayer was transferred at a surface pressure of 40 mN/m. The liposomes were prepared by mixing DPPC:NaDSPE-PEG2K:**RuC_n** in the ratio 100:1:4·10⁻⁴ and then it was dried under nitrogen flow. It was kept under vacuum for 60 minutes and hydrated using phosphate buffer saline (pH 7.7) followed by vortex agitation. These vesicles were extruded with 0.2 μm polycarbonate membrane at 10 °C above the phase transition temperature of the lipid. These vesicles were injected to the microfluidic chamber of lipid monolayer. It was allowed to fuse for 90 min and the residual liposomes were removed by phosphate buffer saline wash.

Fluorescence lifetime correlation spectroscopy (FLCS). The diffusion coefficient of **RuC_n**-labelled supported lipid bilayers were obtained using FLCS, accomplished on a MicroTime 200 system (Picoquant GmbH, Berlin, Germany) consisting of an inverted Olympus X1-71 microscope with an Olympus UPlanSApo 60x/1.2 water immersion objective, a time correlated single photon counting (TCSPC) unit, and a dual single photo avalanche diode (SPAD). The **RuC_n** probes were excited with a 532 nm laser PicoTA from Toptica (Picoquant) with a pulse repetition rate of 20 MHz. 532 nm was

selected as the excitation wavelength as it gave superior S/N ratio in the time trace due to reflectance from the substrate at 440 nm. The excitation light was directed onto the sample through the objective lens by a 440/532rpc dichroic mirror. The emitted fluorescence was also collected through the same objective and filtered by the dichroic mirror and by a 580 nm interference filter. A 50 μm pinhole was used in order to confine the detection volume in the axial direction onto the SPAD. The autocorrelation functions (ACFs) were fitted using Equation C2:

$$G(\tau) = \left[\frac{1}{N} \right] \left[\frac{1}{1 + \left(\frac{\tau}{\tau_{D1}} \right)^{\alpha_1}} \right] + \left[\frac{(1-c)}{\left(1 + \frac{\tau}{\tau_{D2}} \right)^{\alpha_2}} \right] \quad \text{Equation C2}$$

where $G(\tau)$ is the autocorrelation function of fluorescence fluctuations, N is the average number of diffusing fluorophores in the effective volume, τ is the delay time, τ_{D1} and τ_{D2} are the diffusion time of the molecules across the confocal volume of the 1st component and 2nd component respectively, α_1 and α_2 are the anomalous parameters of the 1st and 2nd components, respectively, and c is the contribution of the diffusing species. ACFs were fitted using the two-dimensional model of diffusion to determine the diffusion time and the diffusion coefficient was calculated using Equation C3:

$$D = \frac{\omega^2}{4\tau_D} \quad \text{Equation C3}$$

where D is the diffusion coefficient and ω is the $1/e^2$ radius of the confocal volume. ω was measured using ATTO-532 (Atto TEC, GmbH) dye solution of known diffusion coefficient at 20 °C in water. All measurements were performed with a dye concentration of 10 nM. Three-dimensional diffusion of 10 nM **RuC₁₉** was recorded in acetonitrile and the ACF was fitted using the three-dimensional diffusion model:

$$G(\tau) = \left[\frac{1}{N} \right] \left[\frac{1}{1 + \left(\frac{\tau}{\tau_D} \right)^\alpha} \right] \left[\frac{1}{\sqrt{1 + \left(\frac{\tau}{\tau_D} \right)^\alpha K^2}} \right] \quad \text{Equation C4}$$

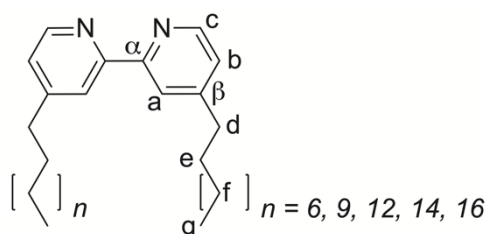
where K is the length to diameter ratio of the confocal volume. The fluorescence lifetime image was also taken in the same MicroTime 200 system. Each sample was acquired for 360 s with a 512 x 512 resolution. Data was analysed using PicoQuant Symphotime software.

C. 2. Synthesis

Materials and reagents. Chemical reagents and solvents were purchased from commercial suppliers and were used without further purification. Sodium ascorbate ($\geq 99\%$) and $\text{NaH}_2\text{PO}_4 \cdot 2\text{H}_2\text{O}$ were purchased from Merck. 2,2'-bipyridine (bpy), 4,4'-dionyl-bpy, $[\text{Re}(\text{CO})_5\text{Cl}]$, and $\text{bpy}-(\text{C}_9)_2$ were purchased from Sigma Aldrich. The lipids (dry powder) 1,2-dimyristoyl-*sn*-glycero-3-phosphocholine (DMPC), 1,2-dipalmitoyl-*sn*-glycero-3-phosphocholine (DPPC), 1,2-distearoyl-*sn*-glycero-3-phosphocholine (DSPC) were purchased from Avanti Polar Lipids and stored at -20°C . Sodium 1,2-distearoyl-*sn*-glycero-3-phosphoethanolamine N-(carbonyl-methoxypolyethylene glycol-2000) (NaDSPE-PEG2K) was purchased from Lipoid and stored at -20°C . *cis*- $[\text{Ru}(\text{bpy})_2\text{Cl}_2]$ was synthesised according to literature, while isolating $[\text{Ru}(\text{bpy})_3](\text{PF}_6)_2$ as a side product after anion exchange with potassium hexafluorophosphate.⁴ Phosphate buffer (1 L, 0.1 M, pH = 7.7) was prepared by dissolving $\text{NaH}_2\text{PO}_4 \cdot 2\text{H}_2\text{O}$ (12 g) in Milli-Q water (500 mL), adjusting the pH with NaOH (≈ 90 mL, 1 M), and diluting further with Milli-Q water up to 1 L. The Avanti Mini-Extruder including polycarbonate extrusion filter (pore size = 0.2 μm , diameter = 19 mm) and filter supports (10 mm) was purchased from Avanti Polar Lipids.

General procedure for the synthesis of 4,4'-($\text{C}_n\text{H}_{2n+1}$)₂-bpy. 4,4'-($\text{C}_n\text{H}_{2n+1}$)₂-bpy ($n = 12, 15, 17, \text{ and } 19$) were synthesised according to a known procedure for 4,4'-(C_9H_{19})₂-bpy.⁵ Tetrahydrofuran was dried over 3 Å molecular sieves overnight and was deoxygenated under N_2 prior to use. To a solution of diisopropylamine (2.4 mM in tetrahydrofuran, 2.7 equiv.) was added a solution of *n*-butyllithium (1.6 M or 2.5 M in hexane, 2.7 equiv.) under N_2 atmosphere. After 1 h at 0°C , 4,4'-dimethyl-2,2'-bipyridine (0.14 mM in tetrahydrofuran, 1.0 equiv.) was added dropwise to the yellow

solution. After another 3 h at 0 °C, 1-bromoundecane (1.4 mM in tetrahydrofuran, 2.7 equiv.) was added dropwise to the red solution and the solution was allowed to warm to room temperature. After 1 day, the reaction mixture was quenched with water. The aqueous phase was extracted with diethyl ether (3 x). The combined organic phases were dried over MgSO₄, the dried solution was filtered, and the filtrate was concentrated under reduced pressure. The crude product **4,4'-(C_nH_{2n+1})₂-bpy** was either recrystallised from pentane (n = 12, 15, and 17) or it was collected by filtration after it precipitated during extraction (n = 19).



4,4'-didodecyl-2,2'-bipyridine (4,4'-(C₁₂H₂₅)₂-bpy): method above, from 4,4'-dimethyl-2,2'-bipyridine (2.0 g, 10.9 mmol); white solid (yield: 3.2 g, 6.5 mmol, 60%). *R_f* = 0.7 (SiO₂, DCM/MeOH 9:1). ¹H NMR (400 MHz, CDCl₃): δ = 8.58 (d, *J* = 5.0 Hz, 2H, c), 8.26 (s, 2H, a), 7.16 (dd, *J* = 5.0, 1.5 Hz, 2H, b), 2.71 (t, *J* = 7.6 Hz, 4H, d), 1.71 (p, *J* = 7.6 Hz, 4H, e), 1.27 (m, 36H, f), 0.90 (t, *J* = 6.7 Hz, 6H, g). ¹³C NMR (100 MHz, CDCl₃): δ = 156.09 (C_q, α), 153.20 (C_q, β), 149.00 (CH, c), 124.08 (CH, b), 121.51 (CH, a), 35.69 (CH₂, d), {32.05, 30.60, 29.79 – 29.45, 22.82 (CH₂, e+f)}, 14.25 (CH₃, g). HRMS (ESI) *m/z* found (calcd): 493.45146 (493.45163, [M+H]⁺). Elemental analysis calcd (%) for C₃₄H₅₆N₂ · H₂O: C 79.94, H 11.44, N 5.48; found: C 80.47, H 11.37, N 5.31.

4,4'-dipentadecyl-2,2'-bipyridine (4,4'-(C₁₅H₃₁)₂-bpy): method above, from 4,4'-dimethyl-2,2'-bipyridine (1.0 g, 5.4 mmol); white solid (yield: 1.2 g, 2.0 mmol, 37%). ¹H NMR (400 MHz, CDCl₃): δ = 8.56 (d, *J* = 5.0 Hz, 2H, c), 8.26 (s, 2H, a), 7.15 (dd, *J* = 5.0, 1.5 Hz, 2H, b), 2.69 (t, *J* = 7.8 Hz, 4H, d), 1.69 (p, *J* = 7.8 Hz, 4H, e), 1.25 (m, 48H, f), 0.87 (t, *J* = 6.8 Hz, 6H, g). ¹³C NMR (100 MHz, CDCl₃): δ = 155.77 (C_q, α), 153.51 (C_q, β), 148.85 (CH, c), 124.19 (CH, b), 121.69 (CH, a), 35.72 (CH₂, d), {32.07, 30.59, 29.85–29.45, 22.84 (CH₂, e+f)}, 14.27

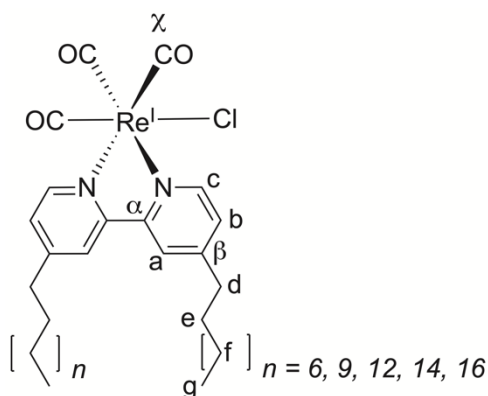
(CH₃, *g*). HRMS (ESI) *m/z* found (calcd): 577.54527 (577.54553, [M+H]⁺). Elemental analysis calcd (%) for C₄₀H₆₈N₂: C 83.27, H 11.88, N 4.86; found: C 83.23, H 11.94, N 4.82.

4,4'-diheptadecyl-2,2'-bipyridine (4,4'-(C₁₇H₃₅)₂-bpy): method above, from 4,4'-dimethyl-2,2'-bipyridine (2.0 g, 10.9 mmol); white solid (yield: 2.2 g, 3.5 mmol, 32%). ¹H NMR (400 MHz, CDCl₃): δ = 8.55 (d, *J* = 5.3 Hz, 2H, *c*), 8.23 (d, *J* = 1.5 Hz, 2H, *a*), 7.13 (dd, *J* = 5.3, 1.5 Hz, 2H, *b*), 2.68 (t, *J* = 6.8 Hz, 4H, *d*), 1.68 (p, *J* = 6.5 Hz, 4H, *e*), 1.25 (m, 56H, *f*), 0.87 (t, *J* = 6.7 Hz, 6H, *g*). ¹³C NMR (100 MHz, CDCl₃): δ = 156.23 (C_q, α), 153.14 (C_q, β), 149.07 (CH, *c*), 124.07 (CH, *b*), 121.49 (CH, *a*), 35.70 (CH₂, *d*), {32.07, 30.62, 29.84, 29.82, 29.80, 29.78, 29.68, 29.58, 29.51, 29.48, 22.84 (CH₂, *e+f*)}, 14.27 (CH₃, *g*). MS (ESI) *m/z* found (calcd): 633.6 (633.6, [M+H]⁺). Elemental analysis calcd (%) for C₄₄H₇₆N₂: C 83.47, H 12.10, N 4.42; found: C 83.43, H 12.07, N 4.39. Colourless single crystals of **4,4'-(C₁₇H₃₅)₂-bpy** were obtained by evaporation of the solvent CDCl₃ at room temperature. The structure and refinement data are shown in the section on single crystal X-ray crystallography (Appendix C.9).

4,4'-dinonadecyl-2,2'-bipyridine (4,4'-(C₁₉H₃₉)₂-bpy): method above, from 4,4'-dimethyl-2,2'-bipyridine (2.0 g, 10.9 mmol); white solid (yield: 3.5 g, 5.0 mmol, 46%). *R_f* = 0.4 (SiO₂, pentane/EtOAc 10:1). ¹H NMR (400 MHz, CDCl₃): δ = 8.56 (d, *J* = 5.0 Hz, 2H, *c*), 8.24 (s, 2H, *a*), 7.14 (dd, *J* = 5.0, 1.7 Hz, 2H, *b*), 2.69 (t, *J* = 7.6 Hz, 4H, *d*), 1.68 (p, *J* = 7.6 Hz, 4H, *e*), 1.25 (m, 64H, *f*), 0.86 (t, *J* = 6.8 Hz, 6H, *g*). ¹³C NMR (100 MHz, CDCl₃): δ = 156.02 (C_q, α), 153.31 (C_q, β), 148.98 (CH, *c*), 124.12 (CH, *b*), 121.57 (CH, *a*), 35.71 (CH₂, *d*), {32.07, 30.61, 29.86-29.46, 22.84 (CH₂, *e+f*)}, 14.27 (CH₃, *g*). HRMS (ESI) *m/z* found (calcd): 689.66953 (689.67073, [M+H]⁺). Elemental analysis calcd (%) for C₄₈H₈₄N₂ · 0.5 H₂O: C 82.57, H 12.27, N 4.01; found: C 82.60, H 12.12, N 3.99.

General procedure for the synthesis of [Re(4,4'-(C_nH_{2n+1})₂-bpy)(CO)₃Cl] (ReC_n): The compounds were synthesised according to known procedures.^{6,7} To a solution of [Re(CO)₅Cl] (typically 0.028 mM in dry toluene, 1.0 equiv. or 1.5 equiv., respectively, in case of ReC₁₉) was added **4,4'-(C_nH_{2n+1})₂-bpy** (1.0 equiv.) under inert atmosphere and the yellow mixture was heated to reflux. After 3 – 48 h, the orange solution was concentrated under reduced

pressure. The residue was redissolved in a minimum amount of diethyl ether and the solution was carefully concentrated until the desired product started to precipitate, which was collected by vacuum filtration. Due to the alkyl chain length, different procedures were followed from this point. For **ReC₉** and **ReC₁₂**, concentration of the filtrate resulted in additional solids, which were reprecipitated by dissolving in acetone and evaporation under reduced pressure. For **ReC₁₅** and **ReC₁₇**, the precipitate was washed with 3 x 20 mL acetone and vacuum dried. For **ReC₁₉**, the precipitate was washed with 3 x 20 mL Et₂O and vacuum dried.



[Re(bpy)(CO)₃Cl] (ReC₀): from [Re(CO)₅Cl] (81 mg, 0.22 mmol) and bpy (35 mg, 0.22 mmol); yellow solid (yield: 86 mg, 0.19 mmol, 83%). Elemental analysis calcd (%) for C₁₃H₈N₂O₃ReCl: C 33.81, H 1.75, N 6.07; found: C 33.67, H 1.74, N 5.99.

[Re(4,4'-(C₉H₁₉)₂-bpy)(CO)₃Cl] (ReC₉): from [Re(CO)₅Cl] (100 mg, 0.28 mmol) and 4,4'-(C₉H₁₉)₂-bpy (113 mg, 0.28 mmol); yellow solid **ReC₉** (yield: 195 mg, 0.27 mmol, 99%). ¹H NMR (400 MHz, CDCl₃): δ = 8.88 (d, *J* = 5.7 Hz, 2H, *c*), 7.95 (s, 2H, *a*), 7.32 (dd, *J* = 5.7, 1.6 Hz, 2H, *b*), 2.78 (t, *J* = 7.7 Hz, 4H, *d*), 1.70 (p, *J* = 7.7 Hz, 4H, *e*), 1.28 (m, 24H, *f*), 0.88 (t, *J* = 6.7 Hz, 6H, *g*). ¹³C NMR (100 MHz, CDCl₃): δ = 197.44 (CO), 190.05 (CO), 156.00 (C_q, α), 155.63 (C_q, β), 152.77 (CH, *c*), 127.23 (CH, *b*), 123.13 (CH, *a*), 35.84 (CH₂, *d*), {31.95, 30.33, 29.55, 29.48, 29.38, 22.77 (CH₂, *e+f*)}, 14.23 (CH₃, *g*). UV-Vis (CHCl₃): λ_{max} (ε): 382 nm (3.86 × 10³ mol⁻¹dm³cm⁻¹). Phosphorescence (CHCl₃): λ_{ex} = 380 nm,

$\lambda_{em} = 582$ nm, $\tau = 76$ ns. HRMS (ESI) m/z found (calcd): 679.28924 (679.29039, $[M-Cl]^+$), 720.31590 (720.31699, $[M-Cl+CH_3CN]^+$), 732.29069 (732.29350, $[M+NH_4]^+$), 737.24709 (737.24824, $[M+Na]^+$). Elemental analysis calcd (%) for $C_{31}H_{44}N_2O_3ReCl$: C 52.12, H 6.21, N 3.92; found: C 52.10, H 6.22, N 3.94.

[Re(4,4'-(C₁₂H₂₅)₂-bpy)(CO)₃Cl] (ReC₁₂): from [Re(CO)₅Cl] (100 mg, 0.28 mmol) and **4,4'-(C₁₂H₂₅)₂-bpy** (136 mg, 0.28 mmol); yellow solid **ReC₁₂** (yield: 146 mg, 0.18 mmol, 67%). ¹H NMR (400 MHz, CDCl₃): $\delta = 8.88$ (d, $J = 5.7$ Hz, 2H, c), 7.96 (s, 2H, a), 7.32 (dd, $J = 5.7, 1.7$ Hz, 2H, b), 2.78 (t, $J = 7.6$ Hz, 4H, d), 1.70 (p, $J = 7.6$ Hz, 4H, e), 1.27 (m, 36H, f), 0.87 (t, $J = 6.7$ Hz, 6H, g). ¹³C NMR (100 MHz, CDCl₃): $\delta = 197.45$ (CO), 190.02 (CO), 156.01 (C_q, α), 155.61 (C_q, β), 152.74 (CH, c), 127.22 (CH, b), 123.14 (CH, a), 35.83 (CH₂, d), {32.02, 30.32, 29.75, 29.73, 29.60, 29.48, 29.46, 29.39, 22.80 (CH₂, e+f)}, 14.24 (CH₃, g). UV-Vis (CHCl₃): λ_{max} (ϵ): 383 nm (3.98×10^3 mol⁻¹dm³cm⁻¹). Phosphorescence (CHCl₃): $\lambda_{ex} = 380$ nm, $\lambda_{em} = 588$ nm, $\tau = 74$ ns. HRMS (ESI) m/z found (calcd): 763.38378 (763.38434, $[M-Cl]^+$), 804.41072 (804.41088, $[M-Cl+CH_3CN]^+$), 816.38649 (816.38752, $[M+NH_4]^+$), 821.34191 (821.34219, $[M+Na]^+$). Elemental analysis calcd (%) for $C_{37}H_{56}N_2O_3ReCl \cdot 2 C_3H_6O$: C 56.47, H 7.49, N 3.06; found: C 56.19, H 7.37, N 3.08.

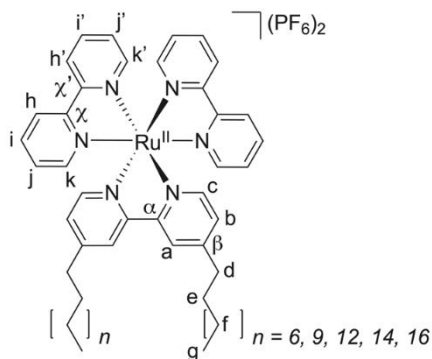
[Re(4,4'-(C₁₅H₃₁)₂-bpy)(CO)₃Cl] (ReC₁₅): from [Re(CO)₅Cl] (107 mg, 0.30 mmol) and **4,4'-(C₁₅H₃₁)₂-bpy** (170 mg, 0.30 mmol); yellow solid **ReC₁₅** (yield: 92 mg, 0.10 mmol, 35%). ¹H NMR (400 MHz, CDCl₃): $\delta = 8.89$ (d, $J = 5.7$ Hz, 2H, c), 7.95 (s, 2H, a), 7.32 (dd, $J = 5.7, 1.6$ Hz, 2H, b), 2.78 (t, $J = 7.7$ Hz, 4H, d), 1.70 (p, $J = 7.6$ Hz, 4H, e), 1.26 (m, $J = 6.6$ Hz, 48H, f), 0.87 (t, $J = 6.7$ Hz, 6H, g). ¹³C NMR (100 MHz, CDCl₃): $\delta = 197.44$ (CO), 190.05 (CO), 155.99 (C_q, α), 155.63 (C_q, β), 152.79 (CH, c), 127.23 (CH, b), 123.13 (CH, a), 35.86 (CH₂, d), {32.05, 30.34, 29.82, 29.80, 29.79, 29.77, 29.75, 29.62, 29.49, 29.41, 22.82 (CH₂, e+f)}, 14.10 (CH₃, g). UV-Vis (CHCl₃): λ_{max} (ϵ): 382 nm (3.80×10^3 mol⁻¹dm³cm⁻¹). Phosphorescence (CHCl₃): $\lambda_{ex} = 380$ nm, $\lambda_{em} = 585$ nm, $\tau = 74$ ns. HRMS (ESI) m/z found (calcd): 847.47678 (847.47820, $[M-Cl]^+$), 888.50452 (888.50475, $[M-Cl+CH_3CN]^+$), 900.48034 (900.48142, $[M+NH_4]^+$), 905.43608 (905.43682, $[M+Na]^+$). Elemental analysis calcd (%) for $C_{43}H_{68}N_2O_3ReCl$: C 58.51, H 7.76, N 3.17; found: C 58.47, H 7.82, N 3.14.

[Re(4,4'-(C₁₇H₃₅)₂-bpy)(CO)₃Cl] (ReC₁₇): from [Re(CO)₅Cl] (88 mg, 0.24 mmol) and **4,4'-(C₁₇H₃₅)₂-bpy** (153 mg, 0.24 mmol); yellow solid **ReC₁₇** (yield: 194 mg, 0.21 mmol, 85%). ¹H NMR (400 MHz, CDCl₃): δ = 8.89 (d, *J* = 5.8 Hz, 2H, *c*), 7.95 (s, 2H, *a*), 7.32 (dd, *J* = 5.7, 1.1 Hz, 2H, *b*), 2.78 (t, *J* = 7.8 Hz, 4H, *d*), 1.71 (p, *J* = 7.8 Hz, 4H, *e*), 1.26 (m, 56H, *f*), 0.88 (t, *J* = 6.9 Hz, 6H, *g*). ¹³C NMR (100 MHz, CDCl₃) δ = 197.43 (CO), 190.06 (CO), 155.98 (C_q, α), 155.63 (C_q, β), 152.79 (CH, *c*), 127.23 (CH, *b*), 123.12 (CH, *a*), 35.86 (CH₂, *d*), {32.06, 30.19, 29.83, 29.81, 29.79, 29.76, 29.63, 29.50, 29.41, 22.82 (CH₂, *e+f*)}, 14.10 (CH₃, *g*). UV-Vis (CHCl₃): λ_{max} (ε): 383 nm (3.83 × 10³ mol⁻¹dm³cm⁻¹). Phosphorescence (CHCl₃): λ_{ex} = 380 nm, λ_{em} = 581 nm, τ = 74 ns. HRMS (ESI) *m/z* found (calcd): 903.53904 (903.54109, [M-Cl]⁺), 944.56588 (944.56766, [M-Cl+CH₃CN]⁺), 956.54294 (956.54341, [M+NH₄]⁺), 961.49829 (961.49881, [M+Na]⁺). Elemental analysis calcd (%) for C₄₇H₇₆N₂O₃ReCl: C 60.13, H 8.16, N 2.98; found: C 60.15, H 8.22, N 2.95.

[Re(4,4'-(C₁₉H₃₉)₂-bpy)(CO)₃Cl] (ReC₁₉): from [Re(CO)₅Cl] (157 mg, 0.44 mmol) and **4,4'-(C₁₉H₃₉)₂-bpy** (200 mg, 0.29 mmol); yellow solid **ReC₁₉** (yield: 161 mg, 0.16 mmol, 56%). ¹H NMR (400 MHz, CDCl₃): δ = 8.87 (d, *J* = 5.7 Hz, 2H, *c*), 7.96 (s, 2H, *a*), 7.31 (dd, *J* = 5.7, 1.4 Hz, 2H, *b*), 2.77 (t, *J* = 7.6 Hz, 4H, *d*), 1.70 (p, *J* = 7.6 Hz, 4H, *e*), 1.25 (m, 64H, *f*), 0.87 (t, *J* = 6.7 Hz, 6H, *g*). ¹³C NMR (100 MHz, CDCl₃): δ = 197.45 (CO), 189.99 (CO), 156.01 (C_q, α), 155.59 (C_q, β), 152.69 (CH, *c*), 127.19 (CH, *b*), 123.16 (CH, *a*), 35.80 (CH₂, *d*), {32.02, 30.30, 29.80, 29.76, 29.73, 29.60, 29.47, 29.37, 22.79 (CH₂, *e+f*)}, 14.23 (CH₃, *g*). UV-Vis (CHCl₃): λ_{max} (ε): 381 nm (3.80 × 10³ mol⁻¹dm³cm⁻¹). HRMS (ESI) *m/z* found (calcd): 1007.56265 (1007.56146, [M+Na]⁺), 1002.60725 (1002.60606, [M+NH₄]⁺). Elemental analysis calcd (%) for C₅₁H₈₄ClN₂O₃Re: C 61.57, H 8.51, N 2.82; found: C 60.93, H 8.38, N 2.76.

General procedure for [Ru(4,4'-(C_nH_{2n+1})₂-bpy)(bpy)₂](PF₆)₂ (RuC_n): The synthesis for **RuC_n** was followed as reported in literature for a similar compound with some modifications.⁵ To a solution of *cis*-[Ru(bpy)₂Cl₂] (typically 0.014 mM in deoxygenated water/ethanol = 1:1 for **RuC₉** and **RuC₁₂** or water/ethanol/chloroform = 1:1:1 for **RuC₁₅**, **RuC₁₇**, and **RuC₁₉**, 1.0 equiv.) was added the respective **4,4'-(C_nH_{2n+1})₂-bpy** (1.0 equiv.) and the reaction

mixture was heated to reflux at 110 °C under inert atmosphere. After 1 – 4 days, the reaction mixture was concentrated under reduced pressure. The crude product was purified as described in the following protocols.



[Ru(bpy)₃](PF₆)₂ (RuC₀): Elemental analysis calcd (%) for C₃₀H₂₄F₁₂N₆P₂Ru: C 41.92, H 2.81, N 9.78; found: C 41.56, H 2.84, N 9.72.

[Ru(4,4'-(C₉H₁₉)₂-bpy)(bpy)₂](PF₆)₂ (RuC₉): from *cis*-[Ru(bpy)₂Cl₂] (0.22 g, 0.44 mmol) and 4,4'-(C₉H₁₉)₂-bpy (0.18 g, 0.44 mmol). For purification, the crude product was dissolved in a minimum amount of water. Saturated aqueous potassium hexafluorophosphate was added and the resulting orange precipitate was collected by vacuum filtration. The precipitate was dried by co-evaporation with toluene and *in vacuo*. RuC₉ was obtained as a red solid (yield: 450 mg, 0.40 mmol, 91%). *R_f* = 0.6 (SiO₂, acetone/water/saturated KNO₃ 100:10:1). ¹H NMR (400 MHz, CD₃CN): δ = 8.49 (d, *J* = 8.2 Hz, 4H, *h+h'*), 8.37 (s, 2H, *a*), 8.04 (t, *J* = 8.0, 2.9 Hz, 4H, *i+i'*), 7.72 (d, *J* = 5.2 Hz, 4H, *k+k'*), 7.54 (d, *J* = 5.5 Hz, 2H, *c*), 7.39 (q, *J* = 6.7 Hz, 4H, *j+j'*), 7.22 (d, *J* = 5.5 Hz, 2H, *b*), 2.79 (t, *J* = 7.8 Hz, 4H, *d*), 1.68 (p, *J* = 7.0 Hz, 4H, *e*), 1.27 (m, 24H, *f*), 0.87 (t, *J* = 6.4 Hz, 6H, *g*). ¹³C NMR (100 MHz, CD₃CN): δ = 157.97 (C_q), 157.55 (C_q), 155.76 (C_q), 152.59 (CH, *k* or *k'*), 152.41 (CH, *k* or *k'*), 151.78 (CH, *c*), 138.51 (CH, *i+i'*), 128.46 (CH, *b, j* or *j'*), 128.42 (CH, *b, j* or *j'*), 128.40 (CH, *b, j* or *j'*), 125.15 (CH, *a*), 125.10 (CH, *h* or *h'*), 35.64 (CH₂, *d*), {32.51, 30.81, 30.08, 29.93, 29.90, 29.74, 23.30 (CH₂, *e+f*)}, 14.32 (CH₃, *g*). ¹⁹F NMR (471 MHz, CD₃CN): δ = -72.77 (d, *J* = 706.7 Hz). UV-Vis (CH₃CN): λ_{max} (ε): 453 nm (1.32 × 10⁴ mol⁻¹dm³cm⁻¹). Phosphorescence (CH₃CN): λ_{ex} = 450 nm, λ_{em} = 617 nm.

HRMS (ESI) m/z found (calcd): 411.19560 (411.19585, $[M-2(\text{PF}_6)]^{2+}$). Elemental analysis calcd (%) for $\text{C}_{48}\text{H}_{60}\text{F}_{12}\text{N}_6\text{P}_2\text{Ru} \cdot 3 \text{H}_2\text{O}$: C 49.44, H 5.70, N 7.21; found: C 49.67, H 5.40, N 7.23.

[Ru(4,4'-(C₁₂H₂₅)₂-bpy)(bpy)₂](PF₆)₂ (RuC₁₂): from *cis*-[Ru(bpy)₂Cl₂] (0.20 g, 0.41 mmol) and **4,4'-(C₁₂H₂₅)₂-bpy** (0.20 g, 0.41 mmol). For purification, the procedure for **RuC₉** was followed. The orange precipitate was further purified by column chromatography on silica gel (dichloromethane/methanol = 99:1 to 90:10). The solvents were removed under reduced pressure and the remaining solids were dried *in vacuo*. **RuC₁₂** was obtained as a red solid (yield: 176 mg, 0.15 mmol, 36%). $R_f = 0.6$ (SiO₂, acetone/water/saturated KNO₃ 100:10:1). ¹H NMR (400 MHz, CD₃CN): $\delta = 8.48$ (dd, $J = 8.2, 1.9$ Hz, 4H, $h+h'$), 8.37 (d, $J = 1.8$ Hz, 2H, a), 8.04 (tq, $J = 8.0, 2.8, 1.5$ Hz, 4H, $i+i'$), 7.71 (dd, $J = 5.2, 1.2$ Hz, 4H, $k+k'$), 7.53 (d, $J = 5.8$ Hz, 2H, c), 7.38 (dq, $J = 7.2, 5.6, 1.3$ Hz, 4H, $j+j'$), 7.22 (dd, $J = 5.8, 1.8$ Hz, 2H, b), 2.78 (t, $J = 7.6$ Hz, 4H, d), 1.68 (p, $J = 7.4$ Hz, 4H, e), 1.25 (m, 36H, f), 0.87 (t, $J = 6.9$ Hz, 6H, g). ¹³C NMR (100 MHz, CD₃CN): $\delta = 158.00$ (C_q), 157.98 (C_q), 157.56 (C_q), 155.78 (C_q), 152.61 (CH, k or k'), 152.42 (CH, k or k'), 151.80 (CH, c), 138.53 (CH, $i+i'$), 128.50 (CH, b, j or j'), 128.44 (CH, b, j or j'), 125.15 (CH, a), 125.11 (CH, $h+h'$), 35.65 (CH₂, d), {32.58, 30.81, 30.32, 30.30, 30.24, 30.12, 30.02, 29.93, 29.74, 23.33 (CH₂, $e+f$)}, 14.35 (CH₃, g). ¹⁹F NMR (471 MHz, CD₃CN): $\delta = -72.33$ (d, $J = 706.2$ Hz). UV-Vis (CH₃CN): λ_{max} (ϵ): 453 nm (1.35×10^4 mol⁻¹dm³cm⁻¹). Phosphorescence (CH₃CN): $\lambda_{\text{ex}} = 450$ nm, $\lambda_{\text{em}} = 616$ nm. HRMS (ESI) m/z found (calcd): 453.24253 (453.24289, $[M-2(\text{PF}_6)]^{2+}$). Elemental analysis calcd (%) for $\text{C}_{54}\text{H}_{72}\text{F}_{12}\text{N}_6\text{P}_2\text{Ru}$: C 54.22, H 6.07, N 7.03; found: C 53.67, H 6.04, N 6.82.

[Ru(4,4'-(C₁₅H₃₁)₂-bpy)(bpy)₂](PF₆)₂ (RuC₁₅): from *cis*-[Ru(bpy)₂Cl₂] (0.21 g, 0.43 mmol) and **4,4'-(C₁₅H₃₁)₂-bpy** (0.25 g, 0.43 mmol). For purification, the crude product was purified via chromatography on silica gel (acetone/water/brine = 8:4:1). The solvents were removed under reduced pressure and the red solid was extracted with chloroform (3 x). The combined organic layers were dried over MgSO₄ and the solvents were evaporated under reduced pressure. Methanol was added and the white precipitate was filtered off. Henceforth, the procedure for **RuC₉** was followed. The orange

precipitate was collected by dissolving in acetone and dried by evaporation under reduced pressure and *in vacuo*. The yield in crude product before addition of hexafluorophosphate was 56% (258 mg, 0.24 mmol). From 105 mg of such crude product, KPF₆ reprecipitation afforded **RuC₁₅** as a red solid in 36% overall yield (82 mg, 0.064 mmol). ¹H NMR (400 MHz, CD₃CN): δ = 8.49 (d, *J* = 8.3 Hz, 4H, *h+h'*), 8.36 (d, *J* = 1.8 Hz, 2H, *a*), 8.04 (tt, *J* = 8.0, 1.8 Hz, 4H, *i+i'*), 7.71 (dd, *J* = 5.7, 1.4 Hz, 4H, *k+k'*), 7.53 (d, *J* = 5.8 Hz, 2H, *c*), 7.38 (dq, *J* = 6.7, 6.5, 1.2 Hz, 4H, *j+j'*), 7.22 (dd, *J* = 5.9, 1.8 Hz, 2H, *b*), 2.78 (t, *J* = 7.8 Hz, 4H, *d*), 1.68 (p, *J* = 7.2 Hz, 4H, *e*), 1.26 (m, 48H, *f*), 0.87 (t, *J* = 6.6 Hz, 6H, *g*). ¹³C NMR (100 MHz, CD₃CN): δ = 158.00 (C_q), 157.98 (C_q), 157.55 (C_q), 155.78 (C_q), 152.61 (CH, *k or k'*), 152.31 (CH, *k or k'*), 151.80 (CH, *c*), 138.52 (CH, *i+i'*), 128.50 (CH, *b, j or j'*), 128.43 (CH, *b, j or j'*), 125.11 (CH, *a+h+h'*), 35.63 (CH₂, *d*), {32.58, 30.79, 30.34, 30.32, 30.29, 30.22, 30.10, 30.02, 29.90, 29.70, 23.33 (CH₂, *e+f*)}, 14.34 (CH₃, *g*). ¹⁹F NMR (471 MHz, CD₃CN): δ = -72.43 (d, *J* = 706.6 Hz). UV-Vis (CH₃CN): λ_{max} (ε): 453 nm (1.32 × 10⁴ mol⁻¹dm³cm⁻¹). Phosphorescence (CH₃CN): λ_{ex} = 450 nm, λ_{em} = 613 nm. HRMS (ESI) *m/z* found (calcd): 495.29007 (495.29032, [M-2(PF₆)]²⁺), 1135.54224 (1135.54474, [M-PF₆]⁺). Elemental analysis calcd (%) for C₆₀H₈₄F₁₂N₆P₂Ru: C 56.29, H 6.61, N 6.56; found: C 57.49, H 7.01, N 6.31.

[Ru(4,4'-(C₁₇H₃₅)₂-bpy)(bpy)₂](PF₆)₂ (RuC₁₇): from *cis*-[Ru(bpy)₂Cl₂] (0.75 g, 1.56 mmol) and 4,4'-(C₁₇H₃₅)₂-bpy (0.98 g, 1.54 mmol). For purification, the crude product was purified via chromatography on silica gel (1st column: acetone/water/brine = 8:4:1, 2nd column: acetone/water/saturated KNO₃ = 100:10:1). The organic solvents were removed under reduced pressure and the red solid was extracted with chloroform (3 x). The combined organic layers were dried over MgSO₄ and the solvent was removed under reduced pressure. The red solid was taken up in methanol and subjected to ion exchange column with Amberlite (50 g, pre-soaked with brine and washed 10 x with water and 3 x with methanol). The solvent was removed under reduced pressure and the obtained red solid was redissolved in a mixture of chloroform and brine. The phases were separated, and the aqueous phase was extracted with chloroform (2 x). The combined organic layers were dried over MgSO₄ and the solvent was evaporated *in vacuo*. Trituration of the solid

in acetone (100 mL) followed by removal of 50 mL of acetone on the rotary evaporator, cooling to room temperature, filtration, and washing with acetone (50 mL) yielded the compound as chloride salt $[\text{Ru}(4,4'-(\text{C}_{17}\text{H}_{35})_2\text{-bpy})(\text{bpy})_2](\text{Cl})_2 \cdot \text{NaCl} \cdot 3 \text{H}_2\text{O}$. The filtrate was poured into saturated aqueous hexafluorophosphate to yield an orange precipitate that was filtered and washed with water and collected from the frit with acetone. Removal of the solvent in vacuo yielded **RuC₁₇** as a red solid (yield: 0.32 g, 0.22 mmol, 14%). ^1H NMR (400 MHz, CD_3CN): δ = 8.49 (d, J = 8.2 Hz, 4H, $h+h'$), 8.36 (d, J = 1.8 Hz, 2H, a), 8.04 (ddt, J = 8.1, 2.3, 1.5 Hz, 4H, $i+i'$), 7.71 (td, J = 5.7, 0.7 Hz, 4H, $k+k'$), 7.54 (d, J = 5.8 Hz, 2H, c), 7.39 (m, J = 7.2, 5.8, 1.3 Hz, 4H, $j+j'$), 7.22 (dd, J = 5.8, 1.8 Hz, 2H, b), 2.78 (t, J = 7.4 Hz, 4H, d), 1.68 (p, J = 7.2 Hz, 4H, e), 1.25 (m, 56H, f), 0.86 (t, J = 6.7 Hz, 6H, g). ^{13}C NMR (100 MHz, CD_3CN): δ = 157.97 (C_q), 157.94 (C_q), 157.51 (C_q), 155.74 (C_q), 152.57 (CH, k or k'), 152.36 (CH, k or k'), 151.77 (CH, c), 138.50 (CH, $i+i'$), 128.48 (CH, b , j or j'), 128.42 (CH, b , j or j'), 128.39 (CH, b , j or j'), 125.09 (CH, $a+h+h'$), 35.60 (CH_2 , d), {32.56, 30.75, 30.31, 30.29, 30.20, 30.07, 29.99, 29.87, 29.68, 23.31 (CH_2 , $e+f$)}, 14.32 (CH_3 , g). UV-Vis (CH_3CN): λ_{max} (ϵ): 453 nm ($1.69 \times 10^4 \text{ mol}^{-1}\text{dm}^3\text{cm}^{-1}$). Phosphorescence (CH_3CN): λ_{ex} = 450 nm, λ_{em} = 615 nm. HRMS (ESI) m/z found (calcd): 523.32126 (523.32168, $[\text{M}-2\text{PF}_6]^{2+}$). Elemental analysis calcd (%) for $\text{C}_{64}\text{H}_{92}\text{F}_{12}\text{N}_6\text{P}_2\text{Ru} \cdot 2 \text{C}_3\text{H}_6\text{O}$: C 57.88, H 7.22, N 5.79; found: C 57.84, H 7.08, N 5.71.

$[\text{Ru}(4,4'-(\text{C}_{19}\text{H}_{39})_2\text{-bpy})(\text{bpy})_2](\text{PF}_6)_2$ (RuC₁₉): from *cis*- $[\text{Ru}(\text{bpy})_2\text{Cl}_2]$ (0.10 g, 0.21 mmol) and **4,4'-(C₁₉H₃₉)₂-bpy** (0.20 g, 0.29 mmol). The crude product was purified via chromatography on silica gel (acetone/water/saturated KNO_3 = 100:10:1). After removing all solvents under reduced pressure, the procedure for **RuC₉** was carried out. **RuC₁₉** was finally obtained as a red solid (yield: 36 mg, 0.026 mmol, 8.9%). R_f = 0.2 (SiO_2 , acetone/water/saturated KNO_3 100:10:1). ^1H NMR (400 MHz, CD_3CN): δ = 8.49 (dd, J = 8.2, 1.7 Hz, 4H, $h+h'$), 8.36 (d, J = 1.8 Hz, 2H, a), 8.04 (tq, J = 7.9, 1.8 Hz, 4H, $i+i'$), 7.71 (d, J = 5.7, 1.4 Hz, 4H, $k+k'$), 7.54 (d, J = 5.8 Hz, 2H, c), 7.39 (dq, J = 6.1, 5.7, 1.6, 1.2 Hz, 4H, $j+j'$), 7.22 (dd, J = 5.8, 1.8 Hz, 2H, b), 2.78 (t, J = 7.9 Hz, 4H, d), 1.68 (p, J = 7.0 Hz, 4H, e), 1.25 (m, 64H, f), 0.87 (t, J = 6.5 Hz, 6H, g). ^{13}C NMR (100 MHz, CD_3CN): δ = 158.01 (C_q), 157.98 (C_q), 157.55 (C_q), 155.78 (C_q), 152.61

(CH, k or k'), 152.40 (CH, k or k'), 151.81 (CH, c), 138.54 (CH, $i+i'$), 128.52 (CH, b, j or j'), 128.45 (CH, b, j or j'), 128.42 (CH, b, j or j'), 125.12 (CH, $a+h+h'$), 35.64 (CH₂, d), {32.59, 30.79, 30.32, 30.23, 30.10, 30.03, 29.90, 29.71, 23.34 (CH₂, $e+f$)}, 14.35 (CH₃, g). UV-Vis (CH₃CN): λ_{\max} (ϵ): 453 nm (1.39×10^4 mol⁻¹dm³cm⁻¹). Phosphorescence (CH₃CN): λ_{ex} = 450 nm, λ_{em} = 615 nm. HRMS (ESI) m/z found (calcd): 551.35195 (551.35304, [M-2(PF₆)]²⁺), 1247.66904 (1247.67080, [M-PF₆]⁺). Elemental analysis calcd (%) for C₆₈H₁₀₀F₁₂N₆P₂Ru²⁺: C 58.65, H 7.24, N 6.04; found: C 58.13, H 7.23, N 5.91.

C. 3. Liposome preparation

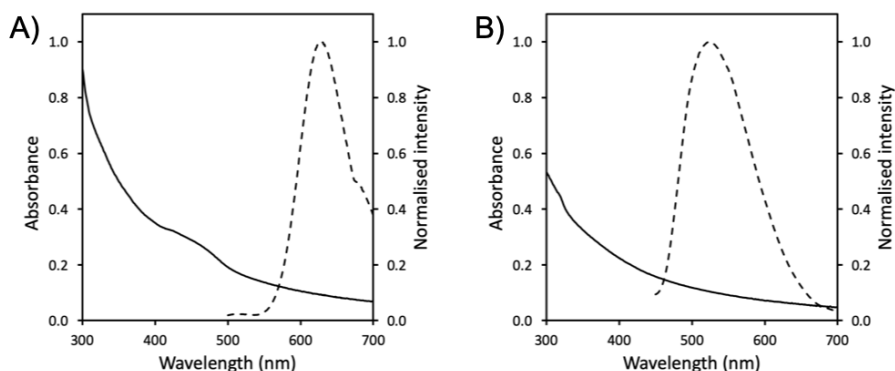


Figure C1. The absorption (solid line) and emission spectrum (dashed line, λ_{exc} = 450 nm for Ru and 380 nm for Re) of A) DSPC:NaDSPE-PEG2K 100:1 liposomes functionalised with **RuC₁₅** in 0.1 M NaH₂PO₄ buffer and B) DPPC:NaDSPE-PEG2K 100:1 liposomes functionalised with **ReC₉** in 0.1 M NaH₂PO₄ buffer. Experimental conditions: [DPPC or DSPC] = 6.25 mM, [NaDSPE-PEG2K] = 62.5 μ M, and [**RuC₁₅** or **ReC₉**] = 25 μ M.

Table C1. Diameter size (d), polydispersity index (PDI), absorption maxima ($I_{abs}^{[c]}$), and emission maxima (I_{em}) of liposomes prepared from lipids, NaDSPE-PEG2K, and **RuC_n** or **ReC_n** in a ratio of 100:1.0:0.4.

Sample ^[a]	DMPC				DPPC				DSPC						
	d (nm)	PDI ^[b]	$I_{abs}^{[c]}$ (nm)	I_{em} (nm)	d (nm)	PDI ^[b]	$I_{abs}^{[c]}$ (nm)	I_{em} (nm)	d (nm)	PDI ^[b]	$I_{abs}^{[c]}$ (nm)	I_{em} (nm)	d (nm)	PDI ^[b]	$I_{abs}^{[c]}$ (nm)
RuC₀	119	0.09	449	608	147	0.10	420	610	149	0.10	-	-	149	0.10	-
RuC₉	124	0.17	425	635	138	0.11	425	629	164	0.09	456	456	164	0.09	456
RuC₁₂	126	0.15	427	632	143	0.11	427	629	170	0.08	425	425	170	0.08	425
RuC₁₅	134	0.13	425	633	134	0.10	425	627	154	0.10	420	420	154	0.10	420
RuC₁₇	126	0.16	425	634	142	0.11	427	630	157	0.09	-	-	157	0.09	-
RuC₁₉	137	0.15	425	633	143	0.10	424	629	149	0.10	465	465	149	0.10	465
ReC₀	142	0.14	-	553	149	0.09	-	554	153	0.10	-	-	153	0.10	-
ReC₉	143	0.13	-	523	148	0.07	-	525	154	0.09	-	-	154	0.09	-
ReC₁₂	140	0.14	-	520, 552	144	0.07	-	-	163	0.08	-	-	163	0.08	-
ReC₁₅	132	0.12	-	531, 551	148	0.10	-	531, 553	153	0.11	-	-	153	0.11	-
ReC₁₇	143	0.14	-	510, 552	149	0.08	-	554	148	0.07	-	-	148	0.07	-
ReC₁₉	141	0.13	-	554	144	0.08	-	554	152	0.10	-	-	152	0.10	-

^[a] Experimental conditions: [DMPC, DPPC, or DSPC] = 6.25 mM, [NaDSPE-PEG2K] = 62.5 μ M, and [**RuC_n**] or [**ReC_n**] = 25 μ M in 0.1 M NaH₂PO₄ buffer. Bulk concentrations [**ReC_n**] and [**RuC_n**] indicate the theoretical concentrations (before extrusion). ^[b] Liposome size is considered to be uniformly distributed when PDI < 0.2. ^[c] I_{abs} could not be determined for rhenium complexes, due to the high levels of lipid scattering at I_{abs} of the rhenium complexes.

Table C2. Diameter size (d), polydispersity index (PDI), absorption maxima (λ_{abs}), and emission maxima (λ_{em}) of photocatalytic liposomes C_n prepared from DPPC, NaDSPE-PEG2K, RuC_n , and ReC_n in a ratio of 100:1.0:0.4:0.4.

Samples ^[a]	d (nm) ^[b]	PDI ^[b]	λ_{em} (nm)
C ₀	130 ± 3	0.066 ± 0.005	601 ^[c] , 607 ^[d]
C ₉	143 ± 9	0.083 ± 0.001	555 ^[c] , 627 ^[c] , 632 ^[d]
C ₁₂	128 ± 5	0.072 ± 0.016	556 ^[c] , 628 ^[c] , 630 ^[d]
C ₁₅	138 ± 2	0.080 ± 0.012	556 ^[c] , 626 ^[c] , 628 ^[d]
C ₁₇	137 ± 11	0.094 ± 0.006	556 ^[c] , 627 ^[c] , 627 ^[d]
C ₁₉	139 ± 3	0.077 ± 0.003	555 ^[c] , 627 ^[c] , 628 ^[d]

^[a] Experimental conditions: [DPPC] = 6.25 mM, [NaDSPE-PEG2K] = 62.5 μ M, [RuC_n] = 25 μ M, and [ReC_n] = 25 μ M in 0.1 M NaH₂PO₄ buffer. Bulk concentrations [ReC_n] and [RuC_n] indicate theoretical concentrations (before extrusion). ^[b] Average over two independent liposome preparations. Liposome size is considered to be uniformly distributed when PDI < 0.2. ^[c] Excited at 380 nm, ^[d] excited at 450 nm.

Table C3. Summary of DLS results obtained before and after light irradiation (t_{irr} = 3 h, λ > 455 nm) for photocatalytic liposomes C_n prepared from DPPC, NaDSPE-PEG2K, RuC_n , and ReC_n in a ratio of 100:1.0:0.4:0.4.

Sample ^[a]	Before irradiation		After irradiation	
	d (nm) ^[b]	PDI ^[b]	d (nm) ^[b]	PDI ^[b]
C ₀	161 ± 4	0.12 ± 0.01	171 ± 5	0.13 ± 0.01
C ₉	157 ± 5	0.11 ± 0.02	172 ± 5	0.18 ± 0.02
C ₁₂	150 ± 4	0.12 ± 0.01	164 ± 4	0.16 ± 0.01
C ₁₅	119 ± 4	0.11 ± 0.02	131 ± 4	0.17 ± 0.01
C ₁₇	158 ± 6	0.10 ± 0.04	165 ± 8	0.11 ± 0.02
C ₁₉	155 ± 6	0.10 ± 0.01	162 ± 6	0.14 ± 0.02

^[a] Experimental conditions: [DPPC] = 625 μ M, [NaDSPE-PEG2K] = 6.25 μ M, [RuC_n] = 2.5 μ M, and [ReC_n] = 2.5 μ M in 0.1 M NaHCO₃ and 0.1 M NaHAsc solutions at 25 °C. Bulk concentrations [ReC_n] and [RuC_n] indicate theoretical concentrations (before extrusion). ^[b] Average over three independent liposome preparations.

Table C4. Diameter size (d) and polydispersity index (PDI) of photocatalytic liposomes prepared from DPPC, NaDSPE-PEG2K, RuC_n and ReC_n in a ratio of 100:1.0:0.4:X with X = 0.0, 0.4, and 1.6, which were used for time-resolved spectroscopy measurements.

Samples ^[a]	d (nm) ^[b]	PDI ^[b]
RuC_9 and 0.0 % ReC_9	146	0.09
RuC_9 and 0.4 % ReC_9	114	0.10
RuC_9 and 1.6 % ReC_9	108	0.18
RuC_{19} and 0.0 % ReC_{19}	136	0.08
RuC_{19} and 0.4 % ReC_{19}	142	0.06
RuC_{19} and 1.6 % ReC_{19}	129	0.09

^[a] Experimental conditions: [DPPC] = 6.25 mM, [NaDSPE-PEG2K] = 62.5 μM , [RuC_n] = 25 μM , and [ReC_n] = 0, 25 or 100 μM in CO_2 -saturated 0.1 M NaHAsc aqueous solution. Bulk concentrations [ReC_n] and [RuC_n] indicate theoretical concentrations (before extrusion). ^[b] Liposome size is considered to be uniformly distributed when PDI < 0.2.

C. 4. Photocatalysis

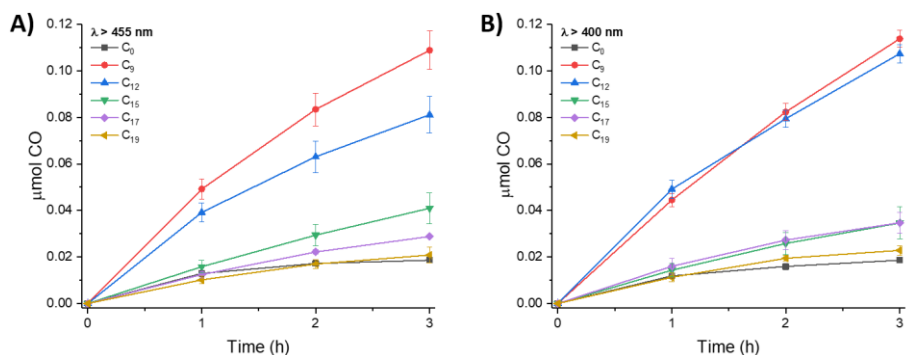


Figure C2. Photocatalytic CO formation after three hours of simulated solar light irradiation (AM 1.5G, 100 mW cm^{-2}) at (A) $\lambda > 455 \text{ nm}$ or (B) $\lambda > 400 \text{ nm}$ as a function of alkyl chain length for DPPC:NaDSPE-PEG2K 100:1 photocatalytic liposomes C_n containing ReC_n - RuC_n with the same n. Experimental conditions: [DPPC] = 625 μM , [NaDSPE-PEG2K] = 6.25 μM , [RuC_n] = 2.5 μM , and [ReC_n] = 2.5 μM in CO_2 -saturated 0.1 M NaH_2PO_4 and 0.1 M NaHAsc aqueous solution (3 mL, pH \approx 6.3) at 25 $^\circ\text{C}$. Bulk concentrations [ReC_n] and [RuC_n] indicate theoretical concentrations (before extrusion). Experiments were performed in triplicates.

Appendix C

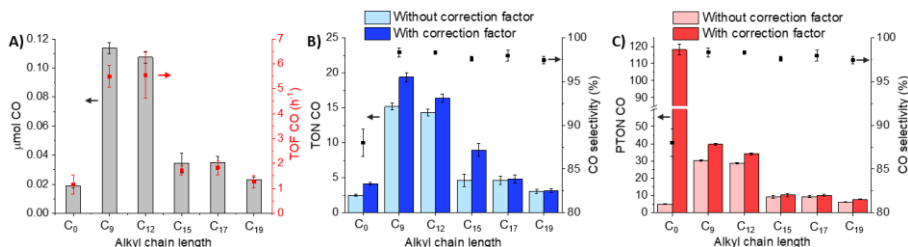


Figure C3. Photocatalytic activity after three hours of simulated solar light irradiation ($\lambda > 400$ nm, AM 1.5G, 100 mW cm^{-2}) as a function of alkyl chain length for DPPC:NaDSPE-PEG2K 100:1 photocatalytic liposomes C_n containing $\text{ReC}_n\text{-RuC}_n$ with the same n : (A) evolved μmol of CO and uncorrected TOF CO; (B) (light blue) uncorrected and (dark blue) corrected TON CO and CO selectivity; (C) (light red) uncorrected and (dark red) corrected turnover number of CO produced per mol of photosensitiser (PTON CO) and CO selectivity. The TONs and TOFs were obtained after three hours and one hour, respectively. The applied correction (η_{immob}) can be found in Figure 3.4 and Table C9. Experimental conditions: [DPPC] = $625 \mu\text{M}$, [NaDSPE-PEG2K] = $6.25 \mu\text{M}$, [ReC_n] = $2.5 \mu\text{M}$ and [RuC_n] = $2.5 \mu\text{M}$; CO_2 -saturated $0.1 \text{ M NaH}_2\text{PO}_4$ and 0.1 M NaHAsc aqueous solution (3 mL , $\text{pH} \approx 6.3$) at $25 \text{ }^\circ\text{C}$. Bulk concentrations [ReC_n] and [RuC_n] indicate theoretical concentrations (before extrusion). Experiments were performed in triplicates.

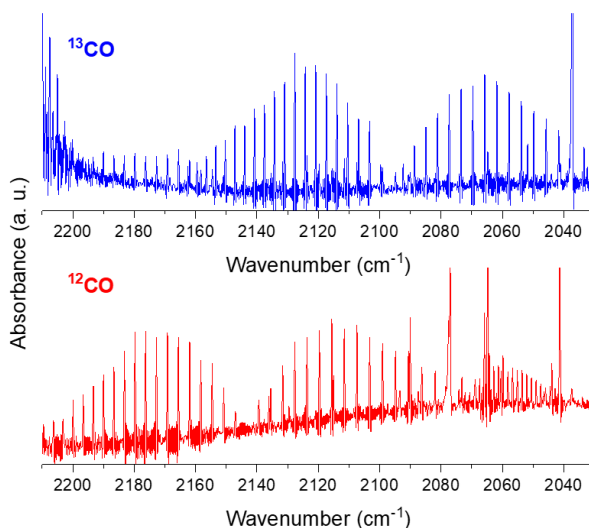


Figure C4. IR absorbance spectra of CO gas obtained from isotopic labelling control experiments using (blue) $^{13}\text{CO}_2$ and (red) $^{12}\text{CO}_2$ as the headspace gas after three hours of photocatalysis with DPPC:NaDSPE-PEG2K 100:1 photocatalytic liposomes C_9 containing ReC_9 and RuC_9 . Experimental conditions: [DPPC] = 6.25 mM , [NaDSPE-PEG2K] = $62.5 \mu\text{M}$, [RuC_9] = $25 \mu\text{M}$, and [ReC_9] = $25 \mu\text{M}$ in $0.1 \text{ M NaH}_2\text{PO}_4$ and 0.1 M NaHAsc . Bulk concentrations [ReC_n] and [RuC_n] indicate theoretical concentrations (before extrusion).

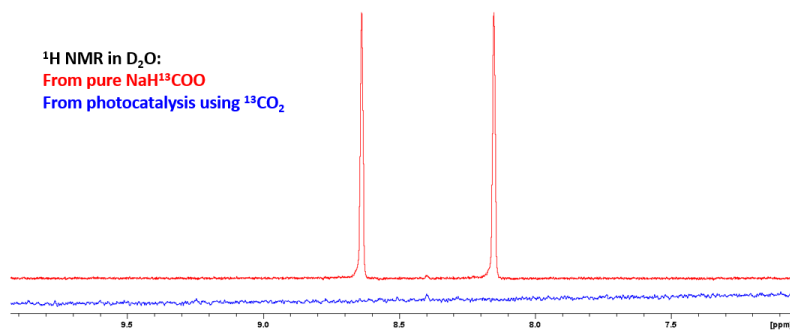


Figure C5. ¹H NMR spectra of (red) isotopically labelled sodium formate and (blue) formate obtained from isotopic labelling control experiments using ¹³CO₂ as the headspace gas after three hours of photocatalysis using DPPC:NaDSPE-PEG2K 100:1 photocatalytic liposomes **C₉** containing **ReC₉** and **RuC₉**. Experimental conditions: [DPPC] = 6.25 mM, [NaDSPE-PEG2K] = 62.5 μM, [**RuC₉**] = 25 μM, and [**ReC₉**] = 25 μM in 0.1 M NaH₂PO₄ and 0.1 M NaHAsc. Bulk concentrations [**ReC_n**] and [**RuC_n**] indicate theoretical concentrations (before extrusion).

Table C5. Summary of photocatalysis results obtained from all alkyl chain lengths in DPPC:NaDSPE-PEG2K 100:1 photocatalytic liposomes C_n containing ReC_n and RuC_n with the same n . All experiments were carried out in CO_2 -saturated 0.1 M NaH_2PO_4 and 0.1 M NaHAsc solutions at 25 °C for three hours under visible light ($\lambda > 400$ or 455 nm), and in triplicates. In addition to CO and H_2 no other photocatalytic products were detected. TOF and PTOF values were calculated by averaging the obtained values of each hour.

Alkyl chain length	λ (nm)	CO (nmol)	H_2 (nmol)	TON CO	TON H_2	PTON CO	PTON H_2	TOF CO (h^{-1})	TOF H_2 (h^{-1})	PTOF CO (h^{-1})	PTOF H_2 (h^{-1})	CO selectivity (%)
C_0	400	18.6 ± 1.0	2.9 ± 1.2	2.5 ± 0.1	0.4 ± 0.2	5.0 ± 0.1	0.8 ± 0.2	1.2 ± 0.4	0.2 ± 0.1	2.3 ± 0.8	0.3 ± 0.1	88 ± 2
	455	18.6 ± 0.9	0.9 ± 0.1	2.5 ± 0.1	0.1 ± 0.1	5.0 ± 0.1	0.3 ± 0.1	1.2 ± 0.5	<0.1	2.5 ± 0.9	0.2 ± 0.1	94 ± 1
C_9	400	113.8 ± 3.7	2.5 ± 0.5	15.2 ± 0.5	0.3 ± 0.1	30.3 ± 0.5	0.7 ± 0.1	5.5 ± 0.4	0.1 ± 0.1	11.0 ± 0.9	0.2 ± 0.1	98 ± 1
	455	108.8 ± 8.3	1.1 ± 0.1	14.5 ± 1.1	0.2 ± 0.1	29.0 ± 1.1	0.3 ± 0.1	5.7 ± 0.9	<0.1	11.3 ± 1.7	0.1 ± 0.1	99 ± 1
C_{12}	400	107.4 ± 3.9	2.0 ± 0.6	14.3 ± 0.5	0.3 ± 0.1	28.6 ± 0.5	0.5 ± 0.1	5.5 ± 0.9	0.1 ± 0.1	11.1 ± 1.8	0.2 ± 0.1	98 ± 1
	455	81.1 ± 7.8	1.4 ± 0.4	10.8 ± 1.0	0.2 ± 0.1	21.6 ± 1.0	0.4 ± 0.1	4.3 ± 0.8	0.1 ± 0.1	8.7 ± 1.6	0.2 ± 0.1	98 ± 1
C_{15}	400	34.6 ± 0.7	0.7 ± 0.2	4.6 ± 0.9	0.1 ± 0.1	9.2 ± 0.9	0.2 ± 0.1	1.7 ± 0.2	<0.1	3.4 ± 0.4	<0.1	98 ± 1
	455	40.9 ± 6.6	0.8 ± 0.3	5.5 ± 0.9	0.1 ± 0.1	10.9 ± 0.9	0.2 ± 0.1	2.0 ± 0.1	<0.1	3.9 ± 0.3	<0.1	98 ± 1
C_{17}	400	34.7 ± 4.4	1.0 ± 0.3	4.6 ± 0.6	0.1 ± 0.1	9.2 ± 0.6	0.3 ± 0.1	1.8 ± 0.3	<0.1	3.7 ± 0.6	<0.1	98 ± 1
	455	28.8 ± 0.3	0.5 ± 0.1	3.8 ± 0.1	<0.1	7.7 ± 0.1	<0.1	1.5 ± 0.2	<0.1	2.9 ± 0.4	<0.1	97 ± 2
C_{19}	400	22.8 ± 2.0	0.5 ± 0.1	3.0 ± 0.3	<0.1	6.1 ± 0.3	0.1 ± 0.1	1.3 ± 0.2	<0.1	2.5 ± 0.5	<0.1	97 ± 1
	455	20.8 ± 3.3	0.5 ± 0.1	2.8 ± 0.4	<0.1	5.5 ± 0.4	0.1 ± 0.1	1.1 ± 0.2	<0.1	2.3 ± 0.4	<0.1	98 ± 1

Table C6. Summary of photocatalysis results for CO gas obtained from all alkyl chain lengths in DPPC:NaDSPE-PEG2K 1001 photocatalytic liposomes C_n containing ReC_n and RuC_n with the same n before and after applying η_{limmob} as correction factor (Table C9). Non-corrected data is also shown in Table C5.

Alkyl chain length	λ (nm)	TON	CO	$corrTON$	CO	PTON	CO	$corrPTON$	TOF CO (h^{-1})	$corrTOF$	CO (h^{-1})	PTOF CO (h^{-1})	$corrPTOF$	CO (h^{-1})
C_0	400	2.5 ± 0.1	4.1 ± 0.2	5.0 ± 0.1	118.1 ± 3.2	1.2 ± 0.4	1.9 ± 0.6	2.3 ± 0.8	55.0 ± 18.4					
	455	2.5 ± 0.1	4.1 ± 0.2	5.0 ± 0.1	118.2 ± 3.0	1.2 ± 0.5	2.1 ± 0.8	2.5 ± 0.9	68.3 ± 21.6					
C_9	400	15.2 ± 0.5	19.4 ± 0.6	30.3 ± 0.5	39.7 ± 0.7	5.5 ± 0.4	7.0 ± 0.6	11.0 ± 0.9	14.4 ± 1.1					
	455	14.5 ± 1.1	18.6 ± 1.4	29.0 ± 1.1	38.0 ± 1.4	5.7 ± 0.9	7.2 ± 1.1	11.3 ± 1.7	14.8 ± 2.3					
C_{12}	400	14.3 ± 0.5	16.4 ± 0.6	28.6 ± 0.5	34.2 ± 0.6	5.5 ± 0.9	6.3 ± 1.0	11.1 ± 1.8	13.2 ± 2.2					
	455	10.8 ± 1.0	12.4 ± 1.2	21.6 ± 1.0	25.8 ± 1.2	4.3 ± 0.8	5.0 ± 0.9	8.7 ± 1.6	10.4 ± 1.9					
C_{15}	400	4.6 ± 0.9	6.3 ± 1.3	9.2 ± 0.9	10.9 ± 1.1	1.7 ± 0.2	2.4 ± 0.3	3.4 ± 0.4	4.1 ± 0.4					
	455	5.5 ± 0.9	7.5 ± 1.2	10.9 ± 0.9	12.9 ± 1.0	2.0 ± 0.1	2.7 ± 0.2	3.9 ± 0.3	4.6 ± 0.3					
C_{17}	400	4.6 ± 0.6	4.8 ± 0.6	9.2 ± 0.6	10.2 ± 0.7	1.8 ± 0.3	1.9 ± 0.3	3.7 ± 0.6	4.0 ± 0.7					
	455	3.8 ± 0.1	4.0 ± 0.1	7.7 ± 0.1	8.5 ± 0.1	1.5 ± 0.2	1.5 ± 0.2	2.9 ± 0.4	3.2 ± 0.4					
C_{19}	400	3.0 ± 0.3	3.1 ± 0.3	6.1 ± 0.3	7.8 ± 0.3	1.3 ± 0.2	1.3 ± 0.3	2.5 ± 0.5	3.3 ± 0.6					
	455	2.8 ± 0.4	2.9 ± 0.5	5.5 ± 0.4	7.1 ± 0.6	1.1 ± 0.2	1.2 ± 0.2	2.3 ± 0.4	2.9 ± 0.6					

Table C7. Summary of photocatalysis experiments obtained from all alkyl chain lengths in DPPC:NaDSPE-PEG2K 1001 photocatalytic liposomes **C_n**. All experiments were conducted in CO₂- or N₂-saturated 0.1 M NaH₂PO₄ and 0.1 M NaHAsc buffer solutions for three hours at 25 °C under visible light ($\lambda > 455$ nm) and in duplicates, except for the first row in C₉ system whose experiments were performed as triplicates. Symbols “√” and “-” stand for “included” and “not included” respectively, and “n. d.” stands for “not detected”.

Alkyl chain length	Components			Gaseous products after three-hour experiments					
	Catalyst	Photosensitiser	Sodium ascorbate	CO ₂	CO (nmol)	H ₂ (nmol)	TON CO	TON H ₂	CO selectivity (%)
C ₀	√	-	√	√	n. d.	n. d.	-	-	-
	-	√	√	√	0.1 ± 0.1	0.1 ± 0.1	-	-	-
C ₉	√	√	√	√	108.9 ± 8.3	1.1 ± 0.1	14.5 ± 1.1	0.2 ± 0.1	99 ± 1
	√	√	√	√ ^[a]	n. d.	n. d.	-	-	-
	√	√	-	√	n. d.	n. d.	-	-	-
	√	√	√	- ^[b]	n. d.	n. d.	-	-	-
	√	-	√	√	n. d.	n. d.	-	-	-
	-	√	√	√	0.2 ± 0.1	n. d.	-	-	-
C ₁₂	√	-	√	√	0.2 ± 0.1	n. d.	-	-	-
	-	√	√	√	n. d.	n. d.	-	-	-
C ₁₅	√	-	√	√	n. d.	n. d.	-	-	-
	-	√	√	√	0.3 ± 0.1	n. d.	-	-	-
C ₁₇	√	-	√	√	0.3 ± 0.1	0.3 ± 0.1	-	-	-
	-	√	√	√	n. d.	n. d.	-	-	-
C ₁₉	√	-	√	√	0.1 ± 0.1	n. d.	-	-	-
	-	√	√	√	0.3 ± 0.1	n. d.	-	-	-

^[a] Experiments were carried out in the dark. ^[b] Experiments were carried out in N₂-saturated solutions.

C. 5. Electrochemistry

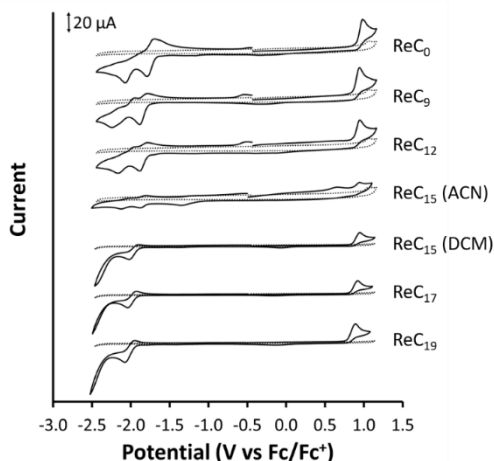


Figure C6. Cyclic voltammograms of solutions of ReC_n (1 mM) in degassed acetonitrile (ReC_0 , ReC_9 , ReC_{12} , and ReC_{15}) or degassed dichloromethane (ReC_{15} , ReC_{17} , and ReC_{19}) with 0.1 M Bu_4NPF_6 electrolyte, measured at 25 °C. The voltammograms were obtained at a scanning rate of 100 mV s^{-1} with a glassy carbon working electrode, Ag/AgCl reference electrode, and a Pt wire auxiliary electrode.

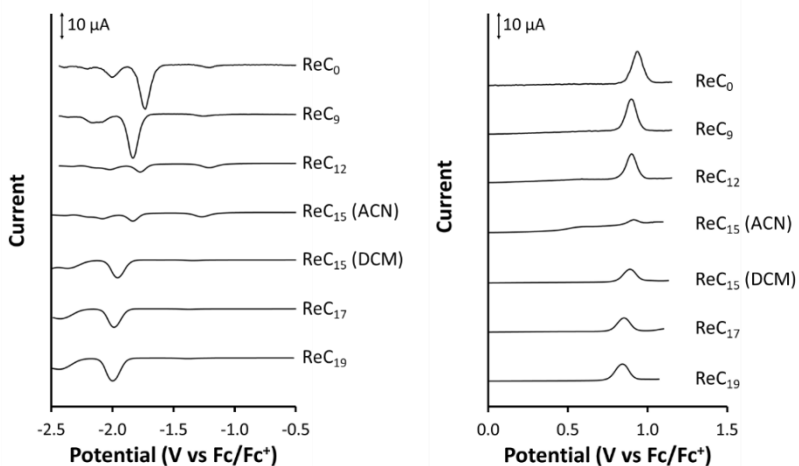


Figure C7. Differential pulse voltammograms of solutions of ReC_n (1 mM) in degassed acetonitrile (ReC_0 , ReC_9 , ReC_{12} , and ReC_{15}) or degassed dichloromethane (ReC_{15} , ReC_{17} , and ReC_{19}) with 0.1 M Bu_4NPF_6 electrolyte, measured at 25 °C. The voltammograms were obtained at a scanning rate of 50 mV s^{-1} with a glassy carbon working electrode, Ag/AgCl reference electrode, and a Pt wire auxiliary electrode.

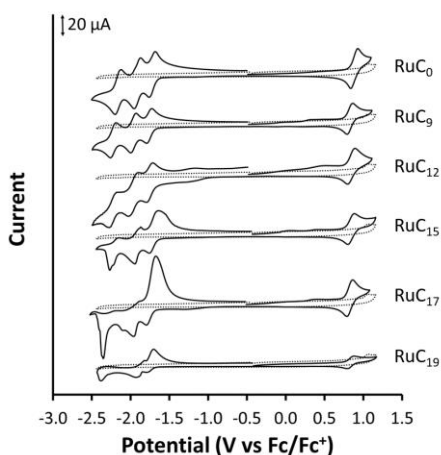


Figure C8. Cyclic voltammograms of solutions of RuC_n (1 mM) in degassed acetonitrile with 0.1 M Bu_4NPF_6 electrolyte, measured at 25 °C. The voltammograms were obtained at a scanning rate of 100 mV s^{-1} with a glassy carbon working electrode, Ag/AgCl reference electrode, and a Pt wire auxiliary electrode.

Table C8. Redox potentials of RuC_n and ReC_n complexes.^[a]

Metal complex	$E_{1/2}$ (oxdn) in V vs. Fc^+/Fc	$E_{1/2}$ (redn) in V vs. Fc^+/Fc
RuC_0	0.88	-1.72, -1.92, -2.16
RuC_9	0.83	-1.76, -1.97, -2.22
RuC_{12}	0.84	-1.70, -1.91, -2.20
RuC_{15}	0.84	-1.70, -1.91, -2.20
RuC_{17}	0.80	-1.76, -1.92, -2.26
RuC_{19}	0.83	-1.74, -1.87, -2.35
ReC_0	0.94	-1.73, -2.00
ReC_9	0.90	-1.83, -2.15
ReC_{12}	0.90	-1.83, -2.12
ReC_{15}	0.91 ^[b]	-1.83 ^[b] , -2.08 ^[b]
	0.89 ^[c]	-1.96 ^[c] , -2.37 ^[c]
ReC_{17}	0.85 ^[c]	-1.99 ^[c] , -2.43 ^[c]
ReC_{19}	0.84 ^[c]	-2.00 ^[c] , -2.44 ^[c]

^[a] These values were obtained at 25 °C in degassed acetonitrile solutions containing 0.1 M tetrabutylammonium hexafluorophosphate and 1 mM metal complex. ^b ReC_{15} was partially soluble in acetonitrile. ^c These values were measured in degassed dichloromethane.

C. 6. Liposome immobilisation efficiency

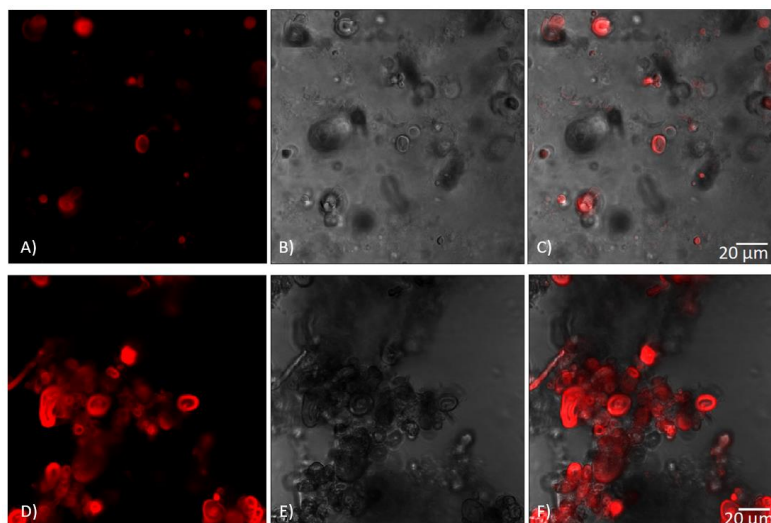


Figure C9. Confocal microscopy of DPPC (A, B, C) and DMPC (D, E, F) giant vesicles containing 2% RuC_{12} in 0.1 M NaH_2PO_4 buffer (pH = 7.7). Figures C9A and C9D are fluorescence images, Figures C9B and C9E are transmission images, and Figures C9C and C9F are overlay images. Images were taken with a Nikon Ti2 microscope at 80x total zoom, 488 nm excitation, and 640 – 680 nm emission.

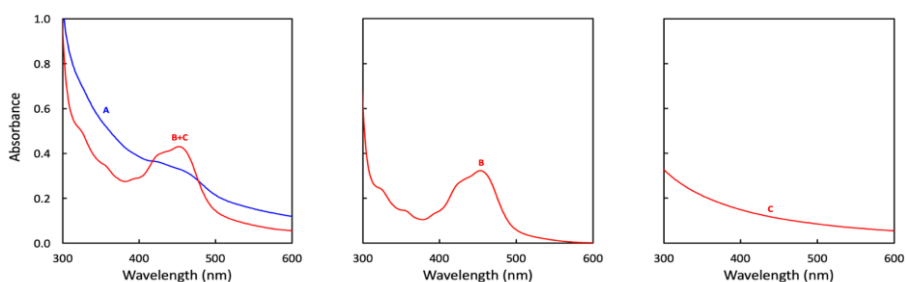


Figure C10. UV-Vis absorption spectra of A) DSPC:NaDSPE-PEG2K 100:1 liposomes functionalised with RuC_{12} in 0.1 M NaH_2PO_4 buffer (blue line), B) RuC_{12} in acetonitrile (no liposomes), C) DSPC:NaDSPE-PEG2K 100:1 liposomes (without RuC_{12}) in 0.1 M NaH_2PO_4 buffer. Red curve in A shows the addition of the absorption spectra of B and C; it obviously does not superpose to the absorption spectrum of the Ru-functionalised liposomes (blue line), illustrating the limits of UV-Vis spectroscopy for quantifying the RuC_{12} concentration in liposomes. Experimental conditions: $[\text{DSPC}] = 6.25 \text{ mM}$, $[\text{NaDSPE-PEG2K}] = 62.5 \text{ } \mu\text{M}$, and $[\text{RuC}_{12}] = 25 \text{ } \mu\text{M}$.

Appendix C

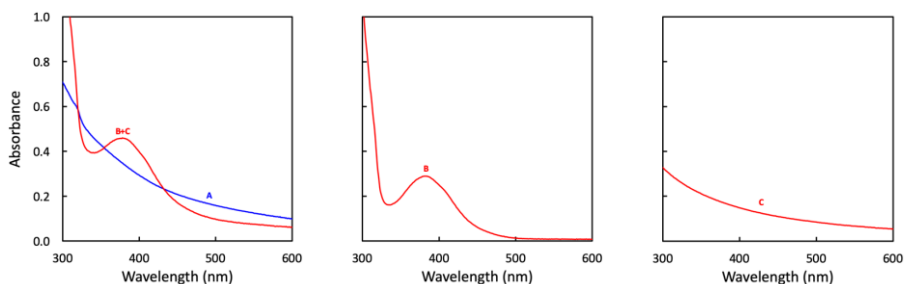


Figure C11. UV-Vis absorption spectra of A) DSPC:NaDSPE-PEG2K 100:1 liposomes functionalised with **ReC₁₂** in 0.1 M NaH₂PO₄ buffer, B) **ReC₁₂** in chloroform (no liposomes), C) DSPC:NaDSPE-PEG2K 100:1 liposomes (without **ReC₁₂**) in 0.1 M NaH₂PO₄ buffer. Red curve in A shows the addition of the absorption spectra of B and C; it obviously does not superpose with the absorption spectrum of the Re-functionalised liposomes (blue line), illustrating the limits of UV-Vis spectroscopy for quantifying the **ReC₁₂** concentration in liposomes. Experimental conditions: [DSPC] = 6.25 mM, [NaDSPE-PEG2K] = 62.5 μM, and [ReC₁₂] = 25 μM.

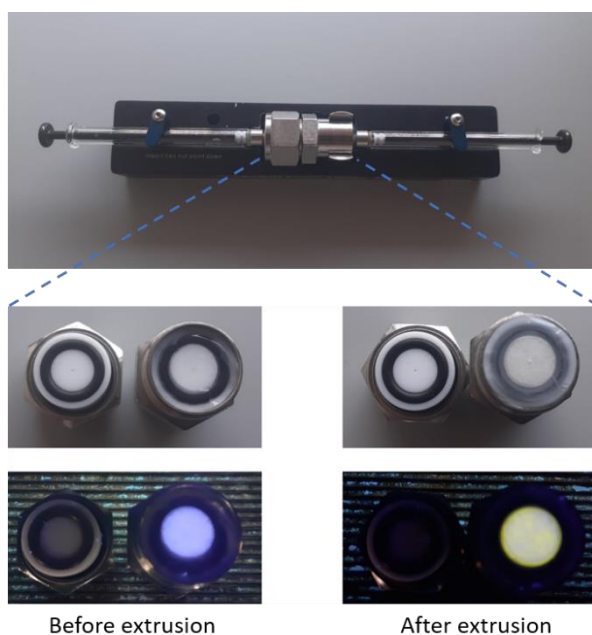


Figure C12. The Avanti Polar Lipids mini-extruder used to prepare liposomes (in this case DPPC:PEG2K:RuC₉:ReC₉ in a ratio 100:1.0:0.4:0.4) and the internal membrane supports including the filter supports and the polycarbonate membrane (0.2 μm) before and after extrusion. A deposit was observed on the filter after extrusion, which coloured brightly yellow under UV light ($\lambda = 366$ nm), which indicated that some **ReC₉** ($\lambda_{\text{abs}} = 380$ nm and $\lambda_{\text{em}} = 582$ nm in chloroform) was present on the filter.

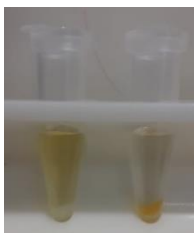


Figure C13. Solutions of $\text{RuC}_0\text{-ReC}_0$ liposomes (left) and $\text{RuC}_9\text{-ReC}_9$ liposomes (right) after ultracentrifugation.

Table C9. Immobilisation efficiencies, determined by ICP-MS, for photocatalytic liposomes C_n prepared from DPPC, NaDSPE-PEG2K, RuC_n , and ReC_n (100:1.0:0.4:0.4).^[a]

Metal complex	$\eta_{\text{extr}}^{[b]}$	$\eta_{\text{encap}}^{[b]}$	$\eta_{\text{immob}}^{[b]}$
RuC_0	$94.9 \pm 5.1\%$	$4.2 \pm 4.2\%$	$3.8 \pm 3.8\%$
RuC_9	$80.3 \pm 1.1\%$	$95.0 \pm 0.8\%$	$76.3 \pm 1.7\%$
RuC_{12}	$86.4 \pm 0.2\%$	$97.0 \pm 0.5\%$	$83.8 \pm 0.3\%$
RuC_{15}	$85.2 \pm 6.3\%$	$99.6 \pm 0.3\%$	$84.9 \pm 6.0\%$
RuC_{17}	$91.2 \pm 5.1\%$	$99.5 \pm 0.2\%$	$90.7 \pm 5.2\%$
RuC_{19}	$78.6 \pm 2.7\%$	$99.2 \pm 0.1\%$	$78.0 \pm 2.6\%$
ReC_0	$95.1 \pm 4.9\%$	$62.0 \pm 5.5\%$	$59.3 \pm 8.2\%$
ReC_9	$80.2 \pm 10.9\%$	$97.5 \pm 0.8\%$	$78.1 \pm 10.0\%$
ReC_{12}	$86.1 \pm 14.0\%$	$97.4 \pm 0.6\%$	$83.7 \pm 13.1\%$
ReC_{15}	$75.2 \pm 22.3\%$	$97.2 \pm 0.6\%$	$73.2 \pm 22.2\%$
ReC_{17}	$96.2 \pm 3.8\%$	$98.4 \pm 1.0\%$	$94.7 \pm 4.7\%$
ReC_{19}	$99.3 \pm 0.7\%$	$96.9 \pm 0.4\%$	$96.2 \pm 1.1\%$

^[a] Experimental conditions: $[\text{DPPC}] = 6.25 \text{ mM}$, $[\text{NaDSPE-PEG2K}] = 62.5 \text{ }\mu\text{M}$, $[\text{RuC}_n] = 25 \text{ }\mu\text{M}$, and $[\text{ReC}_n] = 25 \text{ }\mu\text{M}$ in $0.1 \text{ M NaH}_2\text{PO}_4$ buffer. Bulk concentrations $[\text{ReC}_n]$ and $[\text{RuC}_n]$ indicate theoretical concentrations (before extrusion). ^[b] The errors are based on two independent liposome preparations.

C. 7. Transient absorption spectroscopy

C. 7. 1. Supplementary figures

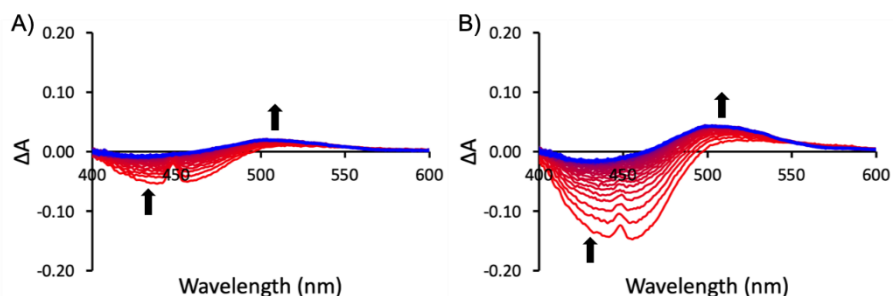


Figure C14. Time-resolved absorption spectroscopy data after laser excitation ($\lambda_{\text{exc}} = 450$ nm, 3.5 mJ per pulse) on a 2 μs timescale (timestep = 0.04 μs) for DPPC-NaDSPE-PEG2K liposome systems C_n consisting of A) RuC_9 and 0.0% ReC_9 and B) RuC_{19} and 0.0% ReC_{19} . Experimental conditions: [DPPC] = 6.25 mM, [NaDSPE-PEG2K] = 62.5 μM , and $[\text{RuC}_n] = 25$ μM in CO_2 -saturated 0.1 M NaHAsc aqueous solution. Bulk concentration $[\text{RuC}_n]$ indicates theoretical concentration (before extrusion). The observed artefact in the data at 450 nm is due to the scattering of laser light.

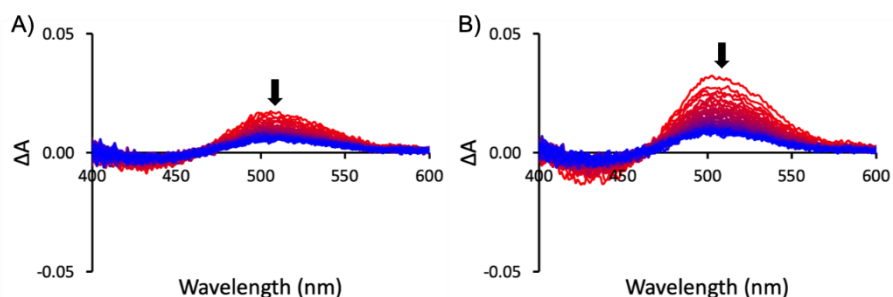


Figure C15. Time-resolved absorption spectroscopy data after laser excitation ($\lambda_{\text{exc}} = 450$ nm, 3.5 mJ per pulse) on a 2 ms timescale (timestep = 0.04 ms) for DPPC-NaDSPE-PEG2K liposome systems C_n consisting of A) RuC_9 and 0.0% ReC_9 and B) RuC_{19} and 0.0% ReC_{19} . Experimental conditions: [DPPC] = 6.25 mM, [NaDSPE-PEG2K] = 62.5 μM , and $[\text{RuC}_n] = 25$ μM in CO_2 -saturated 0.1 M NaHAsc aqueous solution. Bulk concentration $[\text{RuC}_n]$ indicates theoretical concentration (before extrusion).

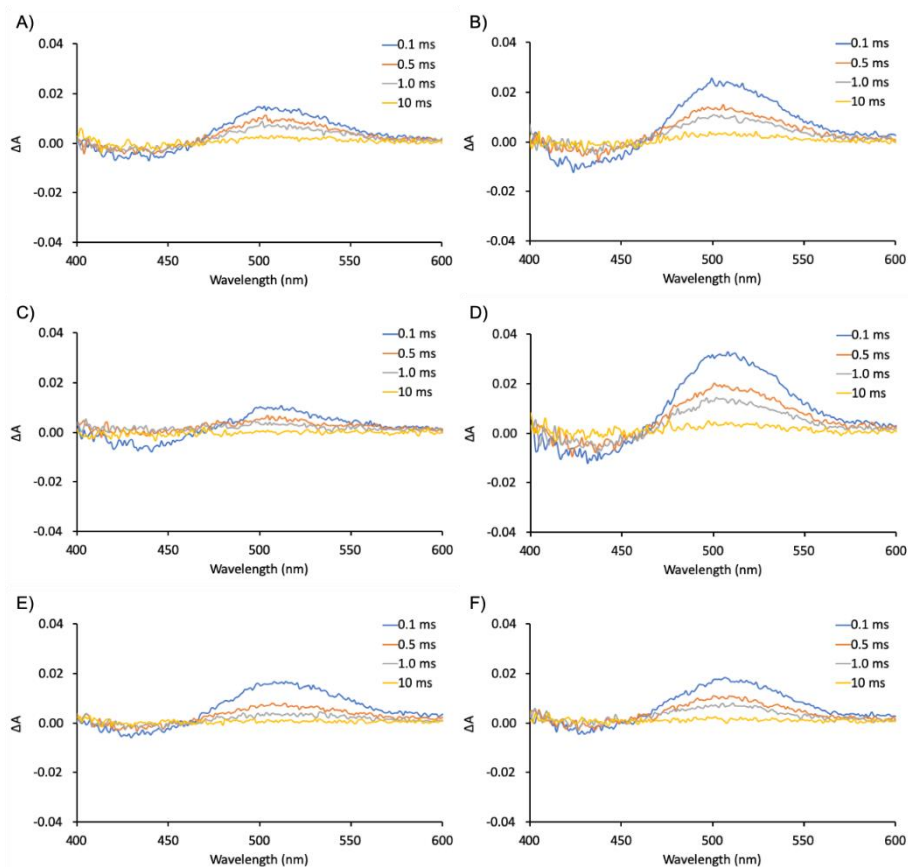


Figure C16. Time-resolved absorption spectroscopy data after laser excitation ($\lambda_{\text{exc}} = 450 \text{ nm}$, 3.5 mJ per pulse) on a 10 ms timescale (timestep = 0.1 ms) for DPPC-NaDSPE-PEG2K liposome systems C_n consisting of A) RuC_9 and 0.0% ReC_9 , B) RuC_{19} and 0.0% ReC_{19} , C) RuC_9 and 0.4% ReC_9 , D) RuC_{19} and 0.4% ReC_{19} , E) RuC_9 and 1.6% ReC_9 , and F) RuC_{19} and 1.6% ReC_{19} . Experimental conditions: [DPPC] = 6.25 mM, [NaDSPE-PEG2K] = 62.5 μM , [RuC_n] = 25 μM , and [ReC_n] = 0, 25 or 100 μM in CO_2 -saturated 0.1 M NaHAsc aqueous solution. Bulk concentrations [ReC_n] and [RuC_n] indicate theoretical concentrations (before extrusion).

C. 7. 2. Kinetic model

In the absence of quencher ReC_n , the rate equation for RuC_n^- is a combination of the formation of RuC_n^- due to reductive quenching of RuC_n^* by HAsc^- and the decay of RuC_n^- due to the second-order charge recombination of RuC_n^- and HAsc^* (Equation C5). The disappearance of RuC_n^* is very fast (μs) in comparison to the disappearance of RuC_n^- (ms). The TA spectroscopy measurements were performed in the ms timescale (10 ms with a timestep

of 0.1 ms) and thus the rate equation for RuC_n^- simplifies to Equation C6. Assuming that $[\text{RuC}_n^-]_0$ equals $[\text{HAsc}^\bullet]_0$ leads to a standard second order rate law (Equation C7) with its solution (Equation C8), which can be rewritten to Equation 3.4.

$$\frac{d[\text{RuC}_n^-]}{dt} = k_{\text{RQ}}[\text{RuC}_n^*][\text{HAsc}^-] - k_{\text{CR}}[\text{RuC}_n^-][\text{HAsc}^\bullet] \quad \text{Equation C5}$$

$$\frac{d[\text{RuC}_n^-]}{dt} = -k_{\text{CR}}[\text{RuC}_n^-][\text{HAsc}^\bullet] \quad \text{Equation C6}$$

$$\frac{d[\text{RuC}_n^-]}{dt} = -k_{\text{CR}}[\text{RuC}_n^-]^2 \quad \text{Equation C7}$$

$$\frac{1}{[\text{RuC}_n^-]} = \frac{1}{[\text{RuC}_n^-]_0} + k_{\text{CR}}t \quad \text{Equation C8}$$

In the presence of quencher ReC_n , the rate equation for RuC_n^- is a combination of the decay of RuC_n^- due to second-order charge recombination of RuC_n^- and HAsc^\bullet and due to first-order quenching by ReC_n (Equation C9). Equation C9 can be solved according to Limburg et al.⁸ to give Equation 3.6 in the main text.

$$\frac{d[\text{RuC}_n^-]}{dt} = -k_{\text{CR}}[\text{RuC}_n^-][\text{HAsc}^\bullet] - k_{\text{Q}}[\text{ReC}_n] \quad \text{Equation C9}$$

C. 7. 3. Data fitting

The average absorbance between 490 – 540 nm was fitted using Equation C10 and C11, which is derived from Equation 3.5 in Chapter 3 using the Lambert-Beer law. At these wavelengths the concentration and absorption of RuC_n^- are strictly proportional to the optical pathlength ($l = 1$ cm) and the molar absorption coefficient ($\epsilon_{505\text{nm}} = 1.2 \times 10^4 \text{ M}^{-1}\text{cm}^{-1}$ for $[\text{Ru}(\text{bpy})_3]^+$ in acetonitrile⁹ was used).

$$A(t) = \frac{A_0}{1 + k'A_0t} + A_\infty \quad \text{Equation C10}$$

$$k' = \frac{k_{\text{CR}}}{\epsilon_{505} l} \quad \text{Equation C11}$$

Table C10. Fitting parameters used to fit the data in Figure 3.5 using Equation C10.

Sample	A_0	$k' \epsilon_{505} c_0$ (μs^{-1})	A_∞ (10^3)
RuC₉ and 0.0 % ReC₉	0.011 ± 0.003	131 ± 7	1.26 ± 0.07
RuC₉ and 0.4 % ReC₉	0.012 ± 0.003	651 ± 103	0.60 ± 0.09
RuC₉ and 1.6 % ReC₉	0.022	334 ± 12	-0.20 ± 0.04
RuC₁₉ and 0.0 % ReC₁₉	0.019 ± 0.004	100 ± 4	1.79 ± 0.07
RuC₁₉ and 0.4 % ReC₁₉	0.0286 ± 0.0004	73 ± 2	1.50 ± 0.06
RuC₁₉ and 1.6 % ReC₁₉	0.0160 ± 0.0003	149 ± 5	0.54 ± 0.05

C. 8. Fluorescence correlation spectroscopy

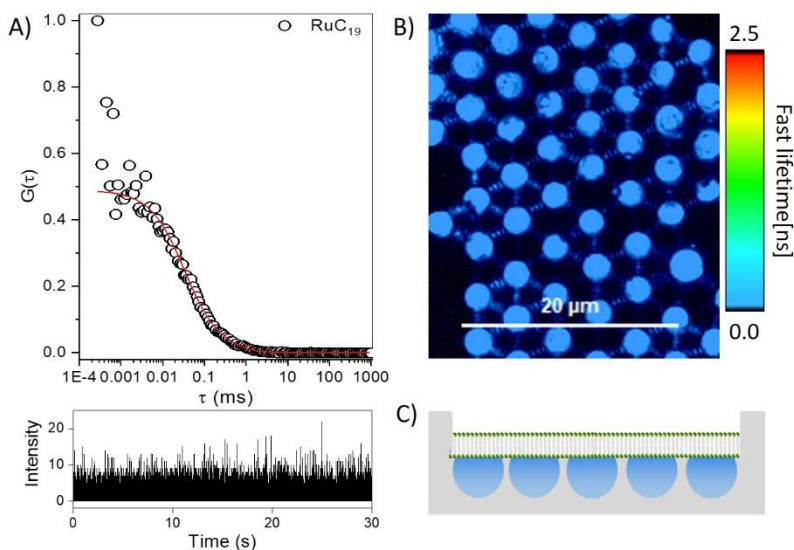


Figure C17. A) top ACF and bottom time trace for diffusion of **RuC₁₉** in acetonitrile. The diffusion coefficient in solution was measured by fitting this curve to a three-dimensional model with D equals $199 \pm 149 \mu\text{m}^2\text{s}^{-1}$ with an α value of 0.99 ± 0.08 . B) Fluorescence lifetime image of MSLBs comprised of DPPC:NaDSPE-PEG2K in a ratio of 100:1. The membrane is labelled with 10 nM DOPE-ATTO 655 and the image shows the fluorescence from the ATTO probe above the pores of the arrays confirming that the bilayer has formed. C) Schematic illustration of aqueous filled microcavity supported lipid bilayer. Note we have included the organic probe to image the bilayer, because the much lower quantum yield of the Ru compound makes it difficult to see it in fluorescence lifetime imaging above the pores against background/scatter from the substrate.

C. 9. Single crystal X-ray crystallography of 4,4'-(C₁₇H₃₅)₂-bpy

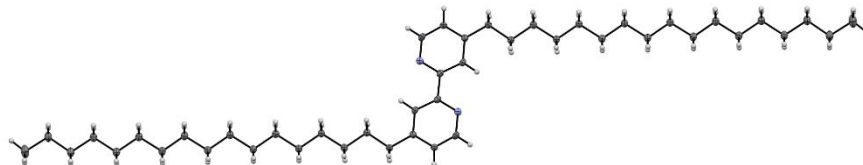


Figure C18. Displacement ellipsoid plots (50% probability level) of 4,4'-(C₁₇H₃₅)₂-bpy at 110(2) K.

Colourless single crystals of 4,4'-(C₁₇H₃₅)₂-bpy were obtained by evaporation of the solvent CDCl₃ at room temperature. The supplementary crystallographic data of 4,4'-(C₁₇H₃₅)₂-bpy can be found under deposition number 2062217 (<https://www.ccdc.cam.ac.uk/structures>). These data are provided free of charge by the joint Cambridge Crystallographic Data Centre and Fachinformationszentrum Karlsruhe.

All reflection intensities were measured at 110(2) K using a SuperNova diffractometer (equipped with Atlas detector) with Cu K α radiation ($\lambda = 1.54178$ Å) under the program CrysAlisPRO (Version CrysAlisPro 1.171.39.29c, Rigaku OD, 2017, Oxford Diffraction / Agilent Technologies UK Ltd, Yarnton, England). The same program was used to refine the cell dimensions and for data reduction. The structure was solved with the program SHELXS-2018/3¹⁰ and was refined on F^2 with SHELXL-2018/3¹⁰. Analytical numeric absorption correction using a multifaceted crystal model was applied using CrysAlisPro. The temperature of the data collection was controlled using the system Cryojet (manufactured by Oxford Instruments). The H atoms were placed at calculated positions using the instruction AFIX 23, AFIX 43 or AFIX 137 with isotropic displacement parameters having values 1.2 or 1.5 Ueq of the attached C atoms.

The structure is ordered. The crystal that was mounted on the diffractometer was a composite of two crystals stuck together (most crystals were significantly twinned). The two crystals are related by a rotation of *ca.* 3.74°

around the *b* direction. The refinement was carried out using the HKLF5 instruction, and the BASF scale factor refines to 0.135(2).

xs2388a	
Crystal data	
Chemical formula	C ₄₄ H ₇₆ N ₂
<i>M_r</i>	633.06
Crystal system, space group	Triclinic, <i>P</i> -1
Temperature (K)	110
<i>a</i> , <i>b</i> , <i>c</i> (Å)	6.4931 (4), 7.0030 (4), 21.8388 (11)
α , β , γ (°)	80.932 (4), 86.310 (5), 86.295 (4)
<i>V</i> (Å ³)	977.10 (10)
<i>Z</i>	1
Radiation type	Cu <i>K</i> α
<i>m</i> (mm ⁻¹)	0.45
Crystal size (mm)	0.29 × 0.09 × 0.02
Data collection	
Diffractometer	SuperNova, Dual, Cu at zero, Atlas
Absorption correction	Analytical CrysAlis PRO 1.171.39.29c (Rigaku OD, 2017) Analytical numeric absorption correction using a multifaceted crystal model based on expressions derived by R.C. Clark & J.S. Reid. ¹¹ Empirical absorption correction using spherical harmonics, implemented in SCALE3 ABSPACK (An Oxford Diffraction Program (1.0.4, gui:1.0.3) © 2005 Oxford Diffraction Ltd.) scaling algorithm.
<i>T_{min}</i> , <i>T_{max}</i>	0.929, 0.991
No. of measured, independent and observed [<i>I</i> > 2 <i>s</i> (<i>I</i>)] reflections	11246, 3934, 1773
<i>R_{int}</i>	0.030
(<i>sin</i> θ / <i>l</i>) _{max} (Å ⁻¹)	0.598
Refinement	
<i>R</i> [<i>F</i> ² > 2 <i>s</i> (<i>F</i> ²)], <i>wR</i> (<i>F</i> ²), <i>S</i>	0.036, 0.093, 0.71
No. of reflections	3934
No. of parameters	210
H-atom treatment	H-atom parameters constrained
$\Delta\rho_{\max}$, $\Delta\rho_{\min}$ (e Å ⁻³)	0.15, -0.18
Computer programs: CrysAlis PRO 1.171.39.29c (Rigaku OD, 2017), SHELXS2018/3 ¹⁰ , SHELXL2018/3 ¹⁰ , SHELXTL v6.10 ¹² .	

C. 10. References

- 1 J. J. Snellenburg, S. Laptенок, R. Seger, K. M. Mullen and I. H. M. van Stokkum, *J. Stat. Softw.*, 2012, **49**, 1–22.
- 2 M. W. H. Hoorens, M. Medved', A. D. Laurent, M. Di Donato, S. Fanetti, L. Slappendel, M. Hilbers, B. L. Feringa, W. J. Buma and W. Szymanski, *Nat. Commun.*, 2019, **10**, 2390.
- 3 G. B. Berselli, N. K. Sarangi, S. Ramadurai, P. V Murphy and T. E. Keyes, *ACS Appl. Bio Mater.*, 2019, **2**, 3404–3417.
- 4 J. E. Collins, J. J. S. Lamba, J. C. Love, J. E. McAlvin, C. Ng, B. P. Peters, X. Wu and C. L. Fraser, *Inorg. Chem.*, 1999, **38**, 2020–2024.
- 5 K. Neuthe, F. Bittner, F. Stiemke, B. Ziem, J. Du, M. Zellner, M. Wark, T. Schubert and R. Haag, *Dyes Pigm.*, 2014, **104**, 24–33.
- 6 L. A. Worl, R. Duesing, P. Chen, L. Della Ciana and T. J. Meyer, *J. Chem. Soc. Dalt. Trans.*, 1991, 849–858.
- 7 N. Ikuta, S. Y. Takizawa and S. Murata, *Photochem. Photobiol. Sci.*, 2014, **13**, 691–702.
- 8 B. Limburg, E. Bouwman and S. Bonnet, *J. Phys. Chem. B*, 2016, **120**, 6969–6975.
- 9 R. S. Khnayzer, V. S. Thoi, M. Nippe, A. E. King, J. W. Jurss, K. A. El Roz, J. R. Long, C. J. Chang and F. N. Castellano, *Energy Environ. Sci.*, 2014, **7**, 1477–1488.
- 10 G. M. Sheldrick, *Acta Crystallogr. Sect. C*, 2015, **71**, 3–8.
- 11 R. C. Clark and J. S. Reid, *Acta Crystallogr. Sect. A*, 1995, **51**, 887–897.
- 12 G. M. Sheldrick, *Acta Crystallogr. Sect. A*, 2008, **64**, 112–122.

Supporting information for Chapter 4

D.1. EPR Spectroscopy

Figure D1 shows the EPR spectrum of **CoC₁₂** at 10 K. The broad and highly anisotropic signal indicates the presence of a high spin Co(II) species, with examples present in literature.^{1,2} Simulations were performed with a g tensor of $g = [g_{xx} \ g_{yy} \ g_{zz}] = [4.79 \ 4.25 \ 1.99]$ and a hyperfine splitting due to the coupling with ⁵⁹Co nucleus ($I = 7/2$) of $A_{zz} = 340$ MHz, which can be seen as eight lines at 350 mT (g_{zz} direction), see Figure D1. As line broadening an H-strain was used with the components 1500 MHz, 4800 MHz, and 240 MHz in the respective g tensor directions.

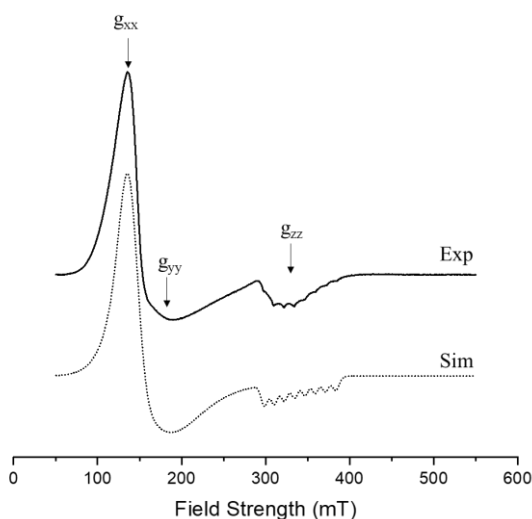


Figure D1. EPR spectrum (solid line) obtained from the frozen solution state of **CoC₁₂** in acetonitrile at 10 K and the corresponding simulation (dotted line). Experimental conditions: microwave frequency 9.502 GHz, microwave power 20 mW, modulation frequency 100 kHz, modulation amplitude 10 G. Simulation parameters: $g = [g_{xx} \ g_{yy} \ g_{zz}] = [4.79 \ 4.25 \ 1.99]$, H-strain (MHz) = [1500 4800 240], hyperfine coupling A_{zz} of 340 MHz.

D.2. Local concentration calculation

When the bulk concentration of the photosensitiser or catalyst is known (i.e. 50 μM **RuC₁₂** and 5 μM **CoC₁₂**), the local concentration in the membrane can be calculated as follows³:

- The average area of DPPC lipid equals 0.7 nm²/molecule.⁴
- Knowing the lipid bulk concentration (5 mM) and the sample volume (3 mL), the number of mole of lipid molecules in the sample is 15 μmol , from which we can deduct the full surface of all lipid bilayers in the sample, knowing there are two faces on a bilayer: the full bilayer surface is $0.7 \text{ nm}^2 * 15 \times 10^{-6} \text{ mol} * 6.022 \times 10^{23} \text{ mol}^{-1} / 2 = 3.15 \times 10^{18} \text{ nm}^2$.
- From the total area of bilayer and the average liposome diameter by DLS (177.9 nm), we can calculate the area of one liposome ($4\pi(d/2)^2$), and the number of liposomes, hence the liposome concentration (in M): $d = 177.9 \text{ nm}$, area of one liposome = $4\pi r^2 \rightarrow r = 177.9/2 = 88.95 \text{ nm}$. The area of one liposome is $9.94 \times 10^4 \text{ nm}^2$.
- Total numbers of liposomes = $3.15 \times 10^{18} \text{ nm}^2 / 9.94 \times 10^4 \text{ nm}^2 = 0.32 \times 10^{14}$.
- Knowing the thickness of a bilayer (4 nm), the area of a liposome ($4\pi r^2$), calculate the volume of the bilayer of one liposome (thickness $\times 4\pi r^2$): Volume of bilayer of one liposome = $9.94 \times 10^4 \text{ nm}^2 * 4 \text{ nm} = 3.98 \times 10^5 \text{ nm}^3$.
- From the volume of the bilayer of one liposome and the total number of liposomes in the sample, we can calculate the total volume of all bilayers in the sample: $0.32 \times 10^{14} \times 3.98 \times 10^5 \text{ nm}^3 = 1.26 \times 10^{19} \text{ nm}^3 = 1.26 \times 10^{-8} \text{ m}^3 = 1.26 \times 10^{-5} \text{ L} = 1.26 \times 10^{-2} \text{ mL} = 0.0126 \text{ mL}$
- Knowing the ratio of total bilayer volume vs. bulk volume (3 mL), we can calculate the local concentration of each species in the volume of the bilayer: ratio between bulk and local concentration is $3 \text{ mL} / 0.0126 \text{ mL} = 238$, local concentration of **RuC₁₂** = $50 \mu\text{M} \times 238 = \mathbf{11.9 \text{ mM}}$ and local concentration **CoC₁₂** = $5 \mu\text{M} \times 238 = \mathbf{1.19 \text{ mM}}$.

D.3. Electrochemistry

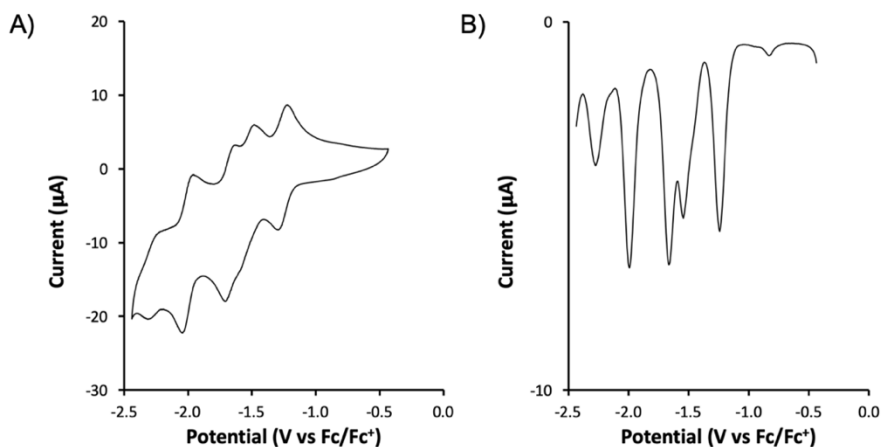


Figure D2. Cyclic voltammogram (A) and differential pulse voltammogram (B) of a solution of CoC_{12} (1 mM) in degassed acetonitrile with 0.1 M Bu_4NPF_6 electrolyte, measured at 25 °C. The cyclic voltammogram and the differential pulse voltammogram were obtained at a scanning rate of 100 mV s^{-1} and 50 mV s^{-1} respectively, with a glassy carbon working electrode, Ag/AgCl reference electrode, and a Pt wire auxiliary electrode. The reductive redox potentials of CoC_{12} were found to be -1.24 , -1.54 , -1.66 , -1.99 , and $-2.27 \text{ V vs Fc}/\text{Fc}^+$.

D.4. Dynamic light scattering

Table D1. Summary of DLS results obtained of the liposome stock and after three independent light irradiation experiments ($t_{irr} = 19$ h, $\lambda_{irr} = 450$ nm) of photocatalytic liposomes prepared from DPPC, NaDSPE-PEG2K, **RuC₁₂**, and **CoC₁₂**. The control experiments (one of the components missing) were performed once.

Lipid	[NaHAsc]	[TCEP]	[RuC ₁₂]	[CoC ₁₂]	pH	Before irradiation ^[a]			After irradiation ^[b]		
						d (nm)	PDI	pH ^[c]	d (nm) ^[c]	PDI ^[c]	
DPPC	0.1 M	0.1 M	50 μ M	50 μ M	5.0	154.7	0.089	4.8 \pm 0.0	154.6 \pm 1.9	0.083 \pm 0.010	
DPPC	0.1 M	0.1 M	50 μ M	25 μ M	5.0	159.3	0.140	4.7 \pm 0.1	161.0 \pm 1.6	0.161 \pm 0.014	
DPPC	0.1 M	0.1 M	50 μ M	5 μ M	5.0	177.9	0.122	4.8 \pm 0.0	171.1 \pm 2.5	0.136 \pm 0.034	
DPPC	0.1 M	0.1 M	50 μ M	1 μ M	5.0	172.1	0.109	4.8 \pm 0.1	165.9 \pm 1.4	0.109 \pm 0.020	
DPPC	0.1 M	0.1 M	50 μ M	5 μ M	3.0	146.5	0.125	2.6 \pm 0.2	147.0 \pm 1.5	0.145 \pm 0.027	
DPPC	0.1 M	0.1 M	50 μ M	5 μ M	4.0	166.5	0.116	4.0 \pm 0.0	156.2 \pm 0.1	0.115 \pm 0.011	
DPPC	0.1 M	0.1 M	50 μ M	5 μ M	6.0	205.3	0.148	6.3 \pm 0.0	> 1000	0.466 \pm 0.033	
DPPC	0.1 M	0.1 M	25 μ M	5 μ M	5.0	161.4	0.120	4.9 \pm 0.1	157.8 \pm 3.6	0.138 \pm 0.026	
DMPC	0.1 M	0.1 M	50 μ M	5 μ M	4.0	158.8	0.155	3.9 \pm 0.0	151.7 \pm 0.9	0.142 \pm 0.008	
DSPC	0.1 M	0.1 M	50 μ M	5 μ M	4.0	171.0	0.101	3.8 \pm 0.1	168.8 \pm 8.3	0.156 \pm 0.021	
DPPC	0.1 M	0.1 M	50 μ M	-	5.0	177.8	0.118	4.7	188.8	0.187	
DPPC	0.1 M	0.1 M	-	25 μ M	5.0	183.8	0.116	4.7	187.2	0.116	
DPPC	0.1 M	-	50 μ M	25 μ M	5.0	157.2	0.120	5.1	165.1	0.156	
DPPC	-	0.1 M	50 μ M	25 μ M	5.0	162.7	0.120	5.1	237.3	0.220	

^[a] Experimental conditions of the liposome stock solutions: [DPPC] = 17.5 mM, [NaDSPE-PEG2K] = 175 μ M, [RuC₁₂] = 175 μ M, and [CoC₁₂] = 3.5, 17.5, 87.5, or 175 μ M in 0.1 M TCEP and 0.1 M NaHAsc solutions at 25 °C. The concentrations [RuC₁₂] and [CoC₁₂] indicate theoretical concentrations (before extrusion). ^[b] Experimental conditions for the photocatalytic liposome samples after irradiation: [DPPC] = 5 mM, [NaDSPE-PEG2K] = 50 μ M, [RuC₁₂] = 50 μ M, and [CoC₁₂] = 1, 5, 25, or 50 μ M in 0.1 M TCEP and 0.1 M NaHAsc solutions at 25 °C. ^[c] Average and the mean absolute deviation over three independent irradiation experiments.

D.5. Control experiments

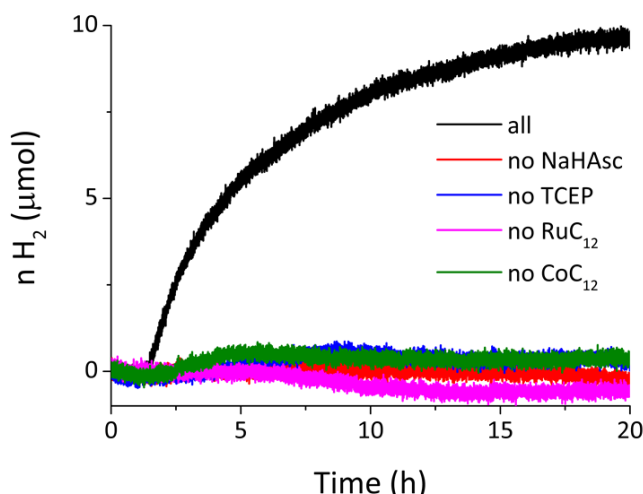


Figure D3. Photocatalytic H₂ generation with liposomes prepared from DPPC, NaDSPE-PEG2K, NaHAsc, TCEP, RuC₁₂, and CoC₁₂ (black curve) and liposomes prepared in absence of one of the components (NaHAsc; red curve, TCEP; blue curve, RuC₁₂; pink curve, or CoC₁₂; green curve). The samples were left in the dark for 1 h and then irradiated with blue light for 19 h. Experimental conditions: [DPPC] = 5 mM, [NaDSPE-PEG2K] = 50 μM, [RuC₁₂] = 0 or 50 μM, [CoC₁₂] = 0 or 25 μM; argon-saturated 0 or 0.1 M NaHAsc and 0 or 0.1 M TCEP aqueous solution, pH = 5, volume 3.5 mL, temperature 25 °C, λ_{irr} = 450 nm, P = 10.6 mW, Φ₀ = 13.7 nmol/s. Bulk concentrations [RuC₁₂] and [CoC₁₂] indicate theoretical concentrations assuming no losses during liposome preparation.

D.6. Quantum yield determination

The quantum yield (QY) for the photocatalytic proton reduction reaction for the fully optimised system (DPPC lipid, 5 μM CoC₁₂, 50 μM RuC₁₂, pH 4) was obtained using the following equation:

$$QY = \frac{\text{\# photochemical events}}{\text{\# photons absorbed by photoactive molecule}} = \frac{TOF_{\max} n_{CoC_{12}}}{\Phi_0 (1 - 10^{-A_{ref}})} \quad \text{Equation D1}$$

In Equation D1, TOF_{max} is the maximum rate of H₂ formation per catalyst molecule in s⁻¹ (TOF_{max} = 81 h⁻¹ = 0.0225 s⁻¹, Table 4.1) and n_{CoC₁₂} is amount

of catalyst molecules in nmol ($5 \mu\text{M CoC}_{12}$ in a 3.5 mL solutions equals 17.5 nmol), Φ_0 the photon flux of the LED in nmol/s, and $(1 - 10^{-A_{\text{ref}}})$ equals the probability of photon absorption by the liposome solution at the irradiation wavelength. Ferrioxalate actinometry was performed to quantify Φ_0 provided by the light source (13.7 nmol/s derived from Figure D4).^{5,6} In this particular system, A_{ref} was not measured experimentally but calculated using the molar absorption coefficients of **RuC**₁₂ ($\epsilon = 1.32 \times 10^4 \text{ M}^{-1} \text{ cm}^{-1}$ at $\lambda = 450 \text{ nm}$ in MeOH)⁷, the pathlength of the photochemical reactor (2.6 cm), and the bulk concentration ($50 \mu\text{M}$) of **RuC**₁₂. Indeed, the experimentally measured absorbance of the photocatalytic liposome solution had a significant deviation from the Beer-Lambert law generated by the scattering due to the presence of the liposomes, in particular in the near-UV domain.⁷ Using these values, the QY for electron transfer was determined to be 0.029 at the maximum rate of the reaction.

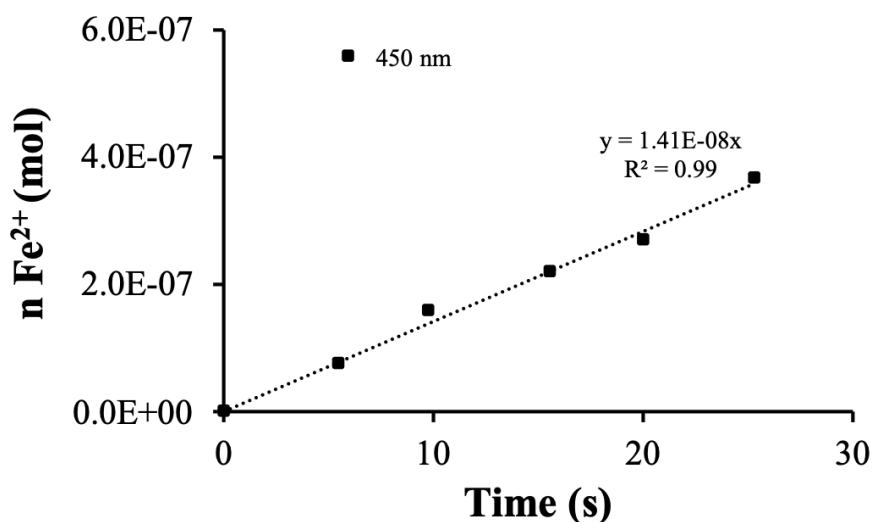


Figure D4. Ferrioxalate actinometry was performed to determine the photon flux Φ_0 (13.7 nmol/s) of the used light source ($\lambda = 450 \text{ nm}$, $P = 10.6 \text{ mW}$) within the photocatalysis setup.^{5,6}

D.7. References

- 1 J.-S. Park, T.-J. Park, K.-H. Kim, K. Oh, M.-S. Seo, H.-I. Lee, M.-J. Jun, W. Nam and K.-M. Kim, *Bull. Korean Chem. Soc.*, 2006, **27**, 193–194.
- 2 D. Skrzypek, I. Madejska and J. Habdas, *Solid State Sci.*, 2007, **9**, 295–302.
- 3 A. Pannwitz and S. Bonnet, in *Supramolecular Catalysts — Design, Fabrication, and Applications*, 2020, pp. 495–528.
- 4 D. Marsh, *Handbook of Lipid Bilayers*, CRC Press, 2013.
- 5 C. G. Hatchard, C. A. Parker and E. J. Bowen, *Proc. R. Soc. Lond. Ser. Math. Phys. Sci.*, 1956, **235**, 518–536.
- 6 J. N. Demas, W. D. Bowman, E. F. Zalewski and R. A. Velapoldi, *J. Phys. Chem.*, 1981, **85**, 2766–2771.
- 7 D. M. Klein, S. Rodríguez-Jiménez, M. E. Hoefnagel, A. Pannwitz, A. Prabhakaran, M. A. Siegler, T. E. Keyes, E. Reisner, A. M. Brouwer and S. Bonnet, *Chem. Eur. J.*, 2021, **27**, 17203–17212.

Samenvatting in het Nederlands

Kunstmatige fotosynthese heeft veel potentie voor de productie van duurzame brandstoffen uit ruim beschikbare bronnen, zoals water, koolstofdioxide (CO₂) en zonlicht. In een kunstmatig fotosynthetisch systeem worden twee chemische reacties gecombineerd, zoals de oxidatie van water en de reductie van protonen of CO₂. Om een dergelijk systeem te maken is het cruciaal om te beschikken over: a) efficiënte absorptie van het licht, b) stabiele katalysatoren voor de oxidatie- en reductiereactie, c) proton- en elektrontransport tussen de locatie waar oxidatie plaatsvindt en de locatie waar reductie plaatsvindt, d) efficiënte ladingsscheiding, en e) een sterk, fotostabiel membraan dat zo min mogelijk moleculaire componenten lekt. Bij natuurlijke fotosynthese wordt aan deze voorwaarden voldaan door middel van compartimentalisatie. Hierbij worden de belangrijkste componenten van het fotosynthetisch systeem van elkaar gescheiden. Een voorbeeld hiervan is het in groene planten voorkomende zuurstof-vormende complex bestaande uit fotosysteem I en II en de elektrontransportketen, die rondom de lipide dubbellaag van het thylakoïdemembraan gelokaliseerd zijn. Het gebruik van bolvormige lipide membranen (zoals liposomen), die het biologische thylakoïdemembraan nabootsen, is een veelbelovende benadering om oxidatiereacties en reductiereacties van elkaar te scheiden door ze onder te brengen in eigen compartimenten. Dit maakt ladingsscheiding gemakkelijker en daarnaast worden ladingsrecombinatie of andere nevenreacties voorkomen. In het in dit proefschrift beschreven onderzoek is geprobeerd om een volledig kunstmatig fotosynthetisch systeem op basis van liposomen te maken. Verschillende belangrijke mijlpalen op deze weg werden bereikt: 1) unidirectionele elektronenoverdracht over een liposomaal membraan van een elektronendonor gelokaliseerd aan de binnenkant van het liposoom naar een elektronenacceptor buiten het liposoom (**Hoofdstuk 2**), en 2) fotokatalytische reductie van CO₂ (**Hoofdstuk 3**) en van protonen (**Hoofdstuk 4**) aan het oppervlak van liposomen. In het werk beschreven in **Hoofdstuk 2** en **Hoofdstuk 5** is daarnaast speciale aandacht besteed aan de

(foto)stabiliteit van het membraan en licht-geïnduceerde lekkage, aspecten die in eerdere studies onderbelicht bleven.

In **Hoofdstuk 2** beschrijven we de synthese van twee metallopeptiden (**WALP23-Ru₂** en **WALP23-Re₂**), die in een membraan ingebed konden worden. **WALP23-Ru₂** en **WALP23-Re₂** zijn ontworpen om licht-geïnduceerde elektronenoverdracht te bewerkstelligen van een elektronendonor in het binnenste compartiment van het liposoom naar een elektronenacceptor buiten het liposoom. Bij bestraling met licht leek **WALP23-Ru₂** snelle elektronenoverdracht door het lipide membraan te geven. Helaas bleek dat de waargenomen fotoreactie het resultaat was van licht-geïnduceerde lekkage van het membraan, waarbij de elektronendonor vrijkwam, gevolgd door licht-geïnduceerde elektronenoverdracht aan de buitenkant van het liposoom. Deze interpretatie werd ondersteund door de toevoeging van Zn²⁺-ionen aan de oplossing. De aanwezigheid van Zn²⁺-ionen in de oplossing verhindert de fotoreactie door het deactiveren van de elektronendonormoleculen, die door het membraan lekten. Bovendien toonden moleculaire dynamica simulaties aan dat de metallopeptiden niet alleen de verwachte oriëntatie aannemen waarbij ze door het membraan heen steken, maar ook een andere oriëntatie kunnen aannemen waarin ze gebonden zijn aan één kant van de lipide dubbellaag. Met **WALP23-Re₂** werd ook elektronenoverdracht gevonden na bestraling met licht, maar in dit geval vond elektronenoverdracht nog steeds plaats na de toevoeging van Zn²⁺-ionen aan de oplossing. **WALP23-Re₂** is daarmee een van de weinige moleculen die in staat is echte transmembraan-elektronenoverdracht te realiseren, terwijl **WALP23-Ru₂** dat niet kan. Dit werk benadrukt de mogelijkheden van kunstmatige metallopeptiden als transmembraanelektronentransporteurs en het belang van het uitvoeren van lekkagestudies voor de ontwikkeling van kunstmatige fotosynthetische systemen op basis van liposomen.

In **Hoofdstuk 3** wordt de synthese beschreven van een reeks op rhenium gebaseerde CO₂-reductie katalysatoren [Re(4,4'-(C_nH_{2n+1})₂-bpy)(CO)₃Cl] (**ReC_n**; 4,4'-(C_nH_{2n+1})₂-bpy = 4,4'-dialkyl-2,2'-bipyridine) en op ruthenium gebaseerde fotosensibilisatoren [Ru(bpy)₂(4,4'-(C_nH_{2n+1})₂-bpy)](PF₆)₂ (**RuC_n**)

met verschillende alkylketens ($n = 0, 9, 12, 15, 17$ en 19). ReC_n en RuC_n werden geïmmobiliseerd op liposomen (volledige systeem = C_n) om fotokatalytische CO_2 -reductie uit te voeren in de aanwezigheid van natrium ascorbaat (NaHAsc) en tris(2-carboxyethyl)phosphine (TCEP) als elektronendonoren. De resultaten van het fotokatalytische proces in de verschillende C_n liposomen bleken sterk afhankelijk te zijn van de lengte van de alkylketen: het omzettingstal voor CO -productie nam af wanneer de lengte van de alkylketen toenam van C_9 naar C_{19} . Deze trend werd geanalyseerd door het percentage RuC_n en ReC_n , dat was geïmmobiliseerd op de liposomen, te kwantificeren met behulp van een inductief gekoppelde plasmamassaspectrometer, door het meten van de snelheid van elektronenoverdracht met behulp van tijdsopgeloste spectroscopie en door laterale diffusiemetingen met behulp van fluorescentielevensduurcorrelatiespectroscopie. De ICP-MS metingen toonden aan dat de lengte van de alkylketen geen belangrijk effect had op de efficiëntie van de immobilisatie van RuC_n en ReC_n . De tijdsopgeloste spectroscopiemetingen onthulden dat elektronen inderdaad sneller werden overgedragen tussen RuC_9 en ReC_9 dan tussen RuC_{19} en ReC_{19} , wat de waargenomen fotokatalytische trend ondersteunde. Tenslotte toonden de laterale diffusiemetingen aan dat de rutheniumcomplexen bestaan als een mengsel van twee subpopulaties in het membraan: een langzame en een snelle populatie. De hogere bijdrage van de snel diffunderende component voor het C_9 systeem, vergeleken met die van het C_{19} systeem, correleerde goed met de grotere elektronenoverdrachtssnelheid tussen de Ru- en Re-complexen die in het eerste geval werd waargenomen. Dit werk heeft een belangrijke voortgang opgeleverd in het fundamentele begrip van supramoleculaire samenstellingen van katalysatoren en fotosensibilisatoren, die op lipide membranen zijn geïmmobiliseerd: langere alkylketens zijn nadelig voor fotokatalyse op liposomen, omdat het de moleculen te hydrofoob maakt, waardoor ze in de kern van het membraan vast komen te zitten. Hierbij verliezen ze hun vermogen om te diffunderen en om elektronen van molecuul tot molecuul te transporteren.

In **Hoofdstuk 4** wordt de synthese van het nieuwe gealkyleerde kobaltpolypyridylcomplex CoC_{12} beschreven. CoC_{12} werd bestudeerd als een

mogelijke protonreductiekatalysator voor fotokatalytische waterstofgeneratie op liposomen in combinatie met de gealkyleerde fotosensibilisator **RuC₁₂** (beschreven in **Hoofdstuk 3**) en NaHAsc en TCEP als elektronendonoren. Het systeem werd geoptimaliseerd door te variëren in de membraanconcentratie van **CoC₁₂** en **RuC₁₂**, de pH en de lipide samenstelling. Een maximaal omzetgetal van 161 H₂ moleculen per katalysator molecuul werd bereikt, wat even hoog is als die van de beste fotokatalytische liposoomsystemen die tot nu toe in de literatuur gepubliceerd zijn. Stabiliteitsstudies toonden aan dat de katalytische activiteit herwonnen kon worden door de toevoeging van vers **RuC₁₂** na een eerste voltooide fotokatalytische meting. Toevoeging van vers **CoC₁₂** leidde echter niet tot verdere waterstofproductie, wat aantoont dat de ontleding van **RuC₁₂** de factor was die de waterstofproductie beperkte. In eerder werk werd de fotokatalytische protonreductie op liposomen beperkt door de stabiliteit van de katalysator in plaats van de stabiliteit van de fotosensibilisator. Dit werk is een belangrijke stap naar een door liposomen ondersteund fotokatalytisch watersplitsingssysteem dat volledig gebaseerd is op ruim beschikbare elementen. Hiervoor is het van belang dat de ruthenium fotosensibilisator vervangen kan worden door een fotosensibilisator die zowel stabiel is alsook gebaseerd op niet-zeldzame elementen.

Hoofdstuk 5 heeft geen betrekking op kunstmatige fotosynthese, maar het beschrijft een samenwerking met de Universiteit van Amsterdam. Een membraanlekkagetest, vergelijkbaar met die beschreven in **Hoofdstuk 2**, is gebruikt om de stabiliteit te meten van liposoommembranen tegen inhoudslekage tijdens verneveling. Verneveling is een veelgebruikte techniek voor medicijnafgifte via de longen. Om dit te kunnen bestuderen werd het zelfdovende fluorofoor calceïne ingekapseld in de binnenste waterige kern van liposomen. Vervolgens werd de lekkage, die werd geïnduceerd door verneveling met verschillende apparaten, bestudeerd met behulp van emissiespectroscopie. De vibrerende mesh-vernevelaars gaven meer dan tien keer zoveel ingekapseld materiaal vrij dan de continue jet-vernevelaars, omdat de energieën die bij het vernevelingsproces betrokken zijn veel groter zijn. Al met al biedt dit werk een uitstekende methodologie

om te beoordelen of een bepaalde liposomale formulering geschikt is voor studies waarbij membraanlekkage moet worden vermeden (**Hoofdstuk 2**). Het toont ook aan dat schijnbaar stabiele liposomen onstabiel kunnen worden bij het uitoefenen van externe stress, zoals door mechanische vernevelaars.

List of Publications

“Performance of a non-local van der Waals density functional on the dissociation of H₂ on metal surfaces”

Mark Wijzenbroek, [David M. Klein](#), Bauke Smits, Mark F. Somers, and Geert-Jan Kroes, *The Journal of Physical Chemistry A*, **2015**, *119*, 12146-12158.

“Roadmap towards solar fuel synthesis at the water interface of liposome membranes”

Andrea Pannwitz*, [David M. Klein*](#), Santiago Rodríguez-Jiménez, Carla Casadevall, Hongwei Song, Erwin Reisner, Leif Hammarström, and Sylvestre Bonnet, *Chemical Society Reviews*, **2021**, *50*, 4833-4855.

* These authors contributed equally to this work.

“Degradation of lipid-based drug delivery formulations during nebulization”

[David M. Klein](#), Albert Poortinga, Frank M. Verhoeven, Daniel Bonn, Sylvestre Bonnet, and Cees J. M. van Rijn, *Chemical Physics*, **2021**, *547*, 111192.

“Shorter Alkyl Chains Enhance Molecular Diffusion and Electron Transfer Kinetics Between Photosensitisers and Catalysts in CO₂-Reducing Photocatalytic Liposomes”

[David M. Klein](#), Santiago Rodríguez-Jiménez, Marlene E. Hoefnagel, Andrea Pannwitz, Amrutha Prabhakaran, Maxime A. Siegler, Tia E. Keyes, Erwin Reisner, Albert M. Brouwer, and Sylvestre Bonnet, *Chemistry – A European Journal*, **2021**, *27* (68), 17203-17212.

“A stable alkylated cobalt catalyst for photocatalytic H₂ generation in liposomes”

[David M. Klein](#), Leonardo Passerini, Martina Huber and Sylvestre Bonnet, *ChemCatChem*, **2022**, *accepted*.

“Interfacial characterization of ruthenium-based amphiphilic photosensitizers”

Yousra Timounay, Andrea Pannwitz, David M. Klein, Anne-Laure Biance, Marlene E. Hoefnagel, Indraneel Sen, Alain Cagna, Marie le Merrer, and Sylvestre Bonnet, *Langmuir*, **2022**, *accepted*.

“A lock-and-kill anticancer photoactivated chemotherapy agent”

Erik P. van Geest, Sina K. Götzfried, David M. Klein, Vadde Ramu, Nadiya Salitra, Sorraya Popal, Corjan van der Griend, Xuequan Zhou, Gregory F. Schneider, and Sylvestre Bonnet, *manuscript submitted*.

“Unidirectional transmembrane photoinduced electron transfer with membrane-embedded metallopeptides”

David M. Klein, Xinmeng Li, Aimee L. Boyle, Rianne van der Pol, G. J. Agur Sevink, Albert M. Brouwer, and Sylvestre Bonnet, *manuscript in preparation*.

Curriculum Vitae

The author of this thesis, David Maarten Klein, was born in Haarlem, the Netherlands, on December 20th, 1993. In 2011 he graduated from the Stedelijk Gymnasium Haarlem. From 2012 to 2015, he performed his BSc studies Molecular Science and Technology at Leiden University and Delft University, with a final thesis entitled “The crystal structure of solid N₂O: insights from first-principles calculations” under the supervision of dr. J. Meyer at Leiden University. From 2015 to 2017, he followed the Chemistry MSc program at Leiden University, with the specialisation Energy & Sustainability, and in parallel he followed the class of excellence “Sustainability: the Molecular Approach” from the Holland Research School of Molecular Chemistry (HRSMC), a collaboration between Leiden University, the University of Amsterdam (UvA), and the Free University of Amsterdam. During his MSc studies, he won the “VNCI Topsector Chemiebeurs” prize (2015) and as a result he performed an internship at LyondellBasell (Rotterdam Botlek). He graduated cum laude in 2017, with a thesis entitled “Developing stable photosensitizers for photocatalytic water oxidation” under the supervision of Prof. dr. S. Bonnet.

His PhD research proposal “Unidirectional electron transfer across lipid bilayers for artificial water splitting using transmembrane peptide-photosensitizer conjugates and liposomes” was granted by the HRSMC. He started hence his PhD studies at Leiden University under the co-supervision of Prof. dr. S. Bonnet and Prof. dr. A. M. Brouwer (UvA). During his PhD studies, he collaborated with dr. S. Rodríguez-Jiménez, dr. C. Casadevall, and Prof. dr. E. Reisner from the University of Cambridge, dr. H. Song and Prof. dr. L. Hammarström from Uppsala University, A. Prabhakaran and Prof. dr. T. Keyes from Dublin University, dr. A. Pannwitz from Ulm University, dr. A. Boyle, dr. A. Sevink, and dr. X. Li from Leiden University, dr. M. Siegler from Johns Hopkins University, and dr. A. Poortinga, Prof. dr. D. Bonn and Prof. dr. C. van Rijn from UvA. He supervised four MSc students and worked as a teaching assistant for the bachelor courses “Practicum Basisvaardigheden”, “Practicum Organische Chemie”, “Inorganische Chemie”, and “Leren

Onderzoeken". Furthermore, he took several post-graduate courses including the HRSMC courses "High Impact Writing" and the Leiden University Courses "Scientific Conduct in Science", "Effective communication in Science", "Communication in Science", "Job Orientation", and "Job Search Skills". He took part within the organisation committee of the HRSMC Sustainability Workshop (2019) and he was also member of the HRSMC PhD platform from 2019 – 2021.

Parts of the results reported in this thesis were presented at several (inter)national conferences as listed below:

- International Conference on Photochemistry, virtual conference, July 2021 (oral, runner-up for best oral presentation award)
- NWO CHEmistry As INnovating Science (CHAINS), virtual conference, December 2021 (poster)
- Symposium of the Holland Research School of Molecular Chemistry, Amsterdam, The Netherlands, November 2019 (poster) and March 2022 (poster)
- Netherlands' Catalysis and Chemistry Conference, Noordwijkerhout, The Netherlands, March 2018 (poster) and March 2019 (poster)
- Autumn School: Advanced Metal-Organic Chemistry and Catalysis, Doorn, The Netherlands, September-October 2018 (poster)

Acknowledgements

The Netherlands Organization for Scientific Research (NWO) is acknowledged for financial support *via* a Holland Research School of Molecular Chemistry (HRSMC) PhD Fellowship. I would like to thank dr. Michael Meijer and dr. Lucien Lameijer for introducing me to the basics of MCBIM chemistry, and for fruitful discussions on chemical synthesis. Furthermore, I would like to thank Dr. Andrea Pannwitz for our weekly literature discussions, which eventually resulted in a peer-reviewed tutorial review (Chapter 1) with the help of Dr. Santiago Rodríguez-Jiménez, Dr. Carla Casadevall, Dr. Hongwei Song, Prof. dr. Erwin Reisner, and Prof. dr. Leif Hammerström. I also would like to thank Andrea, Santiago and Erwin together with Amrutha Prabhakran, Prof. dr. Tia Keyes and dr. Maxime Siegler for their contributions to Chapter 3. Dr. Xinmeng Li, Rianne van der Pol and dr. Agur Sevink are acknowledged for their fruitful collaboration on molecular dynamics simulations of the metallopeptides in Chapter 2. Dr. Aimee Boyle is thanked for her help on preparing the WALP23 peptide and for fruitful scientific discussions on peptide chemistry. Furthermore, Leonardo Passerini and Martina Huber are acknowledged for the EPR measurement on CoC₁₂ in Chapter 4. Moreover, I would like to thank Dr. Albert Poortinga, Prof. dr. Daniel Bonn and Prof. dr. Cees van Rijn for our enjoyable project together on nebulisers (Chapter 5). I would like to thank dr. Erik van Geest for providing me the opportunity to join his project on anti-cancer liposomes together with dr. Sina Götzfried and dr. Ramu Vadde. I would like to thank Andrea, dr. Yousra Timounay, dr. Alain Cagna, dr. Marie le Merrer, and dr. Anne-Laure Bianco for our inspiring meetings about the soapy character of alkylated ruthenium photosensitisers.

I also would like to thank Andrea and Ramu for their technical assistance with confocal microscopy measurements, Dr. Sipeng Zheng, Hans van der Elst, Nico Meeuwenoord, dr. Bobby Florea, and Laura Opdam for MS measurements and ICP measurements, Maximilian Paradiz Dominquez and Michiel Hilbers for their technical assistance with time-resolved absorption spectroscopy measurements at the University of Amsterdam and for their assistance with Glotaran.

Additionally, I would like to thank all the people from the Molecular Photonics group at the University of Amsterdam and the MCBIM group at Leiden University for the nice atmosphere and the enjoyable time together. Especially, I would like to thank the photocatalysis team, Andrea, dr. Agnese Amati, Chengyu Liu, Ehider Polanco, Vasiliki Tsina, for our great time together, our scientific discussions, and for your help on running photocatalysis reactions when I was in quarantine due to covid-restrictions. I also would like to specially thank Christian Marvelous for our discussions on cobalt chemistry. Furthermore, I would like to thank Andrea, Sina, dr. Dennis Dam, dr. Quinten Ducarmon, Olivier Rutgers and Sarah Davidesko for proofreading parts of this thesis. Moreover, I would like to thank Ernst Muller for helping me to design the cover with support of Inbal and Rachel. I would also like to thank my MSc students Huub Adriaanse, Yaroslav Shelomov, Imme Schuringa, and Marlene Hoefnagel for their contributions to this thesis and for giving me the opportunity to experience the role of a supervisor. I would like to acknowledge Prof. dr. Lies Bouwman for advising me to follow the HRSMC honours master, which eventually resulted in the HRSMC research proposal that funded this PhD work, and for her supervision in my first two years of my PhD. Finally I would like to acknowledge my promotores Prof. dr. Sylvestre Bonnet and Prof. dr. Fred Brouwer for their careful supervision, scientific discussions, and support. It was really a pleasure to have you both as my supervisors.

Last but not least, I would like to thank my wife Chawa for supporting me during this PhD journey, first as girlfriend, then as fiancée and finally as wife. I would like to thank our sons Yoav and Elon for letting me become more productive at work in the final years of my PhD as well as for providing me the possibility to work in the middle of the night.

